

GEOLOGICAL INTERPRETATIONS OF A LOW-BACKSCATTER ANOMALY
FOUND IN 12-KHZ MULTIBEAM DATA ON THE NEW JERSEY
CONTINENTAL MARGIN

BY

EDWARD M. SWEENEY, JR.
BA, Bowdoin College, 2003

THESIS

Submitted to the University of New Hampshire
in Partial Fulfillment of
the Requirements for the Degree of

Master of Science
in
Earth Sciences: Ocean Mapping

December, 2008

UMI Number: 1463240

INFORMATION TO USERS

The quality of this reproduction is dependent upon the quality of the copy submitted. Broken or indistinct print, colored or poor quality illustrations and photographs, print bleed-through, substandard margins, and improper alignment can adversely affect reproduction.

In the unlikely event that the author did not send a complete manuscript and there are missing pages, these will be noted. Also, if unauthorized copyright material had to be removed, a note will indicate the deletion.

UMI[®]

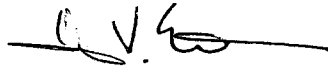
UMI Microform 1463240

Copyright 2009 by ProQuest LLC.

All rights reserved. This microform edition is protected against unauthorized copying under Title 17, United States Code.

ProQuest LLC
789 E. Eisenhower Parkway
PO Box 1346
Ann Arbor, MI 48106-1346

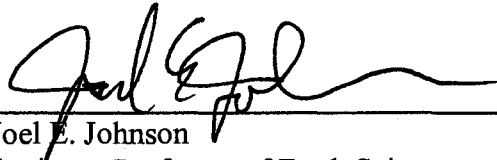
This thesis has been examined and approved.



Thesis Director
James V. Gardner
Research Professor of Earth Sciences



Larry A. Mayer
Professor of Ocean Engineering and Earth Sciences



Joel E. Johnson
Assistant Professor of Earth Sciences



William A Schwab
Geologist, U.S. Geological Survey

October 16th 2008

Date

DEDICATION

This thesis is dedicated to my family and friends for believing in me during my road through graduate school and especially to my mom and dad for always pushing me to do my best both academically and in life.

ACKNOWLEDGEMENTS

After three years of work, there are many people who I have to thank for my master's thesis research at the Center for Coastal and Ocean Mapping (CCOM). Many, many thanks to my advisor Jim Gardner, as well as my thesis committee members Joel Johnson, Larry Mayer and Bill Schwab who have patiently helped me through my graduate research work. Thank you to the National Oceanic and Atmospheric Administration (NOAA) and the Geological Society of America (GSA) for funding my research through NOAA grant NA05NOS4001153 and the GSA graduate student grant program. Thank you again to NOAA and also CCOM and Naval Oceanographic Office (NAVO) for collecting the U.S. Atlantic margin multibeam sonar data set used for this project. Thanks to Steve Carey and Julie Fero at the University of Rhode Island - Graduate School of Oceanography for helping me with cores and allowing me to use their Malvern laser-diffraction particle-size analyzer. Also thanks to core curators at Lamont Doherty Earth Observatory and Woods Hole Oceanographic Institute for allowing me to sample and view core samples. Thank you to those at WHOI who allowed me to come on board the R/V *Knorr* for the 2007 Bermuda Rise coring cruise. Thanks to Peter Rona, Greg Mountain and Ed Laine for discussions on U.S. Atlantic continental margin processes. Thank you to Luciano Fonseca and Barbara Kraft for helping me to understand of acoustic backscatter. Thank you to Lloyd Huff for always checking in on my progress. And thank you to all the students and faculty at CCOM and in the

department of Earth Sciences for your continuous support. And finally, thank you to my family. I couldn't have done this without you!

TABLE OF CONTENTS

DEDICATION.....	iii
ACKNOWLEDGEMENTS.....	iv
TABLE OF CONTENTS.....	vi
LIST OF TABLES.....	viii
LIST OF FIGURES.....	ix
ABSTRACT.....	xv
CHAPTER 1 INTRODUCTION.....	1
1.1 Study Background.....	1
1.2 Research Problem.....	5
1.3 Previous Research in the Region of the Low-Backscatter Anomaly.....	16
1.4 Study Objective.....	17
CHAPTER 2 METHODS.....	18
2.1 Seafloor Mapping Survey.....	18
2.1.1 Data Aquisition.....	18
2.1.2 Data Processing.....	20
2.2 Data Visualization and Analysis.....	22
2.3 Backscatter Classification.....	27
2.4 Chirp Sonar Profile Interpretation.....	28
2.5 Sediment Core Analysis.....	28
2.5.1 Grain-Size Analysis.....	35
2.5.2 Smear-Slide Analysis.....	37
2.5.3 AMS-Radiocarbon Dating.....	39
CHAPTER 3 RESULTS.....	43
3.1 Introduction.....	43
3.2 Multibeam Sonar Bathymetry.....	44
3.3 Multibeam Sonar Backscatter.....	59
3.3.1 Backscatter Strength.....	60
3.3.2 Backscatter Features.....	61
3.3.3 Regional Backscatter Textures.....	67
3.4 Chirp Seismic-Reflection Profiles.....	71
3.5 LDEO Single-Channel Seismic-Reflection Profile.....	82
3.6 Sediment Core Samples.....	85
3.6.1 Core RC10-PC01.....	86
3.6.2 Core EN101-PC01.....	89
3.6.3 Core EN084-GC02.....	94
CHAPTER 4 DISCUSSION.....	97
4.1 Low-Backscatter Anomaly.....	97
4.1.1 Hypothesis 1 – Sediment Deposit.....	97
4.1.2 Hypothesis 2 – Outcropping Stratigraphic Units.....	109
4.1.3 Hypothesis 3 – Presence of Sediment Gas.....	127

4.2 Medium-Backscatter Bridge	132
4.2.1 Turbidite Deposit	133
4.2.2 Debris-Flow Deposit.....	137
4.2.3 Triggering Mechanisms	139
4.2.4 Core EN101-PC01 Sediment Ages.....	140
CHAPTER 5 CONCLUSIONS AND RECOMMENDATIONS	142
5.1 Conclusions.....	142
5.2 Recommendations for Future Work.....	145
REFERENCES	149
APPENDICES	157
APPENDIX A SMEAR-SLIDE DATA	158
APPENDIX B GRAIN-SIZE DATA.....	164

LIST OF TABLES

Table 2.1 Summary table of core samples analyzed for this study.....	30
Table 2.2 Station information used for reservoir corrections applied to radiocarbon age measured for sample 10 cm in core EN101-PC01.	42
Table 3.1 AMS-radiocarbon age results.	93
Table 3.2 Regional reservoir correction values and calibrated calendar age values for radiocarbon ages collected from core EN101-PC01.....	94

LIST OF FIGURES

Figure 1.1 Multibeam backscatter data collected on the U.S. Atlantic continental margin in 2004 and 2005 showing location of the low-backscatter anomaly study area offshore New Jersey. Backdrop is National Geophysical Data Center (NGDC) NOAA ETOPO2 bathymetry data. Data were collected and processed within U.S. Navy restricted zone, but are not presented due to U.S. Navy regulations. MBES data are available at http://www.ccom.unh.edu and ETOPO2 data can be found at http://www.ngdc.noaa.gov/	3
Figure 1.2 Map showing low-backscatter anomaly in 12-kHz MBES backscatter data and nearby bathymetric features. Low-backscatter anomaly outlined in white-dashed line. Bathymetric contours are at 500-m intervals. Backscatter range is from -25 dB (high-backscatter strength) to -51 dB (low-backscatter strength).....	4
Figure 1.3 USGS 6.5-kHz GLORIA sidescan-sonar backscatter data near the low-backscatter anomaly. Location of the low-backscatter anomaly is outlined by the white-dashed line. Bathymetric contours are shown at 500-m intervals.	5
Figure 1.4 Bathymetry map offshore New Jersey showing numerous submarine canyons and channels.....	10
Figure 1.5 Map showing the location of the buried Chesapeake Drift on the U.S. Atlantic margin. Map modified from Tucholke and Mountain (1986) and Pratson and Laine (1989). Bathymetric contours are at 500-m intervals	15
Figure 2.1 Map showing view of 6.5-kHz GLORIA sidescan-sonar mosaic with other layers in <i>ArcGIS</i> . GLORIA data were viewed to compare backscatter intensity near the low-backscatter anomaly found in the multibeam data.	24
Figure 2.2 Map showing collection locations of all NGDC archived cores (yellow dots) over backdrop of multibeam backscatter data and NGDC/NOAA ETOPO2 and Coastal Relief Model bathymetry (sun-illuminated hillshade). The low-backscatter anomaly is outlined by the white-dashed line.....	26
Figure 2.3 Core locations mapped with multibeam backscatter backdrop.	30
Figure 2.4 Recent photographs of core EN101-PC01 showing sample depths. White spaces indicate missing core sections.	31
Figure 2.5 Recent photographs of core EN084-GC01 with sample depths. White space indicates missing core sections.	32
Figure 2.6 Recent photographs of core RC10-PC01 showing sample depths.	33
Figure 2.7 Black and white photographs of core RC10-PC01 showing sample depths.	34
Figure 2.8 Exampe of a smear slide sample showing nannoplankton-rich silty clay sediment from core EN101-PC01 (10 cm) under 100x magnification in plain polarized light. Cross-polarized light (shown in the next figure) shows many of the small grains are calcareous coccoliths.	38
Figure 2.9 Example of a smear slide sample of core EN101-PC01 (10 cm) under 100x magnification in cross-polarized light.	39

Figure 2.10 Locations of the observed ΔR and ΔR error corrections used to compute a distance-weighted average regional reservoir correction for radiocarbon ages in core EN101-PC01. Station site numbers are shown in parentheses. Station information is shown in Table 2.2.....	42
Figure 3.1 Perspective view (looking north) showing gray hillshade of the 12-kHz multibeam bathymetry with NOAA ETOPO2 and Coastal Relief Model as backdrop. Bathymetric image vertical exaggeration (VE) = 10x. Low-backscatter anomaly outlined in white-dashed line. Bathymetric profile AA' across the New Jersey margin showing seafloor gradients. Average slope gradients are shown across the top of the profile. Profile indicates the approximate location of the buried Chesapeake Drift...	45
Figure 3.2 MBES bathymetry data overlaying NOAA ETOPO2 and Coastal Relief Model showing slope canyons that converge into Wilmington channel.	46
Figure 3.3 Bathymetry data (gray sun-illuminated hillshade) showing hummocky and wavy seafloor features near the base of the continental slope where seafloor gradients are low.....	47
Figure 3.4 Bathymetry data showing hummocky seafloor at the terminus of Wilmington channel.....	49
Figure 3.5 Map showing bathymetry data where slope canyons converge into Hudson channel.	50
Figure 3.6 Bathymetry data showing hummocky seafloor at the terminus of Hudson channel.....	51
Figure 3.7 Perspective view (looking landward and upslope) of bathymetry data showing five, small channels (a-e). Contours shown in black at 500-m intervals. Bathymetry image shown with 10x vertical exaggeration and the bathymetric profile shown with 50x vertical exaggeration.	52
Figure 3.8 Bathymetry data (gray sun-illuminated hillshade) showing the small channels extending upslope across the gently dipping seafloor. Thick arrows pointing to upslope channel sections.....	53
Figure 3.9 Map view of bathymetry data showing bowl-shaped depressions near the 3000 m isobath. Channels are labeled a (farthest southwest) through e (farthest northeast).....	54
Figure 3.10 Map view of bathymetry data showing bathymetric depressions within the small channels.....	55
Figure 3.11 Rough seafloor consisting of bathymetric depressions found downslope from small channels.	56
Figure 3.12 Bathymetric perspective image of Knauss Knoll and Krause Foredrift looking landward towards the northwest. Vertical exaggeration = 10x.	57
Figure 3.13 Multibeam sonar bathymetry data (gray, sun-illuminated hillshade) showing sediment ridge near Wilmington channel.....	58
Figure 3.14 Overview of bathymetry data with labeled bathymetric features.....	59
Figure 3.15 Backscatter characterization map using low (-51 to -42 db), medium (-42 to -34 dB) and high (-34 to -25 dB) classifications. Bathymetric contours shown in meters.....	61
Figure 3.16 Multibeam backscatter mosaic in map view showing location of bathymetry features. Low-backscatter anomaly outlined in white dashed line.	

Sediment ridge and break-in-slope near 3000 m isobath shown by black dashed line.	62
Figure 3.17 Perspective view (looking north) of the backscatter data showing the subdivided low-backscatter anomaly (outlined in white). a = section adjacent to Wilmington channel; b = medium backscatter bridge (outlined in red); c = intermediate section; d = lowest backscatter strength section; e = mottled-streaky section. VE=10x.	64
Figure 3.18 Backscatter data showing fan-shaped feature (outlined by white-dashed line) at the terminus of Wilmington channel.	65
Figure 3.19 Backscatter data showing fan-shaped feature (outlined by white-dashed line) at the terminus of Hudson channel.	66
Figure 3.20 Backscatter data showing high-backscatter lobe outline by white-dashed line.	67
Figure 3.21 Backscatter data on the upper continental rise near the base of the continental slope showing mottled backscatter texture.	68
Figure 3.22 Backscatter data showing section of homogenous-backscatter texture between mottled backscatter and low-backscatter anomaly.	69
Figure 3.23 Backscatter data showing rilled-streaky-backscatter texture seafloor area downslope from the low-backscatter anomaly and the homogenous-texture backscatter seafloor.	70
Figure 3.24 Map showing locations of regional backscatter textures and features. Bathymetric contours are at 500-m intervals.	71
Figure 3.25 Map of 3.5-kHz chirp profiles with multibeam backscatter backdrop. Low-backscatter anomaly outlined by white-dashed line. Bathymetric contours shown at 500-m intervals.	72
Figure 3.26 Seismic reflection profiles AA' and BB' collected upslope from the low-backscatter anomaly. Corresponding backscatter strength shown as white for high-backscatter (HBS), gray for medium backscatter (MBS) and black for low backscatter (LBS).	74
Figure 3.27 Seismic reflection profiles CC' and DD' collected upslope and within the low-backscatter anomaly. Corresponding backscatter strength shown as white for high-backscatter (HBS), gray for medium backscatter (MBS) and black for low backscatter (LBS).	75
Figure 3.28 Chirp profiles EE' and FF' collected across the low-backscatter anomaly. High backscatter (HBS) shown in yellow, medium backscatter (MBS) in gray and low backscatter (LBS) in black.	77
Figure 3.29 Chirp profile GG' collected across the low-backscatter anomaly. High backscatter (HBS) shown in yellow, medium backscatter (MBS) in gray and low backscatter (LBS) in black.	78
Figure 3.30 Chirp profiles HH' and II' collected down-slope from the low-backscatter anomaly. MBS = medium backscatter strength; LBS = low-backscatter strength.	80
Figure 3.31 Chirp profiles JJ' and KK' collected down-slope from the low-backscatter anomaly. MBS = medium backscatter strength; LBS = low-backscatter strength.	81

Figure 3.32 Section of LDEO single channel seismic line V2114 shown with multibeam backscatter as the background. Low-backscatter anomaly outlined by the white-dashed line. Bathymetric contours shown at 500-m intervals.	82
Figure 3.33 Segment of LDEO single-channel seismic-reflection line V2114. Corresponding backscatter strength shown in scale bar above profile. High-backscatter strength (HBS) shown in yellow; medium backscatter strength (MBS) shown in gray; low backscatter strength (LBS) shown in black. BSR = Bottom simulating reflector	84
Figure 3.34 Core locations with multibeam backscatter map as backdrop. Contours are shown in black.	85
Figure 3.35 Perspective view (looking north) showing location of core RC10-PC01 with respect to bathymetry data. VE=10x.....	86
Figure 3.36 Perspective view (looking north) showing location of core RC10-PC01 with respect to backscatter data draped over bathymetry data. Low-backscatter anomaly outlined by white dashed line. VE=10x	87
Figure 3.37 Stratigraphic column of core RC10-PC01 with laser-diffraction average grain-size measurements and descriptions. Samples were unavailable below 100 cm core depth (with exception of samples at 298 cm and 725 cm depths). Smear-slide and laser-diffraction mean grain-size data are available in Appendices A and B.	88
Figure 3.38 Perspective view (looking north) showing location of core EN101-PC01 with respect to bathymetry data. VE=10x.....	89
Figure 3.39 Perspective view (looking north) showing location of core EN101-PC01 with respect to backscatter data draped over bathymetry data. Low-backscatter anomaly outlined in white dashed line and medium-backscatter bridge outlined in white solid line. VE=10x	90
Figure 3.40 Average grain size values measured using laser particle-size analyzer for samples collected in piston core EN101-PC01. X-axis values are given in phi and y-axis values are depth in cm. AMS-radiocarbon dates shown in parentheses. Data gaps represent sections of the core that were unavailable for sampling. Smear-slide and laser-diffraction mean grain-size data are available in Appendices A and B.	91
Figure 3.41 Smear slide results for dominant components found in Core EN101-PC01.....	92
Figure 3.42 Plot of AMS-radiocarbon dates. Reservoir corrections shown but not plotted from 10 cm sample.	93
Figure 3.43 Perspective view (looking north) showing collection location of core EN084-GC02 shown with bathymetry data (gray sun-illuminated hillshade). VE=10x	94
Figure 3.44 Perspective view (looking north) showing collection location of core EN084-GC02 shown with backscatter data draped over bathymetry data (light tones = high backscatter; dark tones = low-backscatter). VE=10x	95
Figure 3.45 Average grain size values measured using laser particle-size analyzer for samples collected in gravity core EN084 GC2. X-axis values are given in phi and y-axis values are depth in cm. Data gap represents section of the core that were unavailable for sampling. Smear-slide and laser-diffraction mean grain-size data are available in Appendices A and B.....	96

Figure 4.1 Bathymetry data (gray sun-illuminated hillshade) showing evidence of the small channels extending upslope from the 3000 m isobath.	99
Figure 4.2 Bathymetry data (gray sun-illuminated hillshade) showing sediment transport pathways (white-dashed arrows) across the upper continental rise and through the small channels.....	100
Figure 4.3 Bathymetric profile showing Krause Foredrift and erosion scour at the base of Knauss Knoll.	102
Figure 4.4 Perspective view (looking north) of backscatter data (low backscatter = dark tones; high backscatter = light tones) showing location of bottom photographs analyzed by Schneider et al. (1967). Red arrows indicate direction and relative magnitude of inferred current strength. Low-backscatter anomaly outlined in white. VE=10x	104
Figure 4.5 Perspective view (looking upslope and landward) of bathymetry data (gray sun-illuminated hillshade) showing downslope transport of sediment through small channels (white dashed arrows) and subsequent transport direction of suspended sediment parallel to contours by the WBUC (red arrows). VE=10x	105
Figure 4.6 Perspective view (looking upslope and landward) of backscatter data (low backscatter = black and high backscatter = white) showing downslope transport of sediment through small channels (white dashed arrows) and subsequent transport direction of suspended sediment parallel to contours by the WBUC (red arrows). VE=10x	106
Figure 4.7 Diagram showing erosion, transport and deposition conditions plotted by grain size and current speed. The area outlined in yellow shows measured average grain size of sediment cores analyzed in this study. The range of current speeds measured by the HEBBLE and SYNOP projects (4158-m and 3500-m) near the depth of the low-backscatter anomaly shown at the bottom of the diagram. Modified from Heezen and Hollister (1964).	107
Figure 4.8 (a) Section of LDEO airgun seismic reflection profile showing outcropping seismic reflectors within the low-backscatter anomaly. (b) Interpreted seismic reflector horizons. Seafloor shown in red and subbottom reflectors shown in blue (reflectors not interpreted across data gap).	111
Figure 4.9 Map view of backscatter data showing the direction of the WBUC (as interpreted from the orientation of Krause Drift) relative to the bathymetric contours. Low-backscatter anomaly outlined by white line.	114
Figure 4.10 Map view of backscatter data showing the inferred downslope sediment transport paths through Hudson and Wilmington channels. Low-backscatter anomaly outlined in white solid line. Transport paths shown in white dashed line.	117
Figure 4.11 Perspective view (looking upslope and landward) of bathymetry data (gray sun-illuminated hillshade) showing location of the Baltimore-Toms gather area (outlined by white-dashed line). VE=10x	118
Figure 4.12 Perspective view (looking upslope and landward) of bathymetry data (gray sun-illuminated hillshade) gather area funneling into Hudson channel (outlined by white-dashed line). VE=10x	119
Figure 4.13 Perspective view (looking upslope and landward) of backscatter data draped over bathymetry showing the Wilmington channel fan. VE=10x	120

Figure 4.14 Perspective view (looking upslope and landward) of backscatter data draped over bathymetry showing the Hudson channel fan. VE=10x	121
Figure 4.15 Bathymetry data (gray sun-illuminated hillshade) showing location of ODP Site 905. Baltimore-Toms gather area outlined by black dashed line.	123
Figure 4.16 Map showing location of ODP Site 905 with MBES backscatter data as backdrop. Baltimore-Toms gather area outlined by black dashed line. Bathymetric contours shown in 500-m intervals.	124
Figure 4.17 Map of backscatter data showing region of homogenous backscatter on the relatively steep (0.7°) seafloor. Low-backscatter anomaly outlined by white-dashed line. Bathymetric contours are shown at 500-m intervals.	125
Figure 4.18 Map showing the approximate location of the buried Chesapeake Drift (outlined by white dashed lines) as identified by Tucholke and Mountain (1986) and Pratson and Laine (1989) with respect to MBES backscatter data.	128
Figure 4.19 Bathymetry data (gray sun-illuminated hillshade) showing bathymetric depressions (several indicated by arrows) within and downslope from small channels that may result from gas and fluid escape. Hillshade illumination from the southwest. Contours shown in meters.	131
Figure 4.20 Perspective view (looking north) showing medium-backscatter bridge outlined by solid white line, the low-backscatter anomaly outlined in white-dashed line and other nearby bathymetric features.	133
Figure 4.21 Perspective view (looking north) showing the location of core EN101-PC01 with respect to the medium-backscatter bridge (outlined in red).	134
Figure 4.22 Image showing photograph of section of a possible fine-grained turbidite sequence (260 to 280 cm) within sediment core EN101-PC01. Turbidites highlighted by blue boxes on mean grain size plot.	135
Figure 4.23 Comparison of grain-size analysis with quartz compositions estimated from smear slide analysis.	136
Figure 4.24 Backscatter data and consecutive 3.5-kHz chirp profiles showing medium backscatter bridge. Medium-backscatter bridge outlined in red and low-backscatter anomaly outlined in white. Seismic-reflection profile vertical exaggeration = 65x.	138
Figure 4.25 Map view showing interpretation of upslope slide complex (high-backscatter lobe) mapped by Embley and Jacobi (1986) as possible cause of medium-backscatter bridge.	140
Figure 5.1 Map showing location of the low-backscatter area on the Blake Bahama Outer Ridge.	148

ABSTRACT

GEOLOGICAL INTERPRETATIONS OF A LOW-BACKSCATTER ANOMALY FOUND IN 12-KHZ MULTIBEAM DATA ON THE NEW JERSEY CONTINENTAL MARGIN

by

Edward M. Sweeney, Jr.

University of New Hampshire, December, 2008

A low-backscatter acoustic anomaly was recently mapped on the New Jersey continental margin between Hudson and Wilmington channels using a 12-kHz multibeam echo-sounder (MBES). The presence of the low-backscatter anomaly indicates a change in the physical properties of the seafloor or near sub-surface. Analyses of seafloor and sub-surface acoustic data with previously collected sediment cores suggest three hypotheses as possible geological causes for the anomalously low-backscatter strength: (1) a sediment deposit, (2) an outcrop of sediment strata due to sediment removal and non-deposition, or (3) the presence of gas in the sub-surface sediments. Multibeam bathymetry and backscatter data, high-resolution 3.5-kHz chirp sonar profiles, airgun single-channel seismic-reflection profiles, and sediment cores collected nearby the low-backscatter anomaly most strongly support the hypothesis that the low-backscatter anomaly is an outcrop of older sediments that have been

exposed by Western Boundary Undercurrent (WBUC) erosion and non-deposition induced by local seafloor morphology.

CHAPTER 1

INTRODUCTION

1.1 Study Background

Bathymetric surveys conducted in 2004 and 2005 by the Center for Coastal and Ocean Mapping (CCOM), National Oceanic and Atmospheric Administration (NOAA) and the U.S. Naval Oceanographic Office (NAVOCEANO) mapped part of the U.S. Atlantic continental margin using a 12-kHz multibeam echo-sounder (MBES) (Gardner, 2004; Cartwright and Gardner, 2005; Gardner et al. 2006). This mapping effort collected 403,000 km² of MBES data. These MBES data were used to create 100-m bathymetry and co-registered acoustic-backscatter grids of the seafloor. Along with the MBES data, approximately 38,474 km of 3.5-kHz chirp seismic-reflection profiles were collected to image the shallow sub-surface sediment structure. The chirp subbottom profiles provide high-resolution acoustic images of the sub-surface stratigraphy up to ~60 m beneath the seafloor.

The MBES data and subbottom profiles provide an extensive data set for evaluating geological processes along the U.S. Atlantic continental margin. Multibeam bathymetry data can be combined with co-registered acoustic backscatter strength to identify morphological seafloor features and their acoustic seafloor response. Additionally, the sub-surface chirp sonar profiles show the nature of

acoustic horizons beneath the seafloor and can be used to interpret previous or ongoing sedimentary processes.

The data collected during the 2004 to 2005 MBES survey show an anomalous, low-backscatter region 350 km offshore New Jersey (Figure 1.1). The low-backscatter anomaly is located between Hudson and Wilmington channels, downslope from several small channels on the continental rise near Knauss Knoll (Figure 1.2). The anomalous feature covers a seafloor area of 2,750 km² and has a relative decrease of 10 dB in backscatter strength from the surrounding seafloor. This low-backscatter anomaly occurs in four separate survey lines collected over a span of several days and has boundaries that are not consistent with the edges of the survey line swaths. Although less distinct, the low-backscatter anomaly can also be identified in U.S. Geological Survey 6.5-kHz GLORIA sidescan-sonar data (Figure 1.3).

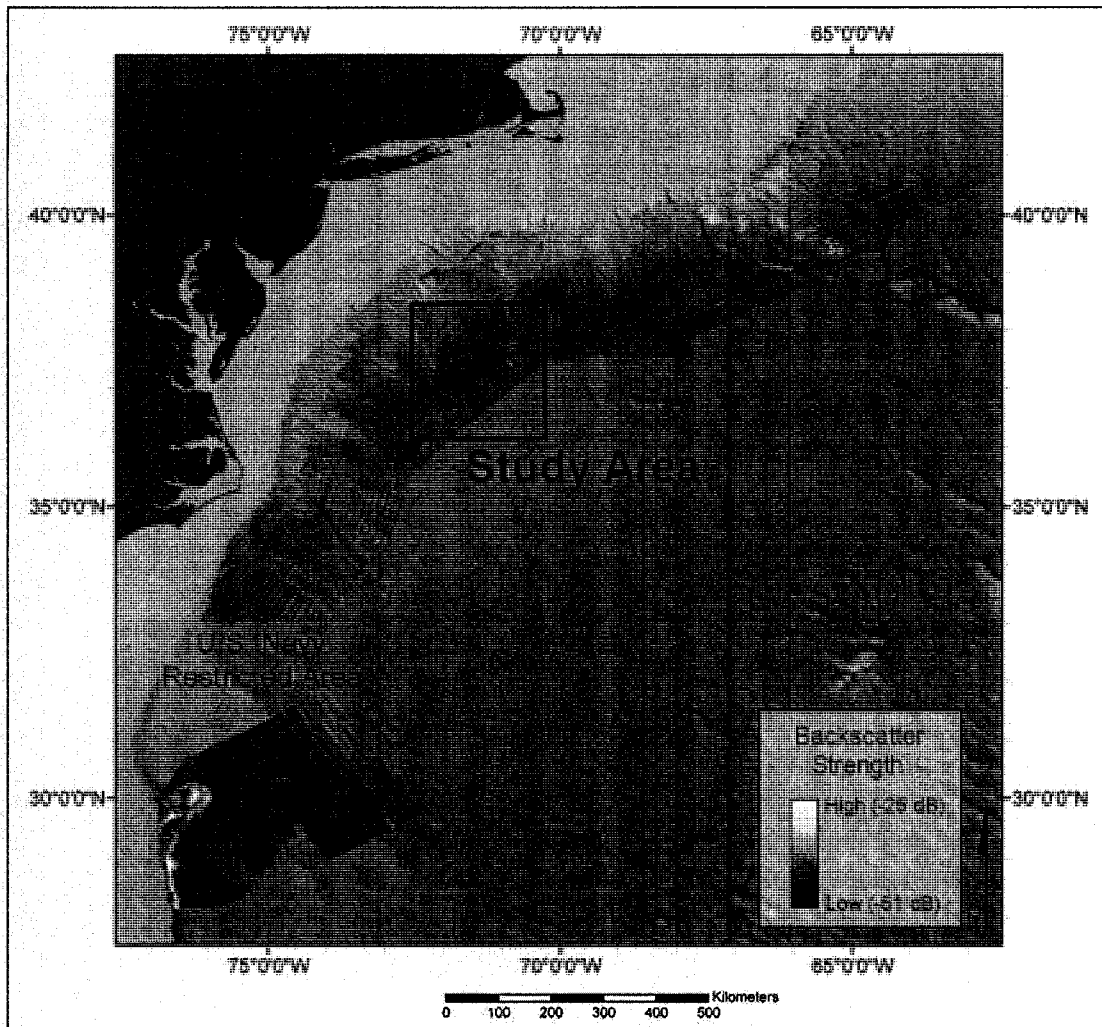


Figure 1.1 Multibeam backscatter data collected on the U.S. Atlantic continental margin in 2004 and 2005 showing location of the low-backscatter anomaly study area offshore New Jersey. Backdrop is National Geophysical Data Center (NGDC) NOAA ETOPO2 bathymetry data. Data were collected and processed within U.S. Navy restricted zone, but are not presented due to U.S. Navy regulations. MBES data are available at <http://www.ccom.unh.edu> and ETOPO2 data can be found at <http://www.ngdc.noaa.gov/>.

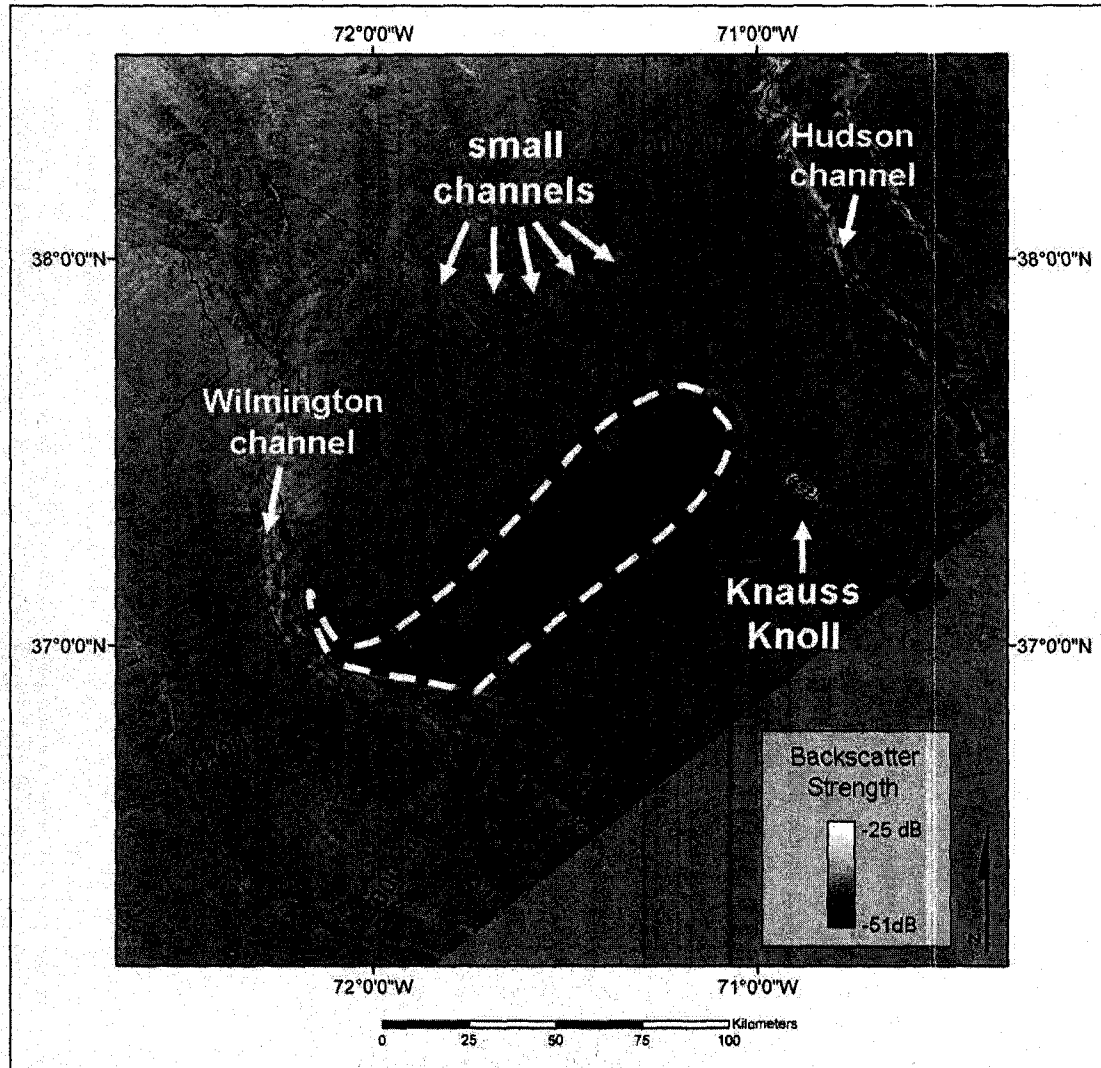


Figure 1.2 Map showing low-backscatter anomaly in 12-kHz MBES backscatter data and nearby bathymetric features. Low-backscatter anomaly outlined in white-dashed line. Bathymetric contours are at 500-m intervals. Backscatter range is from -25 dB (high-backscatter strength) to -51 dB (low-backscatter strength).

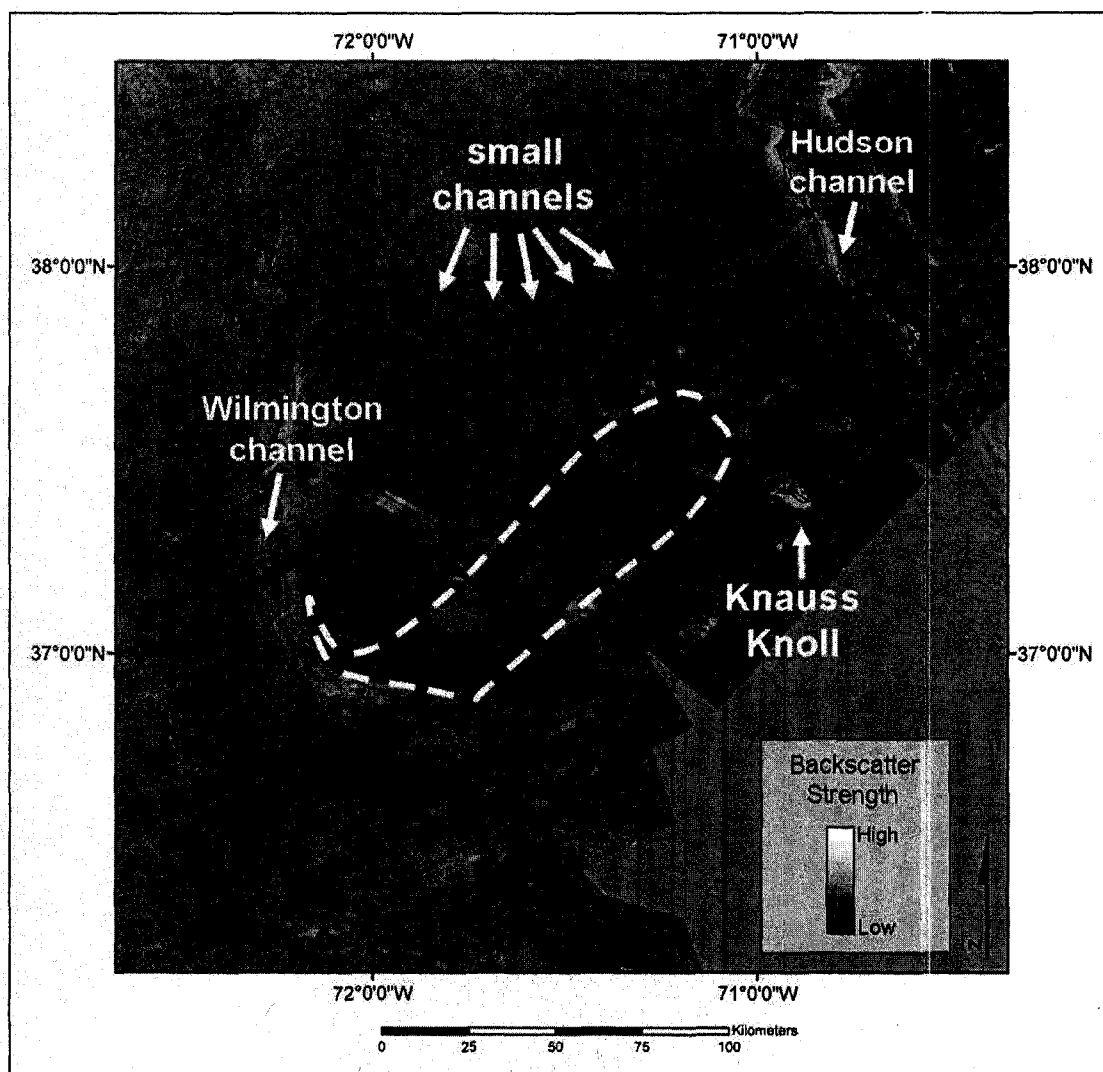


Figure 1.3 USGS 6.5-kHz GLORIA sidescan-sonar backscatter data near the low-backscatter anomaly. Location of the low-backscatter anomaly is outlined by the white-dashed line. Bathymetric contours are shown at 500-m intervals.

1.2 Research Problem

The presence of the low backscatter in several survey lines of the 2004 and 2005 multibeam sonar backscatter data and its occurrence in the USGS GLORIA data set provides evidence that the low-backscatter anomaly is a true seafloor feature and not a data artifact. However, the cause of the low-backscatter anomaly is not

immediately evident from the backscatter data alone because backscatter is controlled by several parameters that are dependent upon the frequency of the sonar being used and the angle of incidence between the acoustic transmission and the seafloor (Jackson et al. 1986; de Moustier and Alexandrou, 1991; Gardner et al. 1991; Fonseca et al. 2002). The parameters that control the seafloor backscatter are interface backscatter due to seafloor surface characteristics and volume backscatter due to inhomogeneities found in the upper few meters of the sediment volume (Hamilton, 1972; Jackson et al. 1986; de Moustier and Alexandrou, 1991; Gardner et al. 1991; Schlee and Robb 1991; Fonseca et al. 2002). Interface backscatter accounts for the spectrum of seafloor roughness (relative to the acoustic wavelength of the sonar transmission) and the acoustic impedance contrast between the seafloor surface and water medium (Jackson et al. 1986; de Moustier and Alexandrou, 1991; Fonseca et al. 2002). Interface backscatter increases when the seafloor is rough relative to the wavelength and when there is a high acoustic impedance contrast between the seafloor and the water medium. Discrete objects within the sediment column such as shells, gas bubbles, burrows and subsurface sediment layers can result in inhomogeneities if the frequency and angle of incidence of the sonar pulse allow penetration into the seafloor (Jackson et al. 1986; Gardner et al. 1991; Fonseca et al. 2002). These features form acoustic impedance contrasts in the sub-surface and can cause increases in the volume backscatter component.

A previous ground-truth investigation of 6.5-kHz sidescan-sonar data shows a complex correlation between lithostratigraphy and backscatter intensity that result from these mechanisms. Gardner et al. (1991) found that areas with low backscatter

returns were composed of sands with a thin surface layer of clay, whereas seafloor with high-backscatter strength was found to be composed of silty clay with thin interbeds of sand within the study area. These findings proved counter-intuitive to the conventional interpretation that backscatter strength has a direct correlation with sediment grain size at the seafloor surface.

These complexities make it difficult to interpret the geoacoustic cause of the low-backscatter anomaly. However, local geological processes may provide clues to its origins. Previous studies have suggested that sediment-gravity processes and deep-sea contour-current sediment processes have been the dominant factors in shaping the middle U.S. Atlantic margin continental slope and rise (Embley, 1980; Mountain and Tucholke, 1985; Poag, 1985; Mountain and Poag, 1987; Pratson and Laine, 1989; Poag, 1992; Mountain et al., 1994; McHugh et al. 2002). In addition, studies have also shown the presence of sub-surface gas (Tucholke et al., 1977; Mountain and Tucholke, 1985; Dillon and Max, 2000; Dillon et al., 1995).

Downslope sediment-gravity processes have occurred in the form of turbidity currents, debris flows, slumps and slides on the continental margin (Heezen and Ewing, 1952; Dietz, 1963; Rona and Clay, 1967; Emery et al., 1970; Embley, 1980; Tucholke and Laine, 1982; Embley and Jacobi, 1986; Pilkey and Cleary, 1986; Schlee and Robb, 1991; Fulthorpe et al., 1996; Fulthorpe et al., 2000; McHugh et al. 2002; Chaytor et al., 2007). A slump occurs when a block of seafloor moves along a rotational, concave-up shear plane with little internal deformation (McHugh et al., 2002). Slumps are typically identified by deep-seated rotational blocks that have experienced minimum translation and deformation (Embley and Jacobi, 1986). Slides

occur when a block of seafloor moves downslope along a planar glide plane with little internal deformation (McHugh et al., 2002). Deposits formed by slides are typically shallow failures that translate over large distances (Embley and Jacobi, 1986). Debris flows are sediment-gravity flows dominated by plastic behavior. Sediment is transported downslope by a debris flow as an incoherent viscous mass and deposited by sediment freezing (Shanmugam, 2000; McHugh et al., 2002). Deposits that result from debris flows typically contain sharp upper and lower contacts, floating clasts, planar clast fabric, inverse grading of clasts, a basal shear zone and moderate to high matrix content (McHugh et al., 2002). Shanmugam (2000) has defined turbidity currents as sediment-gravity flows with Newtonian rheology (meaning that it has no inherent strength) and turbulent state, where sediment is held in suspension by fluid turbulence. Deposits from turbidity currents (known as turbidites) are identified by normal size grading, sharp basal contacts, gradational upper contacts, and Bouma sequences (Bouma, 1962; McHugh et al., 2002). Pratson and Laine (1989) have estimated that these gravity-driven processes have been the depositional agents across 60% of the continental slope and rise and have therefore played an important role in the downslope distribution of sediment on the continental margin.

Evidence of downslope sediment transport processes on the Atlantic continental margin is shown by submarine canyons and channels found on the continental margin (Figure 1.4). Frequent sediment failures have initiated and maintained submarine canyon and channel systems (Twitchell and Roberts, 1982; Farre et al. 1983; Pratson and Coakley, 1996). These features have acted as conduits for sediments that traverse to the outer continental margin by downslope sediment

transport (Ayers and Cleary, 1980; Pilkey and Cleary, 1986). Suspended sediments that spill over channel walls have formed channel levees and have been distributed across the continental rise between channels (Robb et al., 1981; Tucholke and Laine, 1982; Locker, 1989; McMaster et al., 1989; Pratson and Laine, 1989; Schlee and Robb, 1991; Locker and Laine, 1992). In addition, sediments that reach the terminus of channels have been deposited on the outer continental margin to form abyssal fan systems (Tucholke and Laine, 1982; Locker, 1989; McMaster et al., 1989; Locker and Laine, 1992).

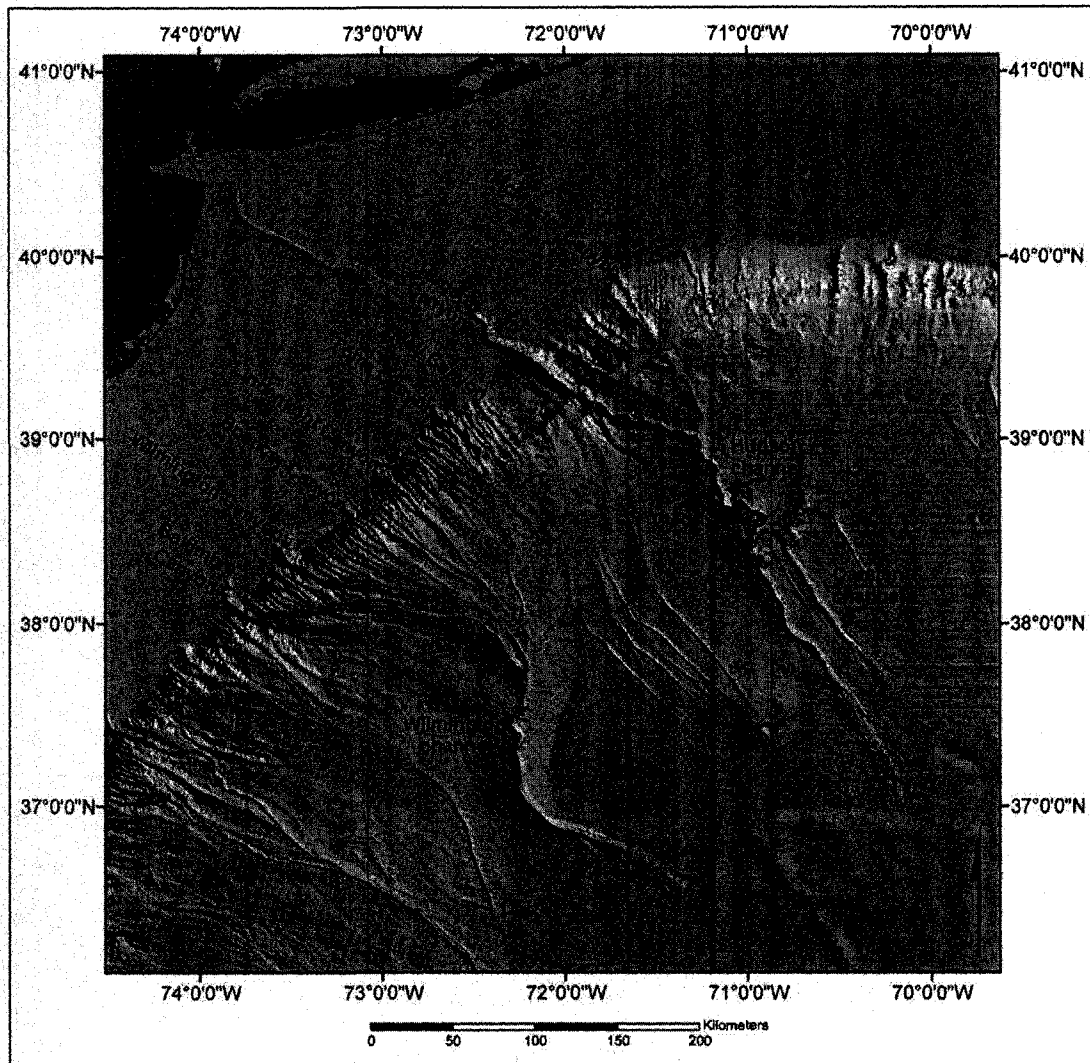


Figure 1.4 Bathymetry map offshore New Jersey showing numerous submarine canyons and channels.

Major slide complexes have also been mapped on the U.S. Atlantic continental slope and rise (Embley, 1980; Embley and Jacobi, 1986; Chaytor et al., 2007). Embley and Jacobi (1986) mapped several large slide complexes along the margin (i.e. near Blake Bahama Outer Ridge and off Georges Bank) that extend across the continental rise, reaching as far as the 5400 m isobath. Their research shows that the upper continental rise offshore New Jersey is characterized by

numerous small slides (Embley and Jacobi, 1986). These small slides have either failed to generate large slide complexes or the large slide complexes have been buried (Embley and Jacobi, 1986).

In addition to downslope sediment processes, contour-parallel sediment transport has occurred on the margin as the result of the Western Boundary Undercurrent (WBUC). The WBUC is a deep-sea geostrophic western boundary current that flows towards the south along the continental margin contours. Current flow is made up of North Atlantic Deep Water that originates from the Norwegian, Mediterranean and Labrador Seas and flows to the south beyond the Blake-Bahama Outer Ridge (Bulfinch et al. 1982; McCave and Hollister, 1985; McCave and Tucholke, 1986). Wüst (1933) first suggested the presence of intensified deep-sea western boundary geostrophic currents in the North Atlantic. However, the geological effects of the Western Boundary Undercurrent were not given significant recognition until many years later when studies by Wüst (1955) and by Stommel (1956) reaffirmed the likelihood of strong western deep-sea currents in the Atlantic.

A study known as the High Energy Benthic Boundary Layer Experiment (HEBBLE) conducted extensive quantitative analysis on the WBUC to understand its flow dynamics and its interaction with sediments at the seabed. These studies show that velocities steadily increase from near-tranquil conditions at seafloor depths of 4000 m to approximately 40 cm/s between 4900 and 5100 m on the Nova Scotian rise (Tucholke et al., 1985). During the study, flows deviated less than 15° from local bathymetric contours on average (Tucholke et al., 1985). The HEBBLE study also measured a high-velocity flow region known as the “core” of the WBUC. Average

current speeds within the core of the WBUC at 5022 m were measured at 32 cm/s, but also reached up to 73 cm/s (Richardson et al., 1981; Bulfinch and Ledbetter, 1984; Driscoll et al. 1985).

Another study known as the SYNoptic Ocean Prediction (SYNOP) Central Array experiment also made measurements on geostrophic flow rates in the Northwest Atlantic Ocean. The SYNOP field program found that mean currents at 3500-m water depth near 68°W and 38°N (offshore the Grand Banks) flowed towards the southwest along bathymetric contours. Measurements of the average speed of these currents were 6 cm/s, with events up to 40 cm/s (Shay et al., 1995).

The depositional influence of the WBUC is evident by the numerous large- and small-scale bathymetric features that have been observed in the western North Atlantic (Stow and Holbrook, 1982; McCave and Tucholke, 1986). Sediment drifts are examples of large-scale bathymetric features formed by the WBUC. These sediment deposits typically have elongate or ridge morphologies and form as the result of sediment accumulation over millions of years (McCave and Tucholke, 1986). Sediment drifts are also recognized by unconformable reflectors in seismic-reflection profiles, thick deposits relative to adjacent sediment cover, thick bedding at the drift axis and thin bedding at the drift margins, weak internal seismic reflectors, and the presence of mud waves and/or undulating reflectors (McCave and Tucholke, 1986). Small-scale features such as sediment waves, ripples and furrows have also been associated with the presence of the deep-sea currents and have been found superimposed on larger sediment drift bodies (Flood, 1983; McCave and Tucholke, 1986). Geological investigations that have used compass-oriented bottom

photography show sedimentary structures such as ripples and sediment streamers in locations of the predicted WBUC (Heezen and Hollister, 1964; Heezen et al., 1966; Schneider et al., 1967).

Further evidence for the presence of deep-sea geostrophic currents is the amount of suspended particulate in the water near the seafloor. This has typically been assessed by the water “cloudiness” or “muddiness.” The content of suspended sediment is thought to be higher with increased current speeds (McCave and Tucholke, 1986). Bottom photographs that show very cloudy bottom waters have been associated with swift deep-sea currents (Schneider et al., 1967).

Sediments that are associated with geostrophic-current controlled deposition are known as contourites (Hollister and Heezen, 1972; Stow and Holbrook, 1982). The two main contourite facies identified by Stow and Holbrook (1982) are muddy and sandy contourites. Muddy contourites are typically homogenous with irregular laminations, layering and lenses and are highly bioturbated (Stow and Holbrook, 1982). Sandy contourites occur in relatively thin layers (1 to 5 cm) or thicker beds (5 to 25 cm) (Stow and Holbrook, 1982). These deposits are bioturbated and featureless or contain horizontal and cross-laminations (Stow and Holbrook, 1982). The stratigraphic composition of contourite sediments varies greatly due to the variability of contour current strength, sediment input and the effects of sediment winnowing and reworking (Stow and Holbrook, 1982).

In addition to downslope and contour-parallel processes, geological processes that result from the presence of gas have also occurred on the Atlantic margin (Tucholke et al., 1977; Mountain and Tucholke, 1985; Dillon et al., 1995; Dillon and

Max, 2000). The presence of gas in margin sediments has resulted in the formation of gas-hydrates, an ice-like crystalline compound composed of methane gas trapped within a lattice of water molecules (Dillon et al., 1995; Dillon and Max, 2000; Bohrmann and Torres, 2006). Gas-hydrates form in marine sediments when water and methane gas are available under the appropriate pressure and temperature conditions (Bohrmann and Torres, 2006).

Seismic evidence for the presence of sub-surface sediment gas and gas-hydrate has been shown by an acoustic horizon known as the bottom-simulating reflector (BSR) (Tucholke et al. 1977; Dillon et al., 1995; Dillon and Max, 2000). The BSR is thought to be an acoustic surface generated by the phase boundary between free gas and gas-hydrate charged sediments (Hovland and Judd, 1988; Kvenvolden, 2000). The interface is caused by fast sound speed in gas-hydrate-rich sediment and slow sound speed in the underlying sediment containing free gas (Kvenvolden, 2000). The BSR is typically distinguishable from other seismic horizons because it cuts across acoustic reflectors and mimics the seafloor (Tucholke et al. 1977; Kvenvolden, 2000).

Mountain and Tucholke (1985) and Mountain (1987) have suggested that the moderately high organic-carbon accumulation rates that formed the buried feature known as the Chesapeake Drift (Figure 1.5) have resulted in the presence of gas on the New Jersey margin. The sediments that form the Chesapeake Drift were derived from the adjacent prograding shelf delta active during the Miocene-Pliocene time (Tucholke and Mountain, 1986). High sediment accumulation rates thought to have been present during the construction of the Chesapeake Drift were likely able to bury

organic material before it could be consumed by benthic organisms (Mountain, personal comm., 2008). These factors may have led to a significant gas reservoir beneath the upper continental rise and the presence of sub-surface gas in the sediments.

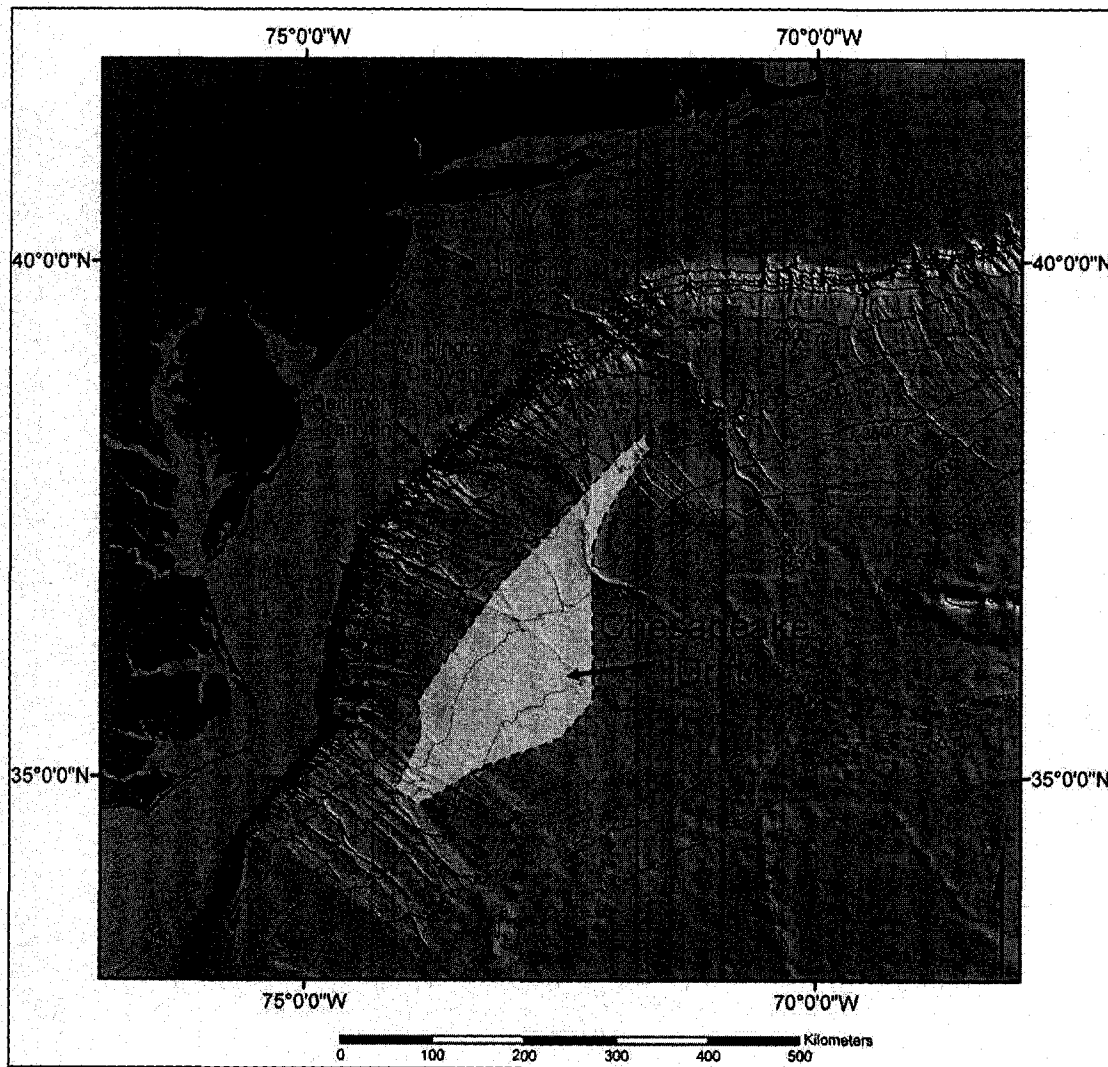


Figure 1.5 Map showing the location of the buried Chesapeake Drift on the U.S. Atlantic margin. Map modified from Tucholke and Mountain (1986) and Pratson and Laine (1989). Bathymetric contours are at 500-m intervals

1.3 Previous Research in the Region of the Low-Backscatter Anomaly

Previous studies have suggested that bottom currents have heavily influenced the seafloor region corresponding to the location of the low-backscatter anomaly (Schneider et al., 1967; Mountain and Tucholke, 1985; Stapleton, 1987; Locker 1989; Pratson and Laine, 1989). Pratson and Laine (1989) suggested the morphology of the seafloor near the low-backscatter anomaly has resulted in accelerated speeds of the WBUC. These locally intensified current speeds have caused erosion and non-deposition of sediments, resulting in an erosion scar where seismic reflectors shown by seismic-reflection profiles outcrop at the surface (Locker, 1989; Pratson and Laine, 1989). Locker (1989) also designated this seafloor region as a “bypass” area. Sediment gravity flows that passed across the region that corresponds to the low-backscatter anomaly are thought to have bypassed it with little deposition due to relatively steeper slopes. Additionally, Locker (1989) suggested that confinement of downslope sediment flows within Hudson and Wilmington channels (Figure 1.2) has caused sediment to bypass around the region corresponding to the low-backscatter anomaly.

Interpretations of 6.5-kHz GLORIA sidescan sonar mosaics have suggested that the areas of uniform low-backscatter between Hudson and Wilmington channels were largely composed of hemipelagic drape (Schlee and Robb, 1991). Schlee and Robb (1991) indicated that down-slope sediment input and pelagic sedimentation processes were dominant on the continental margin near the location corresponding to the low-backscatter anomaly. Although evidence of bottom scouring due to the

WBUC was seen in other regions of GLORIA data, the presence of the WBUC was not apparent in the area near Knauss Knoll (Figure 1.2) (Schlee and Robb, 1991).

1.4 Study Objective

The objective of this study is to investigate the origin of the low-backscatter anomaly on the New Jersey continental margin using the surface and sub-surface MBES data and chirp sonar profiles, along with previously collected seismic reflection data and sediment cores. Several hypotheses for the geological origin of the low-backscatter anomaly are presented based on the 2004 to 2005 bathymetric survey data and previously collected seafloor data.

CHAPTER 2

METHODS

2.1 Seafloor Mapping Survey

Multibeam echosounder (MBES) and 3.5-kHz chirp seismic-reflection data used in this study were collected on 5 cruises conducted in 2004 and 2005 (Gardner, 2004; Cartwright and Gardner, 2005). Three 30-day cruises took place in 2004 aboard the USNS *Henson* and two 30-day cruises in 2005 aboard the USNS *Pathfinder*. A MBES backscatter mosaic was later created for this study and added to the data set. Cruise and post-cruise methods are summarized in the following section. Data sets are available at <http://www.ccom.unh.edu>.

2.1.1 Data Acquisition

MBES data were acquired using a Kongsberg-Simrad EM121A 12-kHz multibeam echosounder. The EM121A is hull-mounted MBES system that creates a fixed 120° swath by forming 121 1° x 1° beams. This geometry provides swath width coverage of 3.4x water depth in the across-track direction. Across-swath bottom coverage was attained using an equiangular beam spacing configuration. Forming acoustic beams spaced by equal angles across the receive sector provides denser spacing for near-nadir beam soundings than an equidistant configuration, reducing sounding gaps between beam footprints. The MBES was operated using a 15-ms

transmit pulse, which achieves a vertical resolution of ~ 0.3 to 0.5% of the water depth or about 12 to 20 m resolution in 4000 m of water (Kongsberg-Simrad system specifications).

Static biases for the EM121A MBES were measured by conducting patch tests before each survey cruise. Offsets in roll, pitch, yaw and timing were corrected during the patch tests to remove static offset biases from the MBES data. Cross-check analyses were also used to determine the statistical difference between depth soundings from crossing lines. These analyses were used to compute the vertical accuracy of the MBES. For further details on the patch test and cross-check analysis procedures used for this MBES data set, refer to Gardner (2004) and Cartwright and Gardner (2005), which can be found at <http://www.ccom.unh.edu>.

Vessel attitude and positioning measurements were collected for vessel motion compensation during the survey. Positioning data were referenced to the WGS84 ellipsoid as the horizontal datum and instantaneous sea level for the vertical reference. Motion data were collected by an interfaced Applanix POS/MV 320 version 3 inertial motion unit (IMU) with a Wide Area Differential-Aided Global Positioning System (DGPS). Fugro SkyFix differential signals provided position fixes within better than 5 m horizontal accuracy (Gardner, 2004; Cartwright and Gardner, 2005). A Hippy motion reference unit (MRU) was used to measure pitch and a Sperry Model Mark 39 gyro was used to monitor yaw. Integration of these sensors provided vessel attitude measurements for real-time motion-compensated beam steering by the EM121A multibeam system.

Sippican model T-10 (maximum depth ~200 m) and Deep Blue (maximum depth ~760 m) expendable bathythermograph's (XBT's) were used during the mapping surveys to calculate the sound-speed profile in the water column. The XBT's measured temperature as a function of water depth. Sound-speed was calculated from the measured water temperature to accurately trace each receive-beam path through the water column. Casts were taken every 6 hours as well as whenever it was found necessary to calculate a new sound-speed profile. The XBT's were calibrated during each patch test by comparing their sound-speed profiles to a sound-speed profile calculated from a SeaBird model SBE-19 CTD.

A hull-mounted ODEC Bathy2000 3.5-kHz chirp subbottom profiler was used to acquire high-resolution shallow seismic-reflection profiles during the MBES surveys. The 3.5-kHz chirp subbottom profiler provides shallow sub-surface images of marine sediments. The chirp system transmits a frequency-modulated (FM) swept pulse over a broad bandwidth instead of a continuous waveform and also creates a beam pattern with minimal side lobes (Leblanc et al. 1992). This results in high signal-to-noise ratio and the ability to detect small acoustic impedance contrasts in sediments (Shock et al., 1988).

2.1.2 Data Processing

The University of New Brunswick - Ocean Mapping Group's *SwathEd* software was used to flag data points in the raw multibeam data that were considered 'bad' soundings. The cleaned data were merged with navigation to produce ASCII grids for both bathymetry and backscatter. ASCII grids of longitude, latitude, and

depth and longitude, latitude and 8-bit digital number value of backscatter were created at 100-m cell-resolution. For more details, see Gardner (2004) and Cartwright and Gardner (2005).

Digital terrain models (DTM's) were created from the processed multibeam bathymetry and backscatter ASCII grids using *Fledermaus* software (see Mayer et al., 2000 for details). Shading and color maps were applied to the gridded data and assembled into *Fledermaus* files to create sun-illuminated color-shaded DTM's. A DTM was created for multibeam bathymetry and another one was created by draping the co-registered backscatter intensity values over the bathymetry.

A multibeam sonar backscatter mosaic was created using *Geocoder* version 3.2 level 2 software to further analyze the EM121A backscatter data for this study. *Geocoder* was developed at CCOM for multibeam sonar backscatter data processing (Fonseca and Calder, 2005). Multibeam sonar data were imported as generic sensor format (.gsf) files. Radiometric and geometric corrections were applied to the backscatter data to account for acoustic losses through the water column, the position of acoustic beams on the seafloor and the effects of the local seafloor slope (Fonseca and Mayer, 2007). Although *Geocoder* is also capable of correcting backscatter data for the sonar beam pattern, these corrections were not made for this study.

The *Geocoder* corrected backscatter data were mosaicked to produce a 100 m cell resolution image projected in Universal Transverse Mercator (UTM) coordinate system (zone 19N). Beam averages were used to compute *Geocoder* backscatter intensity. The corrected backscatter mosaic was used in *Geocoder* to quantitatively measure the average backscatter values in decibels (dB) within seafloor areas. A geo-

referenced backscatter mosaic was also exported for spatial analysis in *ESRI ArcMap* 9 Geographic Information Systems (GIS) software.

Chirp seismic-reflection profile data were processed using *SonarWeb* software. Raw chirp sonar data were imported as DAT files (.dat) into *SonarWeb* and chirp sonar lines were exported as viewable hypertext (.html) and image (.jpg) files. The seismic-reflection profiles were not corrected for changes in sound speed that were incurred within the water column and upon seafloor penetration of the chirp sonar pulse. Therefore, exported HTML and JPEG files also showed chirp sonar data using a constant (1500 m s^{-1}) sound speed.

2.2 Data Visualization and Analysis

The bathymetry data were compiled with pre-existing U.S. Geological Survey (USGS) 6.5-kHz GLORIA sidescan-sonar data, Lamont-Doherty Earth Observatory (LDEO) single-channel seismic-reflection profiles and sediment cores descriptions from the National Geophysical Data Center (NGDC). A GIS project was created using *ESRI ArcMap* GIS software to make spatial comparisons of backscatter intensities between the multibeam data, the GLORIA sidescan-sonar mosaic and collection locations of NGDC cores descriptions within a spatially referenced data frame. Three-dimensional visualization scenes were created using *Fledermaus* software to view seismic reflection profiles within a geo-referenced 3-D data space with multibeam backscatter and bathymetry data.

Fledermaus software was used for viewing the 12-kHz multibeam data and seismic-reflection profiles collected near the low-backscatter anomaly. Data were

viewed as a *Fledermaus* scene in WGS84 geographic projection. Chirp seismic-reflection profiles collected during the 2004 and 2005 bathymetric surveys were imported as geo-referenced vertical image files into *Fledermaus* scenes by entering latitude and longitude coordinates for the start and end control points for each profile line.

A search was also conducted for previously collected single-channel seismic-reflection profiles using the *GeoMapApp* seafloor data archive developed by Lamont-Doherty Earth Observatory. Airgun (25-in³) single-channel seismic-reflection line V2114 collected by LDEO in 1965 was found to cross the low-backscatter anomaly. The digitized section of LDEO profile V2114 crossing the low-backscatter anomaly was extracted from the *GeoMapApp* database as an image (.jpg) file. These data were imported into the *Fledermaus* scene containing multibeam backscatter and bathymetry as a geo-referenced vertical image using start and end control points.

Comparative analysis between backscatter data and seismic-reflection profiles was not made within the *Fledermaus* scene because of the spatial inaccuracies and misalignments that result from using too few control points. The inaccuracies result from along track changes in survey speed.

A GIS map was created using *ESRI ArcMap 9* GIS software to compile the 2004 and 2005 multibeam data sets with 6.5-kHz GLORIA sidescan-sonar data and previously collected sediment cores using the WGS84 geographic coordinate system. A 250-m cell-resolution composite mosaic of the full U.S. Atlantic GLORIA data was downloaded from the U.S. Geological Survey map server website (<http://coastalmap.marine.usgs.gov>) as a TIF image (.tif) with a geo-referencing

world file (.tfw). The horizontal reference datum of the downloaded image was NAD27 - Clarke 1866 referenced geographic coordinate system. The mosaic image was reprojected into WGS84 geographic coordinate system using the *ArcToolbox* “Projections and Transformations” function in *ArcGIS*. This conversion was used to display the GLORIA data within the GIS map in the same projection as the MBES data and sediment core information. The backscatter mosaics were examined together to determine if the low-backscatter anomaly was resolved in both the 6.5-kHz sidescan-sonar data the 12-kHz multibeam backscatter (Figure 2.1).

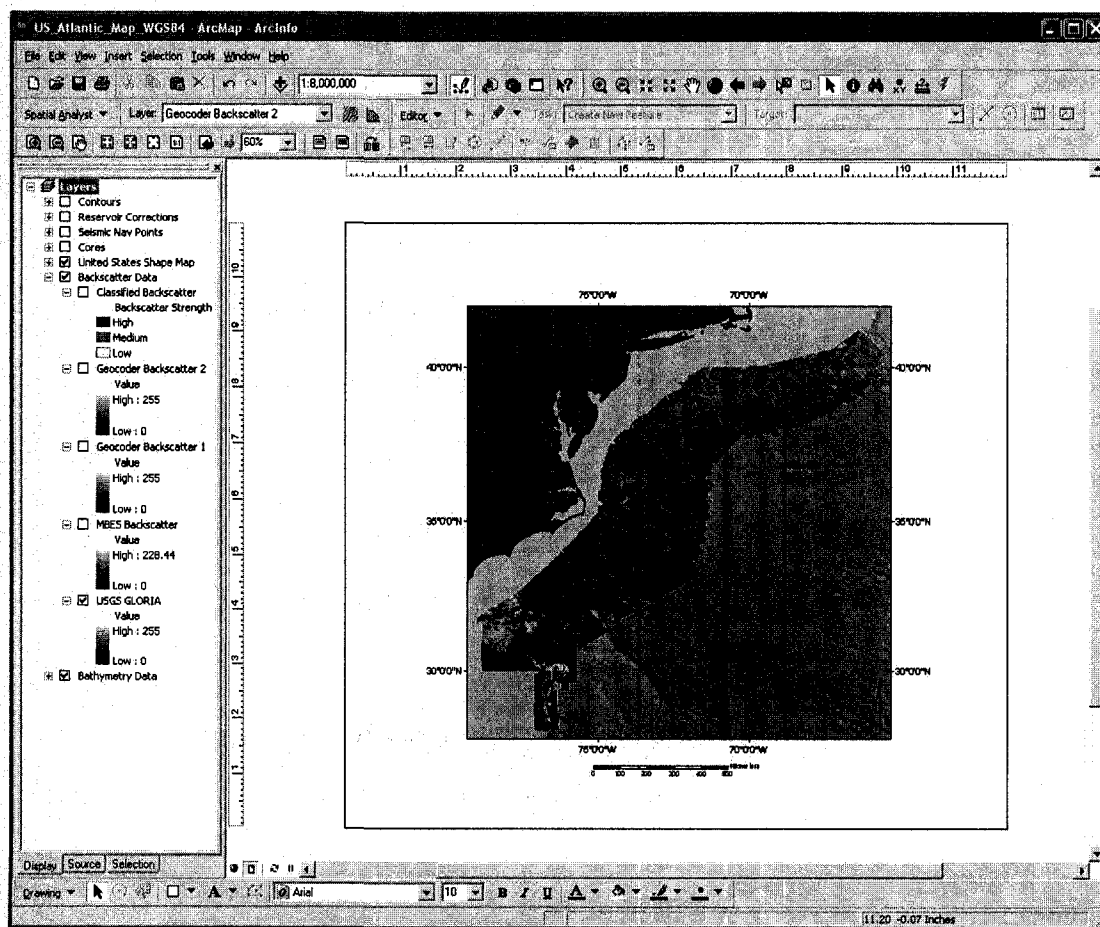


Figure 2.1 Map showing view of 6.5-kHz GLORIA sidescan-sonar mosaic with other layers in *ArcGIS*. GLORIA data were viewed to compare backscatter intensity near the low-backscatter anomaly found in the multibeam data.

Collection locations of sediment cores previously collected on the U.S. Atlantic margin archived at the NGDC database were also plotted in the GIS map with MBES and sidescan-sonar data. Collection locations of core samples from all available core repositories participating in the NGDC data archive were extracted from the NGDC *ArcIMS* map interface and exported as an *ArcGIS* compatible shape file in the WGS84 geographic coordinate system. The exported shape file was plotted as a point shape file in *ArcMap* to identify the spatial location of existing core samples in reference to the low-backscatter anomaly seen in the multibeam data (Figure 2.2).

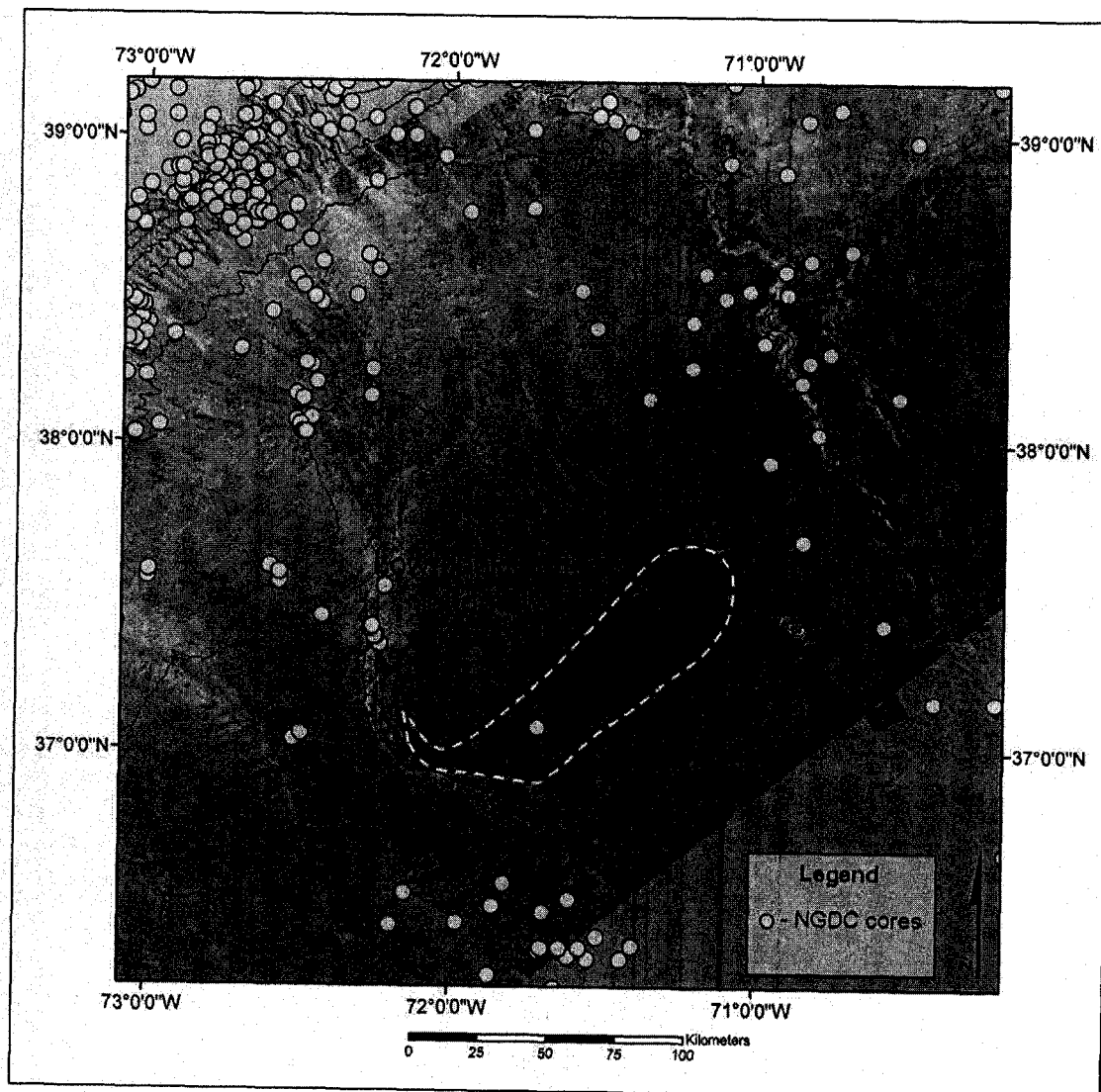


Figure 2.2 Map showing collection locations of all NGDC archived cores (yellow dots) over backdrop of multibeam backscatter data and NGDC/NOAA ETOPO2 and Coastal Relief Model bathymetry (sun-illuminated hillshade). The low-backscatter anomaly is outlined by the white-dashed line.

Latitude and longitude coordinates for the pixel locations of MBES backscatter intensity changes along survey tracklines were found in geo-referenced multibeam backscatter imagery within the GIS map. The coordinates of backscatter strength transitions were then found in the chirp data files created in *SonarWeb*, which provide a latitude and longitude coordinate for each data pixel in the seismic-

reflection profile imagery. This pixel-matching method was used to compare MBES backscatter strength measured at the seafloor with corresponding subbottom structure shown by high-resolution chirp sonar profiles.

Pixel matching was also used to determine correlations between multibeam backscatter data and LDEO single-channel seismic-reflection profile line V2114. Digitized versions of airgun single-channel seismic-reflection profiles within the *GeoMapApp* database provide latitude and longitude coordinates for each pixel within the seismic-reflection line imagery. Locations of backscatter transitions were determined along the survey trackline within the geo-referenced multibeam data and then found within the LDEO airgun single-channel seismic-reflection profile.

2.3 Backscatter Classification

Areas of backscatter strength and “texture” were characterized in the backscatter data into a classification scheme developed for this study. Backscatter strength values were separated into high (-25 to -33 dB), medium (-34 to -42 dB) and low (-43 to -51 dB). Visual patterns identifiable in the acoustic backscatter data were used to characterize the backscatter texture of seafloor regions. Textural characterizations were determined based on the qualitative nature of the backscatter variability and are referred to as “homogenous” where little backscatter variability can be visually identified or as “mottled, rilled, or streaky” where variable backscatter patterns are seen.

2.4 Chirp Sonar Profile Interpretation

Previous studies have interpreted sedimentation processes on the U.S. Atlantic continental margin from 3.5-kHz seismic-reflections profiles (Damuth, 1980; Embley, 1980; Pratson and Laine 1989). These studies have made qualitative correlations between the physical appearance of acoustic stratigraphy found in 3.5-kHz subbottom profiles and sedimentary processes such as sediment drape, mass-wasting, and contour-current reworking. The seismic-reflection profiles for this study were collected using a 3.5-kHz subbottom profiler, however, the Bathym2000 subbottom profiler uses a frequency modulated chirp waveform as its transmit pulse. As a result, higher-resolution and perhaps slightly different physical appearance would be expected from the chirp seismic-reflection data than the continuous wave pulse 3.5-kHz subbottom profiler used by Damuth (1980), Embley (1980) and Pratson and Laine (1989). However, the correlations between sediment processes and reflectors shown by 3.5-kHz subbottom profiles observed in previous studies by Damuth (1980), Embley (1980) and Pratson and Laine (1989) were considered comparable when making interpretations.

2.5 Sediment Core Analysis

The compiled GIS map shows that sediment cores EN101-PC01, EN084-GC02, and RC10-PC01 were collected near the low-backscatter anomaly (Figure 2.3). Cores EN101-PC1 and EN084-GC2 were collected in the 1980's by the University of Rhode Island - Graduate School of Oceanography (URI-GSO) from the R/V *Endeavor* and RC10-PC1 was collected by LDEO from the R/V *Robert Conrad*

in 1965. Cores EN101-PC01 and RC10-PC01 were collected with a piston corer and EN084-GC02 was collected using a gravity corer. Core information is summarized in Table 2.1.

Cores EN101-PC01 and EN084-GC02 were photographed (Figure 2.4 and Figure 2.5) and visually described at the URI-GSO core repository. An original visual core description was also acquired from the URI-GSO core repository for core EN101-PC01. However, no documentation was found for core EN084-GC02. A 2-cm³ sample was collected from both cores every 5 cm down the length of the core and at noticeable facies boundaries for grain-size and smear-slide analyses (Figure 2.4 and Figure 2.5). Sampling intervals were not always constant because of previously sampled and unavailable core sections. Core EN101-PC01 contains numerous voids and sections of previous sample removal. Core EN084-GC02 is nearly complete with the exception of the unavailable section from 120 to 165 cm and was previously unsampled.

Core RC10-PC01 was photographed (Figure 2.6) and visually described at the LDEO core repository. Original photographs (Figure 2.7) and stratigraphic descriptions were also acquired from the LDEO core repository. Two-cm³ samples were collected at 10 cm intervals from the core top to 100 cm and at depths 298 cm and 725 cm by core curators at LDEO for grain-size and smear-slide analyses (Figure 2.6 and Figure 2.7).

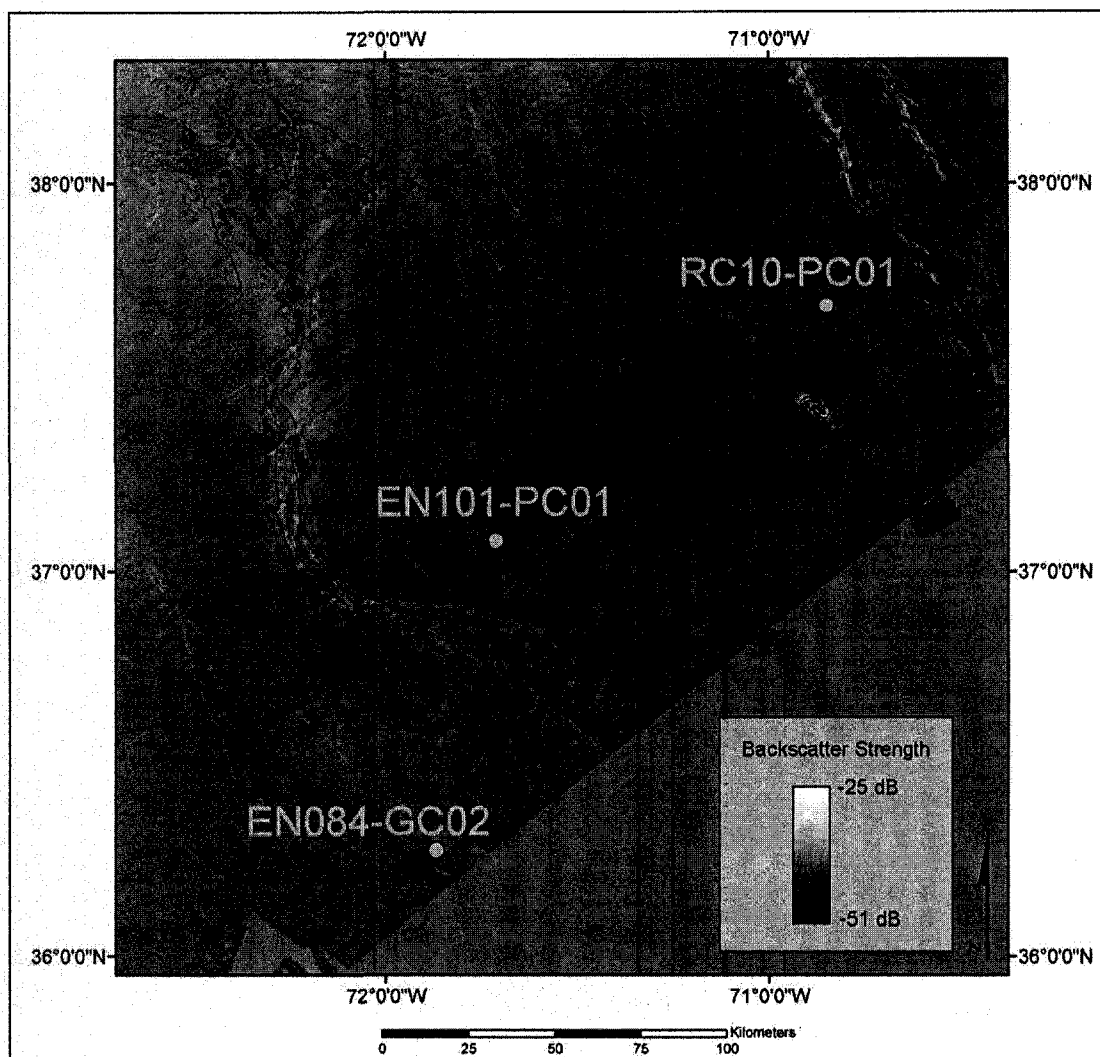


Figure 2.3 Core locations mapped with multibeam backscatter backdrop.

Table 2.1 Summary table of core samples analyzed for this study.

Core ID	Institution	Date	Length (cm)	Core Type	Latitude	Longitude	Water Depth (m)
EN084 GC02	URI-GSO	5/20/1982	280	Gravity	36.270000	-71.868333	4052
EN101 PC01	URI-GSO	6/00/1983	800	Piston	37.075000	-71.713330	3817
RC10 PC01	LDEO	12/3/1965	1059	Piston	37.683000	-70.850000	3911

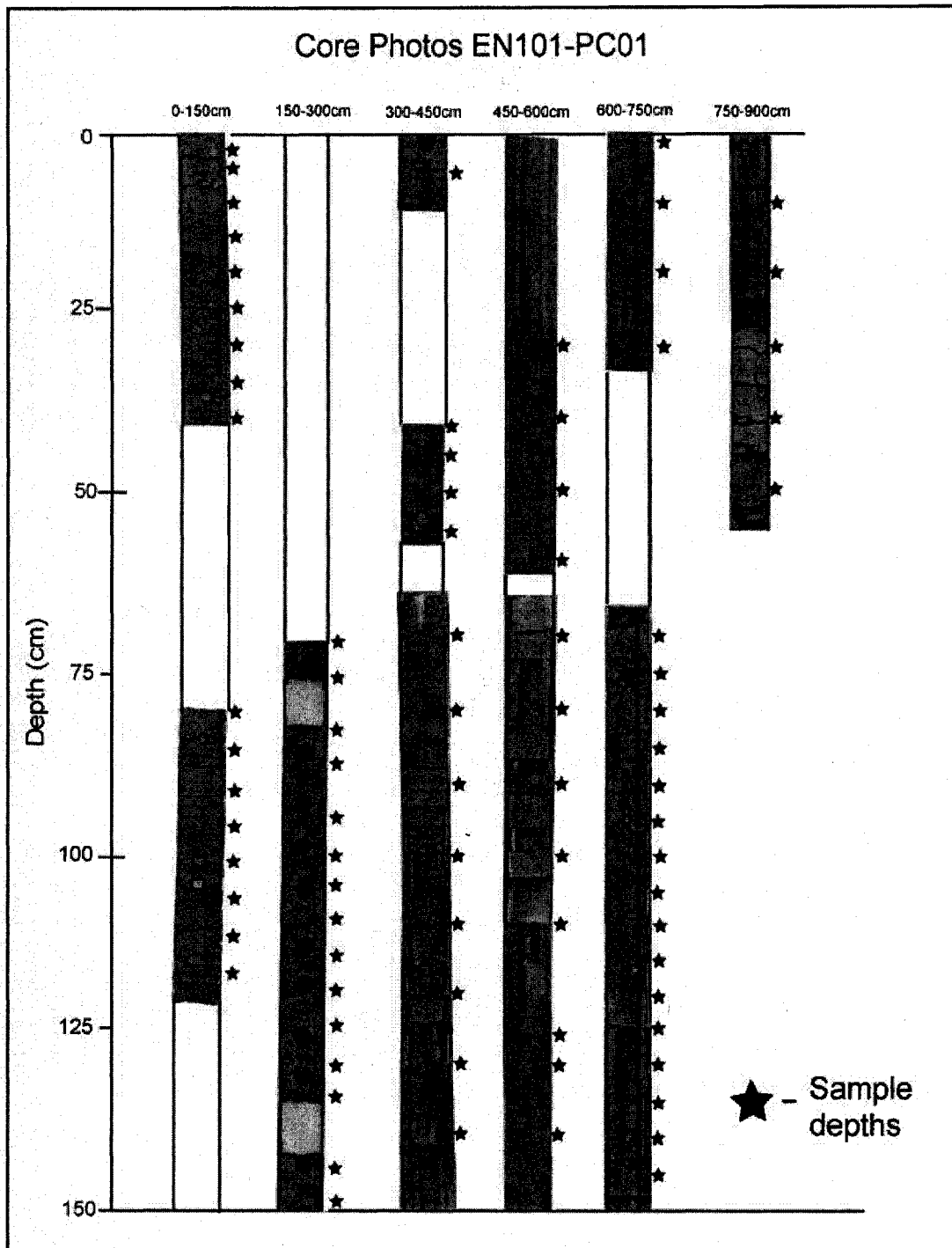


Figure 2.4 Recent photographs of core EN101-PC01 showing sample depths. White spaces indicate missing core sections.

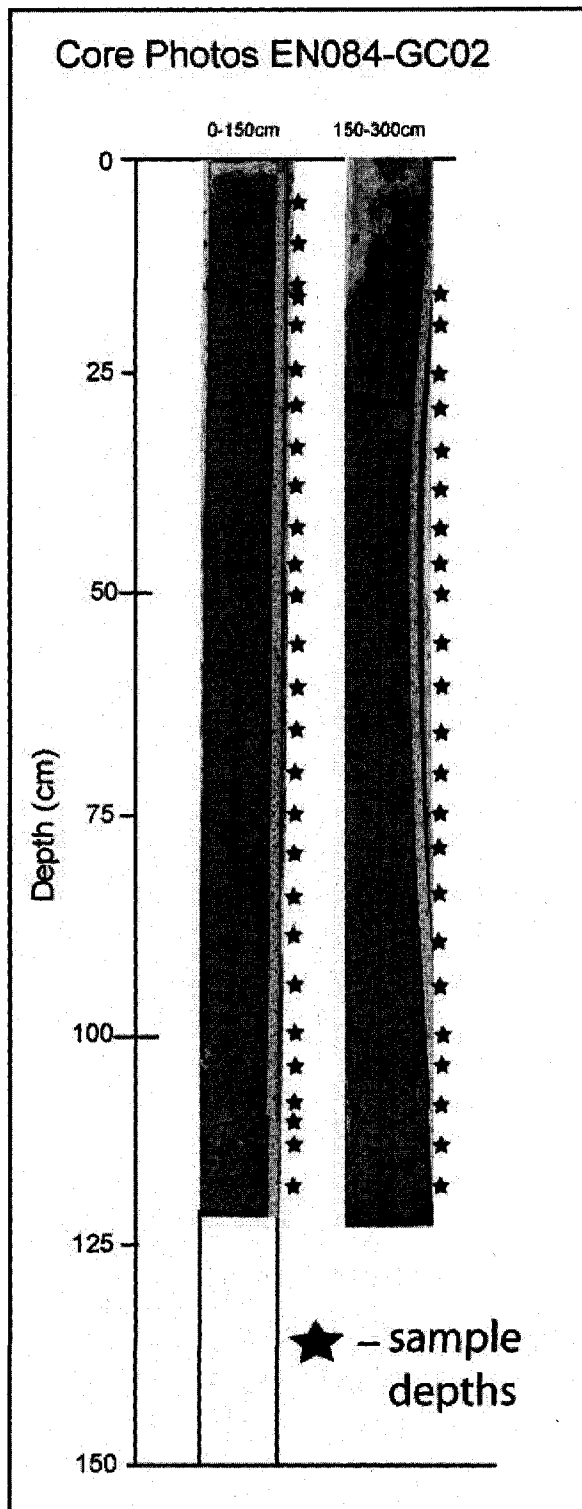


Figure 2.5 Recent photographs of core EN084-GC01 with sample depths. White space indicates missing core sections.

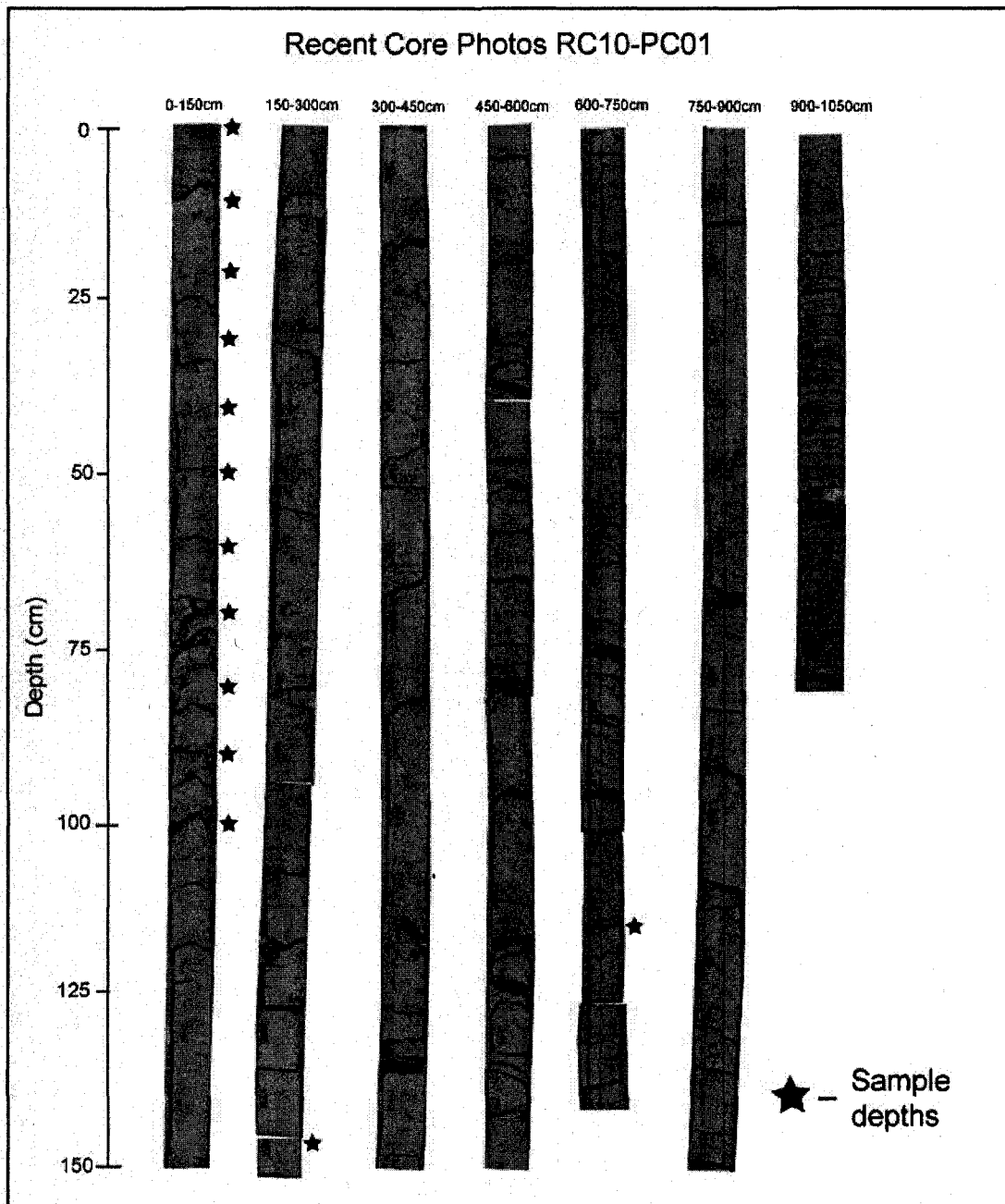


Figure 2.6 Recent photographs of core RC10-PC01 showing sample depths.

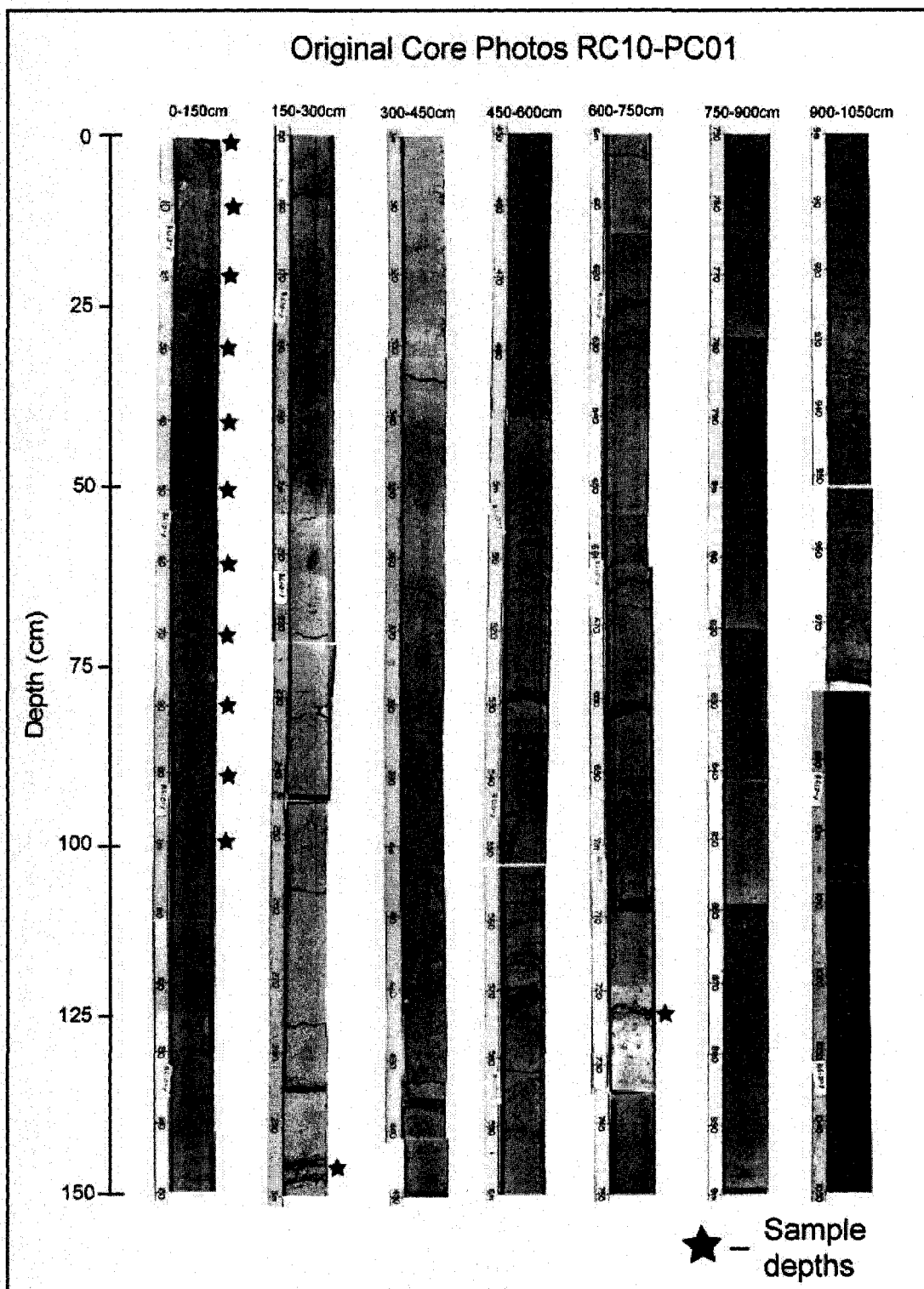


Figure 2.7 Black and white photographs of core RC10-PC01 showing sample depths.

2.5.1 Grain-Size Analysis

Grain-size analyses were performed on each of the sediment core sub-samples at the URI - GSO using a *Malvern Mastersizer Hydro 2000G*. The Malvern Mastersizer measures the distribution of grain size using laser diffraction and is capable of measuring particle diameters from 0.02 μm to 2000 μm with low uncertainties (Malvern manufacturer specifications). Sperazza et al. (2004) determined that the overall uncertainty for particle size analysis at a 95% confidence interval is $\sim 1\%$ using the Malvern Mastersizer 2000. Particle-size distributions are calculated by passing a parallel laser beam through a sediment sample in suspension and measuring the angles of the diffracted light on the instrument's light detector (McCave et al. 1986; Wen et al., 2002; Sperazza et al., 2004). The angular distribution and intensity of the diffracted light are measured and fit to a theoretical model for grain-size distribution and particle properties (Sperazza et al., 2004). Fraunhofer and Mie are the two theories commonly applied in particle-size analysis using laser diffraction (McCave et al. 1986; Wen et al., 2002; Sperazza et al., 2004). Both theories express the relationship between the angular distribution of light intensity and particle radius as a function of the scattering angle and assume that particles are spherical in shape (Wen et al., 2002). The Fraunhofer theoretical diffraction model was used for the sediment analyzed in this study because the refractive index of the analyzed sediment was unknown.

Samples were prepared for grain-size analysis at the University of New Hampshire using a mixed solution of sodium hexametaphosphate (NaPO_3)₆ dispersing agent and hydrogen peroxide (H_2O_2). The mixed solution contained 10 ml

of 4.0 g/l $(\text{NaPO}_3)_6$ and 10 ml of 3% H_2O_2 . The $(\text{NaPO}_3)_6$ was used to break electrostatic forces between clay particles and prevent flocculation during grain-size analysis and H_2O_2 was used to digest organic carbon within the sediment. Sediment samples weighing 0.2 to 0.25 g (wet weight) were added to a solution of $(\text{NaPO}_3)_6$ and H_2O_2 and soaked for 24 hrs or longer. The mixture of sediment, $(\text{NaPO}_3)_6$ and H_2O_2 were immersed in a sonication bath for 10 min prior to grain-size analysis to further disaggregate particles as described in methods by Sperazza et al. (2004). This mixture was poured into the basin of the Malvern Mastersizer Hydro 2000G dispersion unit immediately after sonication for grain-size analysis.

Grain-size data were reported from the Malvern Mastersizer as percent volume of the sample. Percentages were binned using grains sizes for particle diameter in both microns and phi (ϕ) units. The phi scale is a logarithmic function of particle diameter (d) where:

$$\phi = -\log_2(d)$$

The reported percent volume distributions were used to compute the mean grain size for each sediment sample. Average grain sizes were computed using the statistical software package *JMP* version 6 and plotted as a function of the sub-sample depth for each core. Plots were used to show the variability of mean grain size throughout each core and to identify discrete events of grain-size change. Mean grain sizes from the grain-size analysis results are presented in the Results section (Chapter 3).

2.5.2 Smear-Slide Analysis

Sediment composition for cores RC10-PC01, EN101-PC01, and EN084-GC02 was examined by creating smear slides from each sediment sample. A small amount of sediment (scooped using the end of a toothpick) and several drops of deionized water were spread uniformly on a glass slide using a rounded toothpick. The slide was placed on a hot plate ($\sim 120^{\circ}\text{C}$) to evaporate the water from the sediment. A cover slip was glued over the sediment using several drops of optical adhesive and cured under ultraviolet light. Smear slides were viewed using a light-polarizing microscope under plain and cross-polarized light (Figure 2.8 and Figure 2.9).

Visual estimates of mineral-grain types, biogenic components, and grain sizes were recorded using the visual chart for volume percentage by Terry and Chilingar (1955). Relative abundances of sand, silt and clay were estimated using the grain-size definitions by Wentworth (1922). Sediments composed of $>60\%$ siliciclastic components were classified using the textural name (i.e. silt or clay). Sediments containing 40% to 60% biogenic components were classified using the Ocean Drilling Project (ODP) scheme for “mixed sediments” derived by Mazzullo and Graham (1988). The mixed sediment classification scheme names sediments using a fossil modifier followed by the principal siliciclastic component. The fossil modifier is ordered as the minor biogenic constituent followed by the major constituent. The suffix “bearing” was used to describe modifier components with abundances measuring 5% to 10% of the sediment sample and “rich” was used for describing components in the 11% to 40% range. For example, a sample containing 15%

foraminifera, 35% nannofossils and 55% clay would be classified as a foraminifera-rich nannofossil clay.

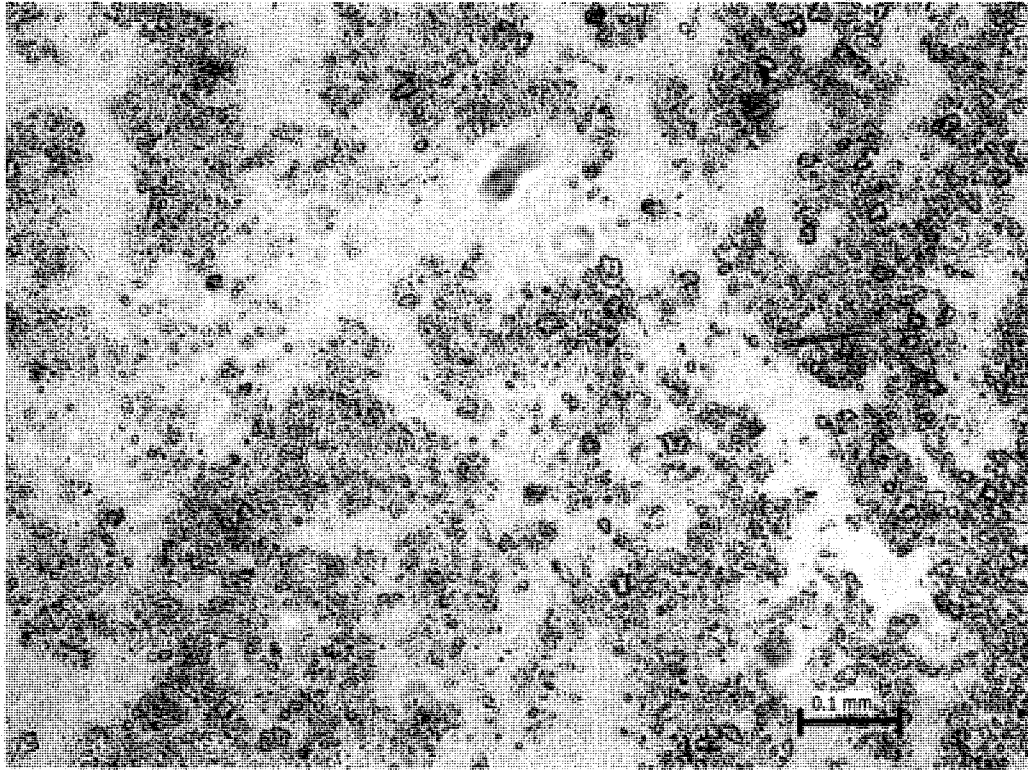


Figure 2.8 Example of a smear slide sample showing nannoplankton-rich silty clay sediment from core EN101-PC01 (10 cm) under 100x magnification in plain polarized light. Cross-polarized light (shown in the next figure) shows many of the small grains are calcareous coccoliths.

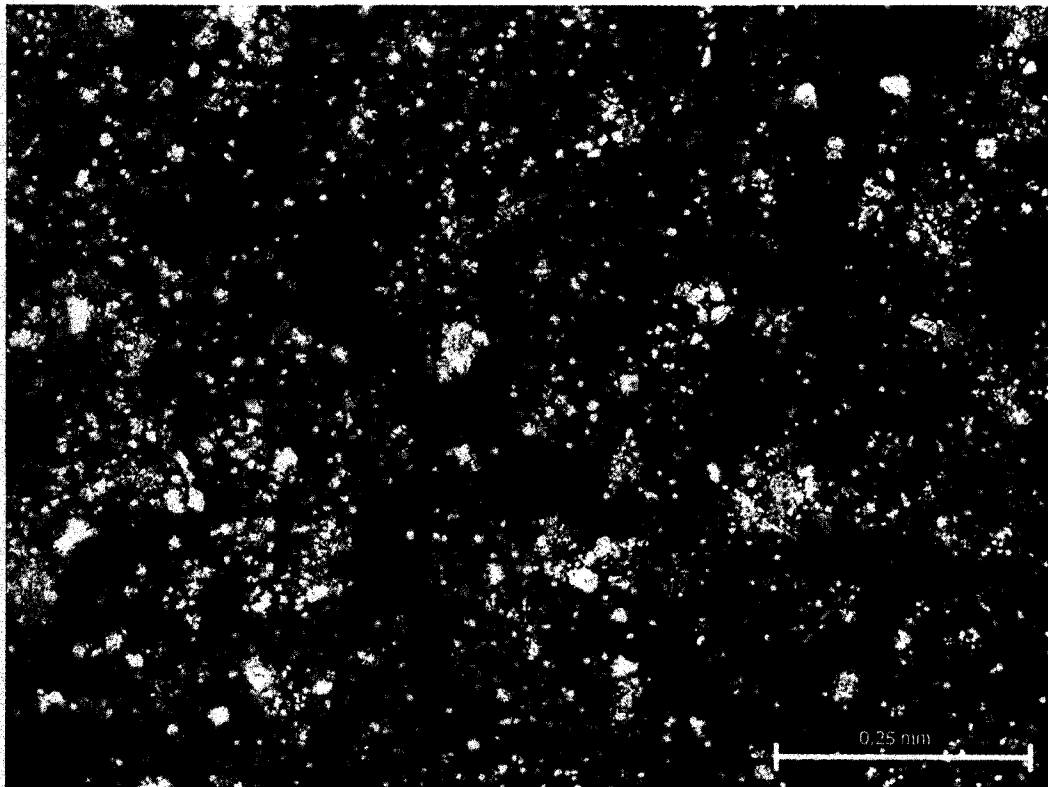


Figure 2.9 Example of a smear slide sample of core EN101-PC01 (10 cm) under 100x magnification in cross-polarized light.

2.5.3 AMS-Radiocarbon Dating

Four sediment samples from depths of 10, 300, 345 and 355 cm from core EN101-PC01 were sieved using a 63- μ m mesh and a mixed species of planktonic foraminifera consisting of *Globorotalia menardii*, *Globoquadrina dutertrei*, *Globigerinoides ruber*, *Globigerinoides sacculifer*, *Sphaeroidinella dehiscens* and *Orbulina universa* were selected for accelerated mass spectrometry (AMS)-radiocarbon dating at the National Ocean Science Accelerated Mass Spectrometry (NOSAMS) facility at Woods Hole Oceanographic Institution. Samples were freeze-dried before sieving using a Labconco Freezone 2.5 freeze drier for 24 hrs to remove water from the sediment. Freeze-dried sediment samples were then

disaggregated using 5g/l solution of $(\text{NaPO}_3)_6$ and shaken for 3 to 4 hrs. Samples were washed through a 63- μm size sieve to separate the coarse-grain sediment fractions at the sand-silt boundary. Planktonic foraminifera were identified and picked using taxonomic species descriptions and photographs by Bé (1977).

Samples were selected from the upper core section as a precaution to remain within the bounds of ^{14}C dating ($\sim 60,000$ yrs) (Plastino et al., 2001) based on estimated sedimentation rates of 1 to 10 cm/1000 yr for the outer New Jersey margin (Mountain et al., 2007). Additionally, foraminifera were not picked from core sections containing evidence of turbidites to avoid misleading ages due to sediment reworking.

Radiocarbon ages were determined at the NOSAMS facility using 5568 yrs as the half-life of radiocarbon following the convention outlined by Stuiver and Polach (1977) and Stuiver (1980). Reservoir corrections were applied to these sample ages using the calibration data set provided by *CALIB* version 5.0 (Stuiver and Reimer, 1993; Reimer et al. 2004). These corrections account for the regional ^{14}C variations in the marine reservoir that deviate from the atmospheric ^{14}C record. The *CALIB* program converts radiocarbon age to calibrated calendar years by calculating the probability distribution of the sample's true age. The calibrated calendar age distribution is calculated using a global marine calibration curve known as Marine04 and a user input local correction (ΔR) and local correction error (ΔR error), which adjusts for differences between the global ocean curve and regional ^{14}C activity that result from local oceanic processes (Stuiver and Braxiunas 1993; Reimer et al. 2004).

Values for ΔR were found for the region near the collection location of core EN101-PC01 using the global data set provided at the website <http://www.calib.qub.ac.uk/marine>. The locations of the regional reservoir corrections were plotted in *ArcMap* GIS software to determine the distances from the location collection of core EN101-PC01 (Figure 2.10). A distance-weighted average was calculated for observed ΔR and ΔR error values located along the New Jersey and Massachusetts coasts and Georges Bank provided by the data set (Table 2.2). The distance-weighted average of these values was used because the data set provided multiple ΔR correction values that were not equidistant from the offshore collection location of core EN101-PC01. The distance-weighted average ΔR and ΔR error values were then implemented in *CALIB* version 5.0 to calculate the calibrated calendar age for the sample from 10 cm depth. Corrections were not applied to samples 300, 345 and 355 cm because the measured radiocarbon ages for these samples were outside the bounds of the *CALIB* program calibration curve, which only exists for samples younger than 26,000 yr.

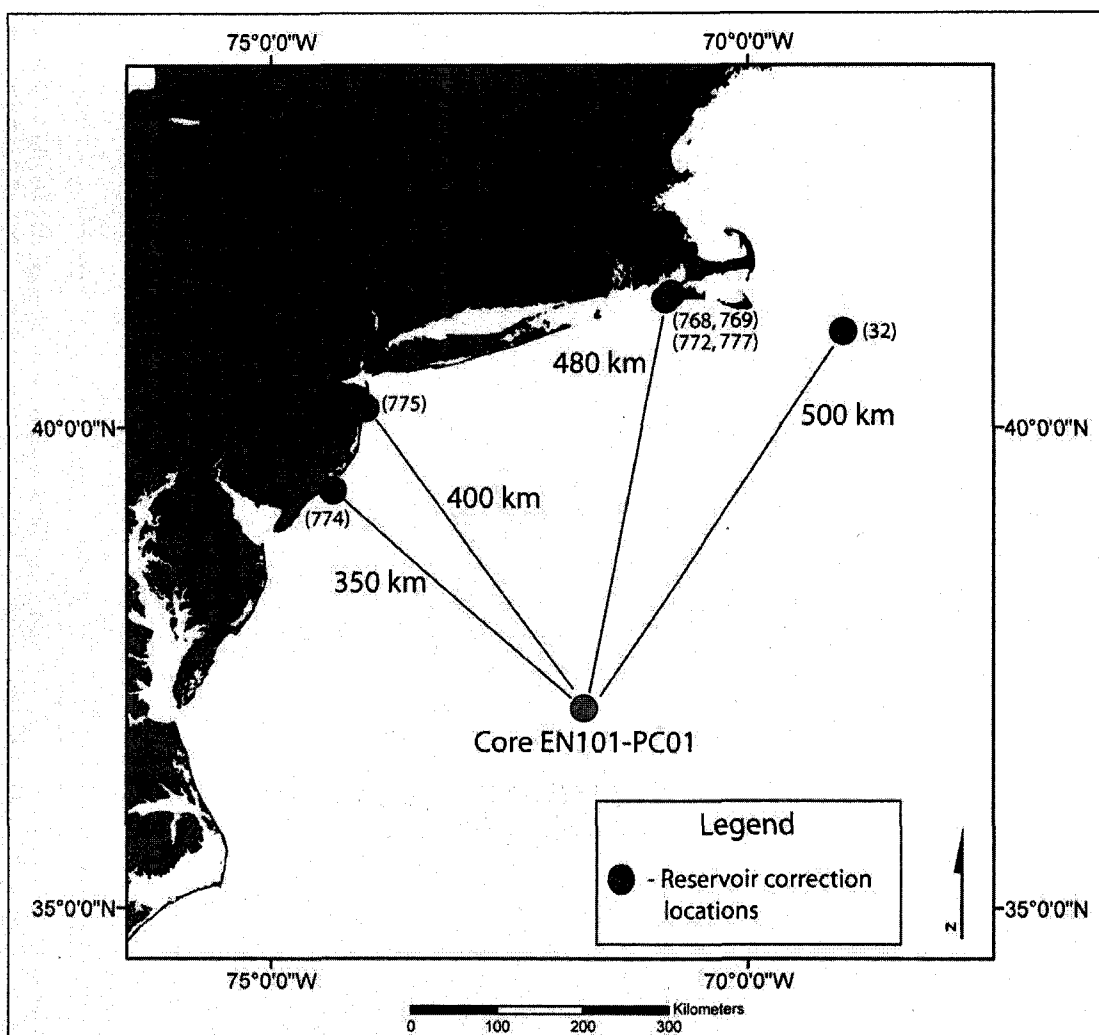


Figure 2.10 Locations of the observed ΔR and ΔR error corrections used to compute a distance-weighted average regional reservoir correction for radiocarbon ages in core EN101-PC01. Station site numbers are shown in parentheses. Station information is shown in Table 2.2.

Table 2.2 Station information used for reservoir corrections applied to radiocarbon age measured for sample 10 cm in core EN101-PC01.

Location	Site	Distance (km)	Distance Weights	ΔR	ΔR error
Georges Bank, Nova Scotia	32	500	0.13	94	22
Vineyard Sound, MA	768	480	0.13	120	40
Vineyard Sound, MA	769	480	0.13	120	60
Vineyard Sound, MA	772	480	0.13	230	70
Atlantic City, NJ	774	350	0.18	170	50
Shark River, NJ	775	400	0.16	130	60
Gay Head, MA	777	480	0.13	140	60
Arithmetic Avg				119	44
Distance Weighted Avg				145	52

CHAPTER 3

RESULTS

3.1 Introduction

The geological characteristics of the seafloor near the low-backscatter anomaly are described in the following section using multiple types of seafloor data. Multibeam sonar bathymetry data are presented to describe the regional seafloor morphology near the low-backscatter anomaly. Slope gradients and seafloor features are identified to determine bathymetric indications for margin sediment processes. Multibeam sonar backscatter data are presented to analyze correlations between the seafloor features identified in the multibeam sonar bathymetry and the measured acoustic response from the seafloor. The acoustic sub-surface stratigraphy is described using 3.5-kHz chirp and airgun single-channel seismic-reflection data. These data show the subbottom structure of seafloor features identified in the MBES data and additionally show sub-surface features that are not evident from the surface seafloor data. The lithologic composition and age of seafloor sediments near the low-backscatter anomaly is described using sediment cores. These samples are described in reference to the sonar data to identify the sediment facies that correspond to the acoustic scattering response seen in the multibeam and sidescan sonar backscatter intensity and subbottom structure observed in the seismic-reflection profiles.

3.2 Multibeam Sonar Bathymetry

The 12-kHz multibeam sonar bathymetry collected offshore New Jersey shows a range in water depths from approximately 2000 m to more than 4400 m (Figure 3.1). The seafloor typically has slope gradients less than 1° within these water depths on the New Jersey continental margin (Figure 3.1). Seafloor gradients decrease from $\sim 1^\circ$ near the upper bounds (~ 2000 m water depth) of the data to $\sim 0.2^\circ$ near the 3000 m isobath. Bathymetry data show a break in slope that occurs near the 3000 m isobath. This break in slope has been identified by Mountain (1985) as the location of the Chesapeake Drift, the buried sediment drift that formed on the middle U.S. Atlantic continental margin during the Pliocene-Miocene ~ 5 to 10 mya. Seafloor gradients increase to $\sim 0.7^\circ$ between the 3000 m to 4100 m isobaths beyond this slope break. This section of seafloor has been previously noted and referred to as the seaward flank of the buried Chesapeake Drift (Mountain and Tucholke, 1985; Mountain, 1987; Pratson and Laine, 1989). Seafloor gradients beyond the 4100 m isobath in the bathymetry data measure $\sim 0.2^\circ$. The low-backscatter anomaly is located on the lower section of the relatively steep ($\sim 0.7^\circ$) seafloor, immediately upslope from the flatter ($\sim 0.2^\circ$) seafloor gradients found beyond the 4100 m isobath (Figure 3.1).

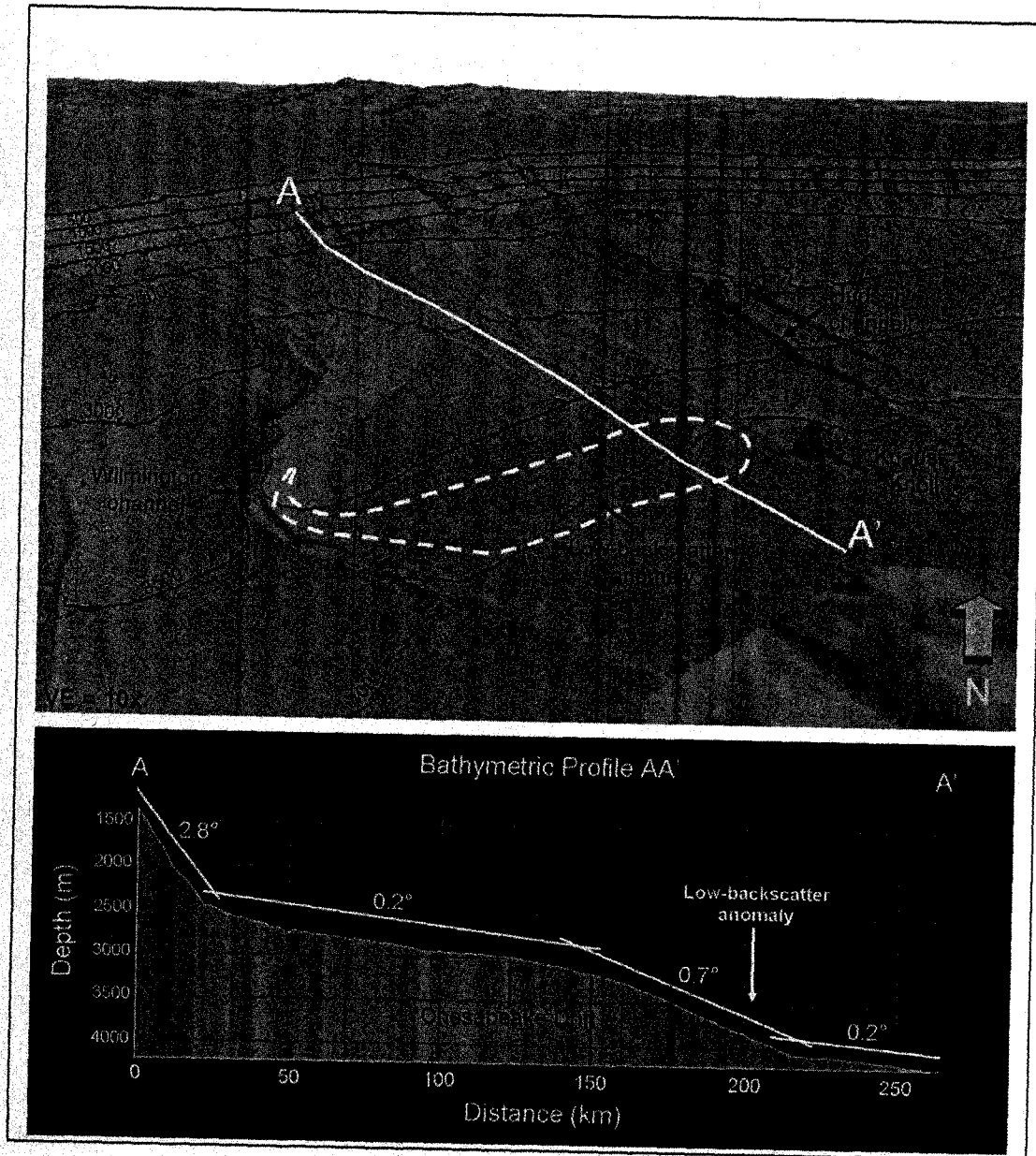


Figure 3.1 Perspective view (looking north) showing gray hillshade of the 12-kHz multibeam bathymetry with NOAA ETOPO2 and Coastal Relief Model as backdrop. Bathymetric image vertical exaggeration (VE) = 10x. Low-backscatter anomaly outlined in white-dashed line. Bathymetric profile AA' across the New Jersey margin showing seafloor gradients. Average slope gradients are shown across the top of the profile. Profile indicates the approximate location of the buried Chesapeake Drift.

The bathymetric data on the New Jersey margin also show that the seafloor is cut by many deep-sea channels. Two of the major channels are Hudson and

Wilmington channels (Figure 3.1). The Wilmington channel (also called the Baltimore-Wilmington channel) begins at the confluence of numerous continental slope canyons (Figure 3.2). This confluence has been referred to as the Baltimore-Toms gather area by Schlee and Robb (1991).

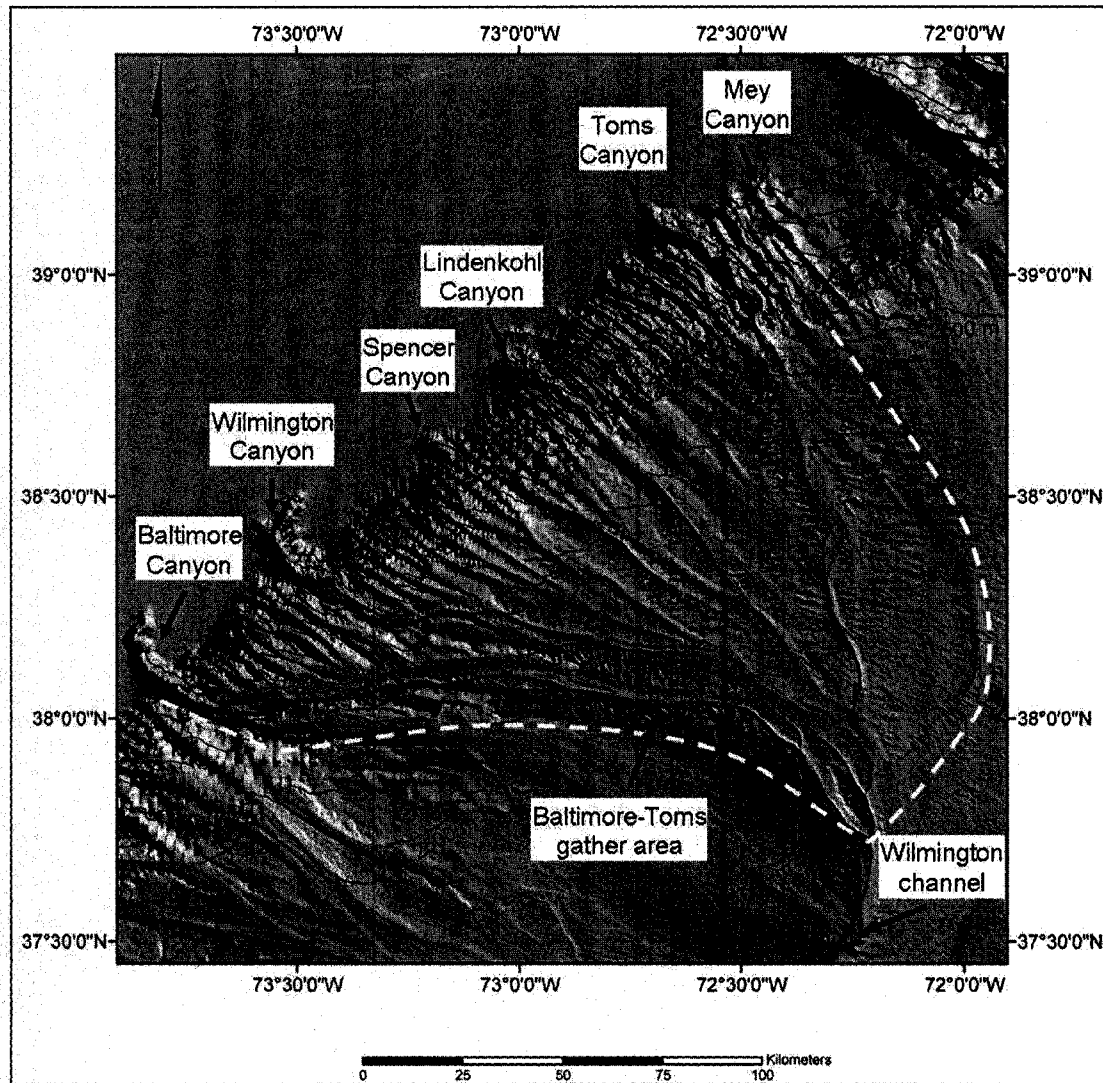


Figure 3.2 MBES bathymetry data overlaying NOAA ETOPO2 and Coastal Relief Model showing slope canyons that converge into Wilmington channel.

Hummocky and wavy seafloor features are observed within the Baltimore-Toms gather area near the base of the continental slope on the upper continental rise where seafloor gradients are low (0.2°) (Figure 3.3). The hummocky seafloor morphology is most prevalent within the gather area above Wilmington channel. However, the wavy seafloor features are also found across the seafloor between the gather area and Hudson channel.

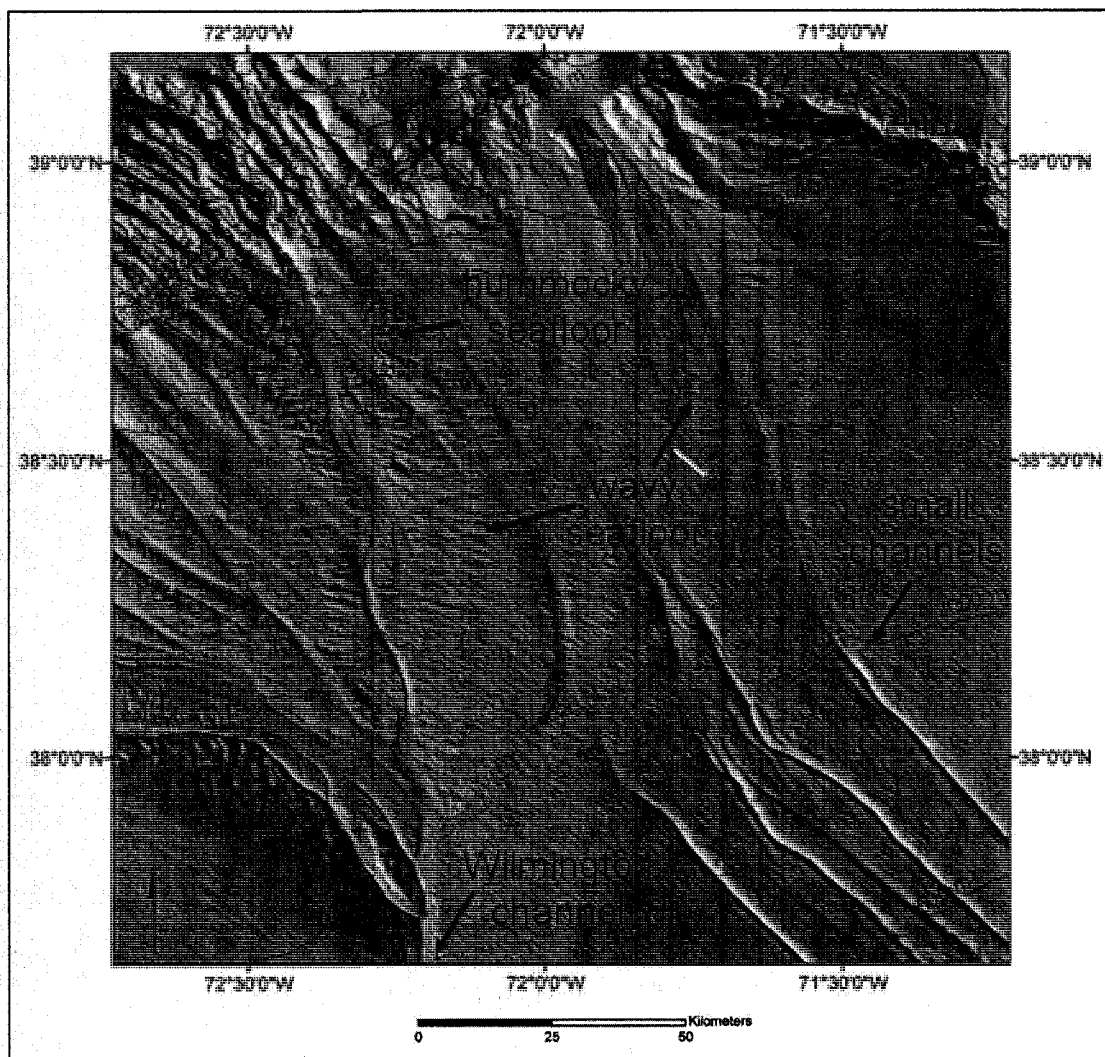


Figure 3.3 Bathymetry data (gray sun-illuminated hillshade) showing hummocky and wavy seafloor features near the base of the continental slope where seafloor gradients are low.

Wilmington channel forms a large bend just beyond the gather area confluence between the 3200 m and 4000 m isobaths. In this section of the channel, the walls are steep and the channel is incised approximately 300 m. The channel begins to shallow in its incision depth from 300 m to less than 75 m beyond the 4000 m isobath and broadens in width from 4 km to 10 km. The bathymetry data show hummocky seafloor immediately outside the main channel to the south beyond the 4000 m water depth (Figure 3.4).

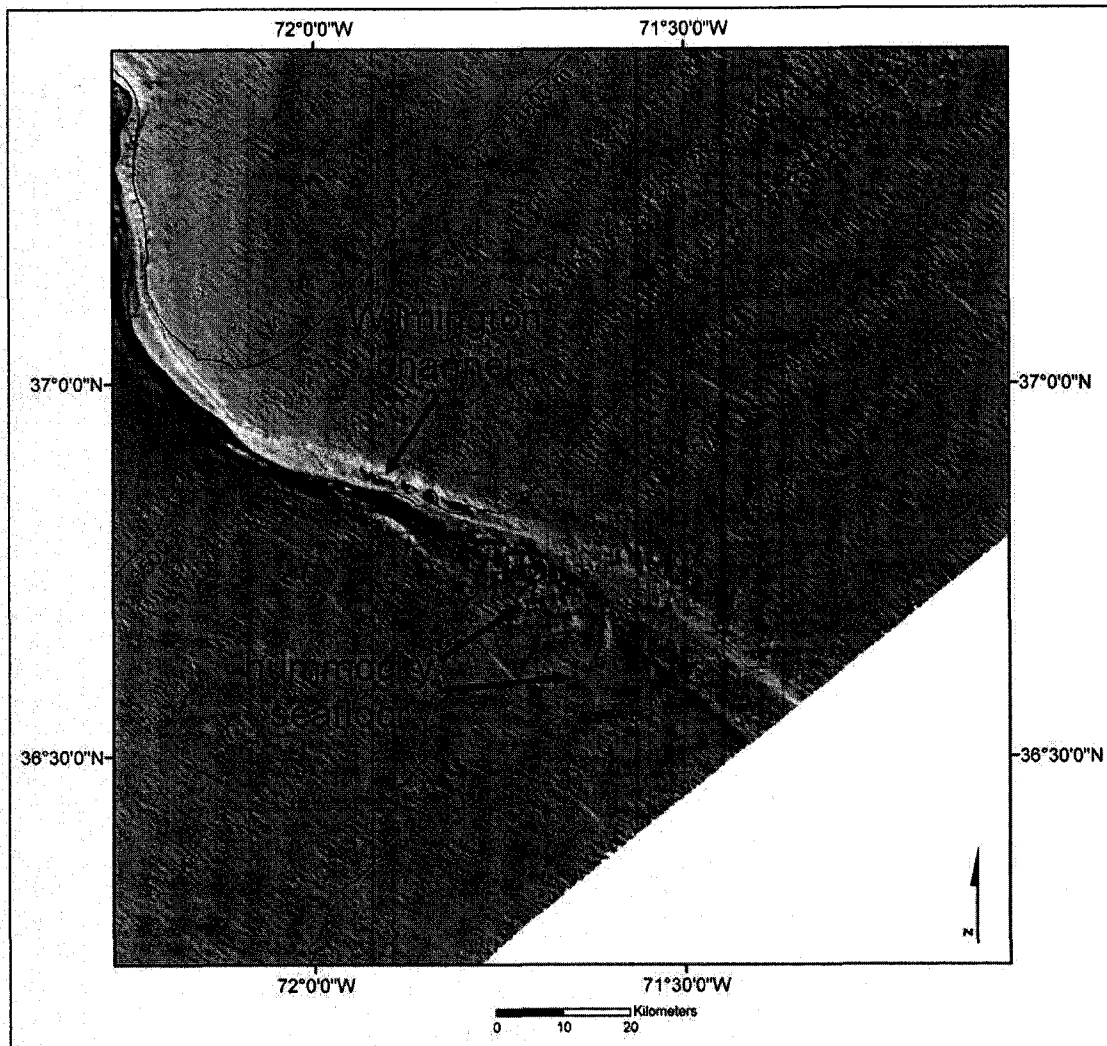


Figure 3.4 Bathymetry data showing hummocky seafloor at the terminus of Wilmington channel.

Hudson channel is located nearly 150 km northwest of Wilmington channel. Bathymetry data show a less distinct gather area than the Baltimore-Toms gather area (Figure 3.5). However, the bathymetry data show several canyons that converge into Hudson channel.

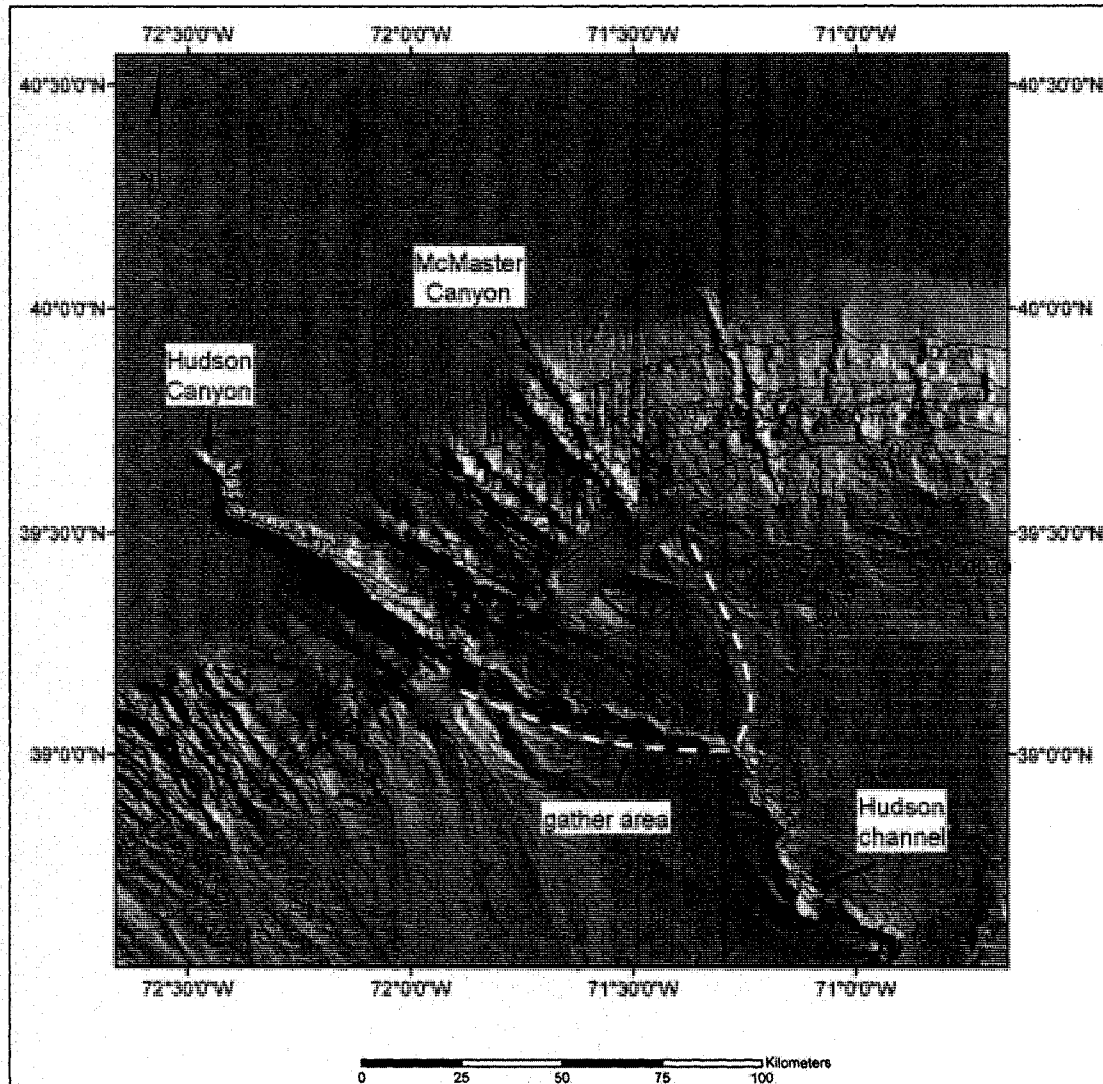


Figure 3.5 Map showing bathymetry data where slope canyons converge into Hudson channel.

Hudson channel increases its incision from 100 m to 150 m near the 2500 m isobath up to 500 m between the 3000 m to 4000 m isobaths. The incision depth shallows to less than 150 m beyond 4000 m water depth and the channel broadens in width from 5 to 11 km. Hummocky seafloor is observed outside of the channel on both sides in this section (Figure 3.6).

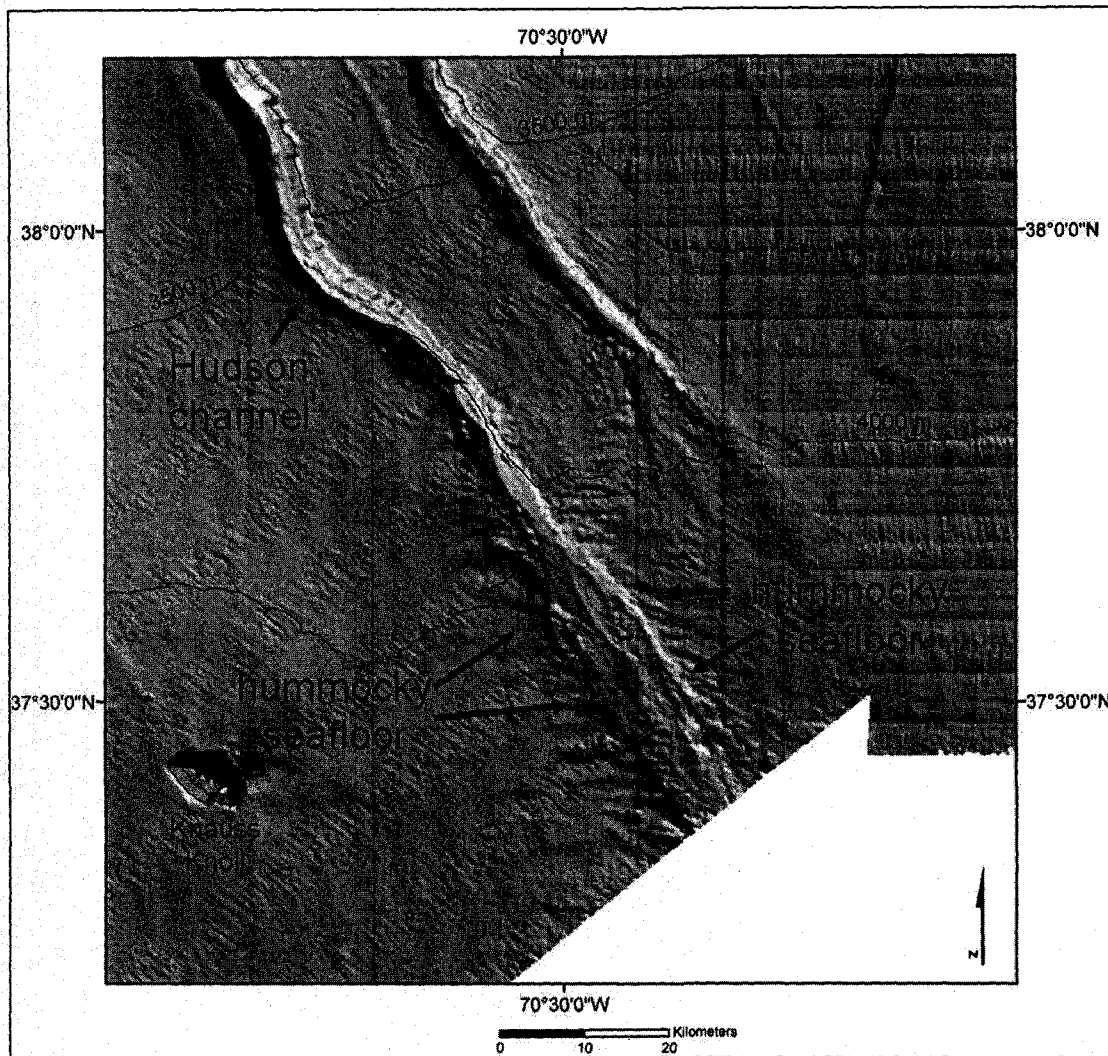


Figure 3.6 Bathymetry data showing hummocky seafloor at the terminus of Hudson channel

The MBES bathymetry data also show five, smaller channels located between Wilmington and Hudson channels. The channels are most distinct on the section of seafloor containing steeper ($\sim 0.7^\circ$) gradients (Figure 3.7). Bathymetric profile BB' shows that channels are 2 to 3 km wide and incise 20 to 100 m into the sediment (Figure 3.7).

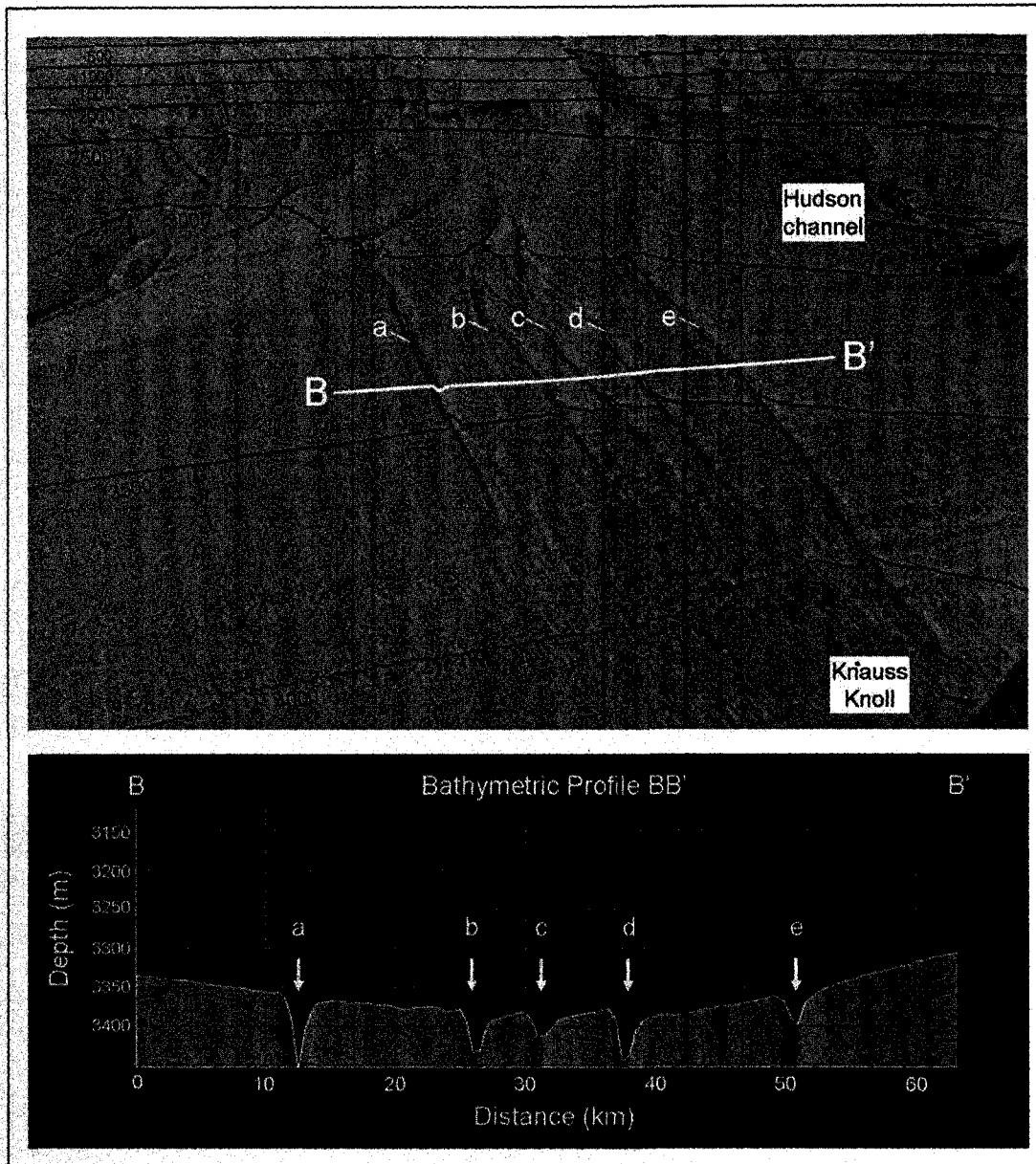


Figure 3.7 Perspective view (looking landward and upslope) of bathymetry data showing five, small channels (a-e). Contours shown in black at 500-m intervals. Bathymetry image shown with 10x vertical exaggeration and the bathymetric profile shown with 50x vertical exaggeration.

The multibeam sonar data also reveal that the small channels extend across the section of gentle seafloor gradients ($\sim 0.2^\circ$) between the 2500 m and 3000 m isobaths (Figure 3.8). Channel incision in this shallow sloping section is typically less than 30 m.

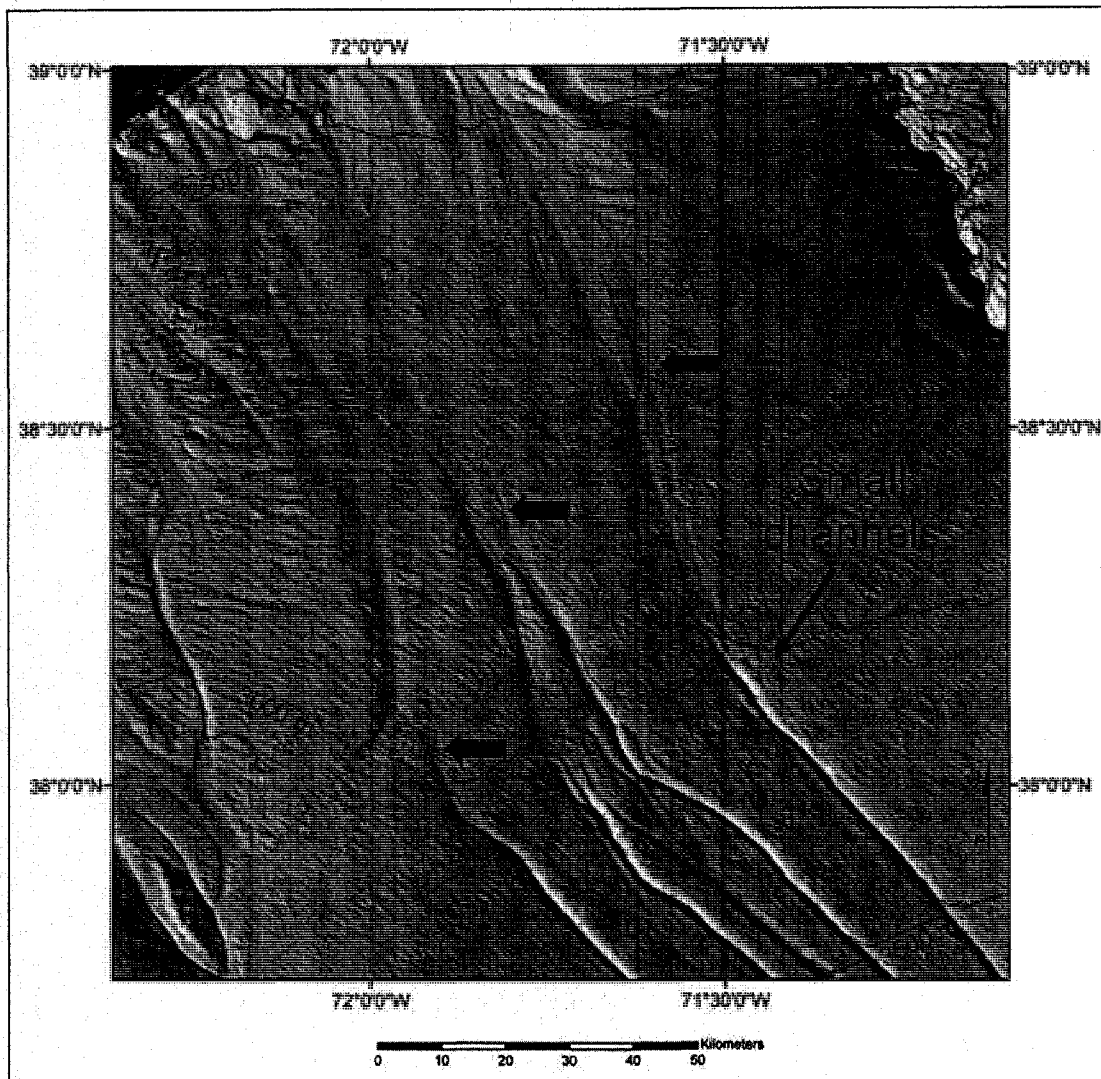


Figure 3.8 Bathymetry data (gray sun-illuminated hillshade) showing the small channels extending upslope across the gently dipping seafloor. Thick arrows pointing to upslope channel sections.

“Bowl-shaped” features within the small channels were previously identified by Butman et al. (2006) and are also observed in the bathymetry data for this study. These bathymetric depressions occur near the 3000 isobath at the start of the steeper seafloor section (Figure 3.9). The bowl-shaped features measure approximately 15 to 40 m in depth.

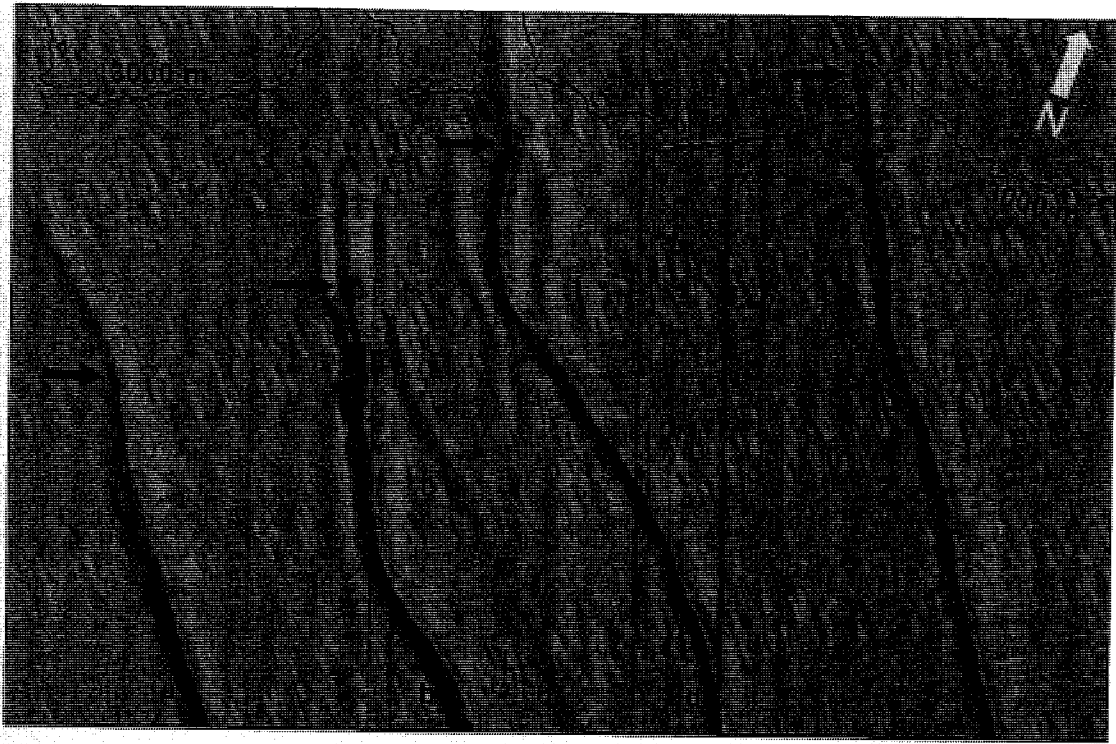


Figure 3.9 Map view of bathymetry data showing bowl-shaped depressions near the 3000 m isobath. Channels are labeled a (farthest southwest) through e (farthest northeast).

Similar bathymetric depressions are also observed further downslope within the small channels (Figure 3.10). These features vary in size, but are generally the width of the channel and measure approximately 20 m in depth.

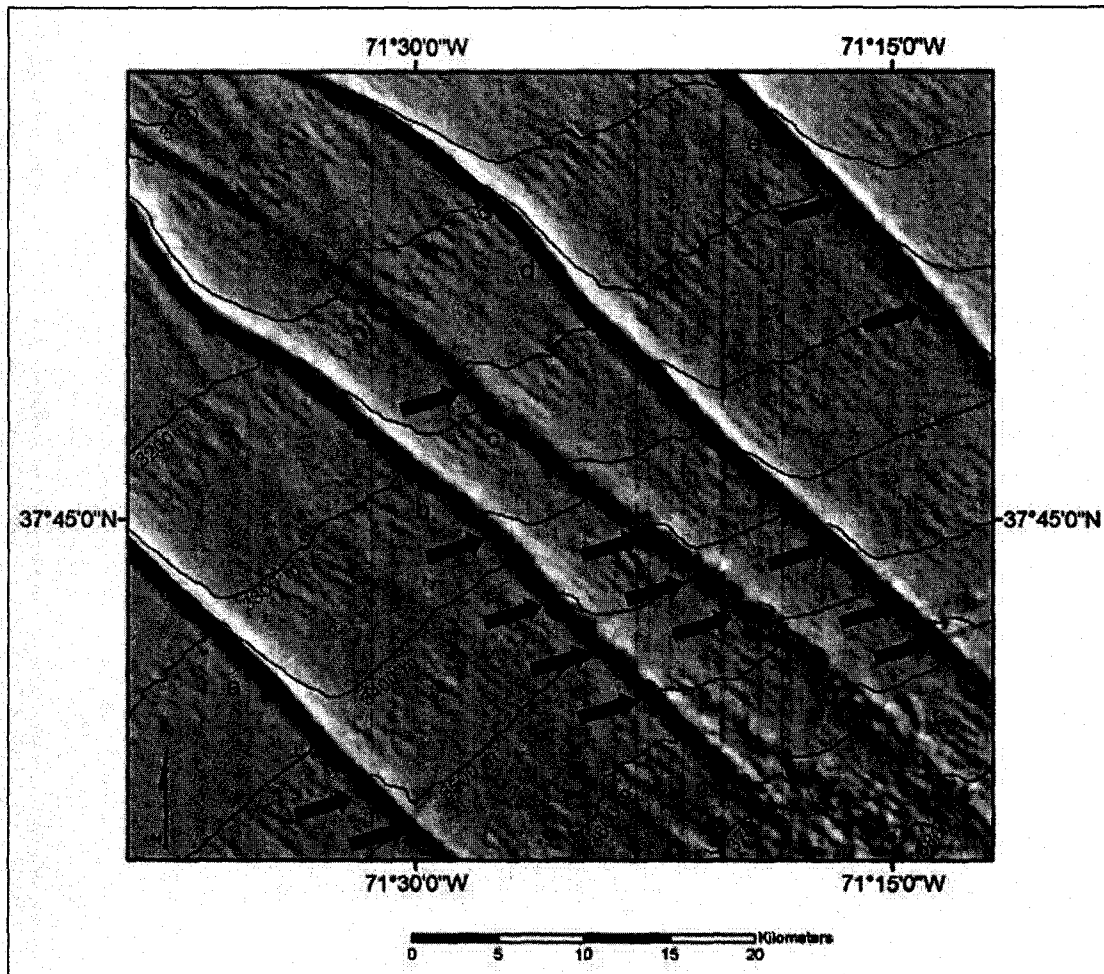


Figure 3.10 Map view of bathymetry data showing bathymetric depressions within the small channels.

The three channels farthest to the west (a to c) appear to terminate within an area of rough seafloor near 4000 m water depth (Figure 3.11). The rough area consists of bathymetric depressions similar to those observed within the small channels. The depressions are smaller than those observed in the small channels and measure up to 2 km wide and 25 m deep. The two channels farthest to the east (d and e) continue beyond the 3600 m isobath outside the rough seafloor, but become less defined once beyond the 4000 m isobath.

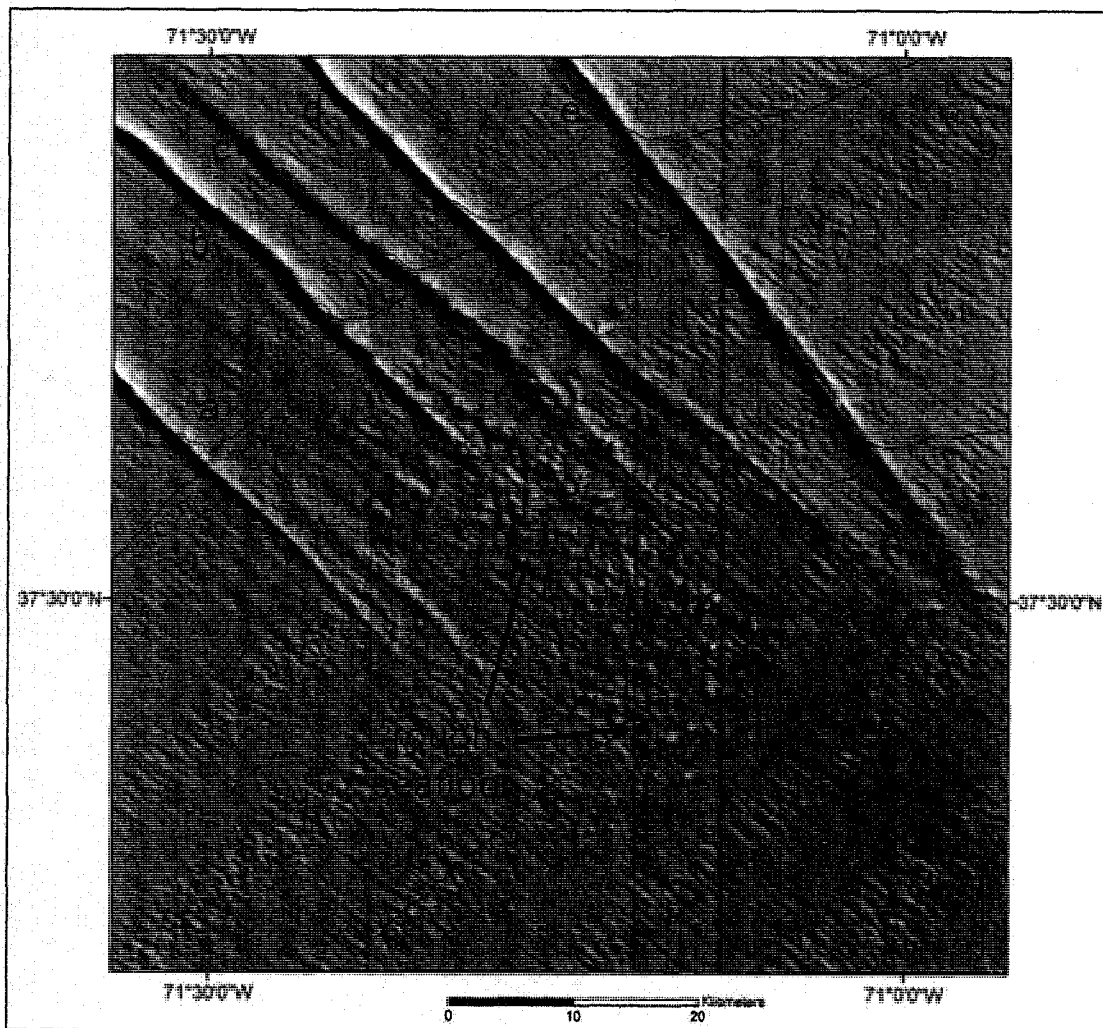


Figure 3.11 Rough seafloor consisting of bathymetric depressions found downslope from small channels.

Knauss Knoll (Lowrie and Heezen, 1967) is located immediately down-slope from the small channels and rough seafloor (Figure 3.12). The base of the seamount is located below 4000 m and the peak rises to above 3000 m water depth. A sediment drift is observed on the seamount's northeast side. The sediment drift is elongate in shape, aligning northeast to southwest ($\sim 225^\circ$ from tail to seamount) and rises upward

as it nears the seamount. The sediment drift was previously observed and named Krause Foredrift by Lowrie and Heezen (1967).

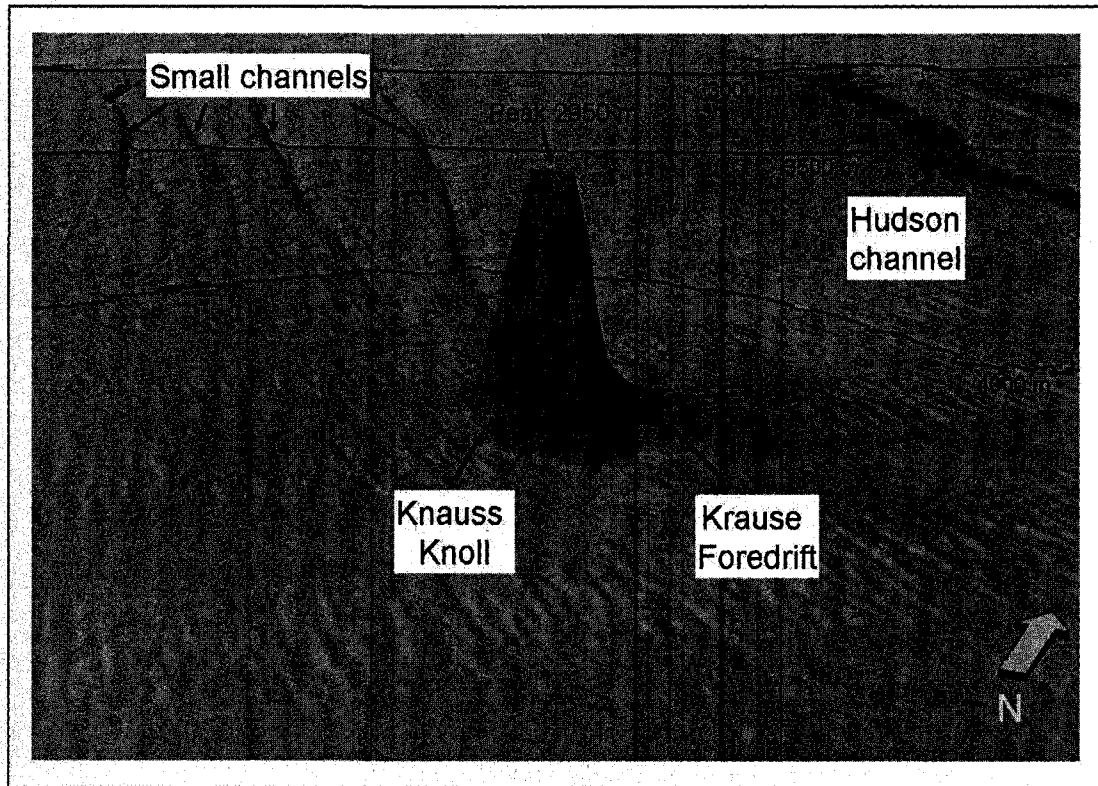


Figure 3.12 Bathymetric perspective image of Knauss Knoll and Krause Foredrift looking landward towards the northwest. Vertical exaggeration = 10x.

The bathymetry data also show a sediment ridge that extends between the 3000-m and 3500-m isobaths near the bend in Wilmington channel (Figure 3.13). The axis of the sediment ridge is oriented northeast-southwest and is parallel to Wilmington channel before the channel begins to turn to the southeast near the 3500 isobath. The ridge extends from the break in slope found at the 3000 m water depth.

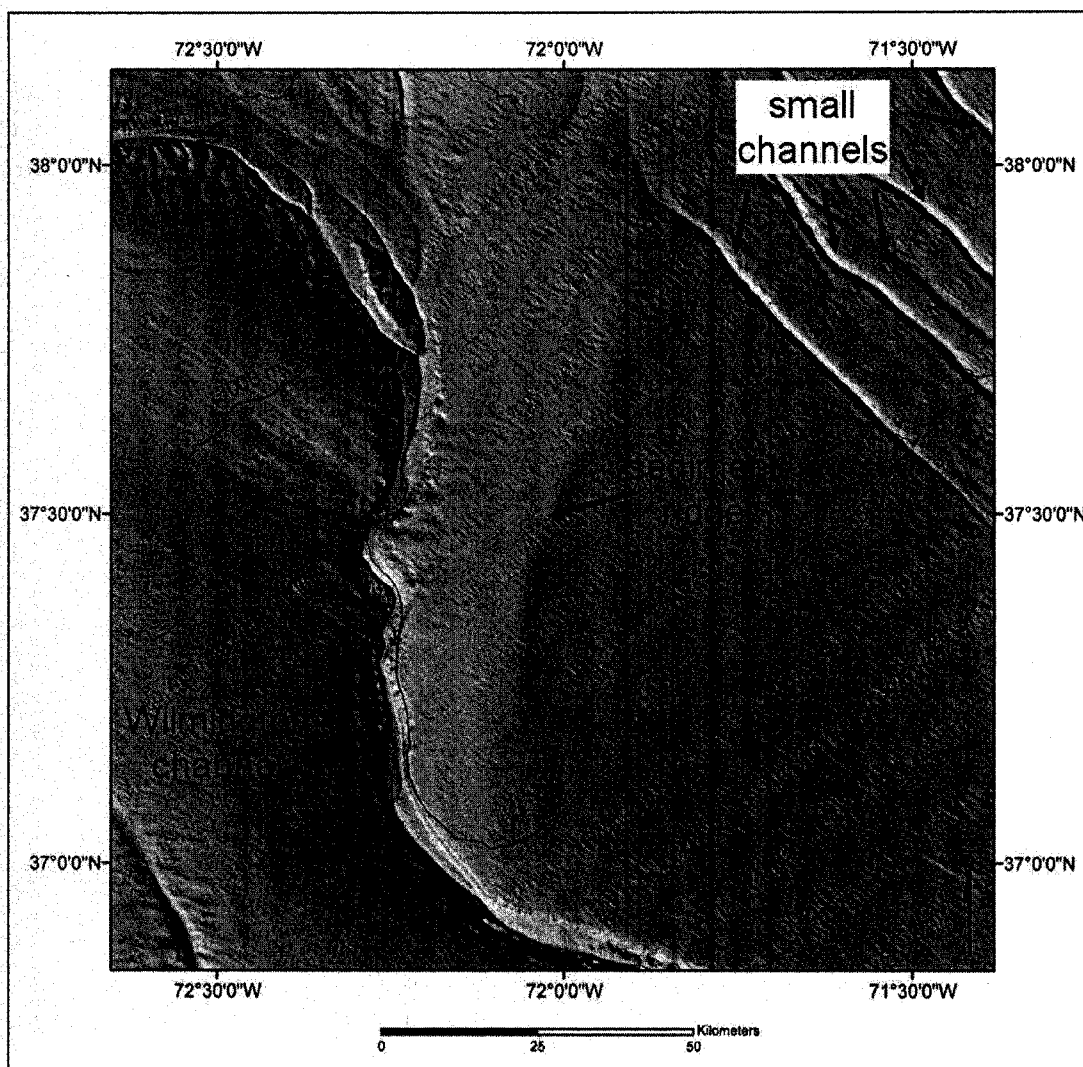


Figure 3.13 Multibeam sonar bathymetry data (gray, sun-illuminated hillshade) showing sediment ridge near Wilmington channel.

An overview of described features shown in the bathymetry data are shown in Figure 3.14.

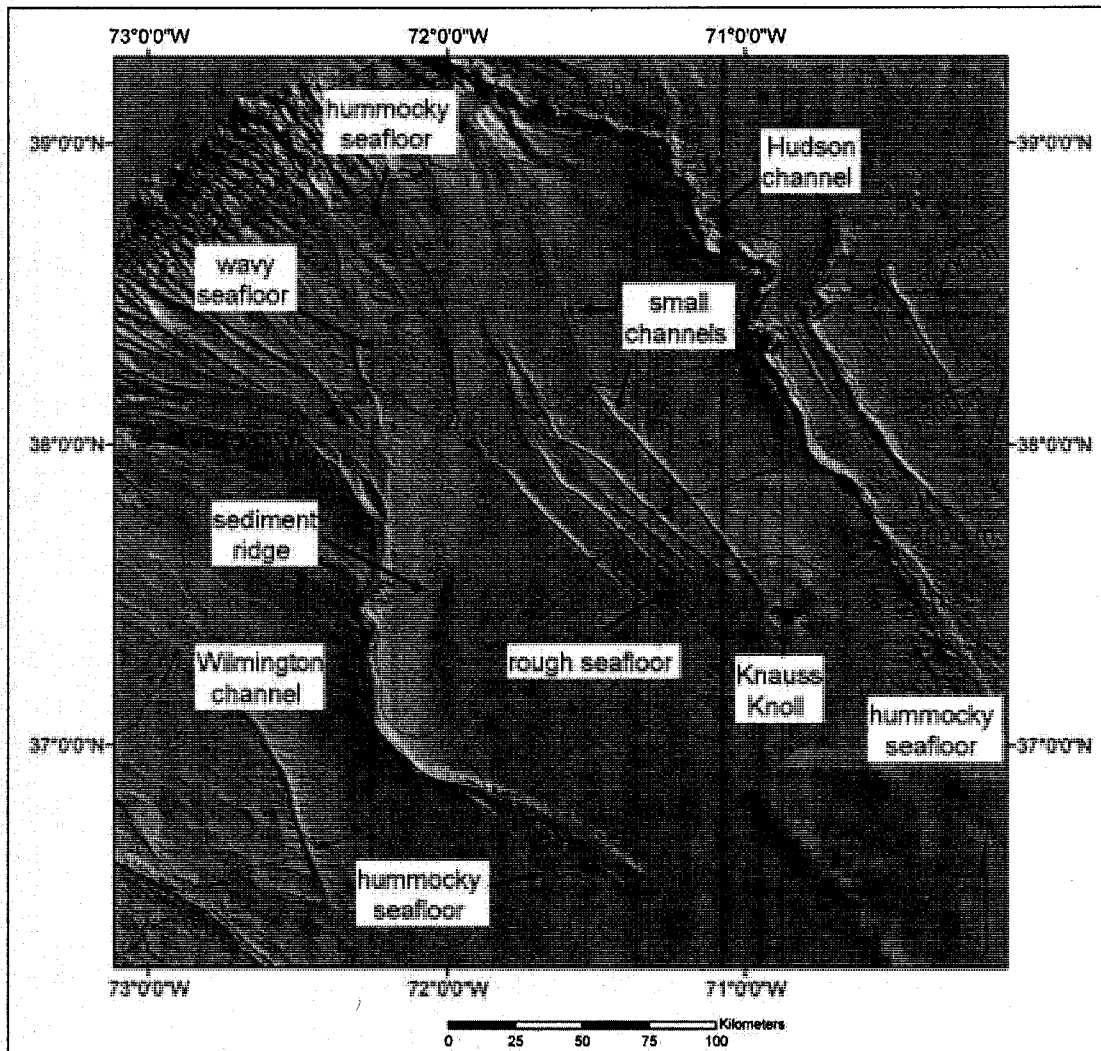


Figure 3.14 Overview of bathymetry data with labeled bathymetric features.

3.3 Multibeam Sonar Backscatter

MBES backscatter data on the New Jersey continental rise are described in the following section. The descriptions are divided into three sections: 1) backscatter strength, 2) backscatter features and 3) regional backscatter textures. The backscatter data ranges from -51 to -25 dB within the seafloor area mapped offshore New Jersey.

These backscatter-strength values have been classified as low (-51 to -42 db), medium (-42 to -34 dB) and high (-34 to -25 dB). An overview map is presented following these descriptions showing both backscatter features and regional textures along with their associated backscatter strength.

3.3.1 Backscatter Strength

The strength-classified backscatter data show predominantly high backscatter on the gently (0.2°) dipping seafloor region of the upper continental rise near the base of the continental slope (Figure 3.15). This area corresponds to the Baltimore-Toms gather area and the seafloor immediately outside of the small channels upslope from the 3000-m isobath., where hummocky and wavy seafloor features are observed in the bathymetry data. Few large areas of high-backscatter are found downslope from the break in slope near the 3000-m isobath between Hudson and Wilmington channels. Small regions of high-backscatter are found on Knauss Knoll and within and at the terminus of Hudson and Wilmington channels.

Large areas of predominantly medium-backscatter strength seafloor are found on the steeper seafloor section and on the seafloor with low slope gradients (0.2°) beyond the 4000-m isobath. Smaller areas of medium backscatter strength seafloor are also found near the base of the slope between the high-backscatter areas.

Low-backscatter strength is found on the relatively steep seafloor (within the low-backscatter anomaly), downslope from the 4000-m isobath at the terminus of Hudson and Wilmington channels and southwest and west of Knauss Knoll.

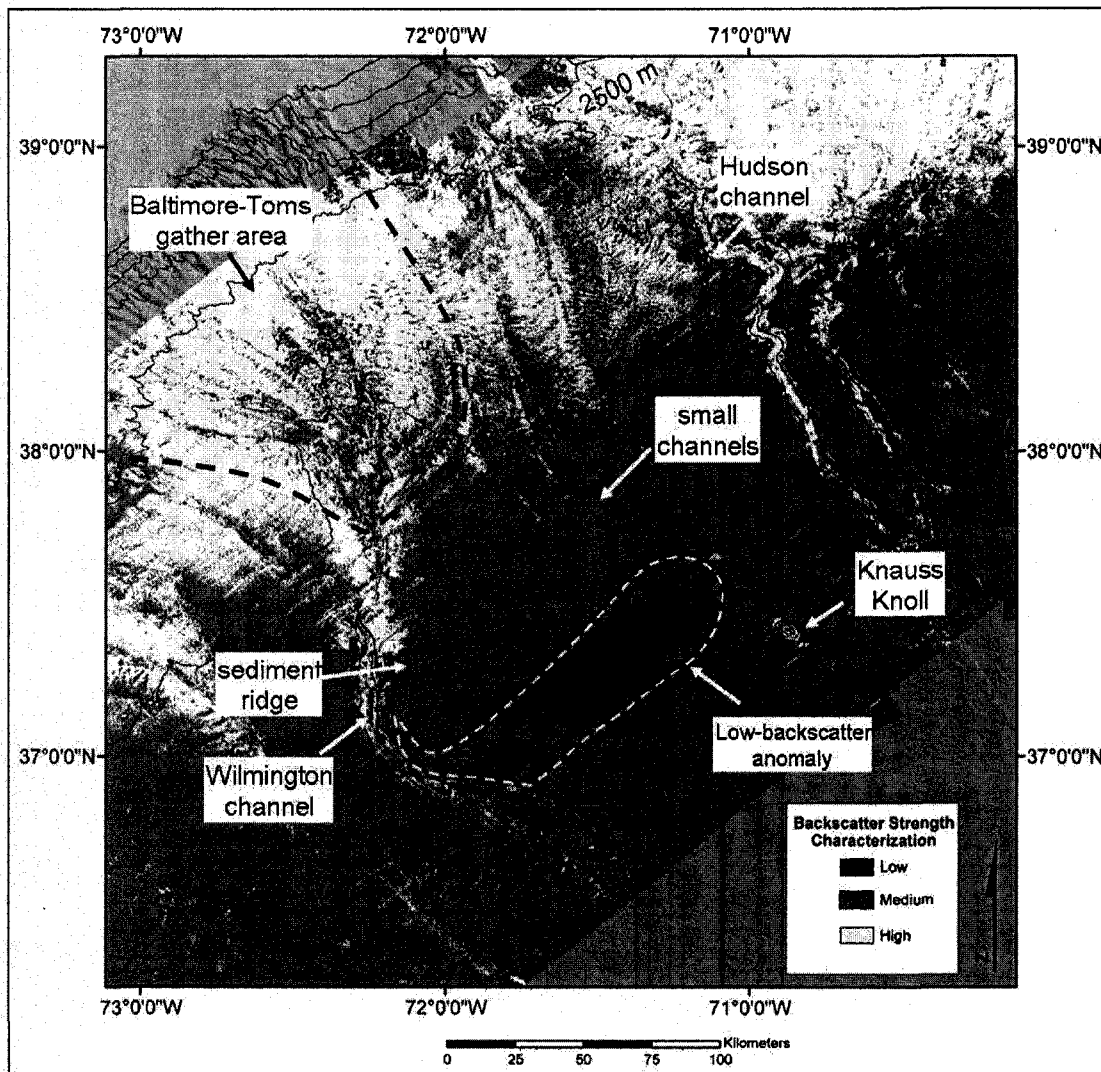


Figure 3.15 Backscatter characterization map using low (-51 to -42 db), medium (-42 to -34 dB) and high (-34 to -25 dB) classifications. Bathymetric contours shown in meters.

3.3.2 Backscatter Features

The backscatter data show an elongate low-backscatter feature oriented northeast to southwest (nearly parallel to the bathymetric contours), located on the section of the relatively steep (0.7°) seafloor area between Hudson and Wilmington channels. This feature is referred to as the “low-backscatter anomaly” (Figure 3.15). It is approximately 110 km long, 40 km wide and covers an area of about 2,750 km².

Other nearby bathymetric features are the small channels that traverse across the northeast section of the low-backscatter anomaly and Knauss Knoll (Figure 3.16).

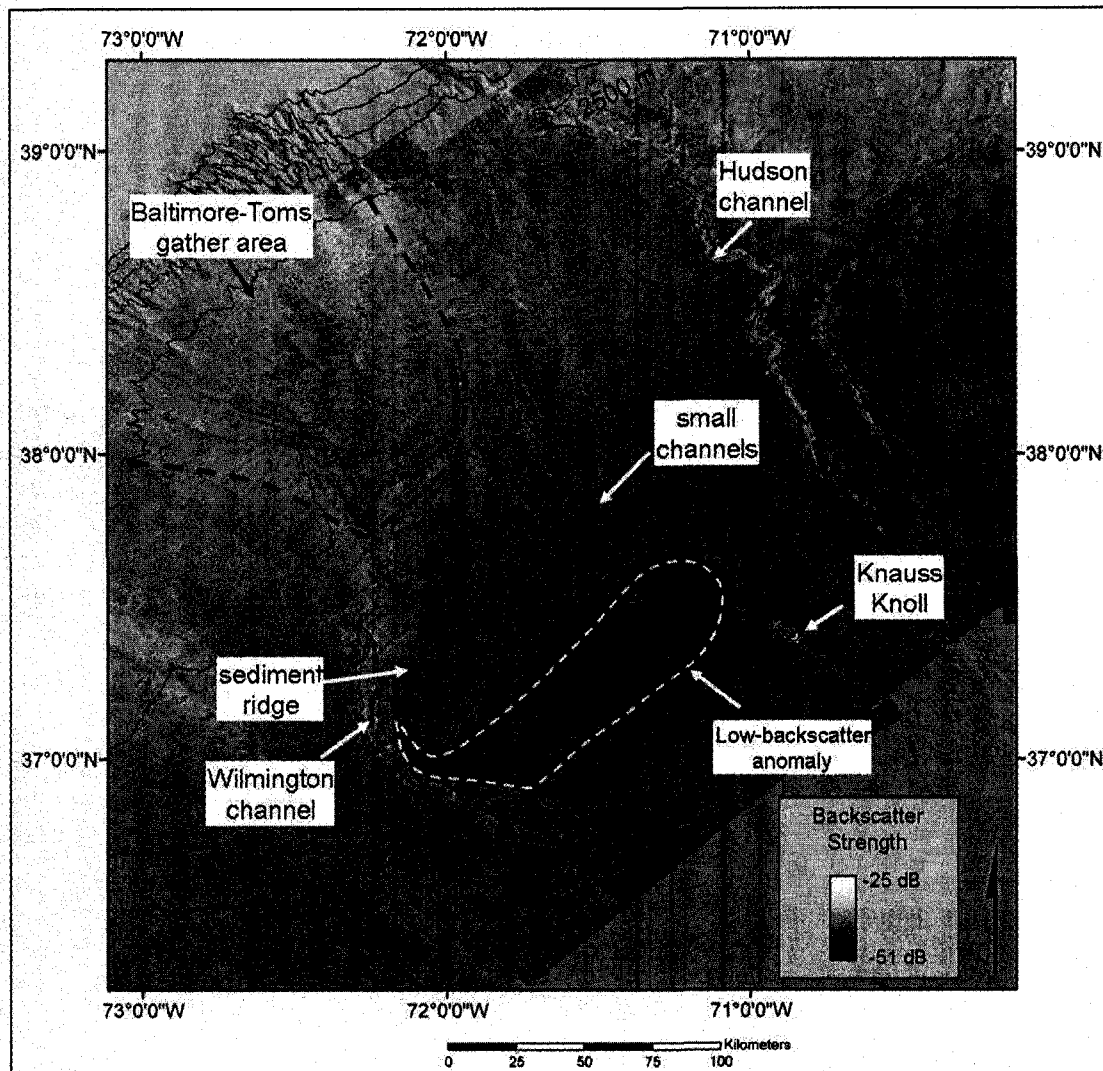


Figure 3.16 Multibeam backscatter mosaic in map view showing location of bathymetry features. Low-backscatter anomaly outlined in white dashed line. Sediment ridge and break-in-slope near 3000 m isobath shown by black dashed line.

The backscatter data show that the low-backscatter anomaly is not uniform in backscatter intensity and can be subdivided into several regions (Figure 3.17). The section located furthest to the southwest immediately adjacent to Wilmington channel

(section a) has an average backscatter strength of -42 dB. This section has a small area that wraps around the sediment ridge found in the bathymetry data.

Section a is bordered on the northeast by medium-backscatter strength seafloor (section b) that crosses the low-backscatter anomaly near Wilmington channel (Figure 3.17). This feature is referred to as the “medium-backscatter bridge.” It is approximately 10 km wide in the slope-parallel direction and extends down-slope across the width of the low-backscatter anomaly. Average backscatter strength from within the medium-backscatter bridge measures -39 dB.

A section with average backscatter of -44 dB (section c) is found immediately to the northeast of the medium backscatter bridge. The section of the anomaly with the lowest intensity (section d) is located adjacent to the intermediate low-backscatter section to the northeast (Figure 3.17). The average backscatter strength within this seafloor area ranges from -48 dB to -51 dB.

A mottled and streaky backscatter texture is found in the region farthest to the northeast (section e) within the low-backscatter anomaly (Figure 3.17). This section of the backscatter data corresponds to the area of rough seafloor at the terminus of the small channels farthest to the southwest. Backscatter streaks extend from the terminuses of the small channels downslope across the low-backscatter anomaly. Average backscatter values in the mottled-streaky backscatter section of the low-backscatter anomaly measure -43 dB.

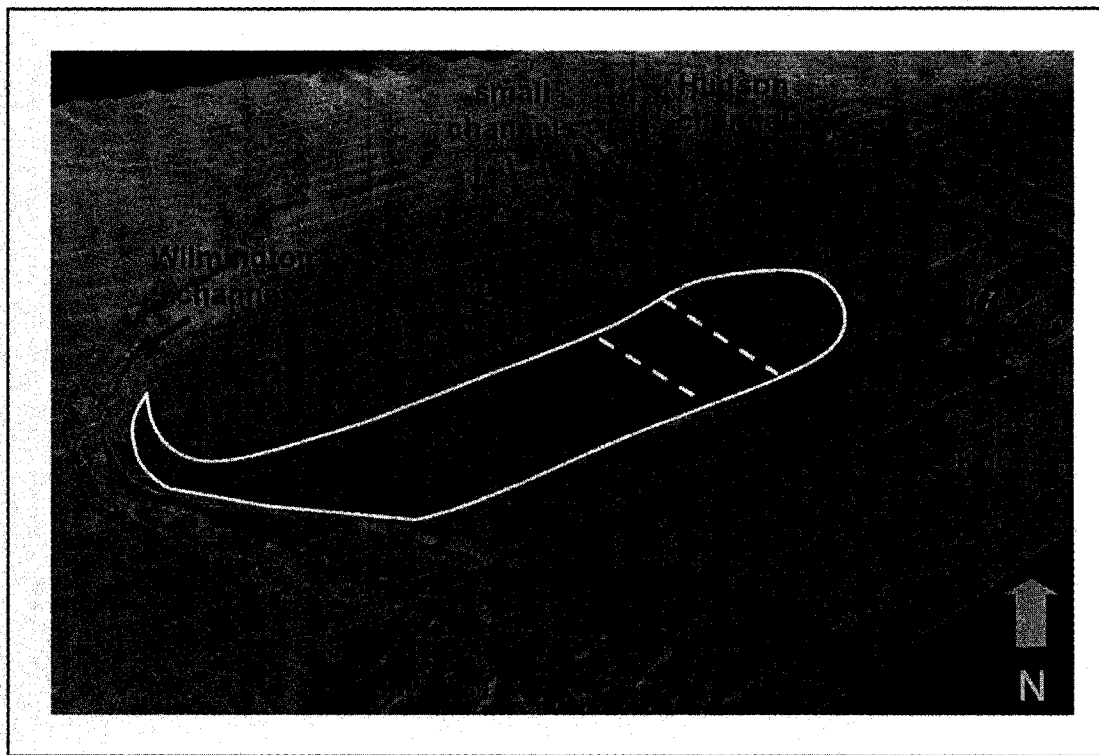


Figure 3.17 Perspective view (looking north) of the backscatter data showing the subdivided low-backscatter anomaly (outlined in white). a = section adjacent to Wilmington channel; b = medium backscatter bridge (outlined in red); c = intermediate section; d = lowest backscatter strength section; e = mottled-streaky section. VE=10x

The backscatter data also show fan-shaped features with variable backscatter strength at the terminuses of both Wilmington and Hudson channels (Figure 3.18 and

Figure 3.19). These areas correspond to the hummocky seafloor outside the channels shown in the bathymetry data on the section of the margin profile (Figure 3.1) that is relatively flat (0.2°). The backscatter texture within the fan-shaped features is mottled and backscatter strength is both medium- and low-backscatter strength.

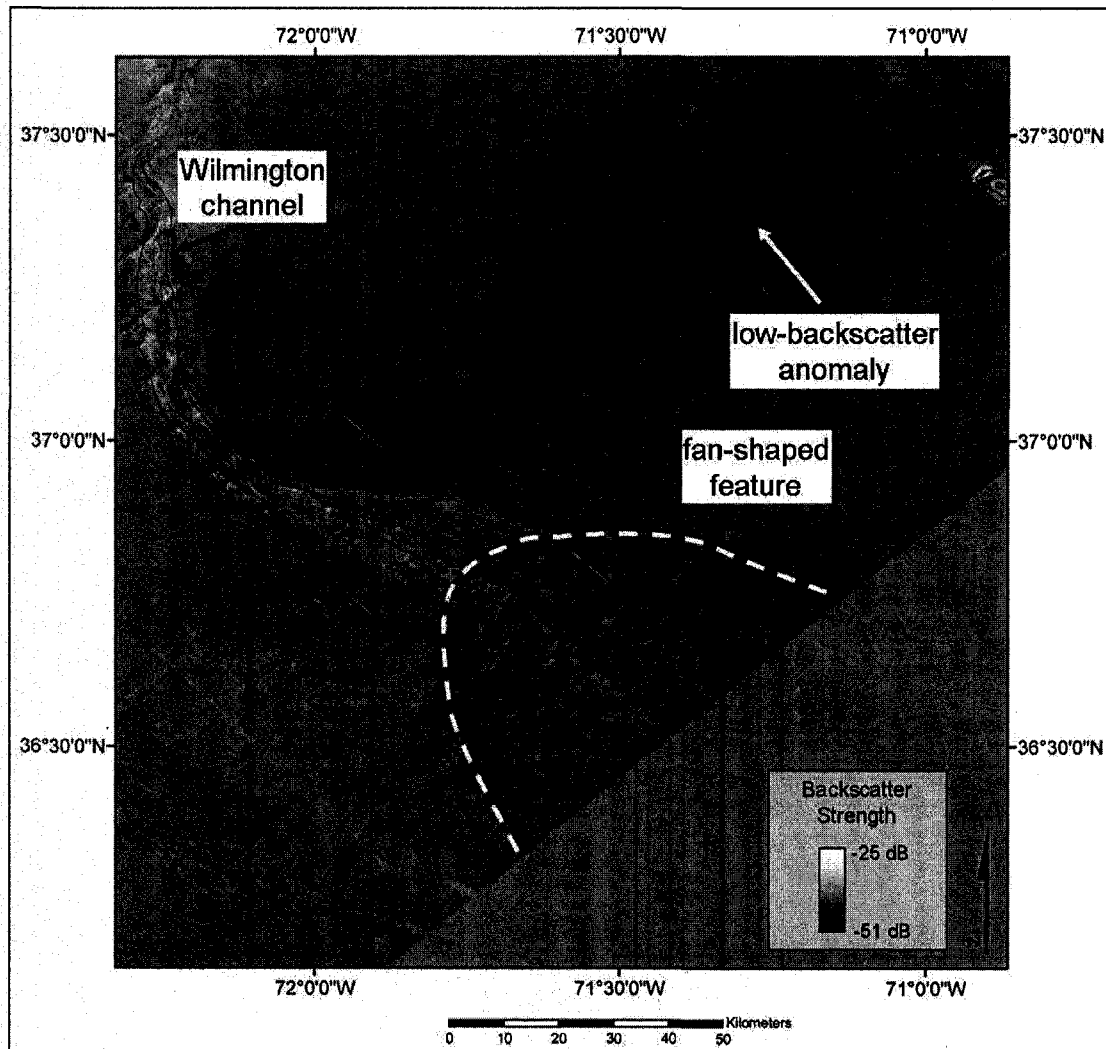


Figure 3.18 Backscatter data showing fan-shaped feature (outlined by white-dashed line) at the terminus of Wilmington channel.

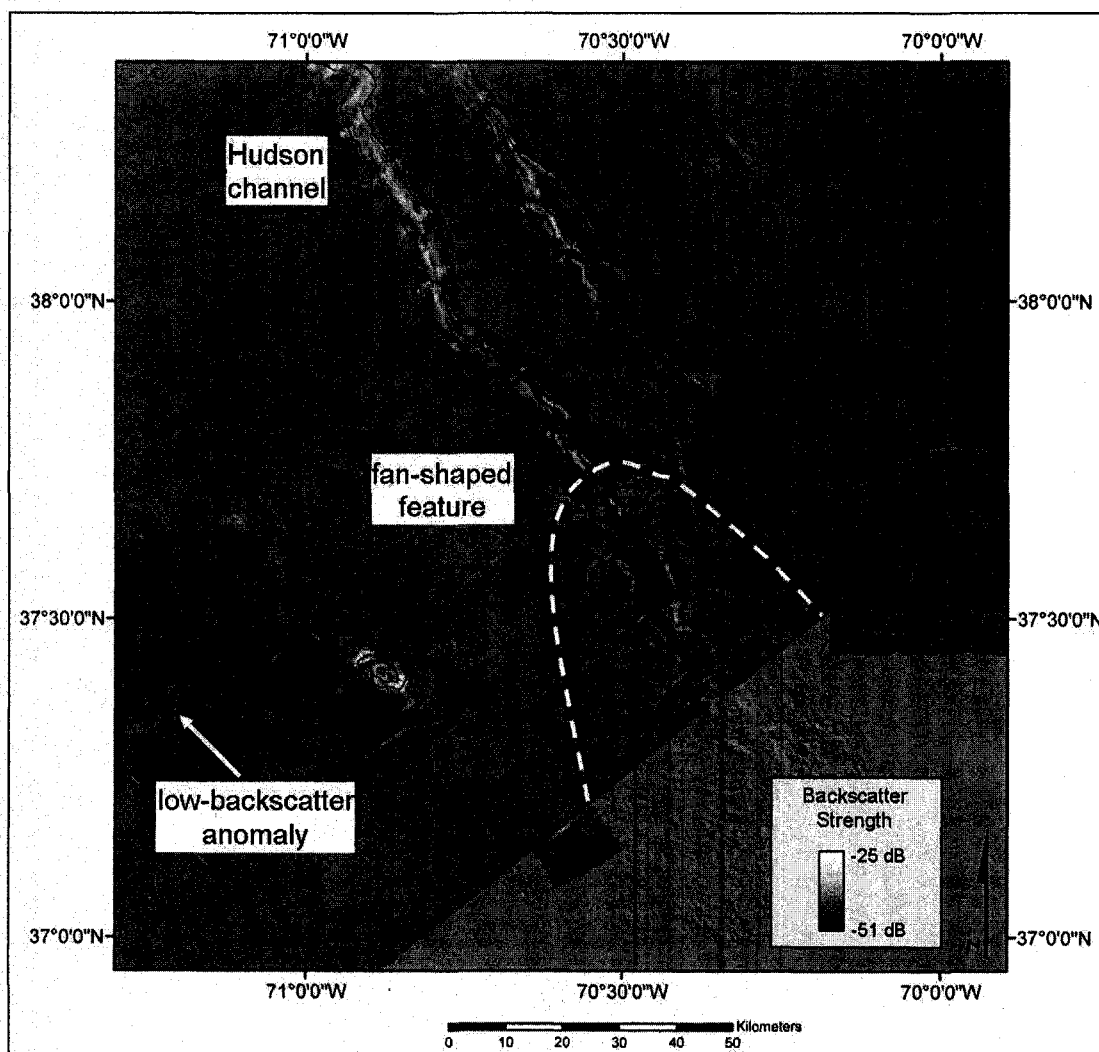


Figure 3.19 Backscatter data showing fan-shaped feature (outlined by white-dashed line) at the terminus of Hudson channel.

Another backscatter feature observed in the backscatter data near the low-backscatter anomaly is a high-backscatter strength, lobe-shaped feature (Figure 3.20). The lobe-shaped feature extends to the southeast from the 2500-m isobath across Wilmington channel.

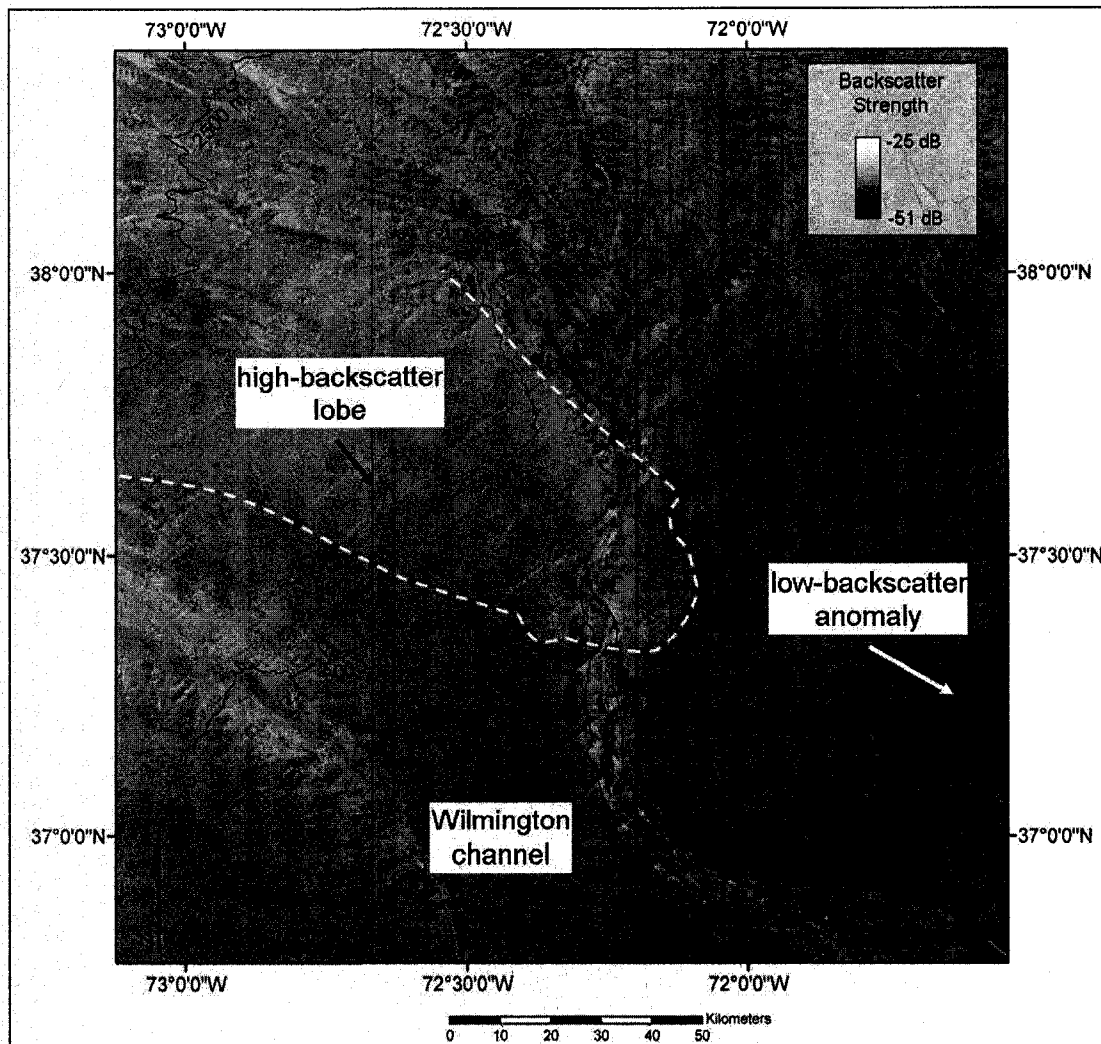


Figure 3.20 Backscatter data showing high-backscatter lobe outline by white-dashed line.

3.3.3 Regional Backscatter Textures

Data show a mottled backscatter texture in the area of seafloor with gradual slope gradients and high-backscatter strength near the base of the continental slope (Figure 3.21). These data correspond to the hummocky and wavy seafloor features shown in the bathymetry data.

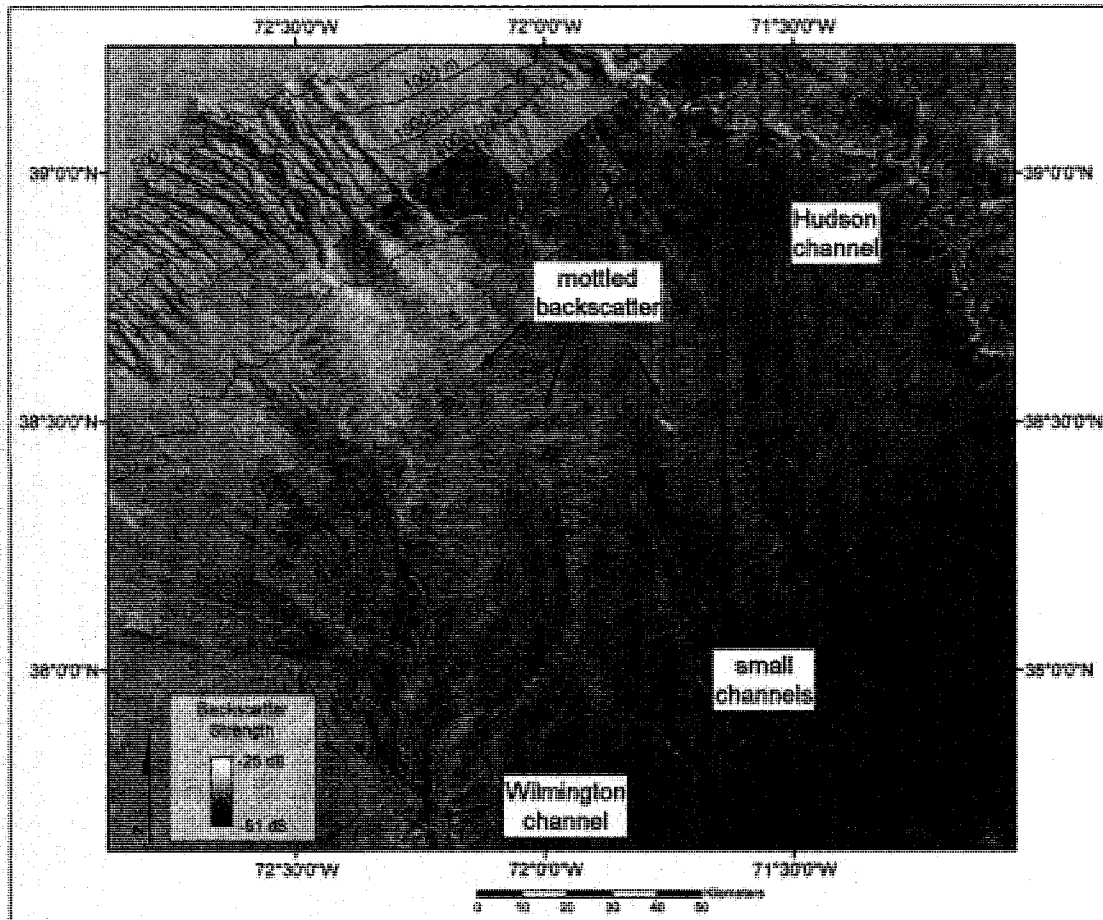


Figure 3.21 Backscatter data on the upper continental rise near the base of the continental slope showing mottled backscatter texture.

The backscatter data show an area of homogenous backscatter texture between the mottled backscatter near the base of the continental slope and the low-backscatter anomaly (Figure 3.22). This section of backscatter texture occurs immediately downslope from the break in slope shown in the bathymetry data near the 3000-m isobath on the relatively steep (0.7°) seafloor area. Small variability within the homogenous-backscatter texture section occurs as the result of the small channels.

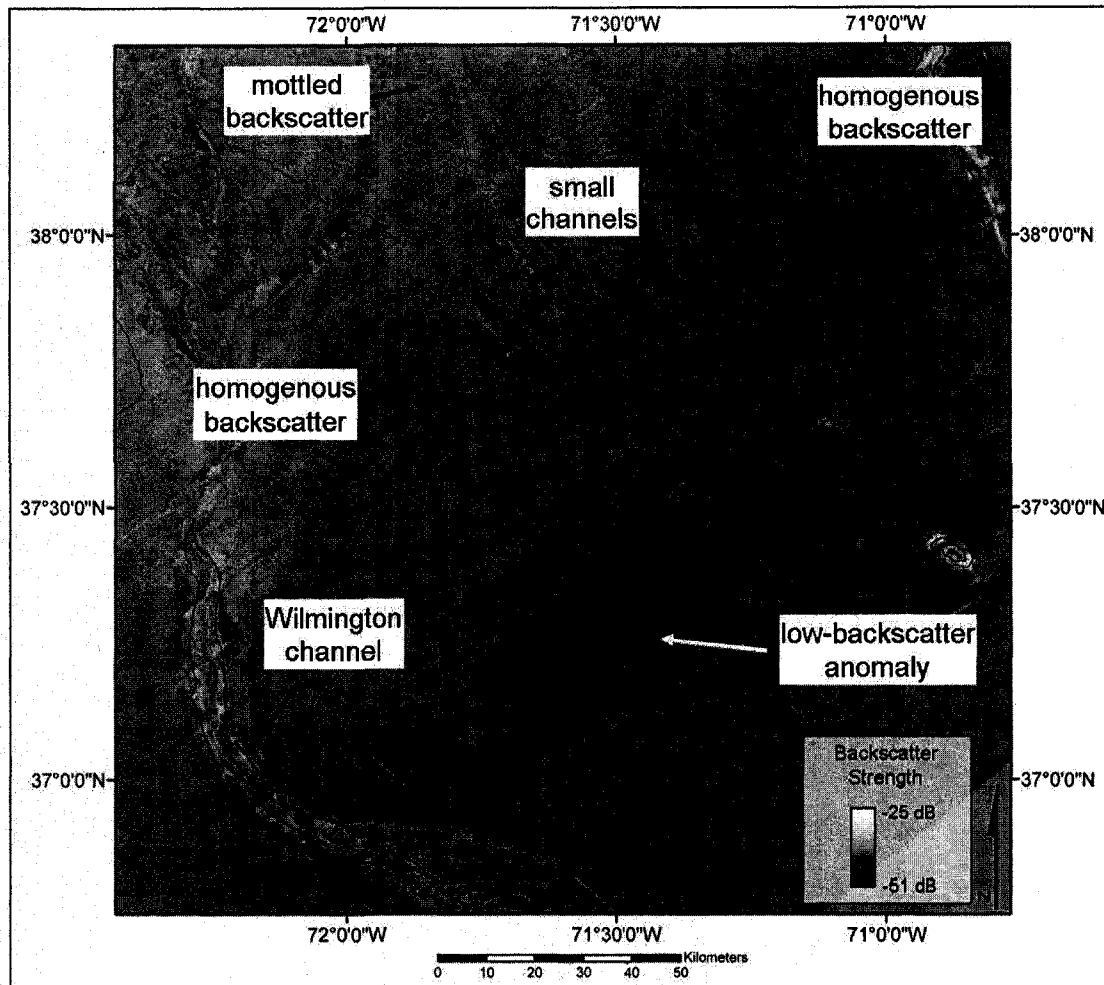


Figure 3.22 Backscatter data showing section of homogenous-backscatter texture between mottled backscatter and low-backscatter anomaly.

The backscatter data immediately southeast of the low-backscatter anomaly show linear, streaky features oriented north-south and backscatter rills oriented east-west (Figure 3.23). This backscatter region corresponds to the relatively flat seafloor shown by the MBES bathymetry data.

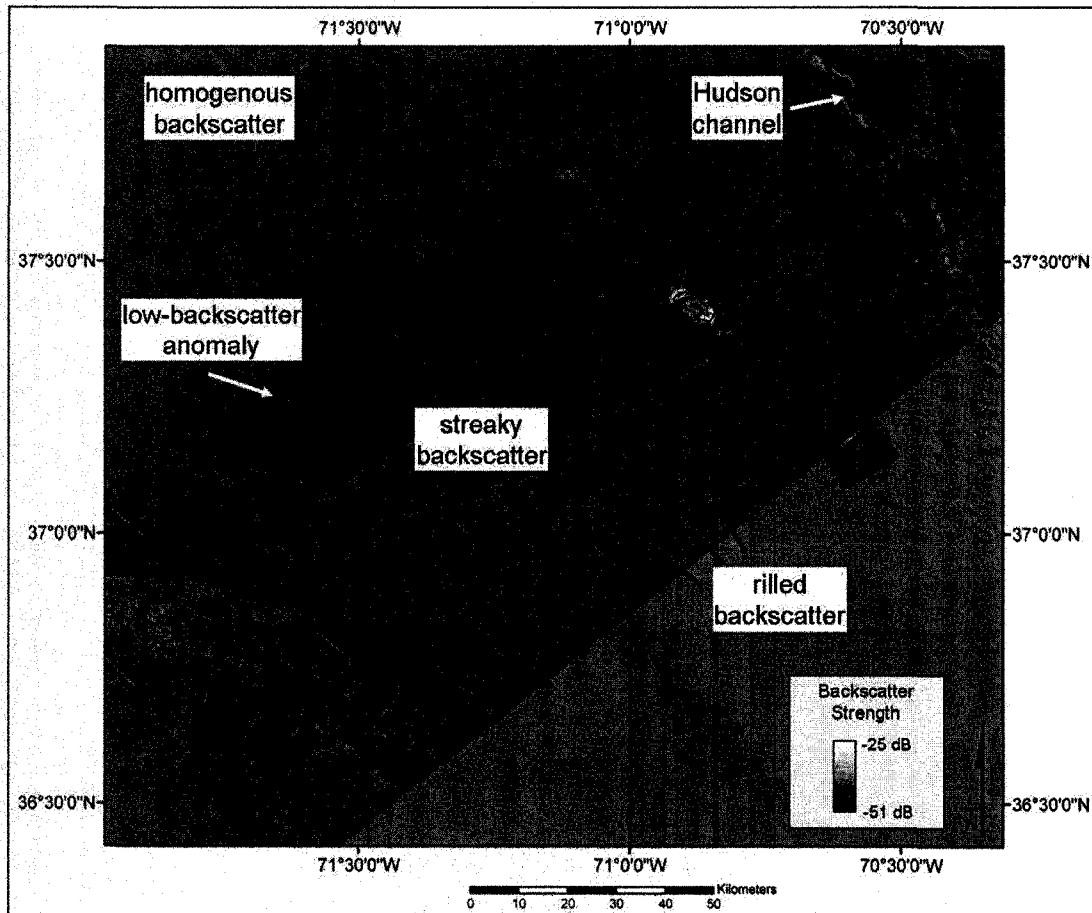


Figure 3.23 Backscatter data showing rilled-streaky-backscatter texture seafloor area downslope from the low-backscatter anomaly and the homogenous-texture backscatter seafloor.

An overview of the backscatter features and associated backscatter strength is shown in Figure 3.24.

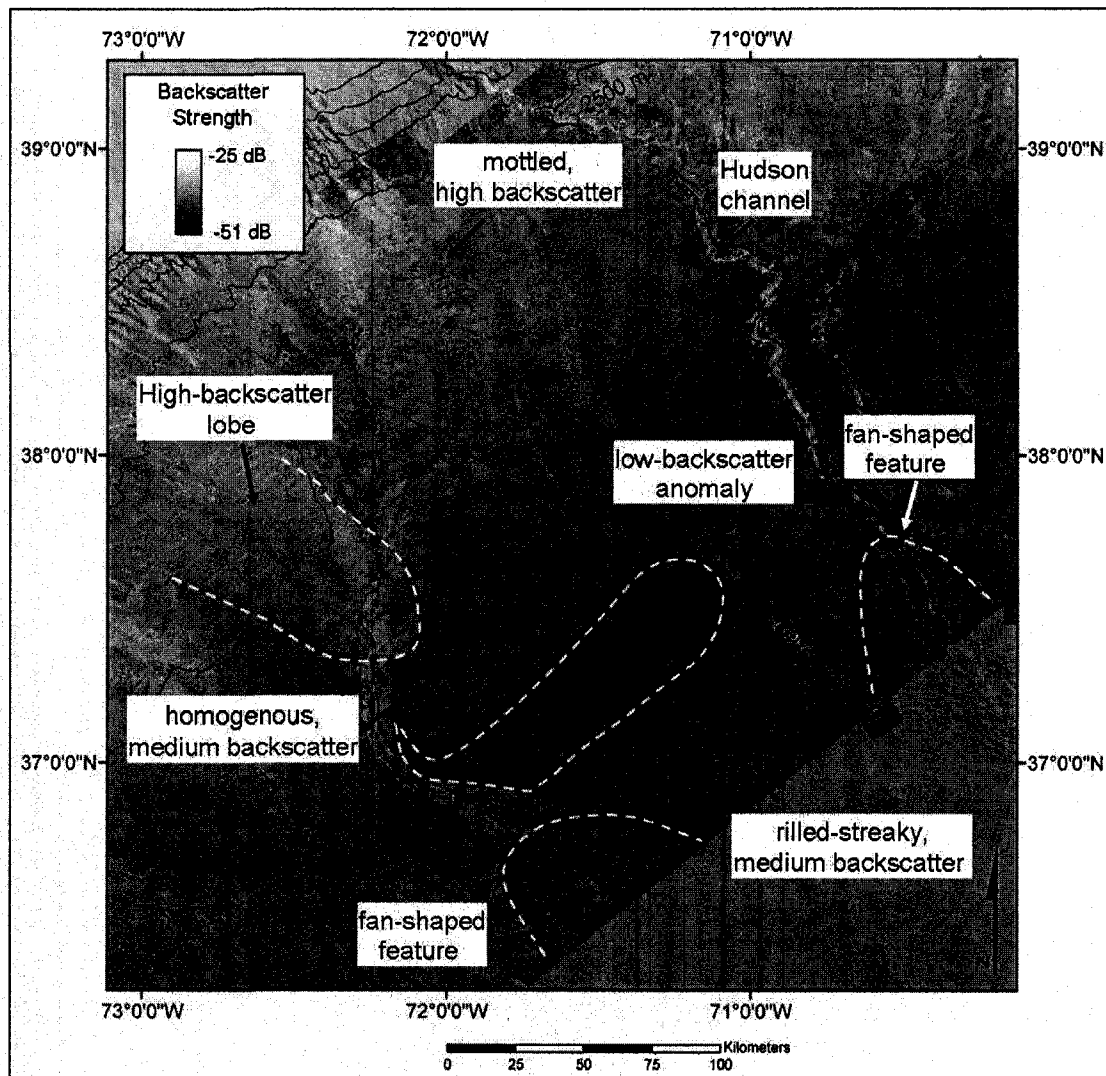


Figure 3.24 Map showing locations of regional backscatter textures and features. Bathymetric contours are at 500-m intervals.

3.4 Chirp Seismic-Reflection Profiles

Chirp sonar profiles were collected in the study region parallel to the contours of the margin along each multibeam sonar survey trackline. These data are presented to compare the sub-surface structure within the anomalous seafloor to the structure beneath the surrounding seafloor. Profile locations are shown with respect to multibeam backscatter data in Figure 3.25.

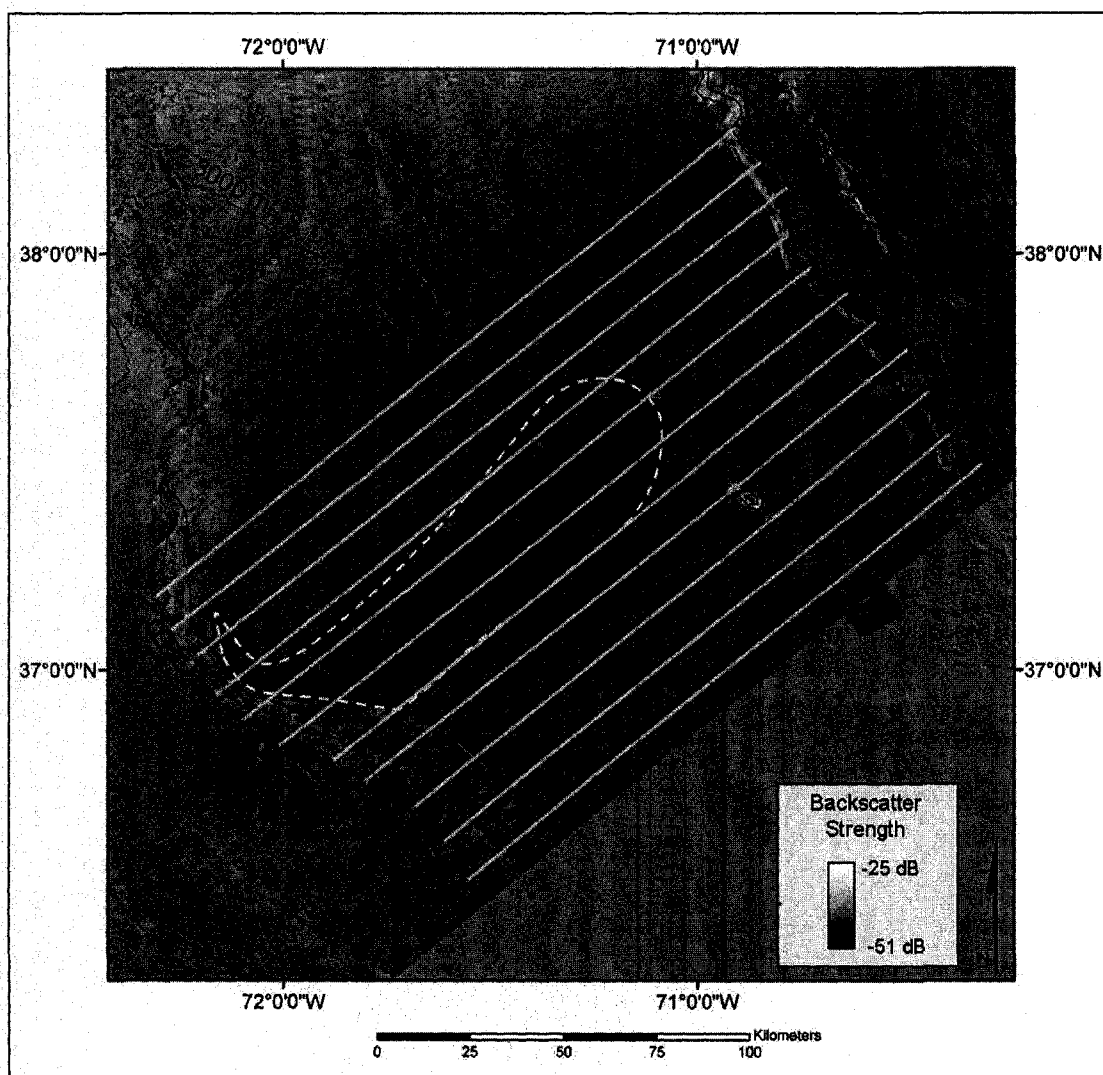


Figure 3.25 Map of 3.5-kHz chirp profiles with multibeam backscatter backdrop. Low-backscatter anomaly outlined by white-dashed line. Bathymetric contours shown at 500-m intervals.

Chirp sonar profiles AA', BB', CC' and DD' were collected in the medium backscatter strength, homogeneous seafloor upslope from the low-backscatter anomaly and between Wilmington and Hudson channels (Figure 3.25). These chirp sonar profiles show good penetration across the medium backscatter strength seafloor and indicate conformable, well-stratified horizontal subbottom reflectors. Horizons

are continuous except where cut by the five, small channels or truncated by Wilmington and Hudson channels. Chirp sonar profiles indicate well built channel levees outside Hudson and Wilmington channels.

Chirp sonar profiles CC' and DD' also indicate sub-surface features. Seismic reflectors in profile CC' show a v-shaped feature between Wilmington channel and the small channels (Figure 3.27). An amphitheater-shaped sequence is shown in chirp profile DD' nearer to Wilmington channel that is ~8 km wide and disrupts the horizontally lying stratified sub-surface reflectors (Figure 3.27). The amphitheater-shaped sequence occurs immediately down-slope from the buried v-shaped acoustic stratigraphy observed in chirp profile CC'. The amphitheater-shaped subbottom feature also occurs immediately upslope from the medium-backscatter bridge. An acoustically transparent, lens-shaped feature is also shown further to the northeast between the amphitheater-shaped sequence and the small channels (Figure 3.27). This feature is ~3 km wide and also disrupts the well-stratified, horizontally lying reflectors.

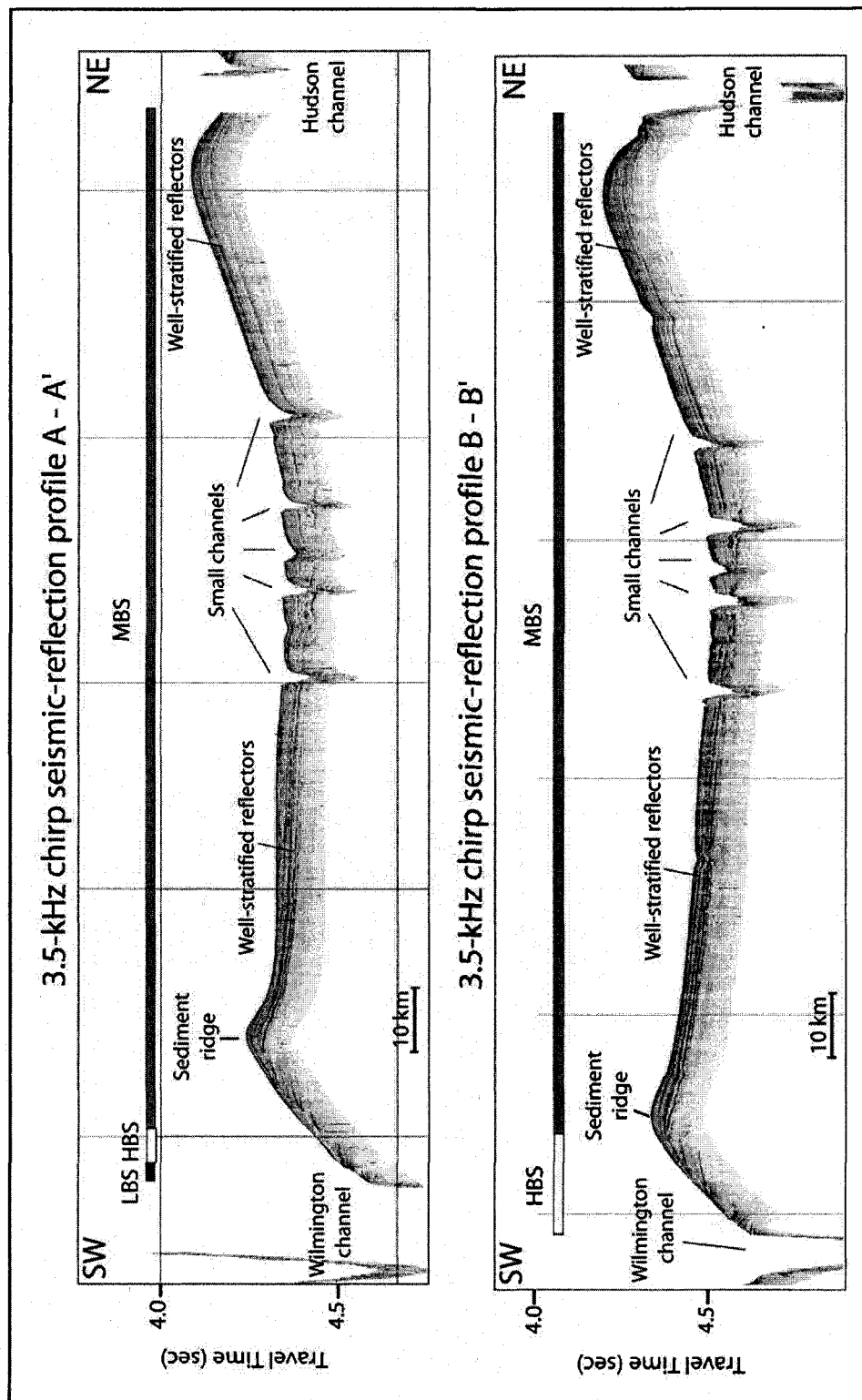


Figure 3.26 Seismic reflection profiles AA' and BB' collected upslope from the low-backscatter anomaly. Corresponding backscatter strength shown as white for high-backscatter (HBS), gray for medium backscatter (MBS) and black for low backscatter (LBS).

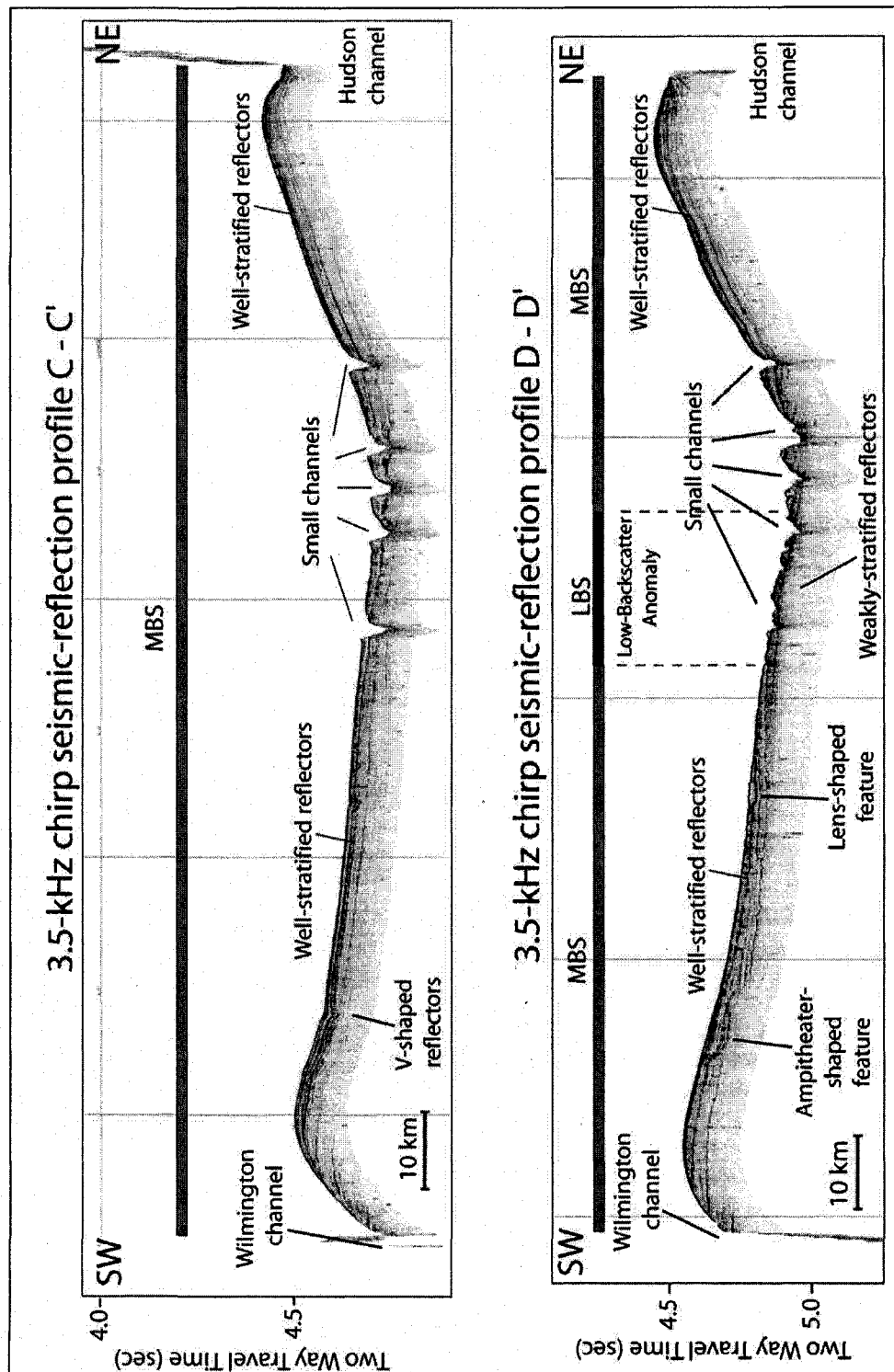


Figure 3.27 Seismic reflection profiles CC' and DD' collected upslope and within the low-backscatter anomaly. Corresponding backscatter strength shown as white for high-backscatter (HBS), gray for medium backscatter (MBS) and black for low backscatter (LBS).

A section of chirp profile DD' also crossed through the low-backscatter anomaly (Figure 3.25). The acoustic stratigraphy in this section of profile DD' shows well-stratified, outcropping subbottom reflectors (Figure 3.27). Chirp seismic-reflection profiles EE', FF' and GG' cross through the low-backscatter anomaly (Figure 3.25) and show weakly-stratified, outcropping subbottom reflectors within the low-backscatter anomaly (Figure 3.28 and Figure 3.29). These profiles show an acoustically transparent, lens-shaped subbottom feature. The lens-shaped feature disrupts horizontally lying sub-surface reflectors and corresponds to the location of the medium-backscatter bridge.

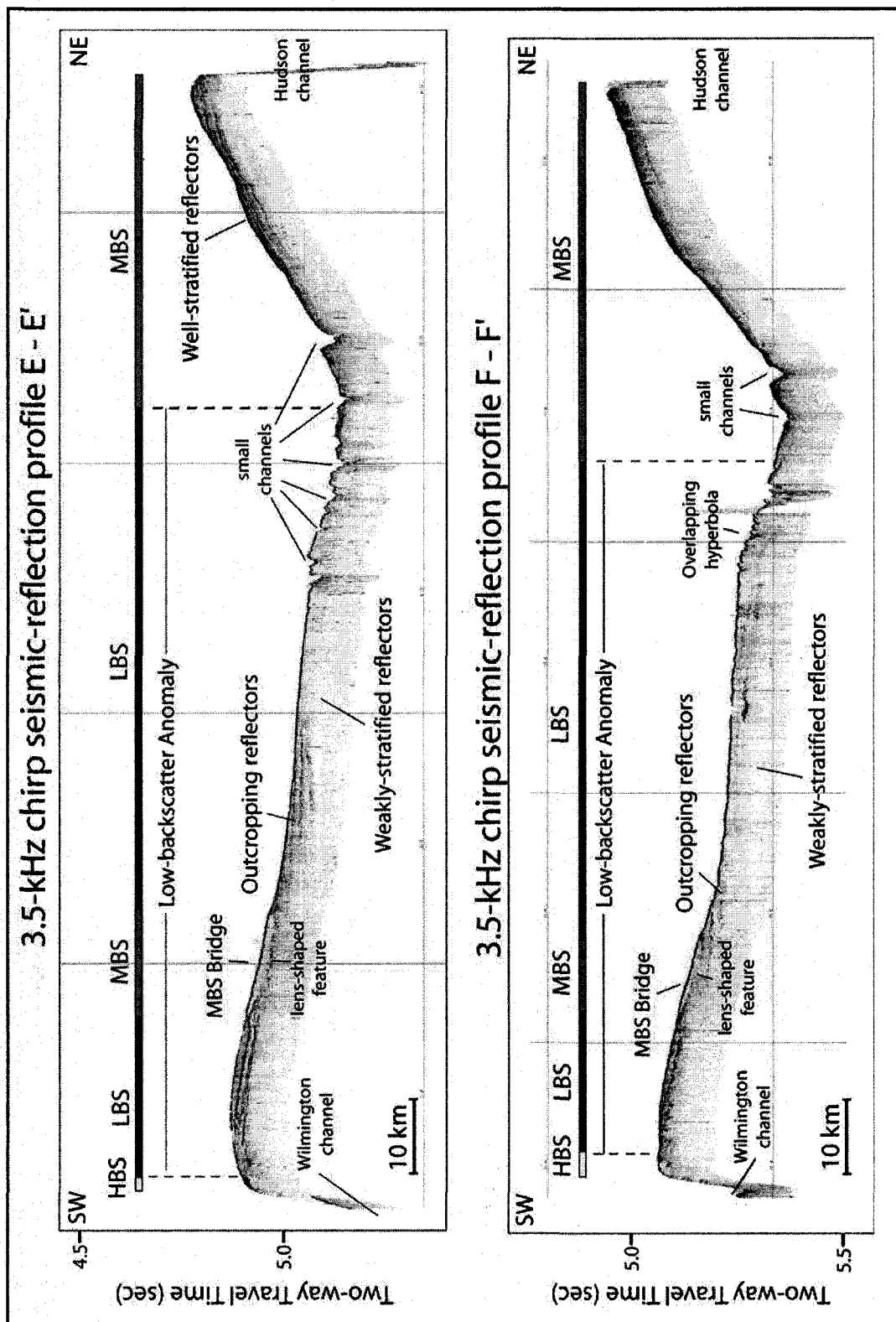


Figure 3.28 Chirp profiles EE' and FF' collected across the low-backscatter anomaly. High backscatter (HBS) shown in yellow, medium backscatter (MBS) in gray and low backscatter (LBS) in black.

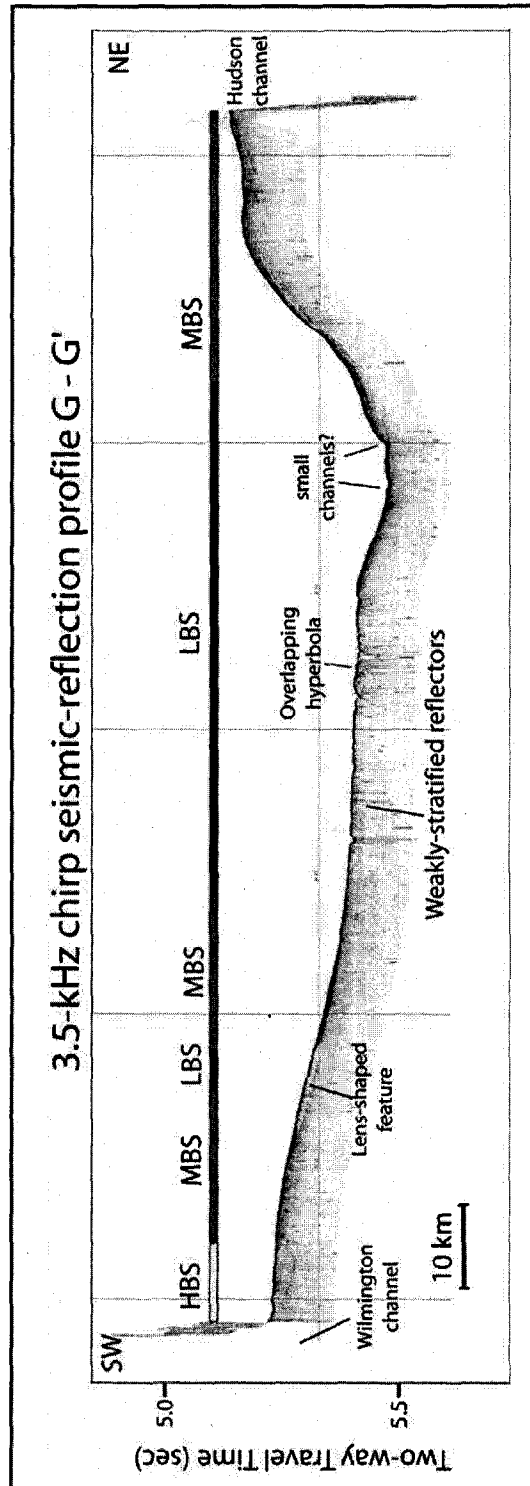


Figure 3.29 Chirp profile GG' collected across the low-backscatter anomaly. High backscatter (HBS) shown in yellow, medium backscatter (MBS) in gray and low backscatter (LBS) in black.

Chirp seismic-reflection profiles HH', II', JJ' and KK' were collected in the region down-slope from the low-backscatter anomaly across medium-backscatter strength seafloor with variable streaky and rilled backscatter texture (Figure 3.25). These profiles also cross through the fan-shaped, mottled backscatter features outside of Wilmington and Hudson channels. These chirp seismic-reflection profiles show horizontal, well-stratified, continuous reflectors with very strong bottom returns (Figure 3.30). Good penetration is shown in the seafloor section corresponding to streaky medium-backscatter, but the data show limited penetration beneath the fan-shaped, mottled backscatter features at the termini of Wilmington and Hudson channels.

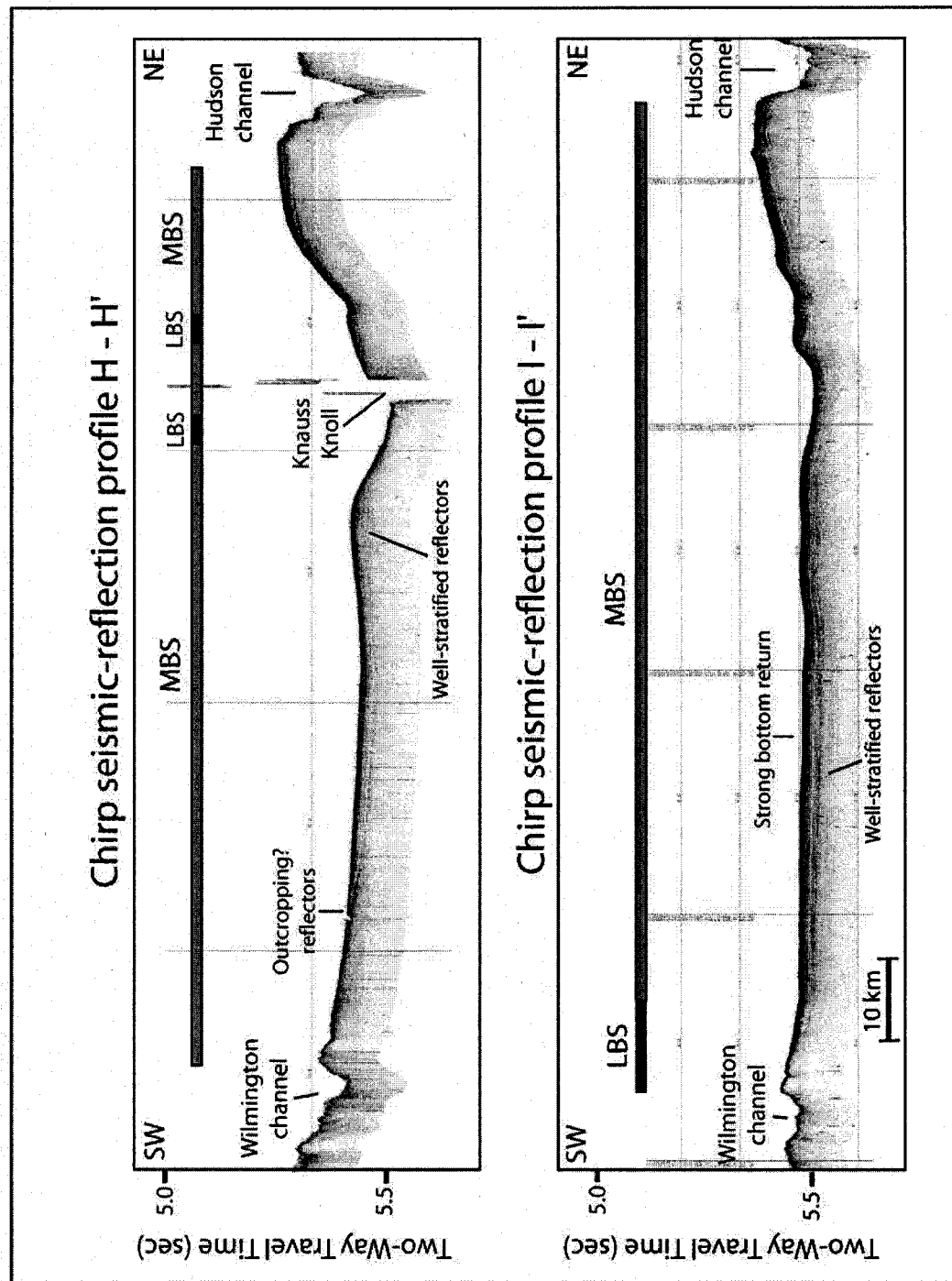


Figure 3.30 Chirp profiles HH' and II' collected down-slope from the low-backscatter anomaly. MBS = medium backscatter strength; LBS = low-backscatter strength.

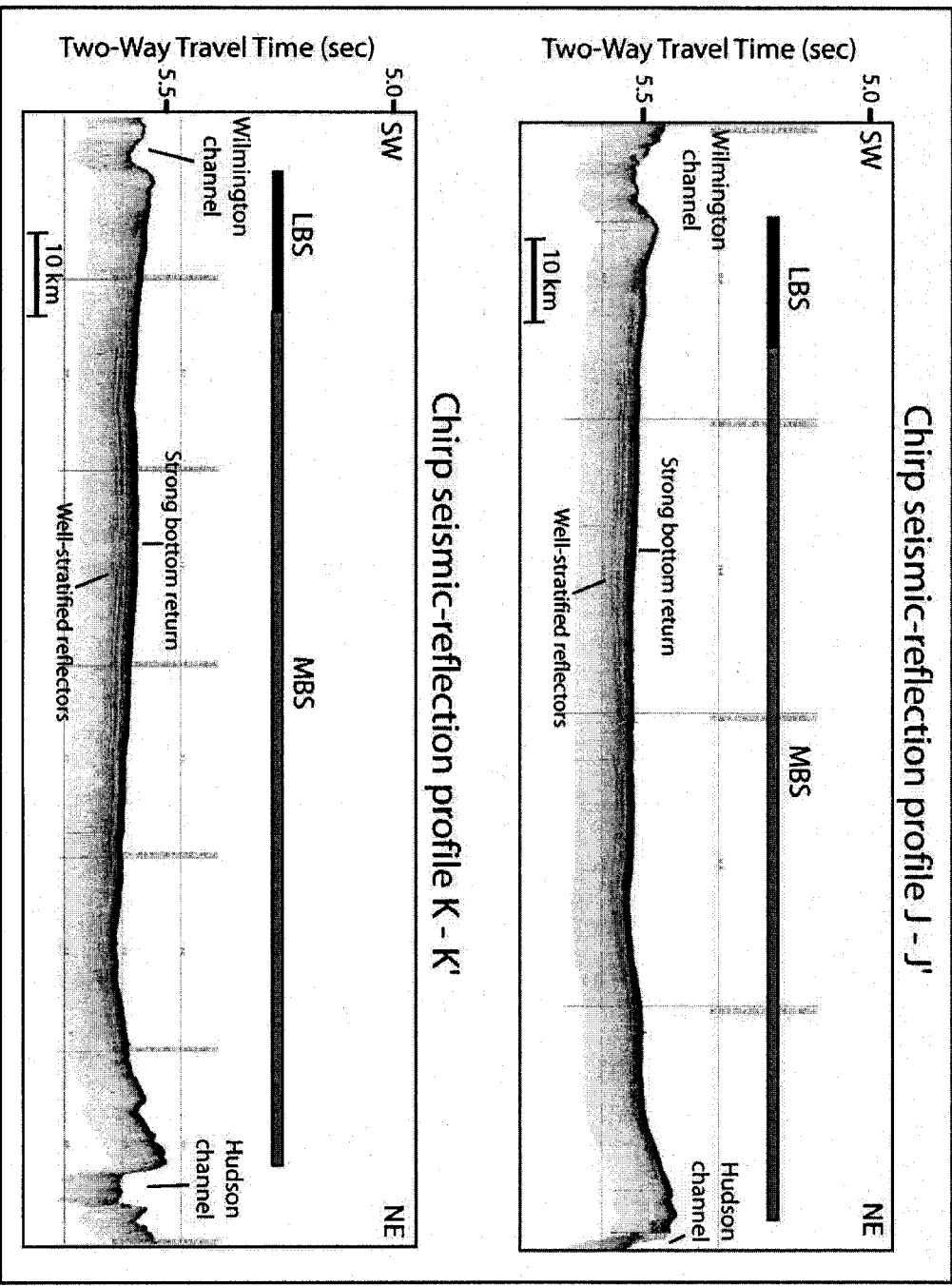


Figure 3.31 Chirp profiles JJ' and KK' collected down-slope from the low-backscatter anomaly. MBS = medium backscatter strength; LBS = low-backscatter strength.

3.5 LDEO Single-Channel Seismic-Reflection Profile

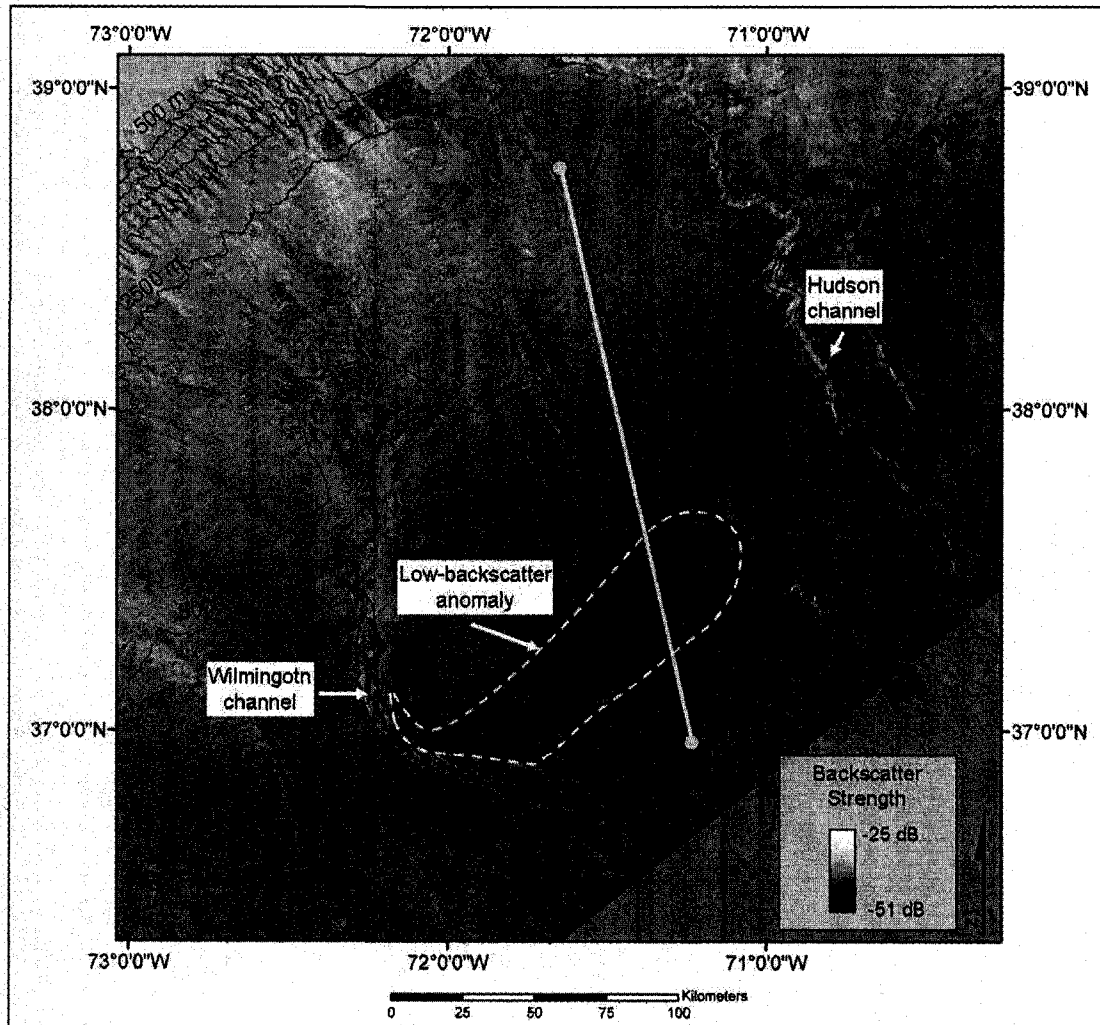


Figure 3.32 Section of LDEO single channel seismic line V2114 shown with multibeam backscatter as the background. Low-backscatter anomaly outlined by the white-dashed line. Bathymetric contours shown at 500-m intervals.

Profile VV' is a short section of Lamont-Doherty Earth Observatory airgun single-channel seismic (SCS) reflection line V2114 that was collected with a nearly north to south orientation across the low-backscatter anomaly (Figure 3.32 and Figure 3.33). The SCS profile shows strong, well-laminated seismic reflectors rise in the

high-backscatter strength section and through the homogenous medium backscatter strength seafloor upslope from the low-backscatter anomaly near the small channels (Figure 3.33). The well-stratified reflectors are underlain by a section of weakly-stratified reflectors near the low-backscatter anomaly. The weakly-stratified reflectors appear to outcrop at the seafloor within the low-backscatter anomaly. Downslope from the low-backscatter anomaly, a wedge of well-stratified, seismic sequence overlies weakly laminated seismic stratigraphy. This wedge corresponds to the relatively flat ($\sim 0.2^\circ$) seafloor with streaky and rilled, medium-backscatter strength.

The seismic-reflection profile also shows a bottom-simulating reflector (BSR) located in the sub-surface upslope from the low-backscatter anomaly, which was previously identified by Tucholke et al. (1977). A BSR is an acoustic horizon that is thought to form at the boundary between sediments containing free gas underlying sediments containing gas-hydrate, which is known as the hydrate stability zone (Kvenvolden, 2000).

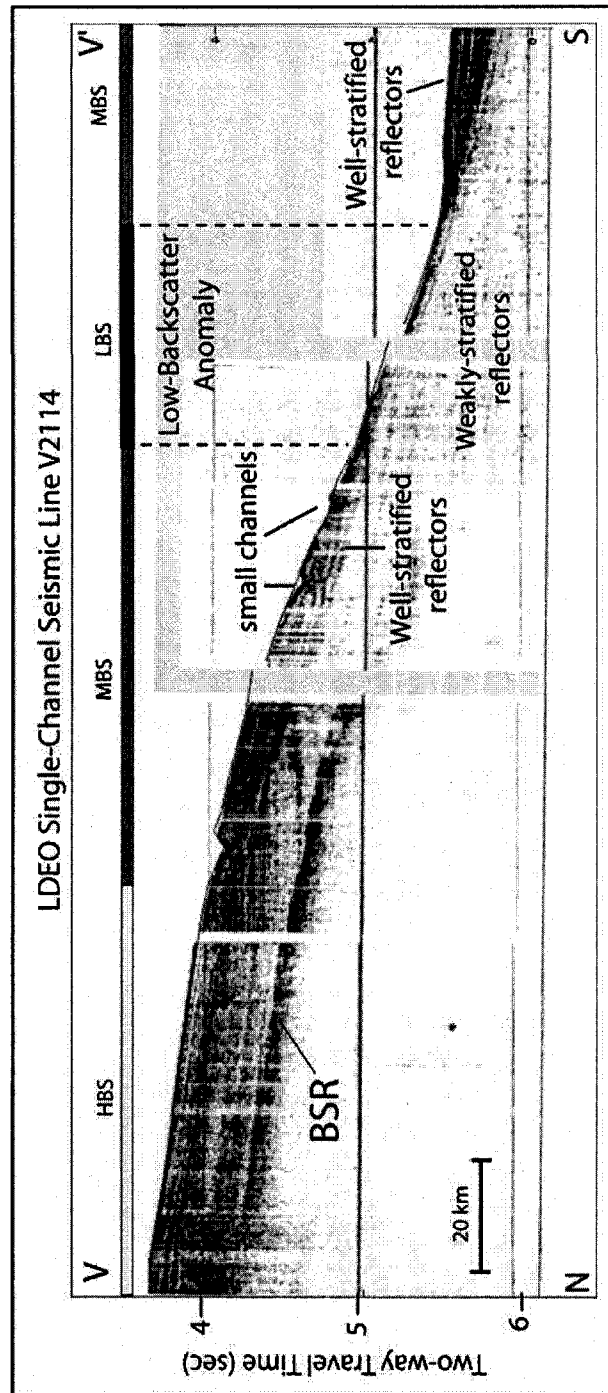


Figure 3.33 Segment of LDEO single-channel seismic-reflection line V2114. Corresponding backscatter strength shown in scale bar above profile. High-backscatter strength (HBS) shown in yellow; medium backscatter strength (MBS) shown in gray; low backscatter strength (LBS) shown in black. BSR = Bottom simulating reflector

3.6 Sediment Core Samples

Grain-size and smear-slide analyses are presented for the three sediment cores located on the continental rise near the low-backscatter anomaly analyzed for this study. Grain-size data are presented as mean grain size in phi values for each sediment sample. Locations of core samples with respect to multibeam backscatter data are shown in Figure 3.34.

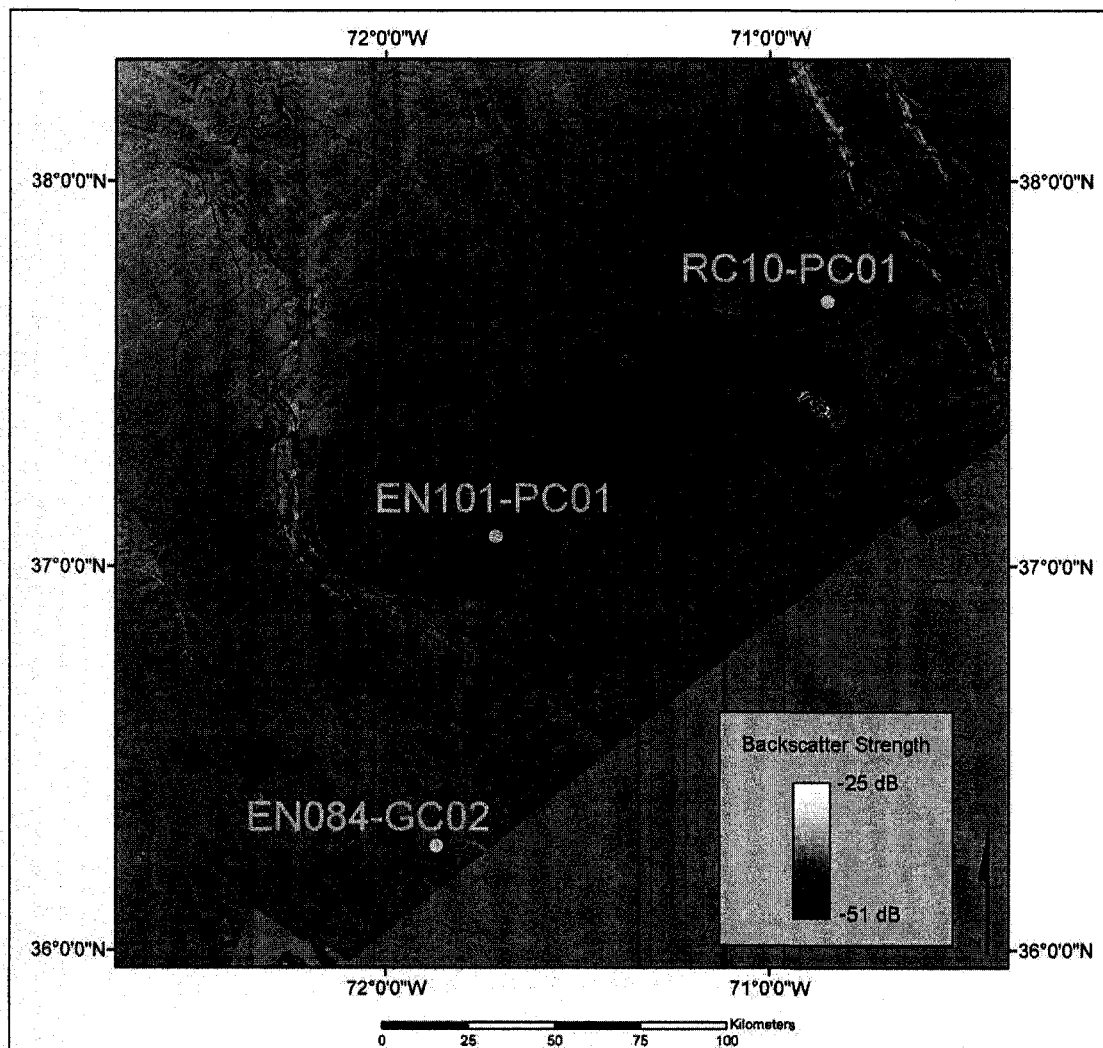


Figure 3.34 Core locations with multibeam backscatter map as backdrop. Contours are shown in black.

3.6.1 Core RC10-PC01

Core RC10-PC01 was collected at 3911 m water depth in medium-backscatter strength seafloor between the low-backscatter anomaly and Hudson channel (Figure 3.35 and Figure 3.36). The 3.5-kHz chirp sonar data show laminated acoustic stratigraphy in this area with strong bottom returns. Visual observations show that sediments are composed of silty clay with foraminifera. Average grain sizes in the top 100 cm of sediment range between 4.8 to 6.9 phi (Figure 3.37). Smear-slide analysis of core sample RC10-PC01 shows that sediments are composed of foraminifera-rich silty clay with silt and sand layers composed of quartz and foraminifera.



Figure 3.35 Perspective view (looking north) showing location of core RC10-PC01 with respect to bathymetry data. VE=10x

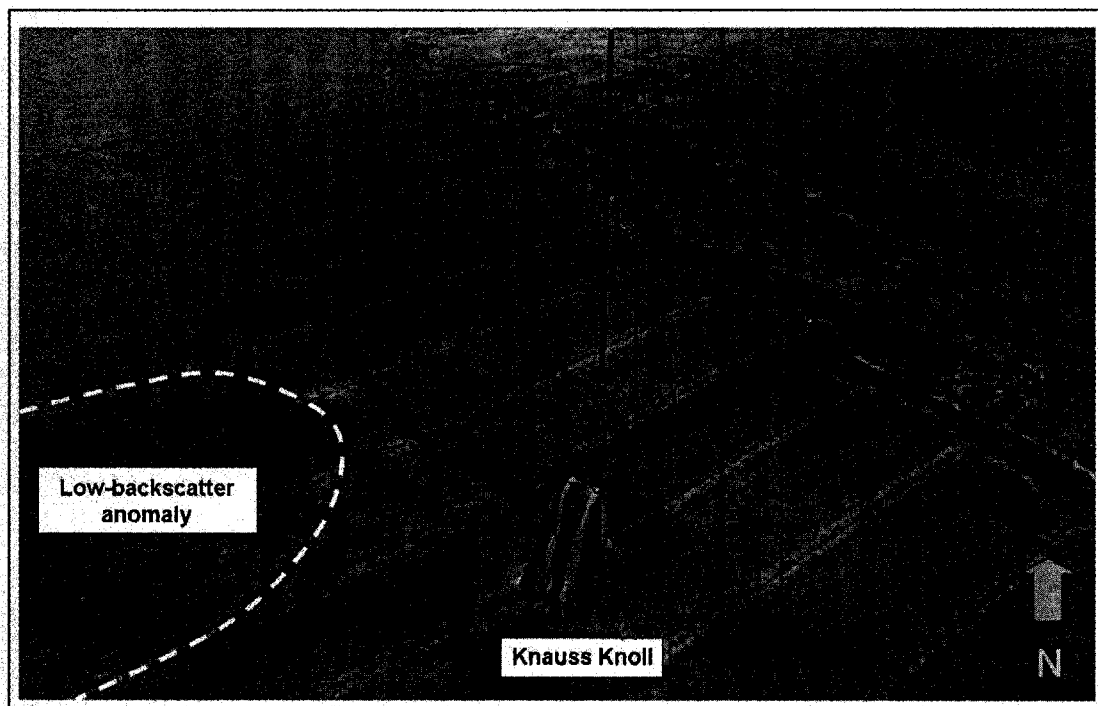


Figure 3.36 Perspective view (looking north) showing location of core RC10-PC01 with respect to backscatter data draped over bathymetry data. Low-backscatter anomaly outlined by white dashed line. VE=10x

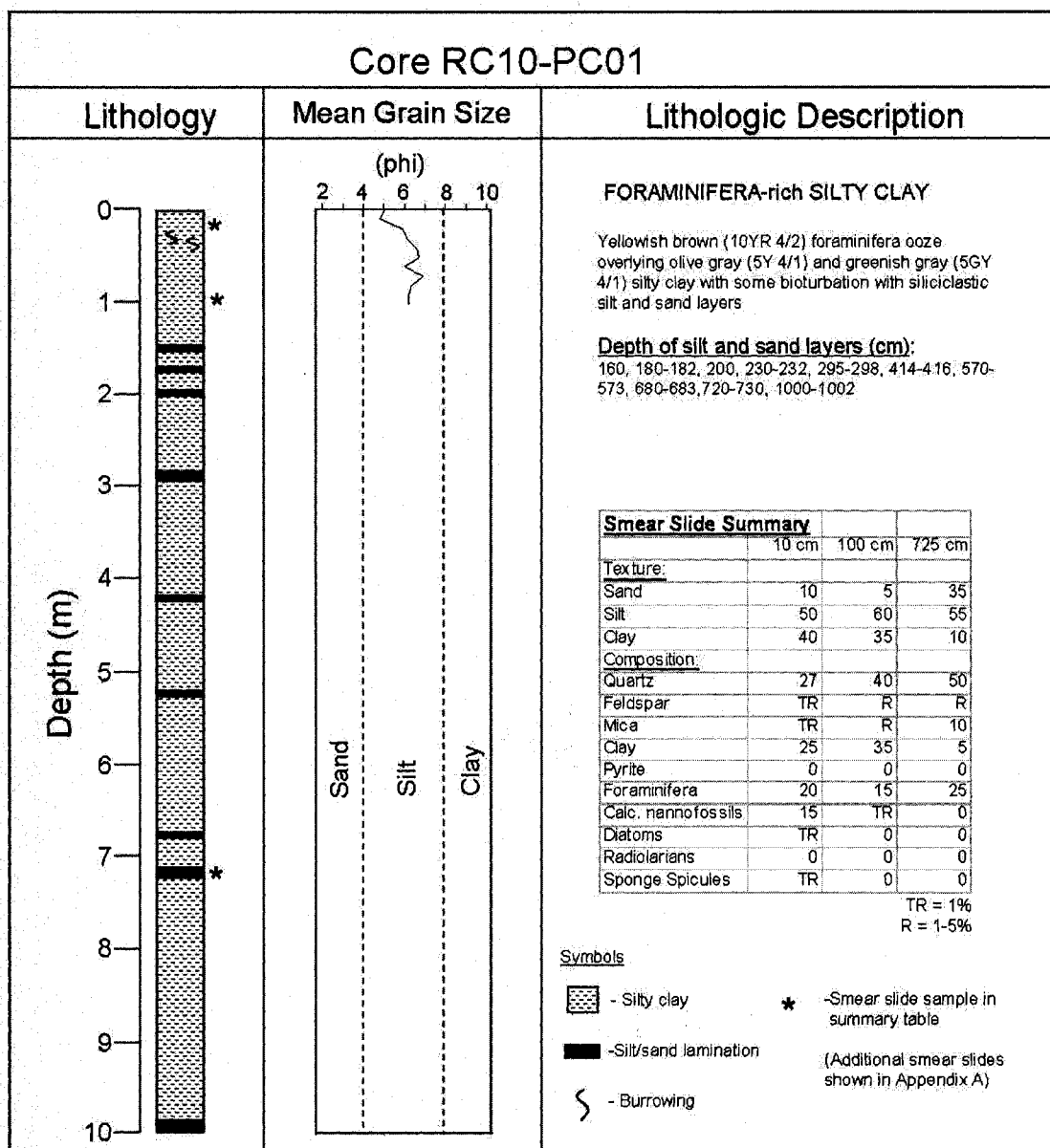


Figure 3.37 Stratigraphic column of core RC10-PC01 with laser-diffraction average grain-size measurements and descriptions. Samples were unavailable below 100 cm core depth (with exception of samples at 298 cm and 725 cm depths). Smear-slide and laser-diffraction mean grain-size data are available in Appendices A and B.

3.6.2 Core EN101-PC01

Piston core EN101-PC01 was collected within the medium-backscatter bridge at a water depth of 3817 m (Figure 3.38 and Figure 3.39). The 3.5-kHz chirp seismic-reflection profiles indicate that the core was collected within the lens-shaped sub-surface feature.

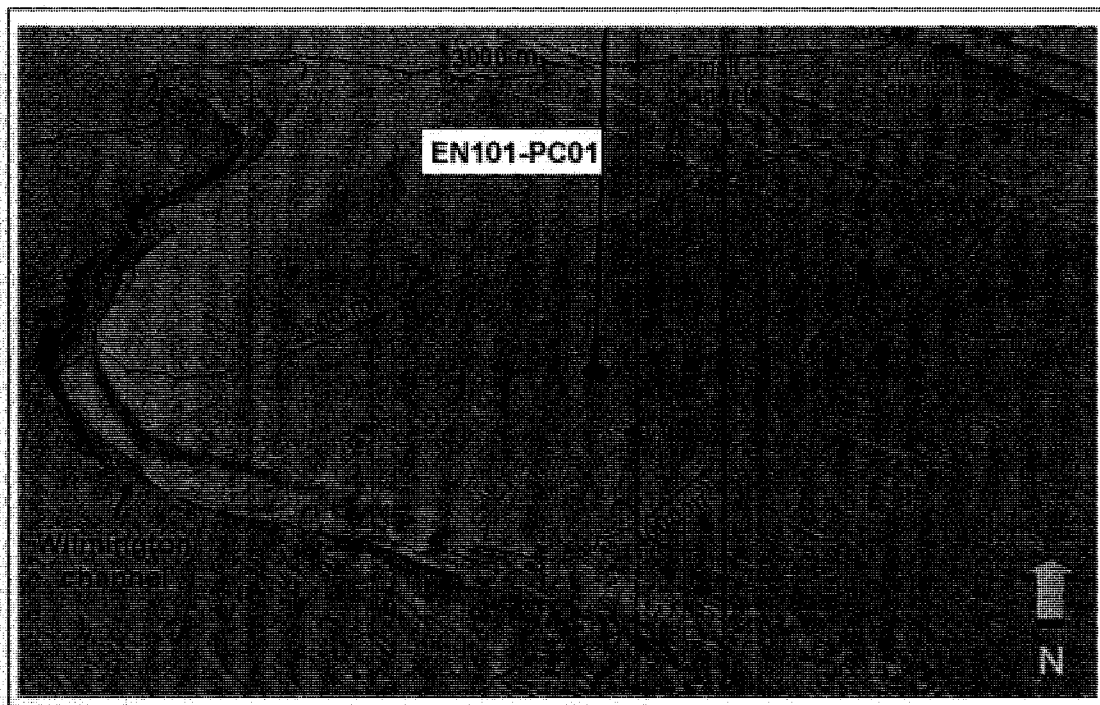


Figure 3.38 Perspective view (looking north) showing location of core EN101-PC01 with respect to bathymetry data. VE=10x

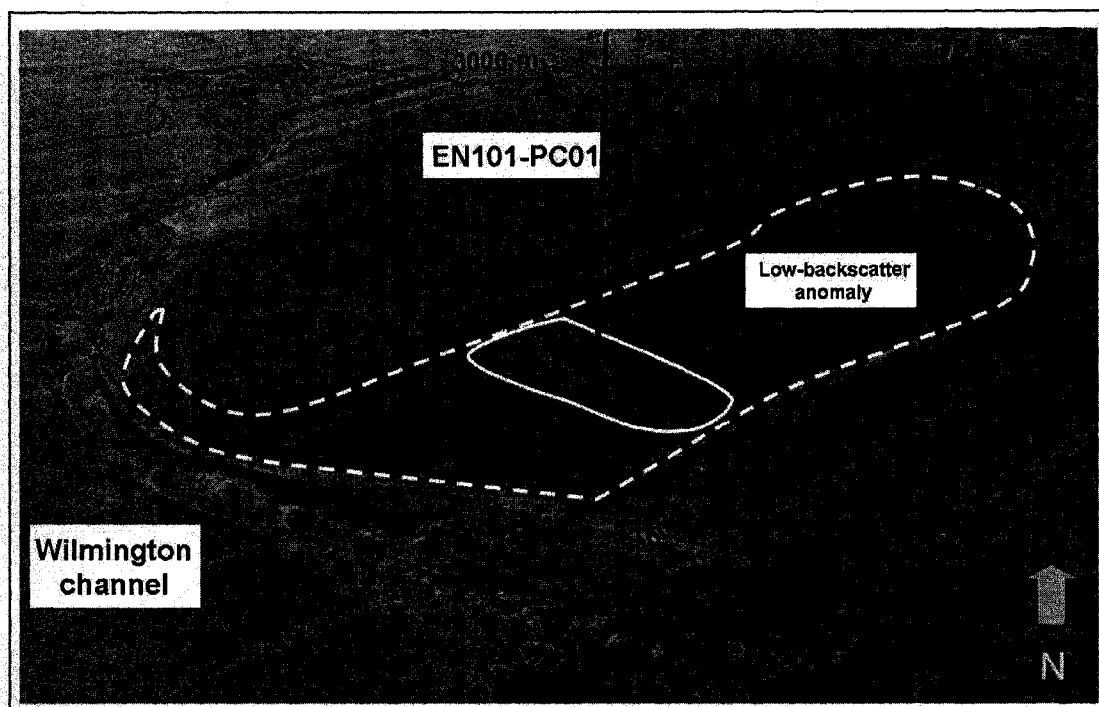


Figure 3.39 Perspective view (looking north) showing location of core EN101-PC01 with respect to backscatter data draped over bathymetry data. Low-backscatter anomaly outlined in white dashed line and medium-backscatter bridge outlined in white solid line. VE=10x

Visual observations show that sediments in core EN101-PC01 are predominantly olive-gray (5Y 3/2) silty clay containing foraminifera assemblages, mottling and authigenic carbonate nodules. Few bedding features were identified in the core stratigraphy. Grain-size analyses show that average grain sizes within the core range between 5.7 to 7.8 phi (Figure 3.40). These data show core sections with continuous homogeneous grain sizes and sections with successions of coarse grain-size intervals. Smear-slide analyses indicate that sediments corresponding to the coarse intervals are composed of silt-size siliciclastic minerals, whereas the homogeneous sediment between coarse layers is typically composed of foraminifera-rich calcareous nannoplankton silty clay.

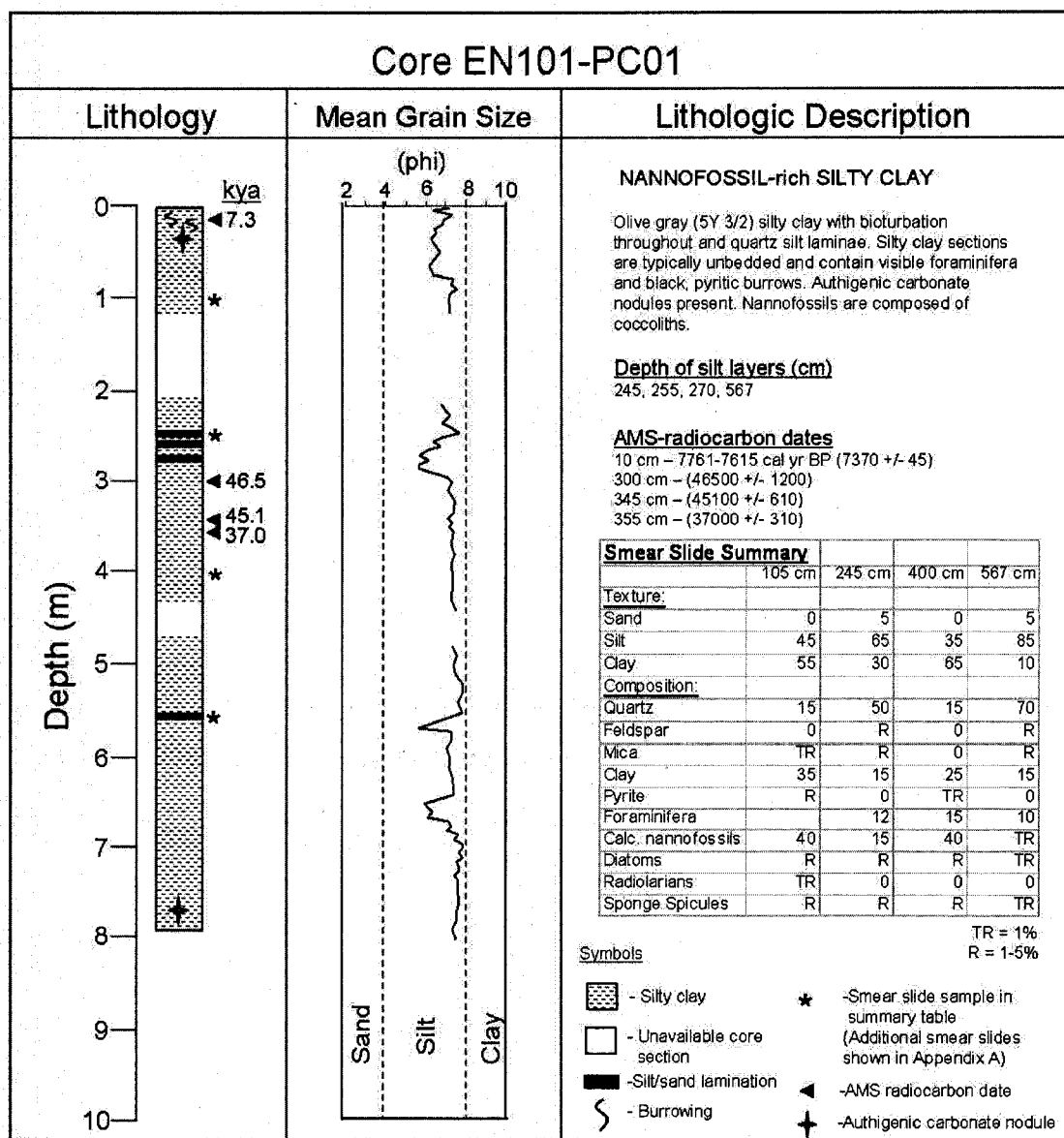


Figure 3.40 Average grain size values measured using laser particle-size analyzer for samples collected in piston core EN101-PC01. X-axis values are given in phi and y-axis values are depth in cm. AMS-radiocarbon dates shown in parentheses. Data gaps represent sections of the core that were unavailable for sampling. Smear-slide and laser-diffraction mean grain-size data are available in Appendices A and B.

Smear slide percentages for the dominant components observed in core EN101-PC01 are shown in Figure 3.41.

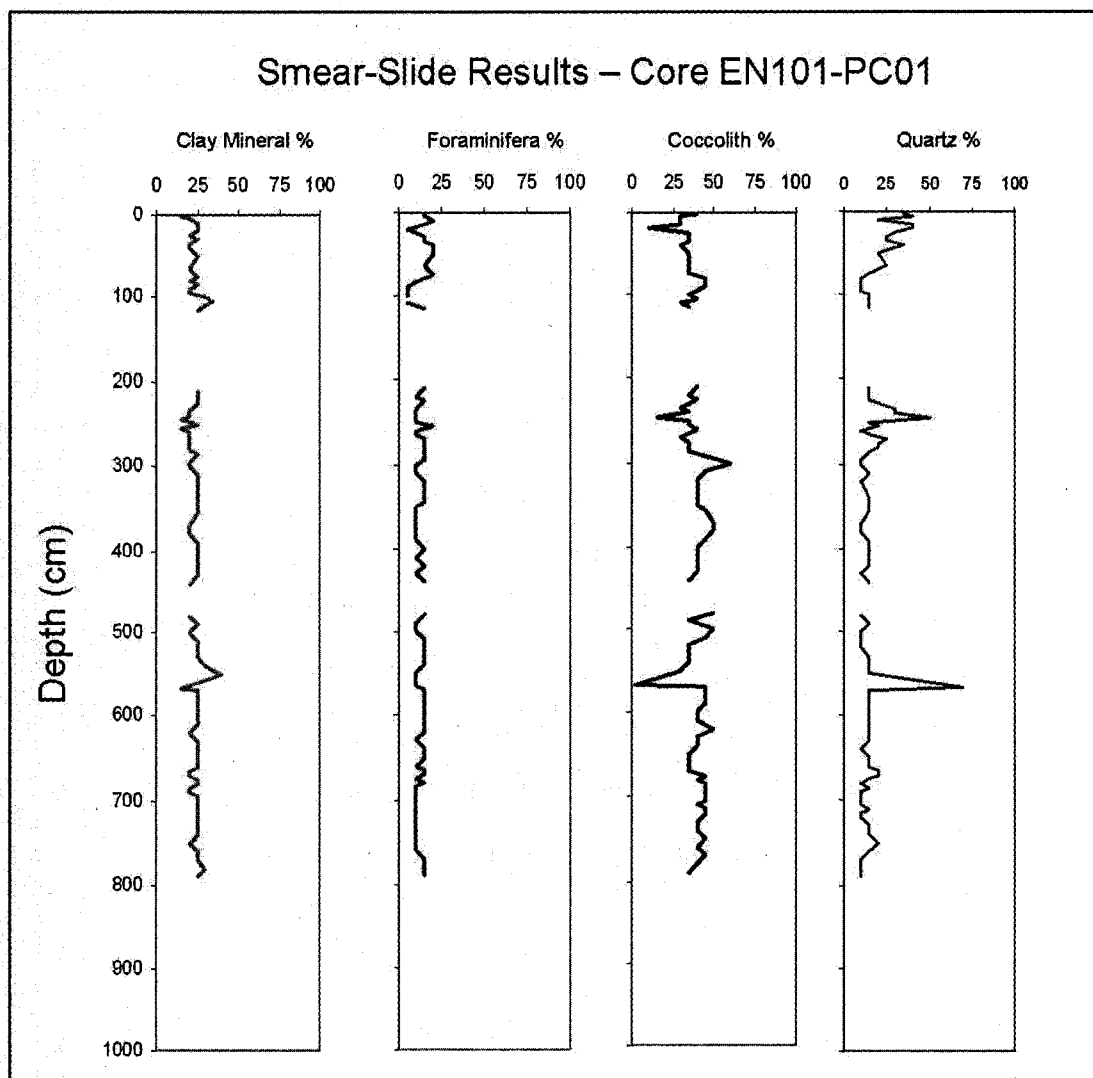


Figure 3.41 Smear slide results for dominant components found in Core EN101-PC01.

AMS-radiocarbon ages from samples taken at 10, 300, 345 and 355 cm depths from core EN101-PC01 are shown in Table 3.1 and plotted in Figure 3.42. Regional reservoir corrections applied to the sample at 10 cm and the resulting calibrated

calendar years are shown in Table 3.2. Calibrated calendar years are shown as 1σ and 2σ distributions. The radiocarbon ages measured at 300 and 345 cm core depth samples show that sediment is older than the sediment age measured in the 355 cm sample.

Table 3.1 AMS-radiocarbon age results.

Accession Numbers	Depth (cm)	d13C	F Modern	Fm Error	14C Age	Age Error
OS-66063	10	1.61	0.3997	0.0024	7370	45
OS-66061	300	1.19	0.0031	0.0004	46500	1200
OS-66051	345	1	0.0037	0.0003	45100	610
OS-66054	355	0.92	0.01	0.0004	37000	310

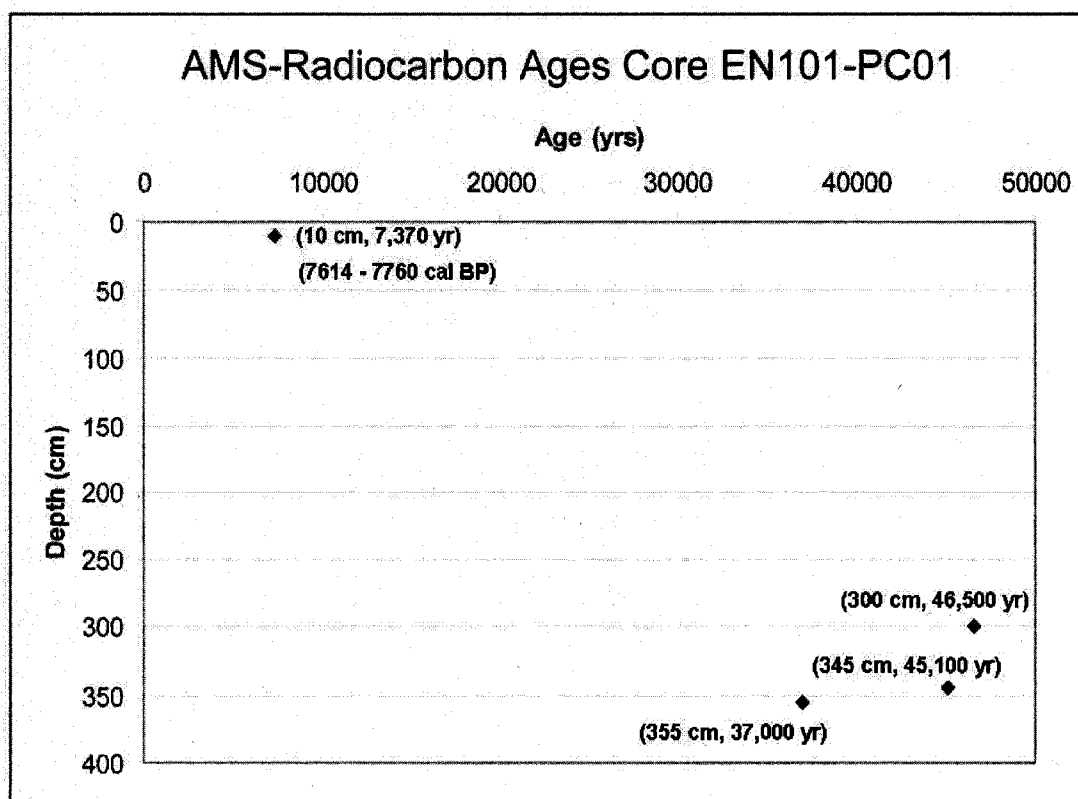


Figure 3.42 Plot of AMS-radiocarbon dates. Reservoir corrections shown but not plotted from 10 cm sample.

Table 3.2 Regional reservoir correction values and calibrated calendar age values for radiocarbon ages collected from core EN101-PC01.

Depth (cm)	ΔR	ΔR Uncertainty	1σ	2σ
10	145	52	7614 - 7760 cal BP	7562 - 7837 cal BP
300				
345				
355				

3.6.3 Core EN084-GC02

Core EN084-GC02 was collected 25 km southwest of Wilmington channel in medium backscatter strength seafloor and at a water depth of 4052 m (Figure 3.43 and Figure 3.44). The 3.5-kHz chirp seismic-reflection profiles show well-laminated acoustic stratigraphy near the core collection location.

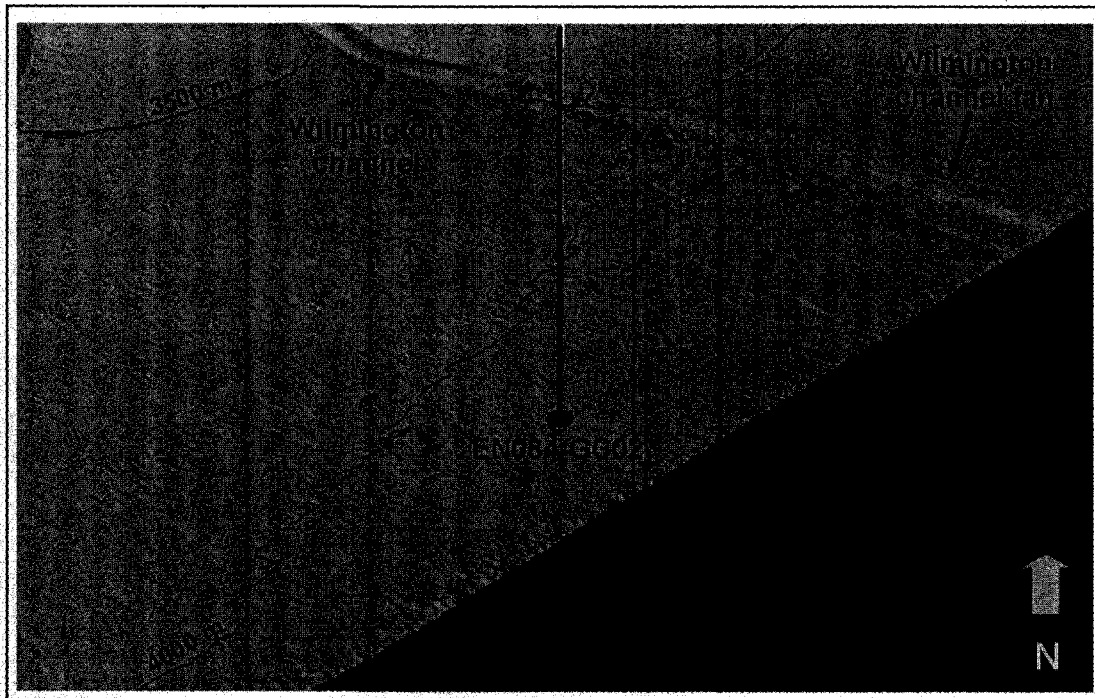


Figure 3.43 Perspective view (looking north) showing collection location of core EN084-GC02 shown with bathymetry data (gray sun-illuminated hillshade). VE=10x

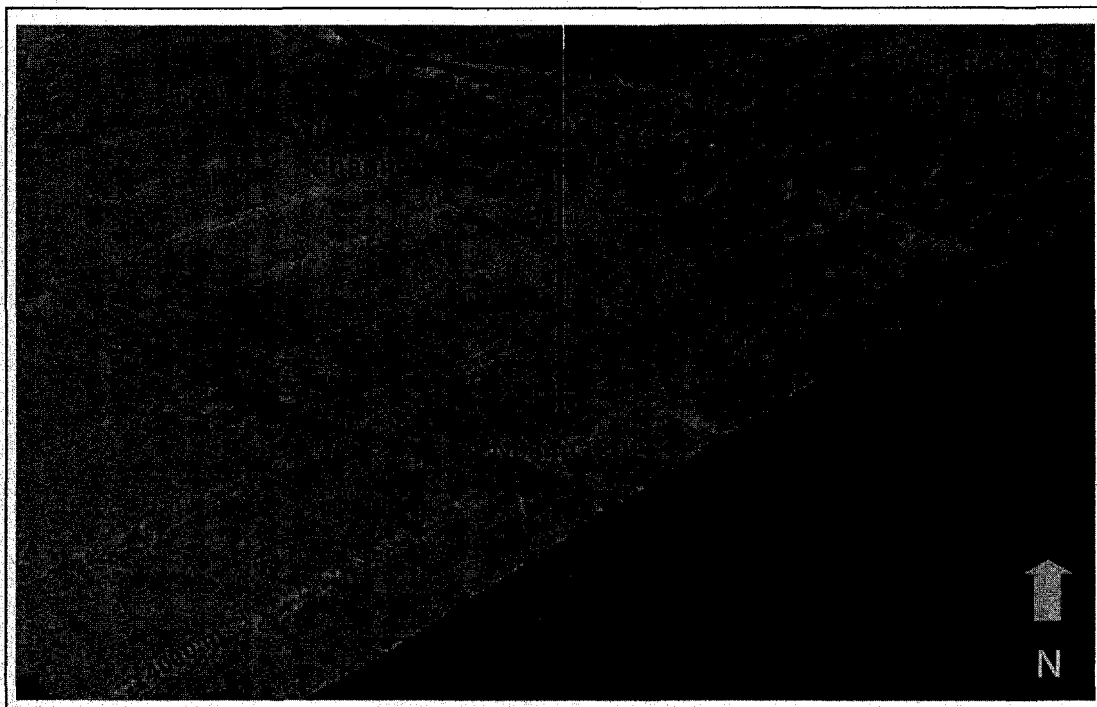


Figure 3.44 Perspective view (looking north) showing collection location of core EN084-GC02 shown with backscatter data draped over bathymetry data (light tones = high backscatter; dark tones = low-backscatter). VE=10x

Visual observations of the core indicate that sediments are predominantly silty clay with intermittent layers of silt sized grains. Silty clay sediments in the upper 16 cm are pale-brown (5YR) in color and are light olive-gray (5Y 5/2) to the bottom of the core. Foraminifera assemblages are visible within the silty clay. Laser diffraction particle-size analyses show that average grain size values range from 7.3 to 3.7 phi (Figure 3.45). These data indicate that core EN084-GC02 contains very distinct events of silt- and fine sand-sized sediment grains. Grain-size data show that some events are graded sediments (fining upward), but others are not clearly graded. Smear slides show that coarse sediment events are predominantly composed of siliciclastic mineral grains with few biogenic components. Sediments between coarse events are

foraminifera-rich nannoplankton silty clay. Coccoliths make up the nannoplankton component.

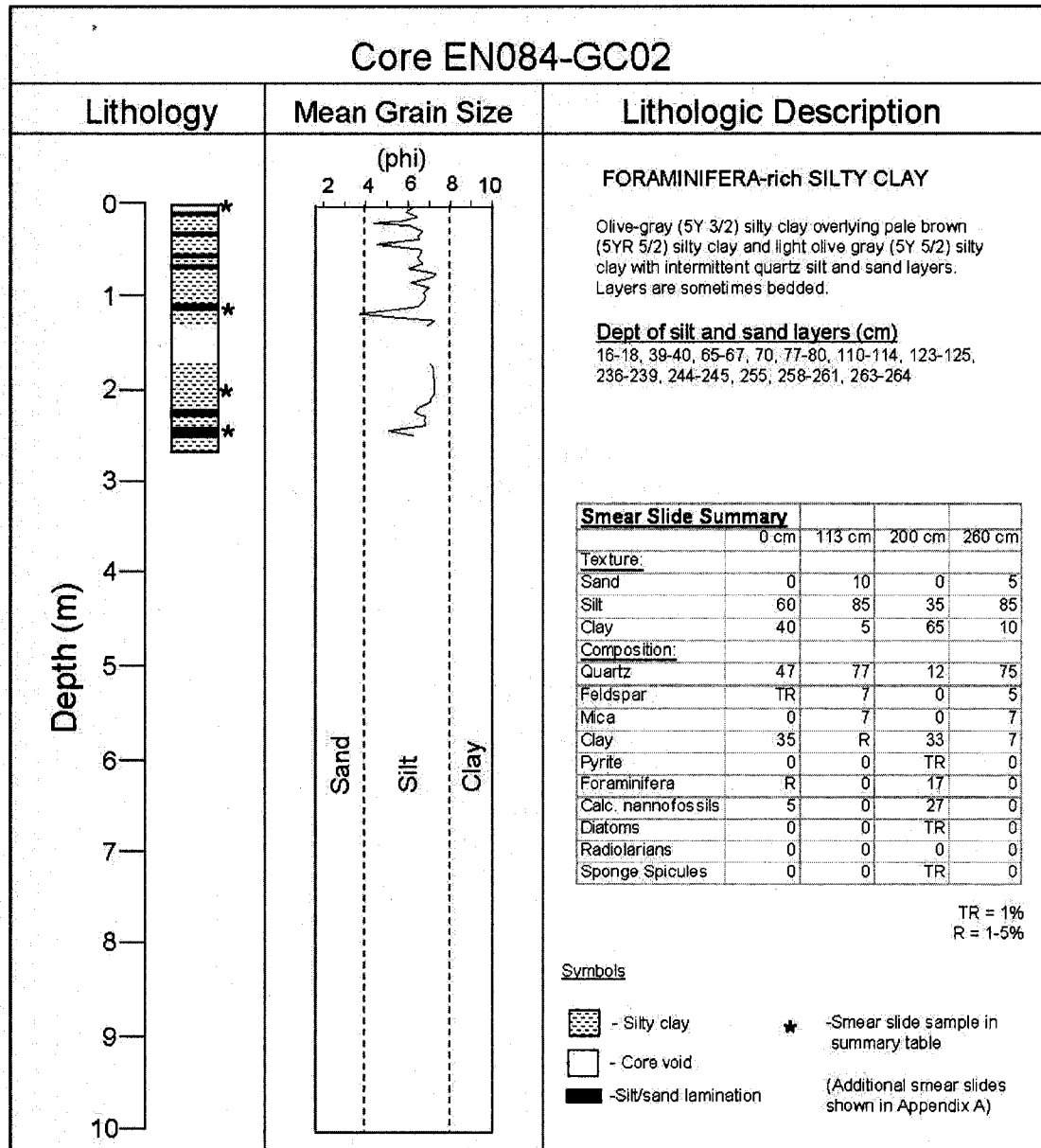


Figure 3.45 Average grain size values measured using laser particle-size analyzer for samples collected in gravity core EN084 GC2. X-axis values are given in phi and y-axis values are depth in cm. Data gap represents section of the core that were unavailable for sampling. Smear-slide and laser-diffraction mean grain-size data are available in Appendices A and B.

CHAPTER 4

DISCUSSION

4.1 Low-Backscatter Anomaly

The features shown by the surface and sub-surface seafloor data suggest the importance of gravity-driven mass-wasting processes and contour-parallel processes on the New Jersey continental margin. In addition, the data suggest the presence of sub-surface gas and/or gas-hydrate. These processes are described in the following section as three working hypotheses for the geological origins of the low-backscatter anomaly. The first hypothesis for the low-backscatter anomaly is that it is a deposit that originated from suspended sediments stripped from turbidity currents that have traveled down the small channels. A second hypothesis is that the low-backscatter anomaly is an outcrop exposed either by erosion caused by the Western Boundary Undercurrent (WBUC) or non-deposition related to bottom currents and local seafloor geomorphology. A third hypothesis is that the low-backscatter anomaly is caused by the presence of gas within the sediments.

4.1.1 Hypothesis 1 – Sediment Deposit

The presence of the five small channels immediately upslope from the low-backscatter anomaly suggests that downslope sediment transport has occurred nearby. Pratson and Laine (1989) envisioned that these small channels originated on the upper

continental rise, approximately 75 km from the base of the continental slope. They suggested that turbidity currents that had bypassed or overflowed the confluence leading to the Wilmington channel had formed the channels.

The bathymetry data analyzed for this study support the interpretation of Pratson and Laine (1989) that downslope sediment transport from the continental slope most likely have formed the small channels. The bathymetry data show that the small channel farthest to the northeast (nearest to Hudson channel) extends upslope to the landward extent of the MBES data near the 2000 m isobath (Figure 4.1 and Figure 4.2). Although more difficult to distinguish, the channels farther to the southwest also extend upslope to this region as well. These data suggest downslope sediment gravity flows from between Mey and Hudson Canyons have formed the small channels as opposed to the adjacent section of margin to the southwest, which all coalesce into Wilmington channel.

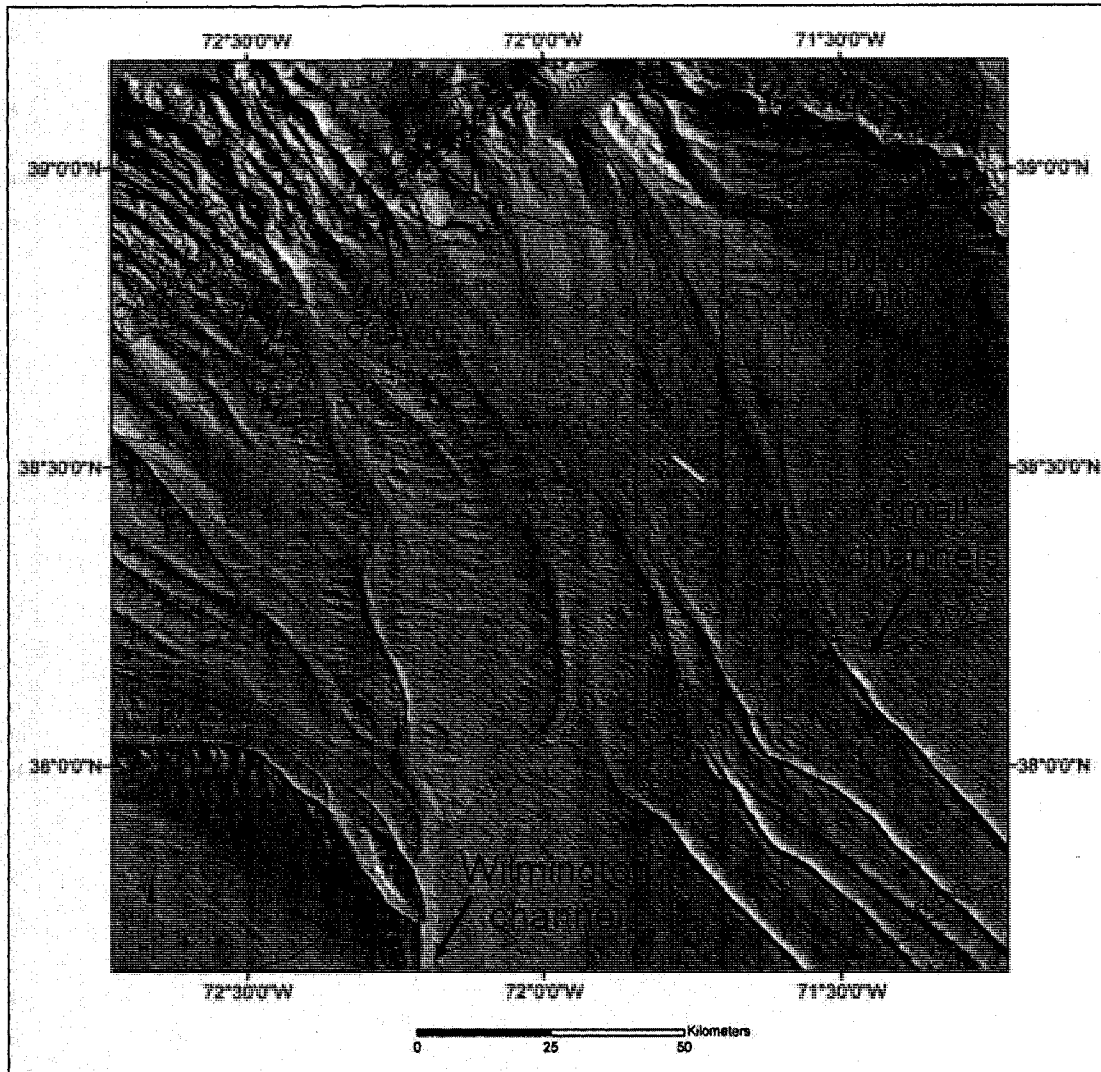


Figure 4.1 Bathymetry data (gray sun-illuminated hillshade) showing evidence of the small channels extending upslope from the 3000 m isobath.

Sediment that has traversed downslope from the continental slope could have crossed the upper continental rise through these small channels towards the section of steeper seafloor near the 3000 m isobath (Figure 4.2). The increase in average slope gradients from approximately 0.2° to 0.7° appears to have been sufficient to increase the erosiveness of turbidity currents in this seafloor section, resulting in deeper channel incision.

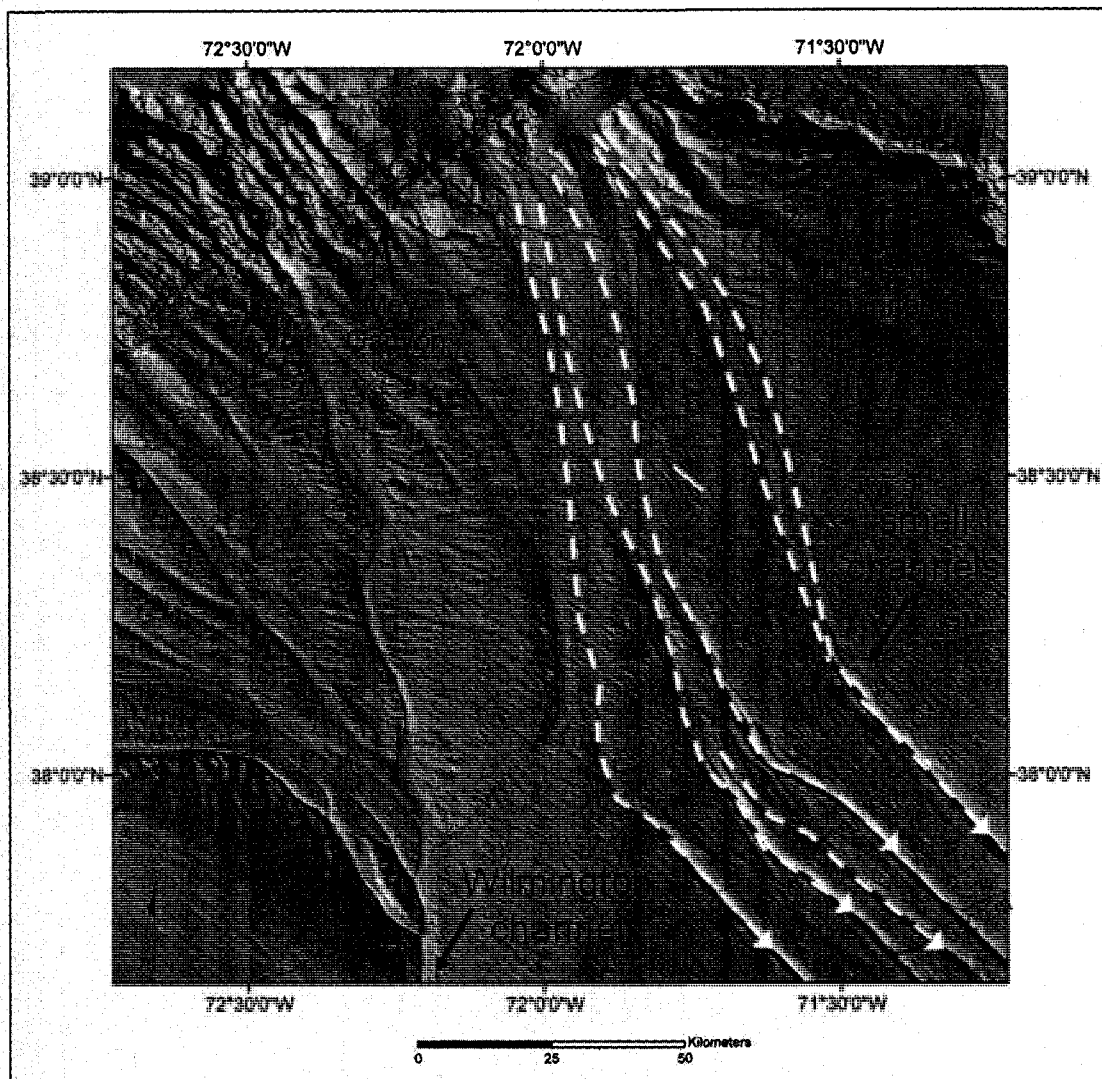


Figure 4.2 Bathymetry data (gray sun-illuminated hillshade) showing sediment transport pathways (white-dashed arrows) across the upper continental rise and through the small channels.

The downslope sediment gravity flows that traveled through the small channels would eventually intersect the high-velocity core of the WBUC. The presence of the WBUC is indicated near the low-backscatter anomaly by Krause Foredrift on the northeast side of Knauss Knoll and the erosional moat on the southern side of the seamount (Figure 4.3). Lowrie and Heezen (1967) argued that

suspended sediments from Hudson Canyon have been carried southwestward by the WBUC. Deceleration of the WBUC flow on the upcurrent face of the seamount allowed sediment to accumulate as the foredrift feature at the base of the seamount (Lowrie and Heezen, 1967). The erosional moat on the southern side of the Knauss Knoll revealed by the bathymetry data in this study and in the previous study by Lowrie and Heezen (1967) suggests that the WBUC has scoured the seafloor. The local acceleration of current due to the obstruction resulted in erosion of seafloor sediment at the downcurrent base of Knauss Knoll (Lowrie and Heezen, 1967).

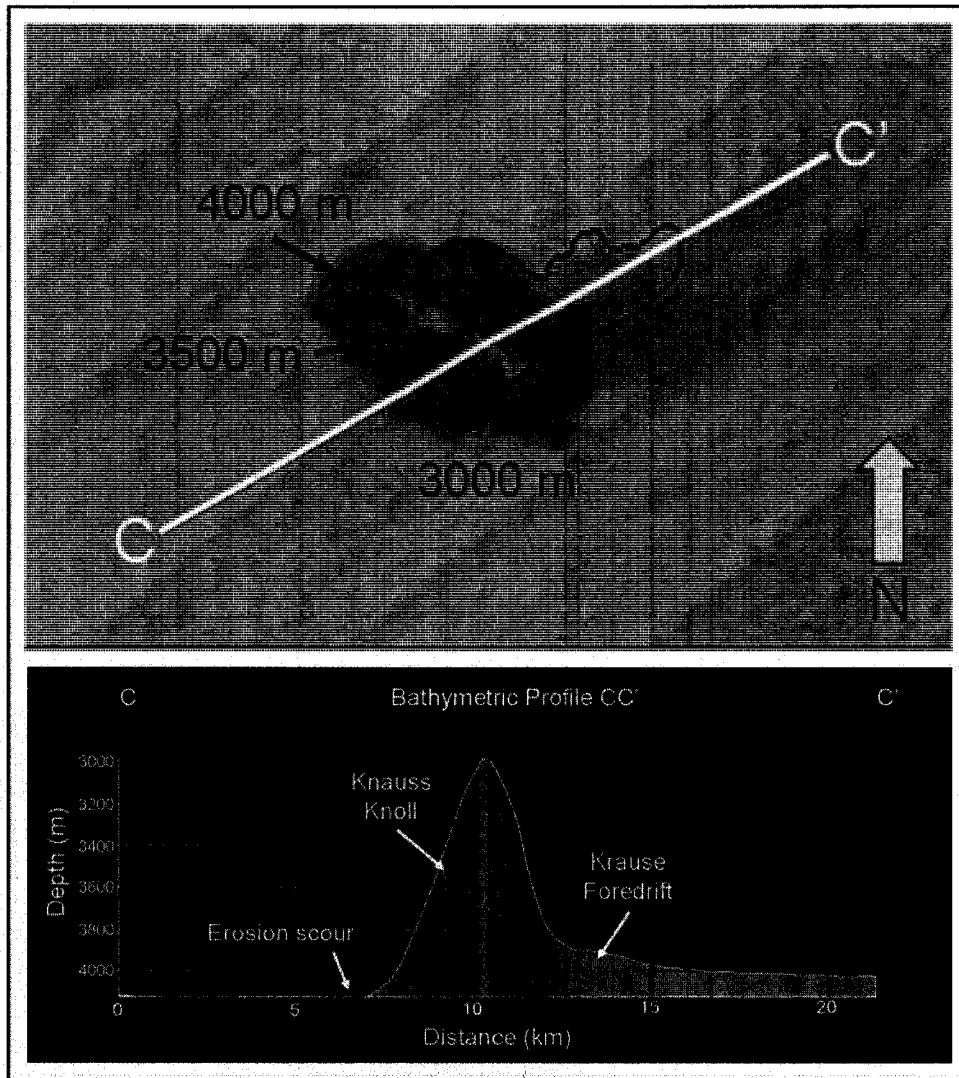


Figure 4.3 Bathymetric profile showing Krause Foredrift and erosion scour at the base of Knauss Knoll.

The evidence of a southwest flow near the 3500 to 4000 m isobaths is consistent with bottom currents measured during the SYNoptic Ocean Prediction (SYNOP) Central Array experiment (Shay et al., 1995), the High Energy Benthic Boundary Layer Experiment (HEBBLE) (Richardson et al., 1981) and bottom photography studies by Schneider et al. (1967). The SYNOP field program identified the WBUC at 3500-m near 68°W and 38°N (~275 km to the northeast of the study

area). These measurements showed that average flow rates of 6 cm/s in 3500-m water depth were towards the southwest along isobaths (Shay et al., 1995). Events of increased flow speeds up to 40 cm/s were also measured offshore the Grand Banks at 3500 m water depth (Shay et al., 1995). The HEBBLE project also found the WBUC near these depths on the Nova Scotian continental rise. Measurements taken at a station located at the 4158 m isobath (at 40° 56.6'N and 63° 44.9'W) show a mean speed of 6.3 cm/s in the southwest (267°) direction, which is nearly parallel to local isobaths. This study found a maximum WBUC speed of 28.5 cm/s (Richardson et al. 1981).

Compass-oriented bottom photographs analyzed by Schneider et al. (1967) also show evidence of swift southwest-flowing currents near the study area. This research reported near tranquil deep-sea current conditions at R/V *Trident* Station 10 in 3104 m water depth (Figure 4.4). However, bottom photographs at *Trident* Station 11 indicate sediment streamers and bottom fauna deflected to the southwest at 3383 m water depth (Schneider et al., 1967). The bottom photographs at *Trident* Station 15 show sediment ripples and streamers and noticeably sediment-laden, “murky” water near the seafloor. Schneider et al. (1967) interpreted these data to suggest not only evidence of the WBUC, but an increase in bottom current speed with depth.

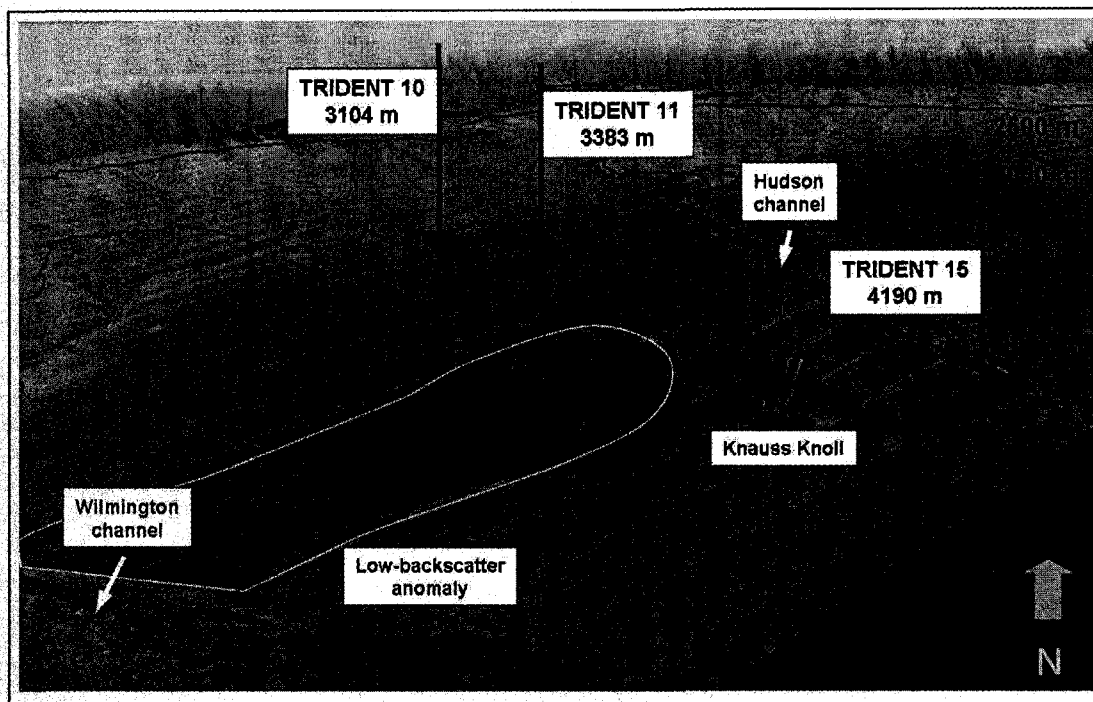


Figure 4.4 Perspective view (looking north) of backscatter data (low backscatter = dark tones; high backscatter = light tones) showing location of bottom photographs analyzed by Schneider et al. (1967). Red arrows indicate direction and relative magnitude of inferred current strength. Low-backscatter anomaly outlined in white. VE=10x

The Western Boundary Undercurrent could have stripped suspended sediments from turbidity currents that overbanked the small channels and transported these sediments to the southwest (Figure 4.5 and Figure 4.6). A Hjulstrom-type curve (Heezen and Hollister, 1964) can be used to estimate the current speeds needed to erode, transport and deposit sediments by grain size. This diagram indicates that the range of WBUC flow speeds (up to 78 cm/s) are within the range needed to transport sediments with grain size from clay to sand in suspension (Figure 4.7).

Based on these critical threshold predictions for sediments and the current meter data collected by the SYNOP and HEBBLE studies at other locations on the

margin within the depth range of the low-backscatter anomaly, flow speeds of the WBUC have likely been capable of transporting clay- to sand-size sediment. These interpretations are supported by the bottom photographs near the low-backscatter anomaly that show sediment streamers and murky water analyzed by Schneider et al. (1967) and the presence of Krause Foredrift at the base of Knauss Knoll.

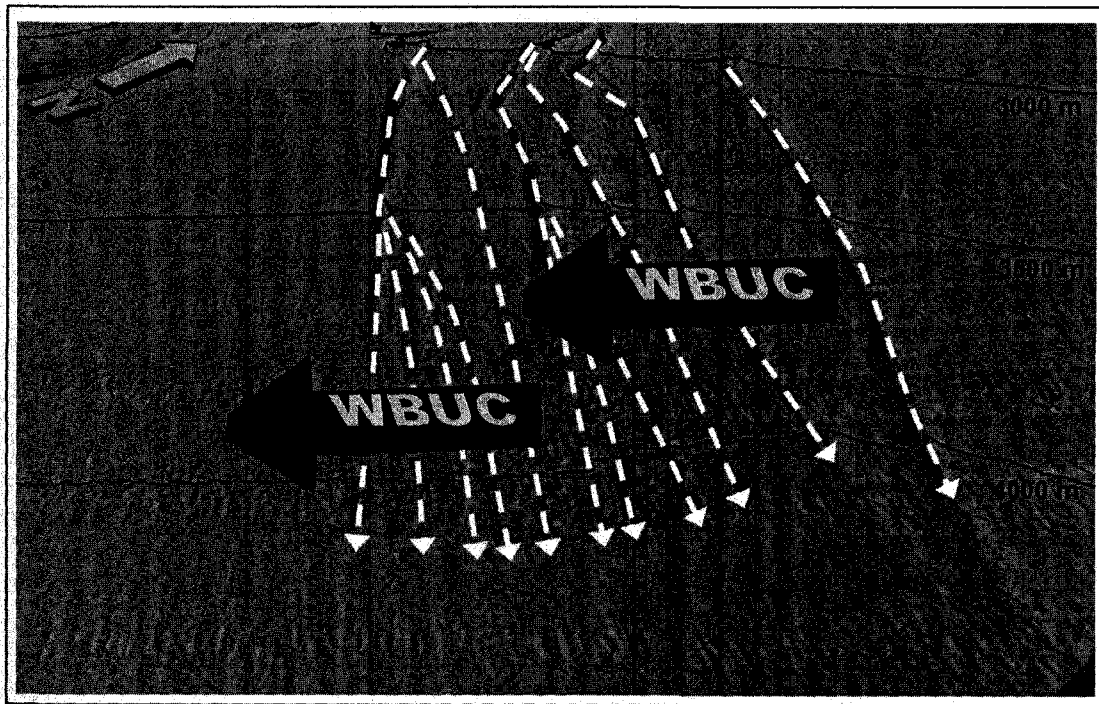


Figure 4.5 Perspective view (looking upslope and landward) of bathymetry data (gray sun-illuminated hillshade) showing downslope transport of sediment through small channels (white dashed arrows) and subsequent transport direction of suspended sediment parallel to contours by the WBUC (red arrows). VE=10x

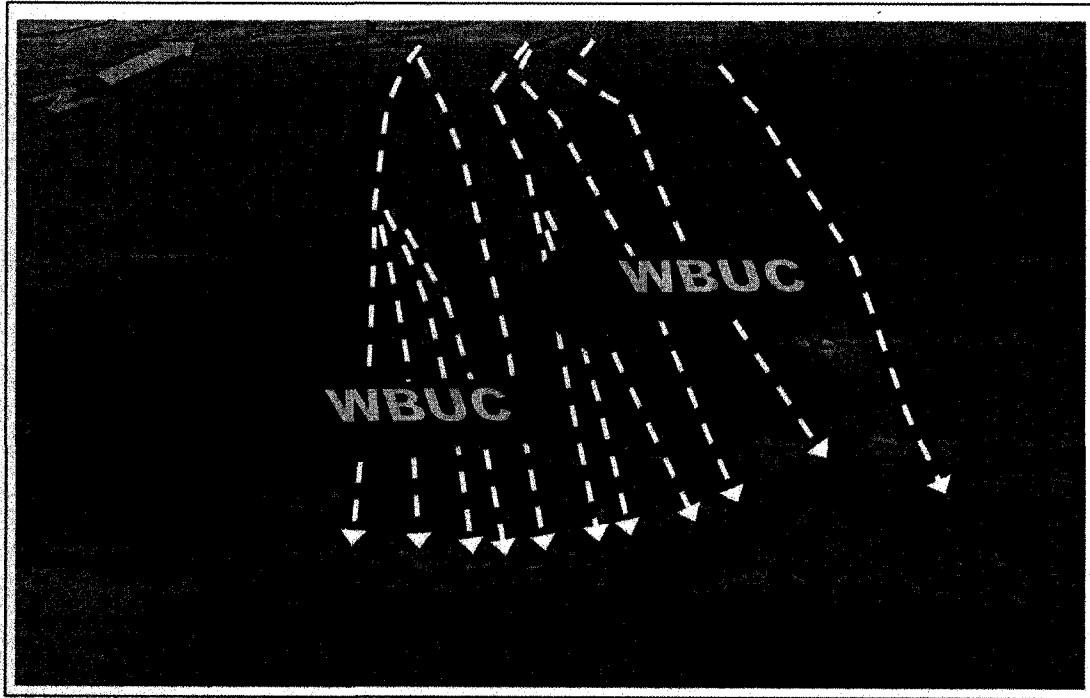


Figure 4.6 Perspective view (looking upslope and landward) of backscatter data (low backscatter = black and high backscatter = white) showing downslope transport of sediment through small channels (white dashed arrows) and subsequent transport direction of suspended sediment parallel to contours by the WBUC (red arrows). VE=10x

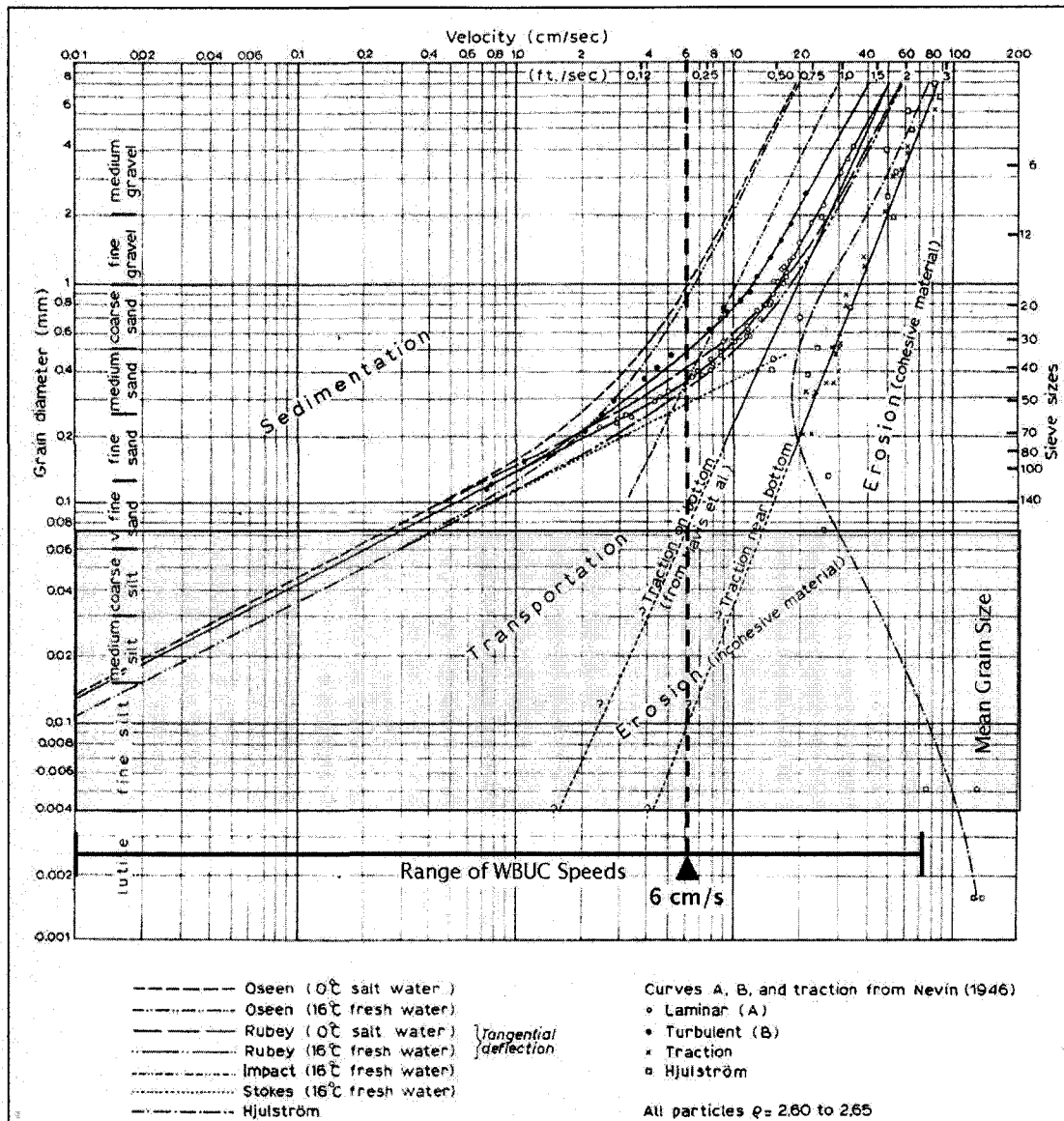


Figure 4.7 Diagram showing erosion, transport and deposition conditions plotted by grain size and current speed. The area outlined in yellow shows measured average grain size of sediment cores analyzed in this study. The range of current speeds measured by the HEBBLE and SYNOP projects (4158-m and 3500-m) near the depth of the low-backscatter anomaly shown at the bottom of the diagram. Modified from Heezen and Hollister (1964).

Deposition of sediments may have occurred to the southwest of the small channels in the downflow direction of the WBUC. The Heezen and Hollister (1964) diagram shows that WBUC speeds less than ~ 0.4 cm/s are necessary for sediment deposition of sediments within the range of samples analyzed for this study (although

the grain size range of sediments within the low-backscatter anomaly is unknown). Although studies have measured that the WBUC has average speeds of ~6 cm/s at depths coinciding with the low-backscatter anomaly, current speed data also indicate greatly varying speeds from near tranquil conditions up to 78 cm/s (Richardson et al., 1981; Shay et al., 1995). Therefore it would be possible for sediments to be deposited across this seafloor region under slower WBUC flow conditions.

It may also be possible that suspended sediment particles have aggregated while transported in suspension. As part of the HEBBLE study, McCave (1985) found that settling of bottom sediments was strongly influenced by mucus binding of clay-sized components. These processes were thought responsible for seafloor sediment compositions that measured ~30% clay in an environment with intermittently strong (averaging 8 to 32 cm/s) bottom currents (McCave, 1985). Or perhaps the grain size of suspended particles is coarser than silt and clay. The Heezen and Hollister (1964) diagram shows that sand-size sediment grains are deposited at current speeds of approximately 6 cm/s. This could suggest that the low-backscatter anomaly sediment deposit is composed of sand-sized sediment grains as opposed to the clay- and silt-sized sediment observed in sediment cores from the surrounding areas.

The decrease in backscatter strength could be caused by smooth seafloor relative to the acoustic wavelength of the MBES. de Moustier and Alexandrou (1991) have suggested that seafloor roughness with a radius of curvature with a root mean square (rms) greater than ~4 cm (or peak-to-peak amplitude ~12 cm) is required to influence 12-kHz MBES backscatter as interface backscatter. The seafloor relief

within the low-backscatter anomaly could be below this threshold, whereas the surrounding areas may be relatively rough in comparison.

In addition, the deposit could be composed of homogenous, fine-grain sediments that have a lower acoustic impedance contrast at the seabed and lower volume backscatter properties within the upper few meters of the sediments than the surrounding regions. The lower acoustic impedance contrast between the water and seafloor could be caused by sediment properties such as high porosity or low sediment density. These sediment properties decrease the acoustic impedance value of the sediment by reducing the overall density (known as saturated bulk density) and the sound speed of the seafloor medium (Hamilton, 1956; Hamilton, 1970). A lack of sediment inhomogeneities within the penetration depth of the sonar transmission could be caused by an absence of coarser sediment layers such as turbidites or contourites within sediment deposit.

4.1.2 Hypothesis 2 – Outcropping Stratigraphic Units

An alternate hypothesis is presented suggesting that the low-backscatter anomaly represents an outcrop of older sediment. Studies have previously suggested that sediments outcrop on the section of the continental margin near the low-backscatter anomaly (Schneider et al., 1967; Mountain and Tucholke, 1985; Locker, 1989; Pratson and Laine, 1989). These studies have suggested that the outcrop has resulted from erosion or non-deposition by the WBUC and local geomorphology.

High-resolution 3.5-kHz chirp sonar profiles EE' and FF' (Figure 3.28) and airgun seismic-reflection profile VV' show that seismic reflectors outcrop within the

low-backscatter anomaly (Figure 4.8). The outcropping reflectors that occur within the bounds of the low-backscatter anomaly suggest that the low-backscatter anomaly is an erosional surface.

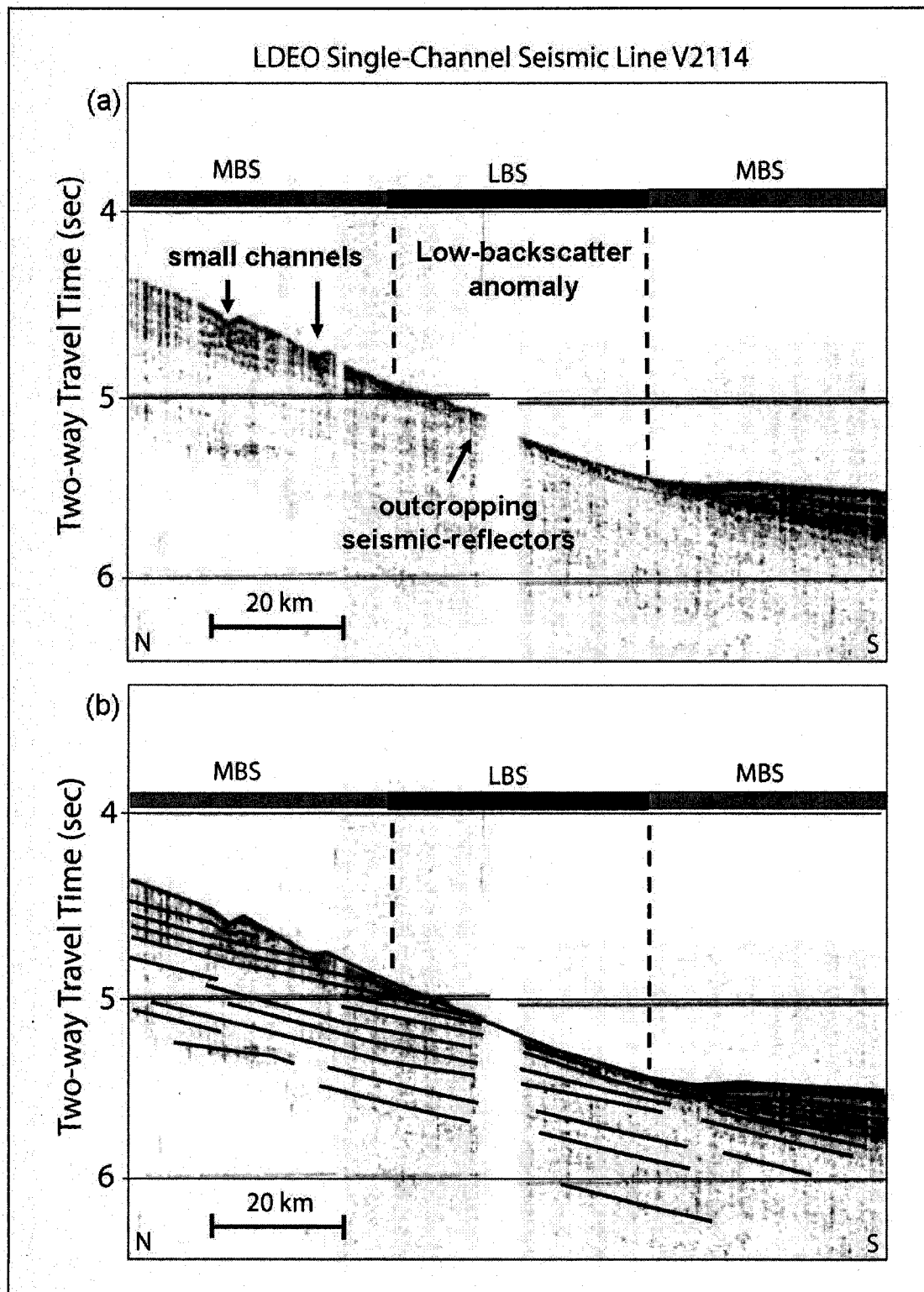


Figure 4.8 (a) Section of LDEO airgun seismic reflection profile showing outcropping seismic reflectors within the low-backscatter anomaly. (b) Interpreted seismic reflector horizons. Seafloor shown in red and subbottom reflectors shown in blue (reflectors not interpreted across data gap).

The most likely cause of eroded seafloor within the low-backscatter anomaly is the WBUC. As previously discussed, the sediment drift and scouring at the base of Knauss Knoll suggests the presence of the WBUC near the low-backscatter anomaly. Data collected in the SYNOP and HEBBLE experiments recorded average bottom speeds of approximately 6 cm/s at 3500 and 4128 m water depths (Richardson et al., 1981; Pickart and Watts, 1990; Shay et al., 1995). In addition, these studies measured events up to 28.5 cm/s on the Nova Scotian margin at 4128 m water depth and 40 cm/s at 3500 m water depth offshore the Grand Banks (Richardson et al., 1981, Shay et al., 1995). Schneider et al. (1967) also interpreted evidence of southwest currents east of the 3600-m isobath in an area corresponding to the location of the low-backscatter anomaly from bottom photographs (Figure 4.4).

Sediment cores from near the low-backscatter anomaly that were analyzed for this study show that average grain sizes of sediments in the top 1 to 2 m are in the fine silt to fine sand range (average grain size = 7.8 to 3.7Φ or 0.004 to 0.076 mm). The Heezen and Hollister (1964) diagram (Figure 4.7) indicates that flow speeds of approximately 4 cm/s are necessary to erode unconsolidated clays and silts and currents in the range of 20 to 300 cm/s are necessary to erode consolidated clay to silt sediments. These relatively fast current speeds are required to erode consolidated silts and clays because of the cohesive properties of clay-rich sediment (McCave, 1982).

The critical thresholds for erosion indicated by the Heezen and Hollister (1964) diagram suggest that unconsolidated sediments and possibly cohesive sediments within the average grain-size range of 7.8 to 3.7Φ or 0.004 to 0.076 mm

could be eroded either by the average flow of the WBUC (~6 cm/s at the depth of the low-backscatter anomaly or more likely by events of intense bottom-current speeds (up to 40 cm/s). Previous studies have recorded erosion of silt and clay sediments due to WBUC flow on the Nova Scotian continental rise (Richardson and Gardner, 1985). Using particle concentrations of suspended sediment from the HEBBLE study area, Richardson and Gardner (1985) concluded that currents at an average rate of 9 cm/s had resuspended sediments with a grain-size mode of 8 μm (~7 phi). This suggests that sediments within the low-backscatter anomaly could have been removed under similar flow conditions if sediments had been compositionally similar to those found on the Nova Scotian rise.

Erosion of surface sediments within the low-backscatter anomaly may have also been enhanced by the local morphology of the continental margin. The bathymetry data show that the low-backscatter anomaly is located at the toe of the relatively steep (0.7°) seafloor. Erosion could have been caused by the onlapping of the stronger section of the WBUC onto the steeper slope. The onlap may have been induced by a slight bend in the margin isobaths (Figure 4.9). The orientation of Krause Drift on the northeast side of Knauss Knoll suggests that the direction of the WBUC has been slightly oblique to the orientation of the bathymetric contours near the low-backscatter anomaly (Figure 4.9). This angle between the steeper slope and the approach direction of the WBUC may have increased sediment erosion.

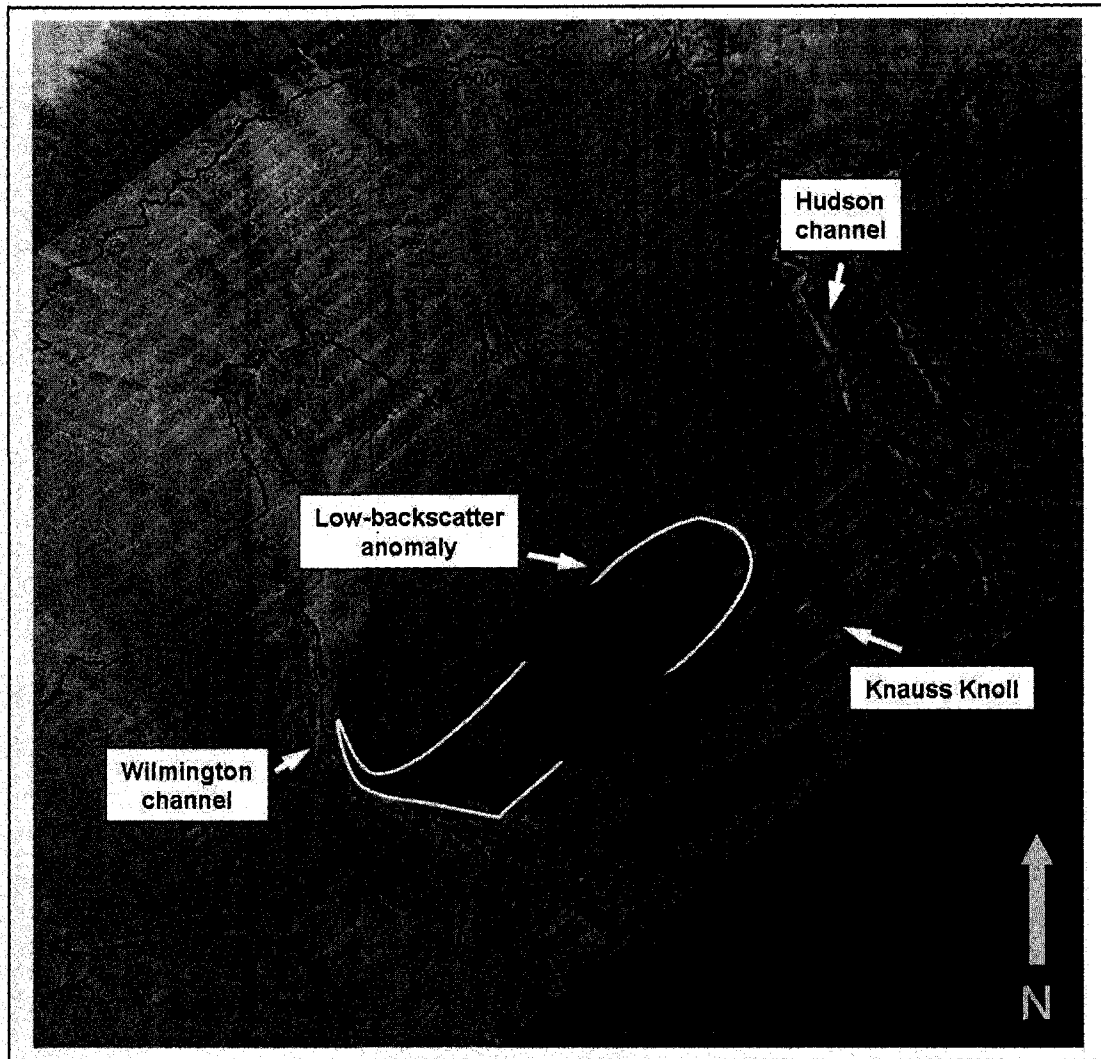


Figure 4.9 Map view of backscatter data showing the direction of the WBUC (as interpreted from the orientation of Krause Drift) relative to the bathymetric contours. Low-backscatter anomaly outlined by white line.

Another possibility is that the low-backscatter anomaly could have been caused by erosion that occurred when the WBUC had greater speeds at shallower depths. Studies have shown that the position of the high-velocity core of the WBUC has varied over the last 25,000 yr (Bulfinch et al., 1982). Sediment grain size and magnetic alignment in mineral grains found in sediment cores collected along the New Jersey margin indicate that the upper boundary of the high-velocity core of the

WBUC currently resides at 4440 +/- 20 m water depth and extends out to water depths of approximately 5200 m (Bulfinch et al., 1982). However, these sediment-core data also show that the high-velocity core of the WBUC was shallower between 17 to 7 ka (Ledbetter and Balsam, 1985). During this interval, the core of the WBUC moved up to 4000 m water depth (Ledbetter and Balsam, 1985).

Erosion of sediments could have occurred during the time period between 17 to 7 ka when the high-velocity axis of the WBUC resided at shallower depths. The high-velocity axis depth of 4000 m interpreted by Ledbetter and Balsam (1985) corresponds to the location of the low-backscatter anomaly and the outcropping sediment reflectors shown on the seismic-reflection profiles.

An outcrop exposed from this or previous erosion episodes could have been preserved due to sediment bypassing. Mountain and Tucholke (1985) have suggested that sediment accumulation from the Late Pliocene through the Quaternary has been minimal in the region of the continental margin where the low-backscatter anomaly is located. In addition, Locker (1989) concluded that the area corresponding to the low-backscatter anomaly has been a bypass zone for sediment gravity flows. This was thought to have been due to the relatively steep slopes of the local seafloor (Locker, 1989) and confinement of sediment gravity flows within Hudson and Wilmington channels (Locker, 1989; Schlee and Robb, 1991).

Funneling and confinement of sediment that has traveled downslope across the upper rise could have been one cause for sediment bypassing. Schlee and Robb (1991) identified funnel-shaped areas above channel convergences in 6.5-kHz GLORIA sidescan-sonar data. These regions were referred to as "gather areas". The

section of seafloor at the base of the New Jersey continental slope where continental slope canyons funnel into the Wilmington channel was named the Baltimore-Toms gather area (Schlee and Robb, 1991).

Multibeam bathymetry data analyzed for this study further suggest that downslope sediment flows have been funneled into Hudson and Wilmington channels across most of the New Jersey margin through the gather areas. The section of continental slope between Baltimore and McMaster Canyons is approximately 220 km across (Figure 4.10). The funnel shape of the Baltimore-Toms gather area upslope from Wilmington channel suggests that sediment gravity flows from the continental slope converge into Wilmington channel (Figure 4.11). A smaller, 50-km wide gather area above Hudson channel also suggests that downslope transport of sediment that has traversed from continental slope canyons has been funneled through the Hudson channel (Figure 4.12). Together, these gather areas cover approximately 85% of the margin upslope from the low-backscatter anomaly between Baltimore and McMaster Canyons.

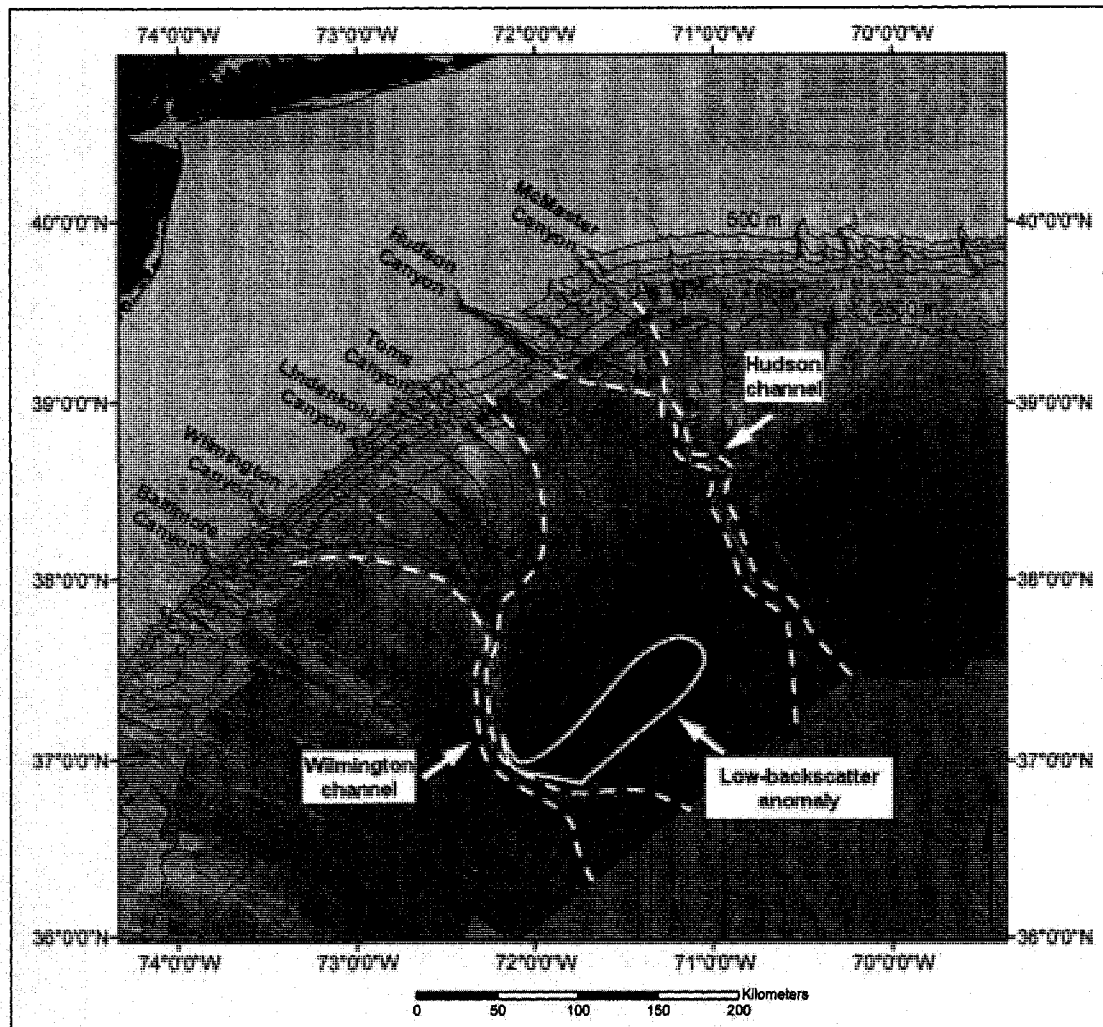


Figure 4.10 Map view of backscatter data showing the inferred downslope sediment transport paths through Hudson and Wilmington channels. Low-backscatter anomaly outlined in white solid line. Transport paths shown in white dashed line.

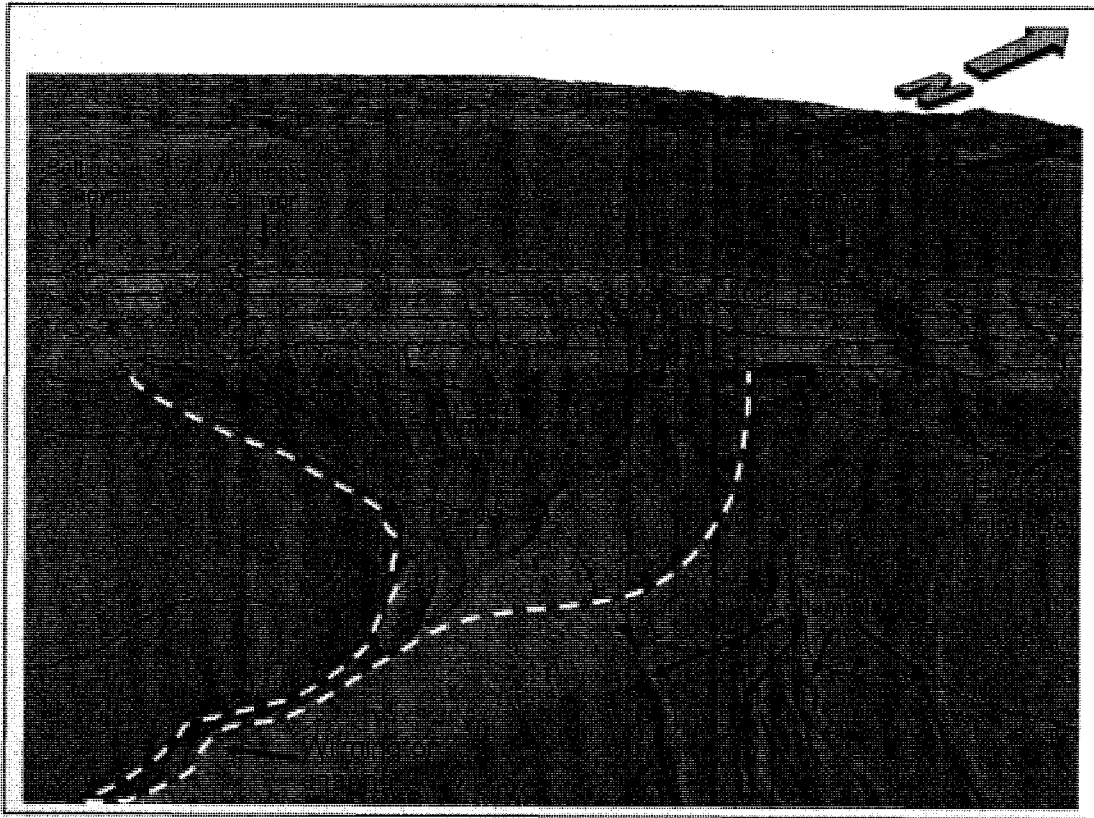


Figure 4.11 Perspective view (looking upslope and landward) of bathymetry data (gray sun-illuminated hillshade) showing location of the Baltimore-Toms gather area (outlined by white-dashed line). VE=10x

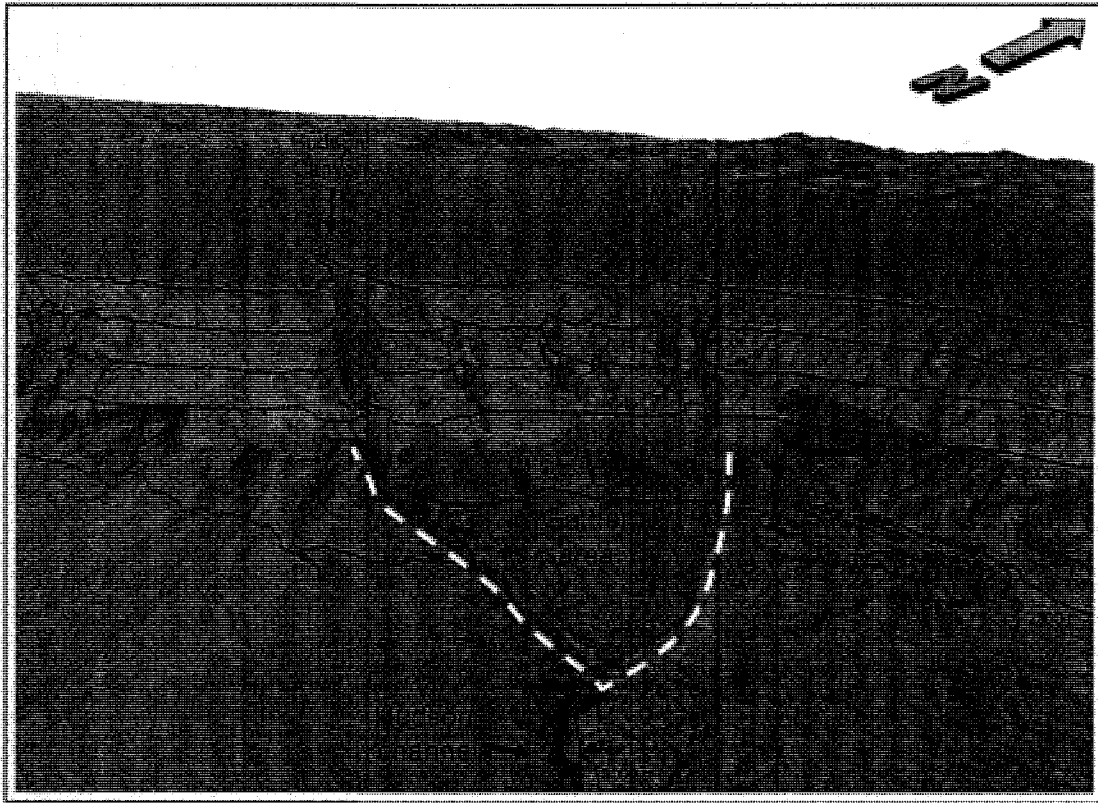


Figure 4.12 Perspective view (looking upslope and landward) of bathymetry data (gray sun-illuminated hillshade) gather area funneling into Hudson channel (outlined by white-dashed line). VE=10x

Schlee and Robb (1991) suggested that the lack of fan morphology on the continental rise beyond the gather areas indicates that Hudson and Wilmington channels have acted as “pass-throughs” for sediment. The surface and subbottom data analyzed for this study also show a lack of features that resemble submarine fans between the 3000 to 4000 m isobaths. This suggests that flows have remained mainly confined within channels in this seafloor section.

The multibeam sonar backscatter data suggest the presence of depositional lobes beyond the 4000 m isobath. The fan-shaped, mottled backscatter features shown at the terminus of both Hudson and Wilmington channels suggests evidence for

dispersal of sediment flows that have traveled through these channels (Figure 4.13 and Figure 4.14). These depositional lobes correspond to the change in seafloor gradient from 0.7° to 0.2° near the 4000 m isobath and to a decrease in channel incision depth from 300 to < 75 m in Wilmington channel and from 500 to < 100 m in Hudson channel. The lack of confinement suggests lateral dispersion and deposition of sediments. The locations of these features suggest that downslope flows have remained mainly confined within the channels until reaching beyond the 4000 m isobath and have bypassed the low-backscatter anomaly.

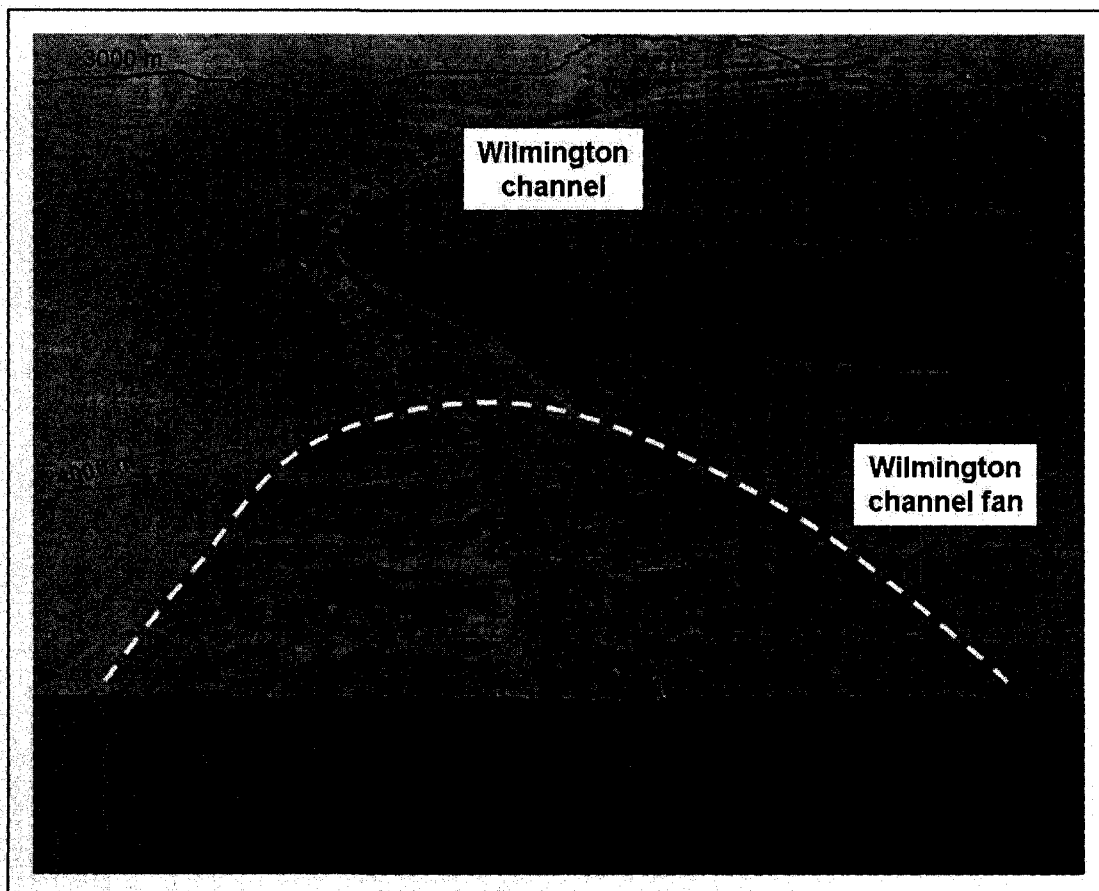


Figure 4.13 Perspective view (looking upslope and landward) of backscatter data draped over bathymetry showing the Wilmington channel fan. VE=10x

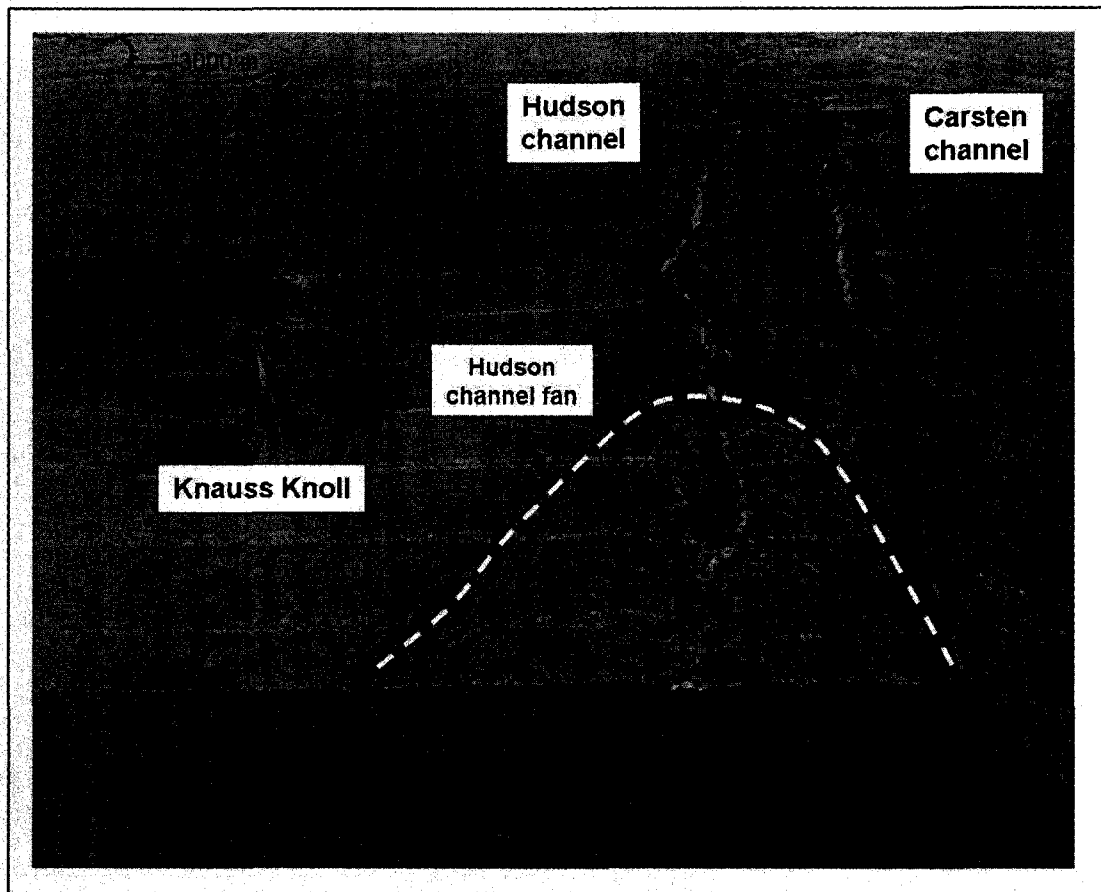


Figure 4.14 Perspective view (looking upslope and landward) of backscatter data draped over bathymetry showing the Hudson channel fan. VE=10x

Chirp seismic-reflection profiles HH', II', JJ' and KK' collected downslope from the low-backscatter anomaly (Figure 3.30 and Figure 3.31) show significantly stronger bottom returns than profiles AA', BB', CC' and DD' collected upslope from the low-backscatter anomaly (Figure 3.26 and Figure 3.27). The strong bottom returns east of the low-backscatter anomaly shown by chirp seismic-reflection profiles suggest that coarser sediments have been deposited in this seafloor section rather than on steeper seafloor section upslope from the low-backscatter anomaly. This coarsening of sediments in the seaward direction also suggests downslope sediment transport around the low-backscatter anomaly. These coarser sediments may have

originated from turbidity currents expelled through the small channels or material expelled from the terminus of Hudson channel that has been transported and deposited to the southwest. Airgun seismic-reflection profile V2114 suggests that these coarser deposits have onlapped onto the area corresponding to the low-backscatter anomaly, as previously interpreted by Mountain (1987), and are most likely younger deposits.

Downslope transport of sediment may have also been inhibited by the gentle slope gradients upslope from the low-backscatter anomaly. Hummocky bathymetry with mottled backscatter texture and high-backscatter-strength seafloor is found between the 2500 m to 3000 m isobaths where slope gradients are low (0.2°). Cores and bottom photographs collected at Ocean Drilling Project (ODP) Site 905 (Figure 4.15 and Figure 4.16) show extensive evidence of mass-wasting within this seafloor area (Shipboard Party, 1994; McHugh et al., 2002). Water-gun and 3.5-kHz seismic-reflection profiles show an acoustically transparent section and hummocky reflectors overlying a well-stratified stratigraphic unit near the surface section (up to 0.2 s below the seafloor) suggesting debris-flow deposits (Shipboard Party, 1994). Video of the seafloor also show large, detached blocks with fractured, coherent strata (Shipboard Party, 1994), which suggests that extensive downslope sediment-failure deposits have occurred.

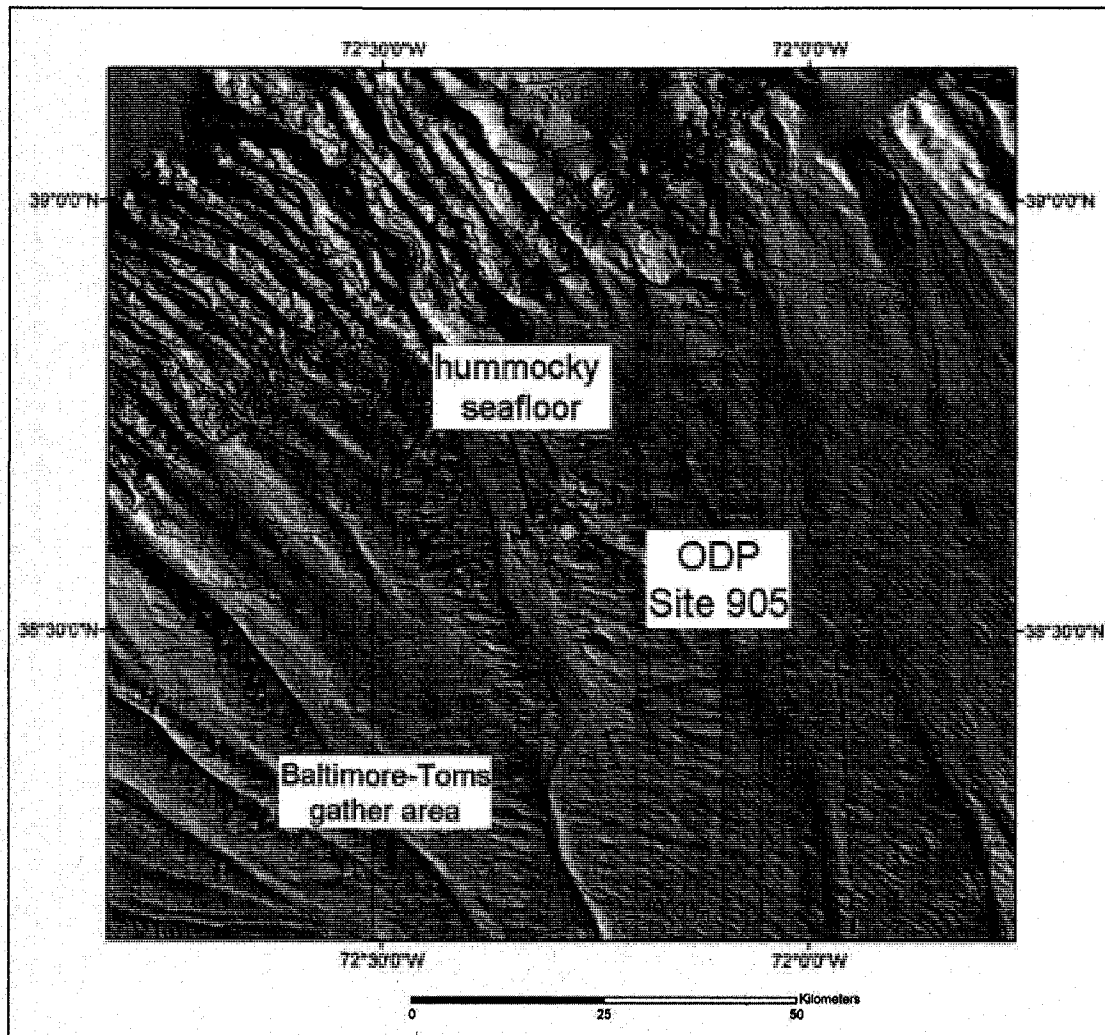


Figure 4.15 Bathymetry data (gray sun-illuminated hillshade) showing location of ODP Site 905. Baltimore-Toms gather area outlined by black dashed line.

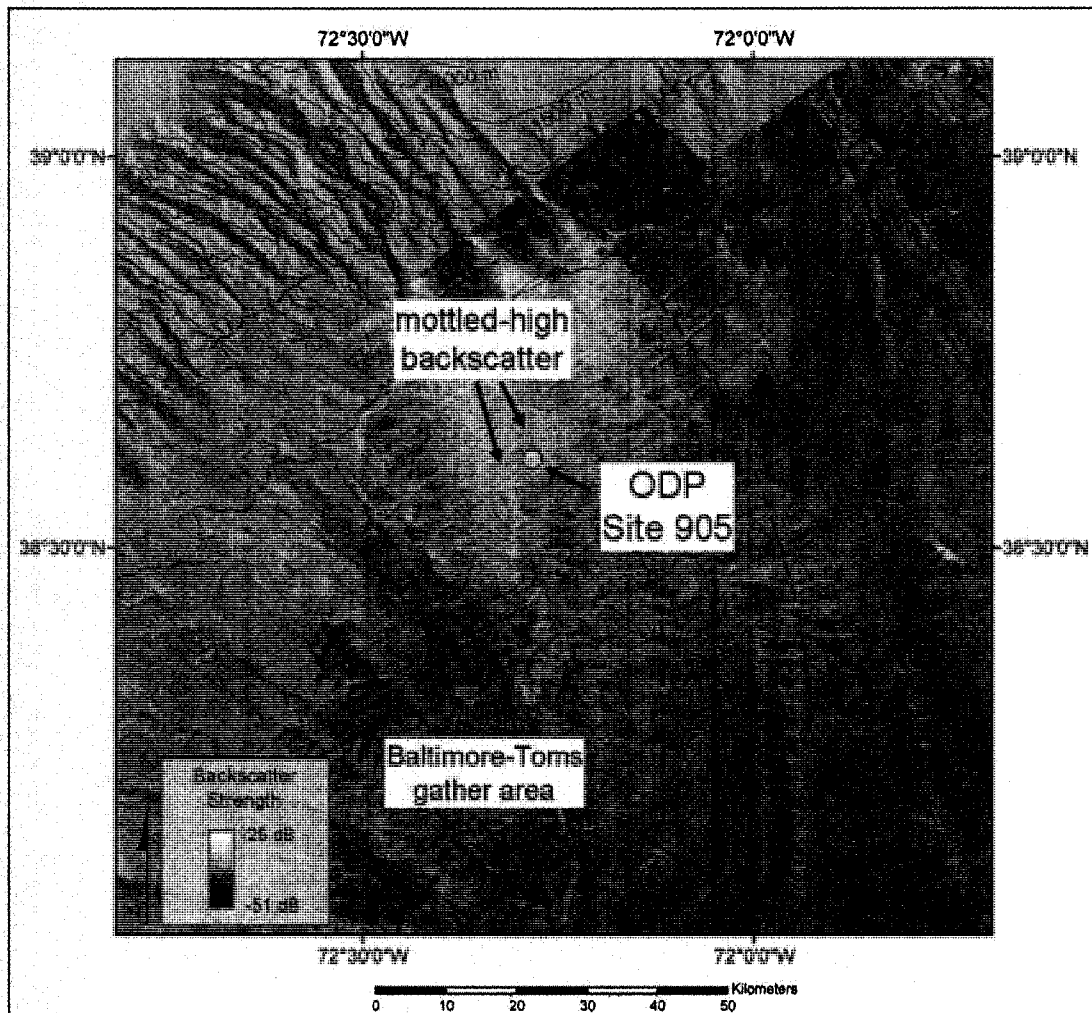


Figure 4.16 Map showing location of ODP Site 905 with MBES backscatter data as backdrop. Baltimore-Toms gather area outlined by black dashed line. Bathymetric contours shown in 500-m intervals.

Homogenous backscatter texture is found on the relatively steeply (0.7°) dipping seafloor downslope from the gentle slope gradients with hummocky bathymetry and mottled, high-backscatter strength seafloor. Chirp profiles AA', BB', CC', and DD' from steeply dipping region show well-stratified, conformable subbottom reflectors and good penetration in this region (Figure 3.26 and Figure

3.27). These data suggest an absence of debris-flow deposits, slumps and slides and that sediment deposition has been predominantly hemipelagic drape, as previously suggested by Schlee and Robb (1991).

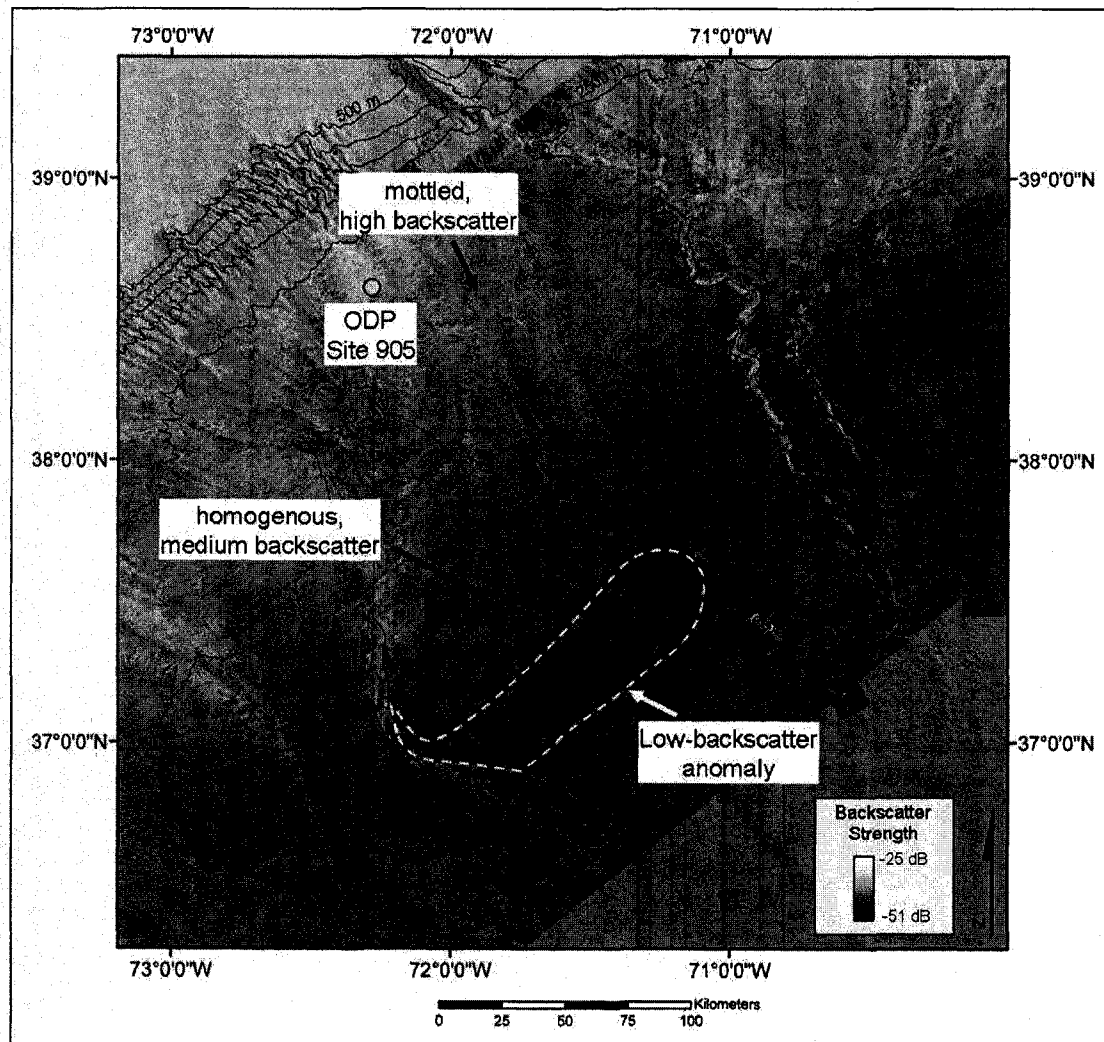


Figure 4.17 Map of backscatter data showing region of homogenous backscatter on the relatively steep (0.7°) seafloor. Low-backscatter anomaly outlined by white-dashed line. Bathymetric contours are shown at 500-m intervals.

This distribution of mass-flow deposits on the New Jersey margin suggests that the low-backscatter anomaly has remained mostly protected from sediment

introduced by mass-flows to this region that originated upslope on the steeper continental slope. The shielding could have preserved the outcrop that had been previously been exposed by WBUC erosion or could have prevented substantial sediment deposition through time.

The data also suggest that not all sediment that has traveled downslope across the margin has bypassed through Hudson and Wilmington channels or been shielded by the shallow slope gradients found upslope from the low-backscatter anomaly. The small channels shown by the bathymetry data provide evidence that sediments have crossed the gentle gradients (0.2°) and reached the low-backscatter anomaly by suspended gravity-sediment flows such as turbidity currents (Figure 4.2). However, absence of well-defined fan morphology at the termini of the small channels suggests that these sediments could have been redirected by an intensified WBUC without significant deposition or may have bypassed the low-backscatter area due to the steeper slope gradients (0.7°) and been deposited on the section of flatter (0.2°) seafloor downslope from the 4000-m isobath.

As previously discussed under hypothesis 1, the decrease in backscatter strength could be caused by relatively smooth seafloor (less than 12 cm peak-to-peak seafloor relief) as compared to the surrounding areas. The smoother seafloor could be due to the influence of bottom currents, whereby seabed features may have been smoothed or unable to form under the current speeds found within the low-backscatter anomaly. Sediments within the outcrop could also have a lower acoustic impedance contrast at the seabed and/or fewer sediment inhomogeneities in the upper few meters of the sediment column due to higher water content or lower sediment

density within the low-backscatter anomaly in comparison to the surrounding areas. Higher water content within the sediments may result from a change in sediment porosity or could be related to water seepage along stratigraphic horizons that outcrop within the low-backscatter anomaly. The lack of sediment inhomogeneities could be caused by an absence of coarser sediment layers such as turbidites or contourites within exposed sediment strata. The absence of these layers may have resulted from a decreased input of sediment gravity flows or from weaker/deeper bottom currents during the time that sediments were deposited.

4.1.3 Hypothesis 3 – Presence of Sediment Gas

A third hypothesis is that sub-surface gas has caused the low-backscatter anomaly. Previous studies have suggested the presence of a large gas reservoir on the New Jersey margin (Tucholke et al., 1977; Tucholke and Mountain, 1986; Mountain, 1987; Dillon et al., 1995). Tucholke and Mountain (1986) and Mountain (1987) suggested that the gas reservoir has formed as the result of rapid burial of organic material in sediments derived from a shelf delta during the Miocene. These sediments were thought to have formed the feature referred to as the Chesapeake Drift by Mountain and Tucholke (1985), part of which underlies the seafloor region immediately upslope from the low-backscatter anomaly (Figure 4.18). Dillon et al. (1995) also mapped a region thought to contain gas-hydrate on the New Jersey margin.

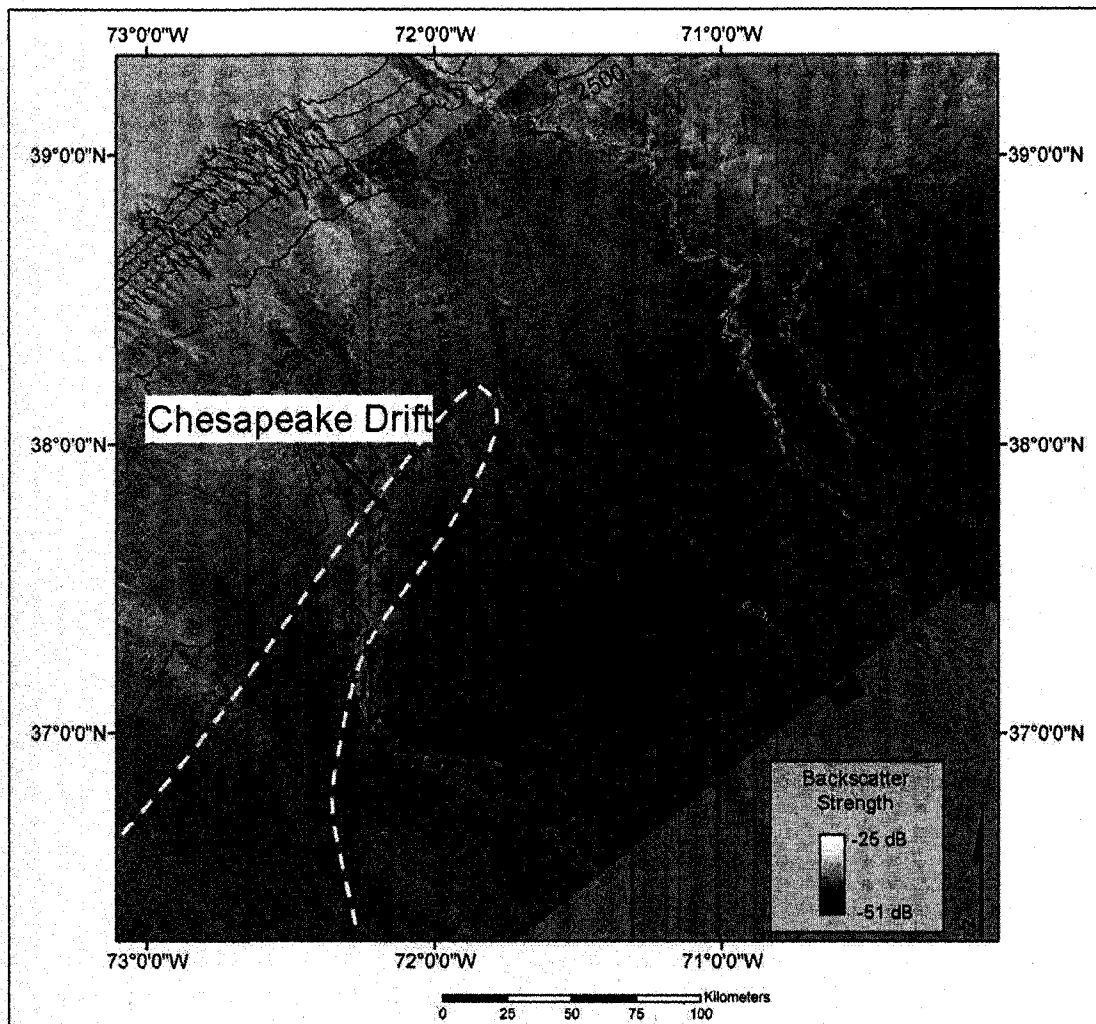


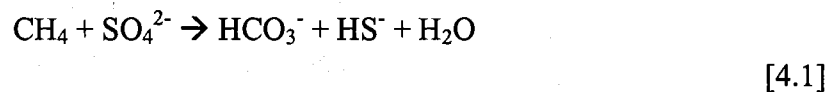
Figure 4.18 Map showing the approximate location of the buried Chesapeake Drift (outlined by white dashed lines) as identified by Tucholke and Mountain (1986) and Pratson and Laine (1989) with respect to MBES backscatter data.

The bottom-simulating reflector (BSR) shown by LDEO seismic-reflection line V2114 (Figure 3.33) suggests the presence of sub-surface gas and gas hydrate on the New Jersey margin (Tucholke et al., 1977). The BSR is thought to be an acoustic surface generated by the phase boundary between free gas and gas-hydrate-charged sediments (Hovland and Judd, 1988; Kvenvolden, 2000). The interface is caused by

fast sound speed in gas-hydrate rich sediment and slow sound speed in the underlying sediment containing free gas (Kvenvolden, 2000).

The seismic stratigraphy within the low-backscatter anomaly also suggests the presence of sub-surface gas. High-resolution 3.5-kHz seismic-reflection profiles EE', FF' and GG' (Figure 3.28 and Figure 3.29) and LDEO airgun seismic-reflection profile V2114 (Figure 3.33) indicate weakly stratified acoustic reflectors within the low-backscatter anomaly. The absence of seismic reflectors could be the result of "gas-blanking," whereby the presence of sediment gas causes subsurface reflector horizons to be masked. Many observations of gas-blanking have been associated with gas-hydrate accumulations (Dillon and Max, 2000).

Authigenic carbonate nodules found in core EN101-PC01 also suggest the presence of methane in the sediments. Authigenic carbonates have been found in seafloor environments such as gas seeps where fluids are enriched in methane (Bohrmann and Torres, 2006) and in known gas-hydrate zones such as Hydrate Ridge on the Cascadia margin (Bohrmann et al., 1998; Bohrmann and Torres, 2006). One of the processes that can form authigenic carbonate is anaerobic oxidation of methane (AOM) by methane oxidation and sulfate reduction (Boetius et al. 2000; Bohrmann and Torres, 2006). The net reaction is given by Boetius et al. (2000) as:



This reaction occurs when upward migrating methane (CH_4) and downward diffusing sulfate (SO_4^{2-}) are consumed to form bicarbonate (HCO_3^-), bisulfide (HS^-) and water

(Ussler and Paull, 2008). The high concentrations of bicarbonate in the sediment pore waters can then bind calcium ions to precipitate carbonate.

The bathymetric depressions shown in the bathymetry data (Figure 4.19) within the small channels and within the mottled section of the low-backscatter anomaly downslope from the small channels also could suggest the presence of gas sapping or pockmarks. Butman et al. (2006) previously interpreted that pore-water or gas discharge formed these bathymetric depressions. Hovland and Judd (1988) indicated that pockmarks can form as the result of fluid and gas escape from seafloor sediments. As fluid and gas ascends to the seafloor, these materials fluidize the sediments and eject them into the water column (Hovland and Judd, 1988). Suspended sediments from the pockmarks could have been removed by currents or transported downslope through the small channels. The bathymetric depressions found within the small channels may suggest evidence of pockmark strings. Chains of pockmarks have been recorded previously in the Norwegian Trench (Hovland and Judd, 1988). These Norwegian Trench strings of pockmarks extend for several hundreds of meters in a line. The depressions within the channels may be larger analogues to these features found in the Norwegian Trench.

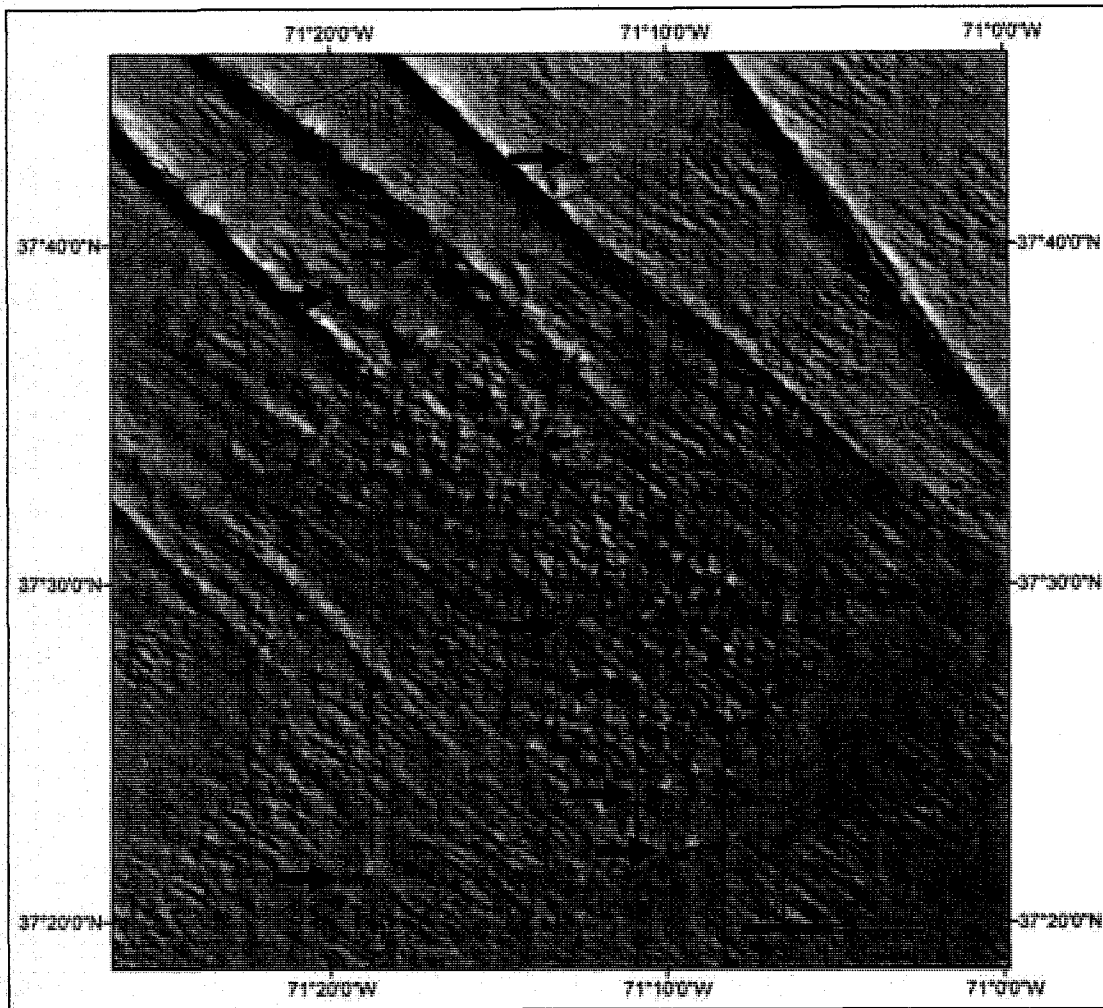


Figure 4.19 Bathymetry data (gray sun-illuminated hillshade) showing bathymetric depressions (several indicated by arrows) within and downslope from small channels that may result from gas and fluid escape. Hillshade illumination from the southwest. Contours shown in meters.

The presence of these features suggests a regional existence of sub-surface gas and gas seepage near the low-backscatter anomaly. This could suggest that sediments at the seabed within the bounds of the low-backscatter anomaly contain greater quantities of sub-surface gas than the surrounding regions. This change in gas-saturation could result in the low-backscatter response of this area of seafloor.

4.2 Medium-Backscatter Bridge

A geological interpretation for the medium-backscatter bridge (Figure 4.20) is presented in this section. Previous interpretations have suggested a mass flow deposit in the area corresponding to the medium-backscatter bridge (Embley and Jacobi, 1986; Pratson and Laine, 1989). High-resolution 3.5-kHz chirp seismic-reflection profiles analyzed for this study support these interpretations and show a sequence of sub-surface reflectors that suggest the debris-flow originated from slope failure on the eastern flank of a sediment ridge immediately upslope from the medium-backscatter bridge. Sediment core EN101-PC01, which was collected from the medium-backscatter bridge, suggests that successive turbidites formed the medium-backscatter bridge feature.

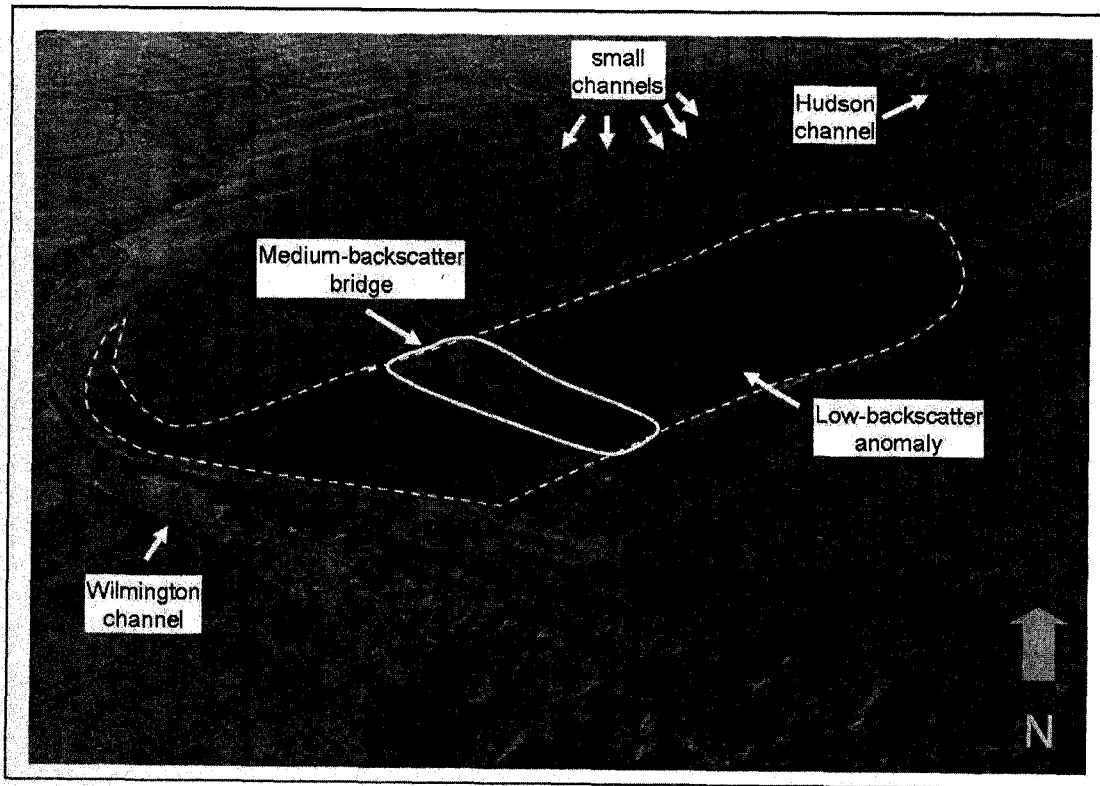


Figure 4.20 Perspective view (looking north) showing medium-backscatter bridge outlined by solid white line, the low-backscatter anomaly outlined in white-dashed line and other nearby bathymetric features.

4.2.1 Turbidite Deposit

Stratigraphic analysis of core EN101-PC01 (Figure 4.21) suggests that the medium-backscatter bridge is a deposit formed by several turbidity currents. Consecutive coarse grain size layers shown by laser-diffraction particle-size analysis (Figure 4.22) give evidence that episodic deposition of coarser-grained sediment has occurred at the location of the medium-backscatter bridge. The episodic discrete changes in average grain size in core EN101-PC01 suggest the occurrence of fine-grained turbidites. Sections of several of the coarse-grain layers (T_1 and T_2) show normal sediment grading, which is typically found in deep-sea turbidites (Shanmugam, 2000). Although physical observations do not show clear evidence of

Bouma Sequences (Figure 4.22), these data show some of the stratigraphic features found within the fine-grained turbidite model proposed by Stow and Shanmugam (1980). The thin, convolute laminations found underlying normal-graded sediment that contains a silt lens could be the bottom and middle sections of the fine-grain turbidite model. The convolute laminations were identified by increases in grain size and higher quartz component than the overlying layers.

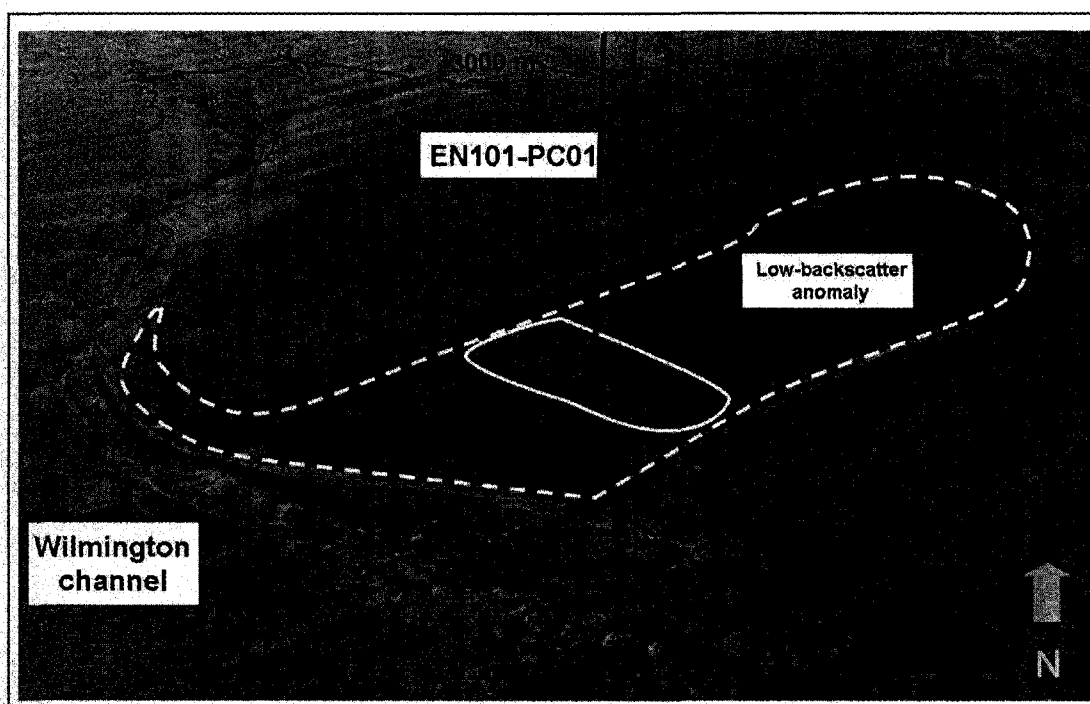


Figure 4.21 Perspective view (looking north) showing the location of core EN101-PC01 with respect to the medium-backscatter bridge (outlined in red).

In addition, some of the coarse grain size layers have a high (>25%) quartz component in smear slide samples compared to the composition of the background (non-turbidite) sediments (Figure 4.23). This change in composition suggests that a

discrete change in sediment input, which could be a result of deposition of turbidity current material.

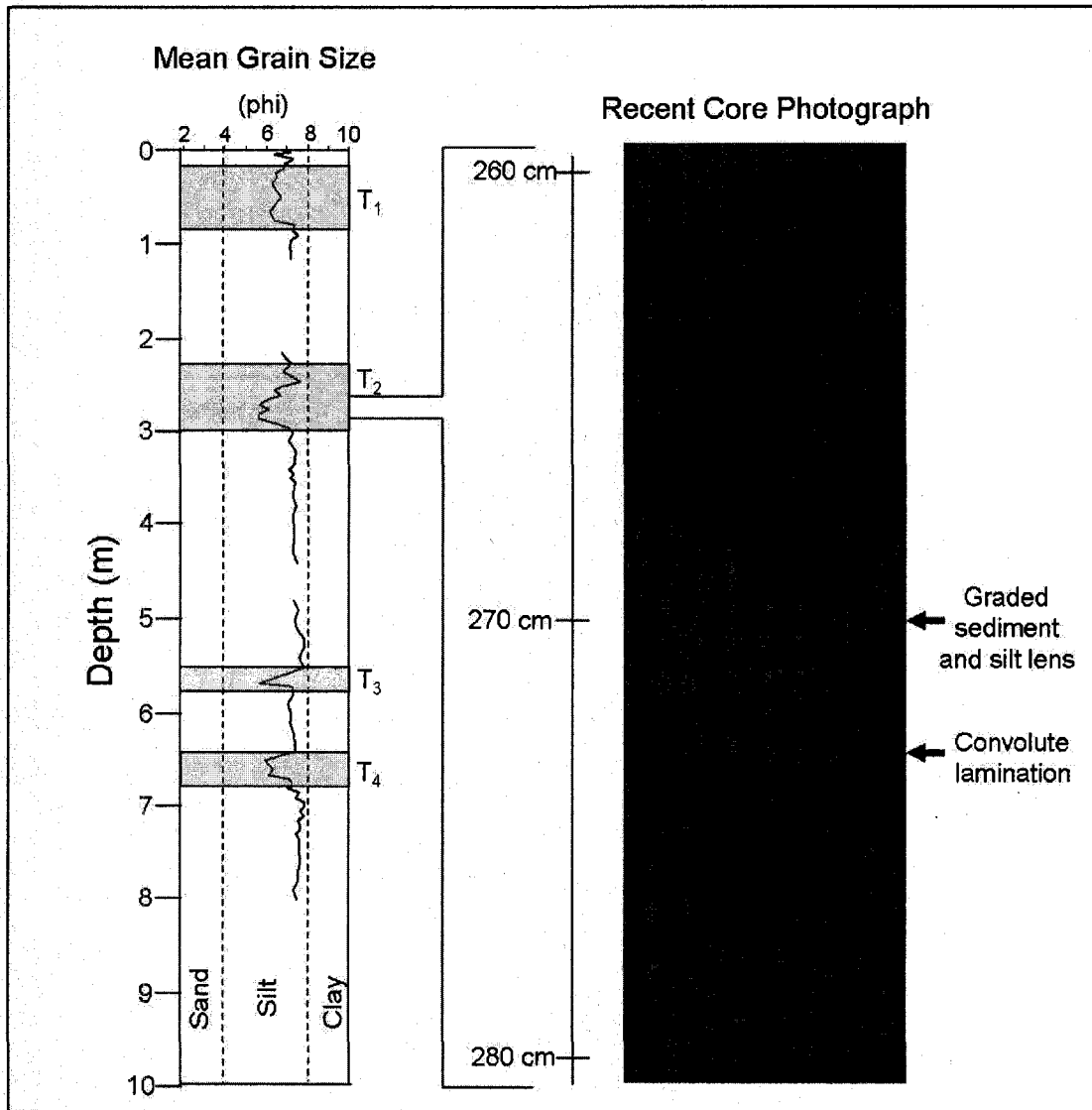


Figure 4.22 Image showing photograph of section of a possible fine-grained turbidite sequence (260 to 280 cm) within sediment core EN101-PC01. Turbidites highlighted by blue boxes on mean grain size plot.

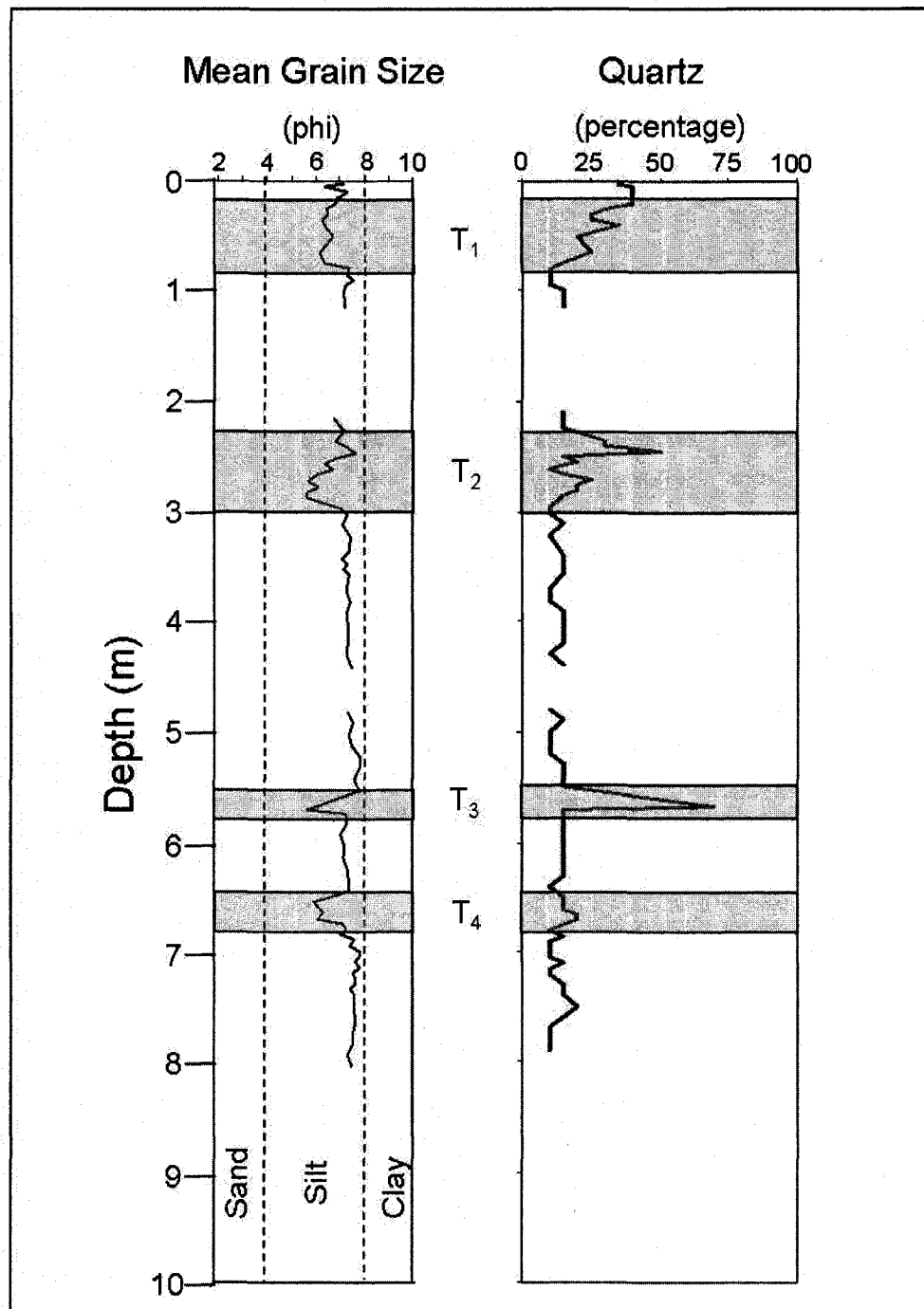


Figure 4.23 Comparison of grain-size analysis with quartz compositions estimated from smear slide analysis.

4.2.2 Debris-Flow Deposit

Although stratigraphic analyses of core EN101-PC01 shows the presence of turbidite layers, there is not a clear correlation with chirp sonar records that suggest the medium-backscatter bridge is a turbidity current deposit. The sequence of the acoustically transparent, lens-shaped features beneath the medium-backscatter bridge and the amphitheater-shaped and v-shaped sub-surface reflectors shown by chirp sonar data upslope from the medium-backscatter bridge suggests that the medium-backscatter bridge is a debris-flow deposit (Figure 4.24). Embley and Jacobi (1986) interpreted similar lens-shaped masses of acoustically incoherent sub-surface in 3.5-kHz subbottom records as debris-flow deposits.

The debris flow likely initiated upslope from the medium-backscatter bridge near profile AA'. The amphitheater-shaped feature shown in profile BB' suggests that non-deformational sediment failure such as a slide or a slump may have initially caused the sediment-gravity flow. The acoustically transparent lens found in profiles CC', DD, and EE' suggests that the sediment failure may have induced or transformed into a debris flow.

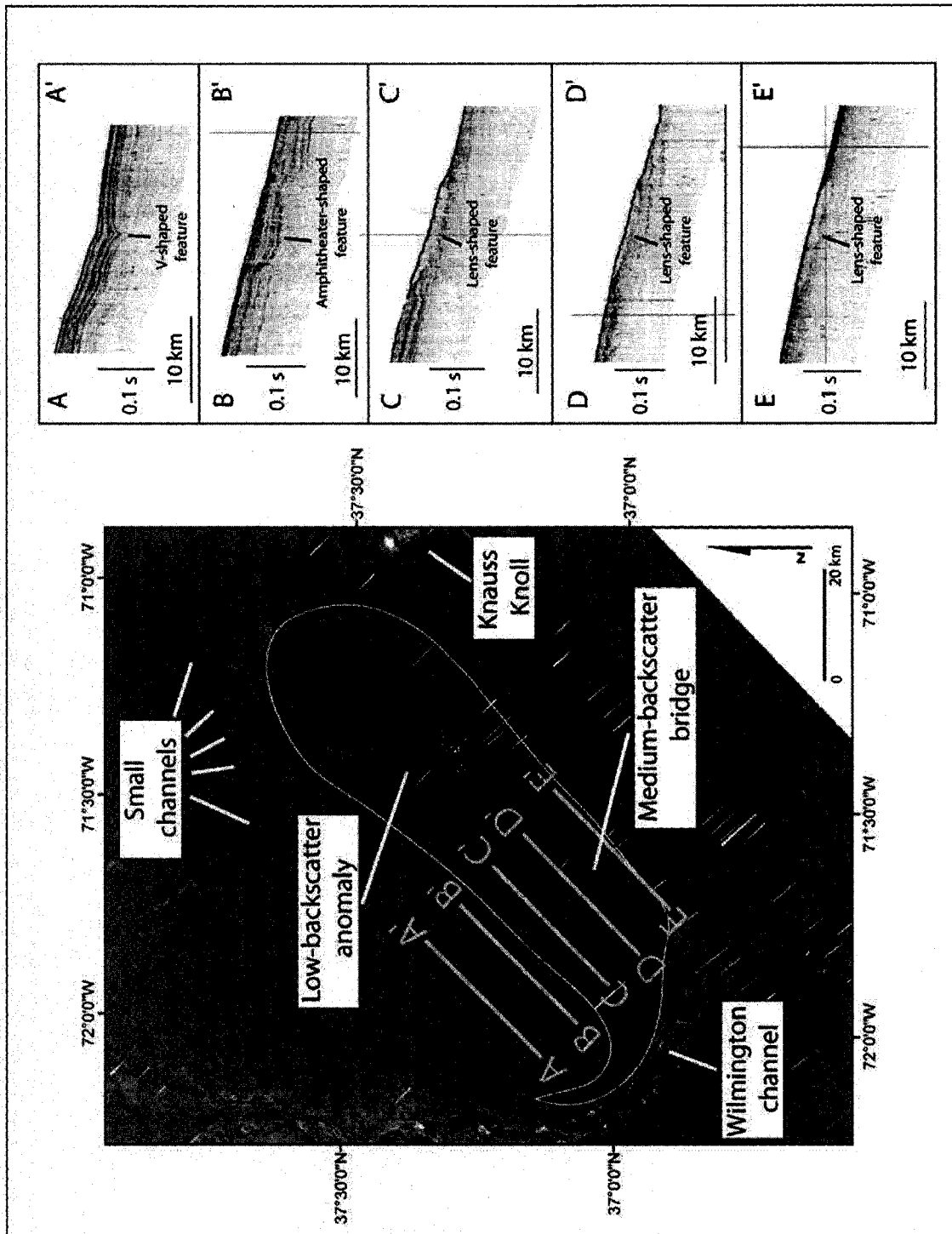


Figure 4.24 Backscatter data and consecutive 3.5-kHz chirp profiles showing medium backscatter bridge. Medium-backscatter bridge outlined in red and low-backscatter anomaly outlined in white. Seismic-reflection profile vertical exaggeration = 65x

4.2.3 Triggering Mechanisms

One of the causes for the sediment failure that formed the medium-backscatter bridge could have been oversteepening due to toe removal at the base of the relatively steep ($\sim 0.7^\circ$) seafloor. As previously discussed, the presence of the WBUC and truncated sediment reflectors shown by chirp seismic-reflection profiles that cross the low-backscatter anomaly suggest that sediment erosion may have occurred in the region corresponding to the low-backscatter anomaly. Sediment removal caused by the WBUC could have caused slope instability of the seafloor and resulted in the mass-wasting event that formed the medium-backscatter bridge.

The debris flow or sequence of turbidity currents that formed the medium-backscatter bridge across the low-backscatter anomaly could have also been initiated by another larger slide that occurred upslope from the medium-backscatter bridge. The medium-backscatter bridge aligns with the downslope axis of the large lobe of high-backscatter located to the northwest of Wilmington channel (Figure 4.25). Previous studies by Embley and Jacobi (1986) have mapped a slide complex made up of a number of coalescing blocky slides and debris-flow deposits that correspond to this high-backscatter feature. An impact between one of the slides that form this complex and the sediment ridge located on the southeast side of Wilmington channel could have triggered the sediment failure on the seaward side of the ridge.

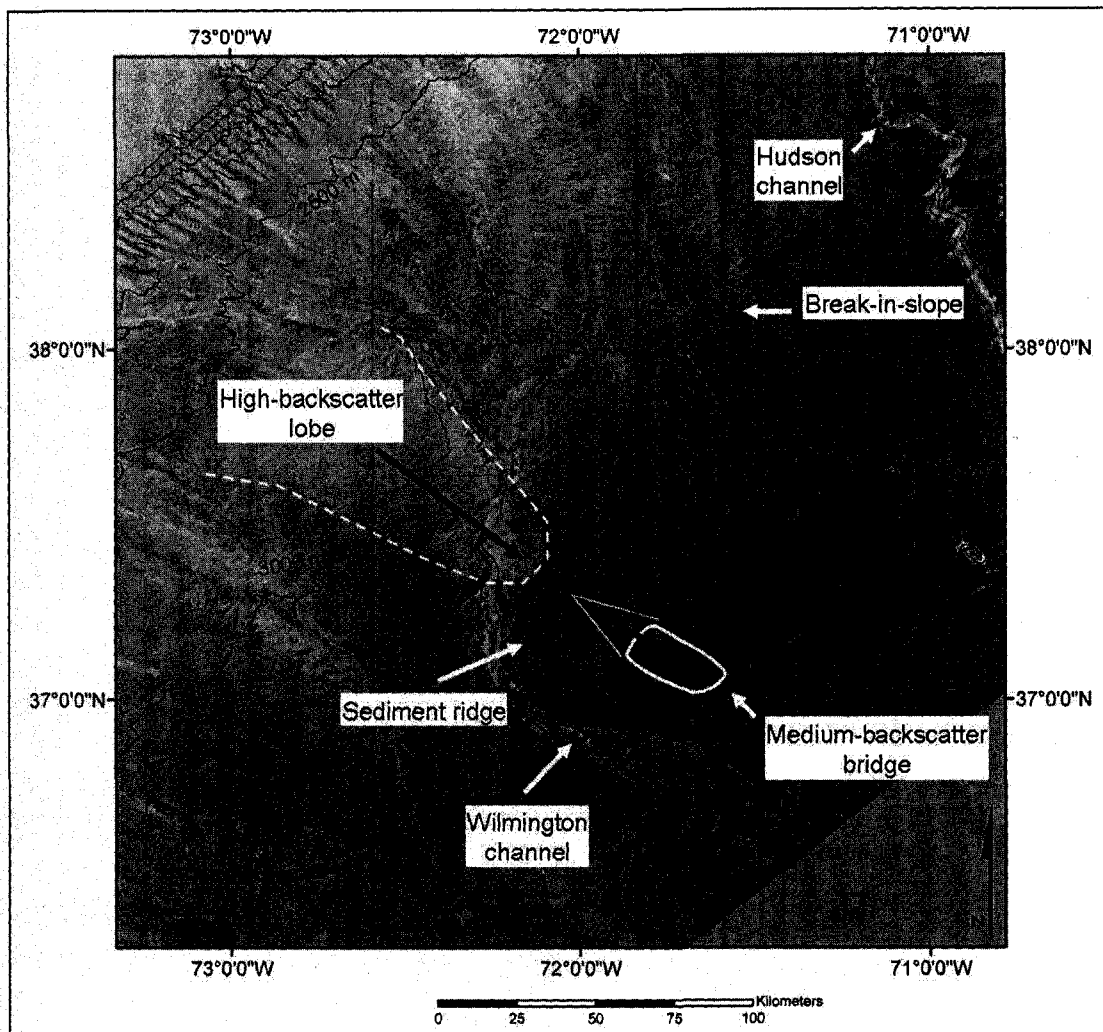


Figure 4.25 Map view showing interpretation of upslope slide complex (high-backscatter lobe) mapped by Embley and Jacobi (1986) as possible cause of medium-backscatter bridge.

4.2.4 Core EN101-PC01 Sediment Ages

A study by Stapleton (1987) measured the physical properties of sediment in core EN101-PC01 that was collected in the medium-backscatter bridge and found that the sediments are overconsolidated. These data and 3.5-kHz seismic-reflection profiles led Stapleton (1987) to conclude that 10 to 20 m of overburden sediment had been removed by erosion from the seafloor region near core EN101-PC01. If 10 to 20

m of sediment were removed, extrapolated sedimentation rates of ~ 7 to 11 cm kyr^{-1} found in this study and in previous studies (Embley, 1980) suggest that sediments at the top of core EN101-PC01 would be older than 70 kyr in age. However, calibrated radiocarbon ages from the top of core EN101-PC01 show that sediments from within the medium-backscatter bridge across the low-backscatter anomaly are younger than 6 kyr. Linear extrapolations using sedimentation rates from radiocarbon ages show that only 40 to 70 cm of sediment has been removed from the sediment core top, as opposed to 10 to 20 m found by Stapleton (1987). This indicates a disagreement between the radiocarbon dates found in this study and conclusions by Stapleton (1987).

Radiocarbon dating suggests that very little (40 to 70 cm) sediment has been removed from the seafloor where the core was collected. The 40 to 70 cm of sediment missing from the top of core EN101-PC01 could have been lost during piston coring, as explained by Ross and Riedel (1967) instead of by sediment erosion. Although these data do not suggest erosion of surface sediments in core EN101-PC01 and the medium-backscatter bridge, the radiocarbon age constraints do not clearly dismiss the hypothesis suggesting sediment erosion has caused the low-backscatter anomaly. Erosion likely occurred prior to the debris flow.

CHAPTER 5

CONCLUSIONS AND RECOMMENDATIONS

5.1 Conclusions

Multibeam sonar backscatter data collected in 2004 and 2005 along the U.S. Atlantic continental margin show an anomalous low-backscatter feature on the New Jersey continental margin. This feature had not been clearly mapped in previous seafloor studies. Without ground-truth data collected from within the low-backscatter anomaly, it is impossible to determine the exact composition and nature of sediment strata responsible for the anomalously low backscatter strength at this location. However, three possible geological explanations have been presented using interpretations of the data analyzed for this study.

1) The low-backscatter anomaly could be caused by a sediment deposit composed of sediment supplied by several nearby small channels. Sediment suspended by turbidity currents that have traveled down-slope through the channels have been transported to the southwest by the Western Boundary Undercurrent. These sediments have been deposited across the seafloor corresponding to the low-backscatter anomaly.

2) The low-backscatter anomaly is an outcrop of older sediment strata that has resulted from surface sediment erosion and/or non-deposition. Sediment removal has likely resulted from an intensification of the WBUC due to the local seafloor

bathymetry or was caused by a shallowed and stronger WBUC high-velocity core. Additionally, sediments that traveled down-slope across the margin bypassed the anomalous area through Wilmington and Hudson channels. The gentle slope gradients on the upper continental rise further shielded sediments to this area by stopping sediments traversing the margin as gravity-driven flows. Sediments that traveled down-slope could have also bypassed the region due to the relatively steeper seafloor gradients and presence of the WBUC.

3) The presence of gas in the sub-surface sediments has caused a low-backscatter response from this seafloor region.

Bottom photographs collected during a study by Schneider et al. (1967) at 3400 m and 4200 m depths near the low-backscatter anomaly suggest that speeds of the WBUC are capable of suspended sediment transport. However, it is difficult to interpret from the available current-meter and grain-size data whether conditions within the low-backscatter anomaly have more likely caused deposition or erosion. The Heezen and Hollister (1964) diagram (Figure 4.7) suggests that average current speeds (~ 6 cm/s) found in other areas of the margin at similar depths as the low-backscatter anomaly would likely create sediment transport or erosion conditions as opposed to sediment deposition within the range of grain sizes observed in sediment cores collected nearby the anomaly. Other studies (Tucholke and McCave, 1986) have suggested that deposition of fine-grain sediment can occur at current speeds less than 15 cm/s, which was observed during the HEBBLE study (McCave, 1985). Interpretation is further complicated by the broad range of current speeds (from

tranquil up to 78 cm/s) that have been measured for the WBUC and by cohesive strength of fine-grain sediments.

However, the outcropping reflectors shown by the chirp sonar data and airgun seismic-reflection profiles from the low-backscatter anomaly strongly suggest that erosion has occurred within the low-backscatter anomaly as opposed to sediment deposition. A feature that might suggest the low-backscatter anomaly is a depositional lobe cannot be identified either in the chirp sonar seismic-reflection data or in the MBES bathymetry data.

In addition, it is not clear that the turbidity current and contour current processes described under hypothesis 1 could form a sediment deposit that is homogenous in sediment composition within the penetration limits of the MBES and GLORIA sidescan sonar. Although it is likely that both processes could occur simultaneously, turbidity currents and contour currents are both episodic in nature. As a result, deposition that originates from these mechanisms would likely produce a sediment profile that is inhomogeneous in sediment composition.

Therefore, although the sediment transport and subsequent deposition processes described under hypothesis 1 are plausible explanations for the origins of the low-backscatter anomaly, the seafloor data examined for this study suggest that hypothesis 2 is a more likely explanation for the low-backscatter anomaly than is hypothesis 1.

It is also not clear from the data analyzed for this study that the presence of sub-surface gas can fully explain the presence of the low-backscatter anomaly. The bathymetric depressions that resemble pockmarks are found in the northeast section

of the low-backscatter anomaly, but not in the section nearer to Wilmington channel. These features would likely be ubiquitous throughout the anomaly if high amounts of sediment gas were present throughout the feature.

The acoustically transparent lens shown by chirp sonar data suggests that the medium-backscatter bridge across the low-backscatter anomaly is likely formed by a debris-flow deposit. Although sediment core EN101-PC01 shows the presence of several turbidite layers, it is difficult to envision that these layers have resulted in the medium-backscatter bridge feature. The stratigraphy shown by core EN101-PC01 represents a small (~8 cm diameter) section of the seafloor, whereas the several chirp sonar profiles that image the subbottom structure across and upslope from the medium-backscatter bridge provide a more regional view. This debris-flow likely occurred as a single catastrophic event induced by oversteeping due to WBUC erosion or was triggered by a slide or earthquake that occurred upslope. This event likely occurred after the formation of the low-backscatter anomaly.

5.2 Recommendations for Future Work

This research shows the presence of a low-backscatter anomaly on the New Jersey continental margin and indicates an excellent opportunity for future research. The primary recommendation for the “next step” would be to collect sediment cores within the low-backscatter anomaly preserving the surface sediments (gravity core, box core and/or multicore), along with a sample attaining several meters of penetration (piston core).

The seafloor sediment type and near-surface lithostratigraphy could be found by conducting grain-size analysis and smear-slide analysis on samples from sediment cores. Investigations of these samples could help to address the geology of the seafloor within the low-backscatter anomaly. These results could be compared to results of this thesis research to determine if there is a change in the composition of near-surface sediment stratigraphy within and outside of the low-backscatter anomaly.

Measurements on the physical properties of the sediment such as porosity, saturated bulk density, and sound speed could be used to address the geacoustic cause of the decreased backscatter strength. Some of these measurements have previously been conducted on sediment core EN101-PC01 by Stapleton (1987). The geacoustic analysis on a sediment core collected within the low-backscatter anomaly could be used for comparison of acoustic stratigraphy within and outside of the anomalous feature to evaluate possible acoustic reasons for the change in backscatter strength.

Geological explanations of the low-backscatter anomaly presented as hypotheses for this thesis research could be further investigated by this sediment core analysis. AMS-radiocarbon dating of planktonic foraminifera sampled from a core from the low-backscatter anomaly could be used to determine age constraints for the seafloor sediments. This would help to determine whether the anomaly is an exposed section of older sediments or composed of recently deposited material. Sediments could also be measured for gas content to determine if sediments are saturated in gas. These data could be compared to other seafloor samples collected outside of the

backscatter anomaly to resolve whether the low-backscatter return represents a significantly different sediment facies type from the surrounding seafloor.

In addition to a sediment core, bottom photography or videography would be recommended to address bottom roughness and the presence/intensity of the WBUC within the low-backscatter anomaly. Photographs could provide visual evidence for sediment transport in this area.

A long-term current-meter array across the low-backscatter anomaly could further resolve whether there is a change in WBUC speeds in this region. Measurements collected near the seafloor could be used to determine if this area corresponds to the landward limit of the high-velocity flow of the WBUC core.

A comparative study is also recommended to help understand the anomalously low-backscatter seafloor found on the New Jersey margin. Backscatter data show a region of seafloor on the Blake Bahama Outer Ridge (BBOR) that may be analogous to the low-backscatter anomaly offshore New Jersey. An area of low-backscatter strength (~ 45 dB) occurs near the coordinates 75° W and 30° (Figure 5.1). Unlike the New Jersey margin low-backscatter anomaly, this low-backscatter zone has been sampled by previous studies (Deep Sea Drilling Leg 11 and Woods Hole Oceanographic Institute research cruise KNR140). Analysis of these data could provide further clues to understanding the causes of the low-backscatter anomaly on the New Jersey margin.

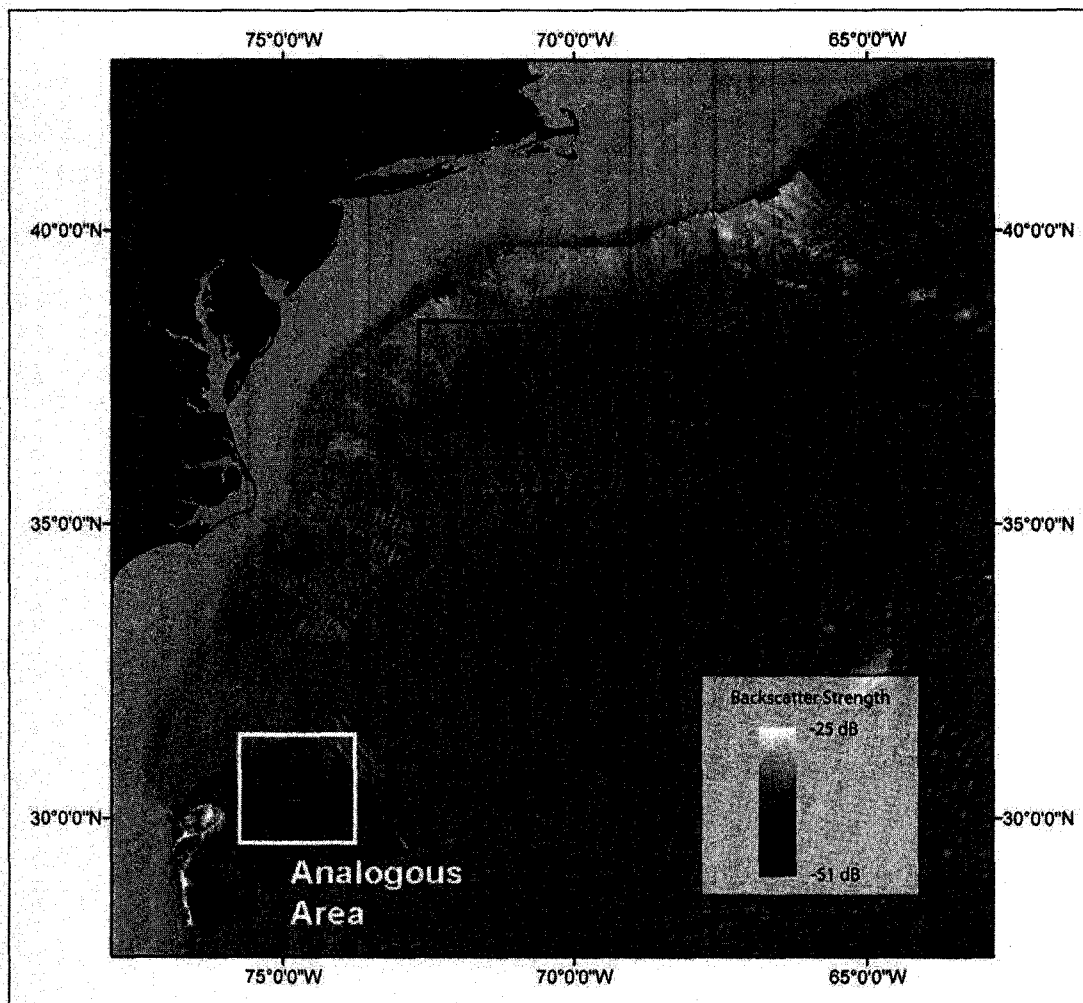


Figure 5.1 Map showing location of the low-backscatter area on the Blake Bahama Outer Ridge.

REFERENCES

- Anderson, A.L. and Hampton, L.D., 1980, Acoustics of gas-bearing sediments. I. Background: *Journal of the Acoustical Society of America*, v. 67, p. 1865 – 1889.
- Ayers, M.W. and Cleary, W.J., 1980, Wilmington fan: mid-Atlantic lower rise development: *Journal of Sedimentary Petrology*, v. 50, p. 235-245.
- Bé, A.W.H., 1977, An ecological, zoogeographic and taxonomic review of recent planktonic foraminifera, in Ramsay, A. T. S., ed., *Oceanic Micropalaeontology*, Volume 1 and 2, Acad. Press, London, 100 pp.
- Borhmann, G., Greinert, J., Suess, E. and Torres, M., 1998, Authigenic carbonates from the Cascadia subduction zone and their relation to gas hydrate stability: *Geology*, v. 26, p. 647-650.
- Borhmann, G. and Torres, M.E., 2006, Gas Hydrates in Marine Sediments, in, Schulz, Horst D. and Zabel, Matthias, eds., *Marine Geochemistry*: Springer Berlin Heidelberg, New York, p. 481-512.
- Bouma, A.H., 1962, *Sedimentology of Some Flysch Deposits: A Graphic Approach to Facies Interpretation*. Elsevier, Amsterdam. 168 pp.
- Bulfinch, D.L., Ledbetter, M.T., Ellwood, Brooks B., and Balsam, William L., 1982, The High-Velocity Core of the Western Boundary Undercurrent at the Base of the U.S. Continental Rise: *Science*, v. 215, p. 970-973.
- Bulfinch, D.L. and Ledbetter, M.T., 1984, Deep Western Boundary Undercurrent Delineated by Sediment Texture at the Base of the North Atlantic Continental Rise: *Geo-Marine Letters*, v. 3, p. 31-36.
- Butman, B., Twitchell, D.C., Rona, P.A., Tucholke, B.E., Middleton, T.J. and Robb, J.M., 2006, Seafloor Topography and Backscatter Intensity of the Hudson Canyon Region Offshore New York and New Jersey, U.S. Geological Survey Open File Report 2004-1441.
- Cartwright, D. and Gardner, J.V., 2005, U.S. Law of the Sea cruise to map the foot of the slope and 2500-m isobath of the Northeast US Atlantic continental margin: Legs 4 and 5. Center for Coastal & Ocean Mapping/Joint Hydrographic Center Rept. 27 pp.
- Chaytor, J.D., Twitchell, D.C., Ten Brink, U.S., Buczkowski, B.J. and Andrews, B.D., 2007, Revisiting Submarine Mass Movements along the U.S. Atlantic

- Continental Margin: Implications for the Tsunami Hazards, *in* Lykousis, V., Sakellariou, D. and Locat, J., eds., *Submarine Mass Movements and Their Consequences*, p. 395-403.
- Clennell, M.B., Judd, A. and Hovland, M., 2000, Movement and Accumulation of Methane in Marine Sediments: Relation to Gas Hydrate, *in* Max, Michael D., ed., *Natural Gas Hydrate in Oceanic and Permafrost Environments*: Kluwer Academic Publishers, Boston, p. 105-122.
- Damuth, J.E., 1980, Use of High-Frequency (3.5-12 kHz) Echograms in the Study of Near-Bottom Sedimentation Processes in the Deep-Sea: A Review: *Marine Geology*, v. 38, p. 51-75.
- de Moustier, C. and Alexandrou, D., 1991, Angular dependence of 12-kHz seafloor acoustic backscatter: *The Journal of the Acoustical Society of America*, v. 90, p. 522-531.
- Dietz, R., 1963, Collapsing Continental Rises: An Actualistic Concept of Geosynclines and Mountain Building: *Journal of Geology*, v. 71, p. 314-333.
- Dillon, W.P., Fehlhaber, K., Coleman, D.F., Lee, M.W. and Hutchinson, D.R., 1995, Maps Showing Gas-Hydrate Distribution off the East Coast of the United States: U.S. Geological Survey Miscellaneous Field Studies Map MF-2268.
- Dillon, W.P. and Max, M.D., 2000, The U.S. Atlantic Continental Margin; the Best-Known Gas Hydrate Locality, *in* Max, M.D., ed., *Natural Gas Hydrate in Oceanic and Permafrost Environments*. Kluwer Academic Publishers, Netherlands, p. 157-170.
- Driscoll, M.L., Tucholke, B.E. and McCave, I.N., 1985, Seafloor Zonation in Sediment Texture on the Nova Scotian Lower Continental Rise, *in* Nowell, A.R.M. and Hollister, C.D., eds., *Deep Ocean Sediment Transport – Preliminary Results of the High Energy Benthic Boundary Layer Experiment*: *Marine Geology*, v. 66, p.25-41.
- Embley, R.W., 1980, The Role of Mass Transport in the Distribution and Character of Deep-Ocean Sediments with Special Reference to the North Atlantic: *Marine Geology*, v. 38, p. 23-50.
- Embley, R.M. and Jacobi, R., 1986, Mass wasting in the western North Atlantic, *in* Vogt, P.R. and Tucholke, B.E., eds., *The Geology of North America, Volume M, The Western North Atlantic Region*: Geological Society of America.
- Emery, K.O., Uchupi, E., Phillips, J.D., Bowin, C.O., Bunce, E.T., and Knott, S.T., 1970, Continental Rise off Eastern North America: *The American Association for Petroleum Geologists Bulletin*: v. 54, p. 44-103.

- Farre, J.A., McGregor, B.A., Ryan, W.B.F. and Robb, J.M., 1983, Breaching the Shelfbreak: Passage from youthful to mature phase submarine canyon evolution, *in* Stanley, D.J. and Moore, G.T., eds., *The shelfbreak: Critical interface on continental margins*: Society of Economic Paleontologists and Mineralogists Special Publication 33, p. 25-39.
- Flood, R.D., 1983, Classification of sedimentary furrows and a model for furrow initiation and evolution: *Geological Society of America Bulletin*, v. 94, p. 630-639.
- Fonseca, L., Mayer, L., Orange, D., and Driscoll, N., 2002, The high-frequency backscattering angular response of gassy sediments: Model/data comparison from the Eel River Margin, California: *Journal of the Acoustical Society of America*, v. 111, p. 2621-2631.
- Fonseca, L. and Calder, B., 2005, Geocoder: An efficient backscatter map constructor: U.S. Hydrographic Conference, San Diego, CA, March 29-31, Conference Proceeding.
- Fonseca, L. and Mayer, L., 2007, Remote estimation of surficial seafloor properties through the application Angular Range Analysis to multibeam sonar data: *Marine Geophysical Research*, v. 28, p. 119-126.
- Fulthorpe, C.S., Mountain, G.S., and Miller, K.G., 1996, Mapping Neogene Depositional Geometries, New Jersey Continental Slope, Leg 150 Drilling Area, *in* Mountain, G.S., Miller, K.G., Blum, P., Poag, C.W. and Twitchell, D.C. (eds.), 1996 *Proc. ODP. Sci. Results*, 150: College Station, TX (Ocean Drilling Program). p 269-281.
- Fulthorpe, C.S., Austin Jr., J.A. and Mountain, G.S., 2000, Morphology and distribution of Miocene slope incisions off New Jersey: Are they diagnostic of sequence boundaries?: *Geological Society of America Bulletin*, v. 112, p. 817-828.
- Gardner, J.V., 2004, U.S. Law of the Sea cruise to map the foot of the slope and 2500-m isobath of the Northeast US Atlantic continental margin CRUISES H04-1, 2 and 3. Center for Coastal & Ocean Mapping/Joint Hydrographic Center Rept. 61 p.
- Gardner, J.V., Field, M.E., Lee, H., Edwards, B.E., Masson, D.G., Kenyon, N., and Kidd, R.B., 1991, Ground-Truthing 6.5-kHz Sidescan Sonar Sonographs: What Are We Really Imaging?: *Journal of Geophysical Research*, v. 96, p. 5955-5974.
- Gardner, J.V., Mayer, L.A. and Armstrong, A., 2006, Mapping Supports Potential Submission to U.N. Law of the Sea: *Eos Transactions AGU*, v. 87, p. 157, 160.
- Hamilton, E.L., 1956, Low Sound Velocities in High-Porosity Sediments: *The Journal of the Acoustical Society of America*, v. 28, p. 16-19.

- Hamilton, E.L., 1970, Reflection Coefficients and Bottom Losses at Normal Incidence Computed from Pacific Sediment Properties: *Geophysics*, v. 35, p. 995-1004.
- Hamilton, E.L., 1972, Compressional Wave Attenuation in Marine Sediments: *Geophysics*, v. 37, p. 620-646.
- Heezen, B.C. and Ewing, M., 1952, Turbidity Currents and Submarine Slumps, and the 1929 Grand Banks Earthquake: *American Journal of Science*, v. 250, p. 849-873.
- Heezen, B.C. and Hollister, C., 1964, Deep-Sea Current Evidence from Abyssal Sediments: *Marine Geology*, v. 1, p. 141-174.
- Heezen, B.C., Hollister, C., Ruddiman, W.F., 1966, Shaping of the Continental Rise by Deep Geostrophic Contour Currents: *Science*, v. 152, no. 3721, p. 502-508.
- Hollister, C.D. and Heezen, B.C., 1972, Geological effects of ocean bottom currents: western North Atlantic, in Gordon, A.L., ed., *Studies in Physical Oceanography*, v.2. Gordon and Breach, New York, p.37-66.
- Hovland M. and Judd, A.G., 1988, *Seabed Pockmarks and Seepages: Impact on Geology, Biology and the Marine Environment*, Graham and Trotman Inc., London, 293 p.
- Jackson, D.R., Winebrenner, D.P. and Ishimaru, A., 1986, Application of the composite roughness model to high-frequency bottom backscattering: *The Journal of the Acoustical Society of America*, v. 79, p. 1410-1422.
- Kvenvolden, K.A., 2000, Natural Gas Hydrate: Introduction and History of Discovery, in Max, Michael D., ed., *Natural Gas Hydrate in Oceanic and Permafrost Environments*. Kluwer Academic Publishers, Boston, p. 9-16.
- Ledbetter, M.T., and Balsam, W.L., 1985, Paleooceanography of the Deep Western Boundary Undercurrent on the North American continental margin for the past 25 000 yr: *Geology*, v. 13, p. 181-184.
- Locker, S.D., 1989. Cenozoic Depositional History of the Middle U.S. Atlantic Continental Rise. Ph.D. Thesis, Univ. Rhode Island, Kingston, R.I., 180 pp.
- Locker, S.D. and Laine, E.P., 1992, Paleogene-Neogene depositional history of the middle U.S. Atlantic continental rise: mixed turbidite and contourite depositional systems: *Marine Geology*, v. 103, p. 137-164.
- Lowrie, A. and Heezen, B.C., 1967, Knoll and Sediment Drift Near Hudson Canyon: *Science*, v. 157, p.1552-1553.

- Mayer, L.A., Paton, C.W., Gee, L., Gardner, J.V., and Ware, C.W., 2000, Interactive 3-D Visualization: A tool for seafloor navigation, exploration, and engineering, *Proceedings of the IEEE Oceans*, Vol. 2., p. 913-920.
- Mazzullo, J.M. and Graham, A.G. (eds.), 1988, *Handbook for shipboard sedimentologists*. ODP Tech. Note, 8.
- McCave, I.N., Bryant, R.J., Cook, H.F. and Coughanowr, C.A., 1986, Evaluation of a laser-diffraction-size analyzer for use with natural sediments: *Journal of Sedimentary Petrology*, v. 56, p. 561-564.
- McCave, I.N. and Tucholke, B.E., 1986, Deep current-controlled sedimentation in the western North Atlantic, *in* Vogt, P.R. and Tucholke, B.E., eds., *The Geology of North America, Volume M, The Western North Atlantic Region*: Geological Society of America.
- McHugh, C.M.G., Damuth, J.E., and Mountain, G.S., 2002, Cenozoic mass-transport facies and their correlation with sea-level change, New Jersey continental margin: *Marine Geology*, v. 184, p. 295-334.
- McHugh, C.M.G. and Olson, H.C., 2002, Pleistocene chronology of continental margin sedimentation: New insights into traditional models, New Jersey: *Marine Geology*, v. 186, p.389-411.
- McMaster, R.L., Locker, S.D. and Laine E.P., 1989, The Early Neogene Continental Rise off the Eastern United States: *Marine Geology*, v. 87, p. 137-163.
- Mountain, G.S. and Tucholke, B.E., 1985, Mesozoic and Cenozoic Geology of the U.S. Atlantic Continental Slope and Rise, *in* Poag, C.W., ed., *Geologic Evolution of the United States Atlantic Margin*: Van Nostrand Reinhold, New York, p. 293-341.
- Mountain, G.S., 1987, Underway Geophysics during Leg 95, *in* Poag, C.W., Watts, A.B., et al., *Init. Repts. DSDP, 95*: Washington (U.S. Govt. Printing Office), p. 601-631.
- Mountain, G.S., Miller, K.G., Blum and Leg 150 Shipboard Scientific Party, 1994, *Proceedings of the Ocean Drilling Program, Initial reports, Volume 150*: College Station, Texas, Ocean Drilling Program, 885 p.
- Mountain, G.S., Burger, R.L., Delius, H., Fulthorpe, C.S., Austin, J.A., Goldberg, D.S., Steckler, M.S., McHugh, C.M., Miller, K.G., Monteverde, D.H., Orange, D.L. and Pratson, L.F., 2007, The long-term stratigraphic record on continental margins: *Special Publication of the International Association of Sedimentologists*, v. 37, p. 381-458.

Plastino, W., Kaihola, L., Bartolomei, P. and Bella, F., 2001, Cosmic Background Reduction In The Radiocarbon Measurement By Scintillation Spectrometry At The Underground Laboratory Of Gran Sasso: Radiocarbon, v. 43, p. 157-161.

Pilkey, O.H, and Cleary, W.J., 1986, Turbidite sedimentation in the northwestern Atlantic Ocean basin, *in* Vogt, P.R. and Tucholke, B.E., eds., The Geology of North America, Volume M, The Western North Atlantic Region: Geological Society of America.

Poag, C.W., 1985, Cenozoic and Upper Cretaceous Sedimentary Facies and Depositional Systems of the New Jersey Slope and Rise, *in* Poag, C.W., ed., Geological Evolution of the United States Atlantic Margin: Van Nostrand Reinhold Co., New York, p. 343-365.

Poag, C.W. and Mountain, G.S., 1987, Late Cretaceous and Cenozoic Evolution of the New Jersey Continental Slope and Upper Rise: An Integration of Borehole Data with Seismic Reflection Profiles, *in* Poag, C.W., Watts, A.B., et al., Init. Repts. DSDP, 95: Washington (U.S. Govt. Printing Office), p. 673-724.

Poag, C.W, 1992, U.S. Middle Atlantic Continental Rise: Provenance, Dispersal, and Deposition of Jurassic to Quaternary Sediments, *in* Poag, C. Wylie and de Graciansky, Pierre Charles, eds., Geological Evolution of Atlantic Continental Rises: Van Nostrand Reinhold Co., New York, p. 100-156.

Pratson, L.F. and Laine, E.P., 1989, The Relative Importance of Gravity-Induced versus Current-Controlled Sedimentation during the Quaternary along the Mideast U.S. Outer Continental Margin Revealed by 3.5 kHz Echo Character: Marine Geology, v. 89, p. 87-126.

Pratson, L.F. and Coakley, B.J., 1996, A model for headward erosion of submarine canyons induced by downslope-eroding sediment flows: Geological Society of America Bulletin, v. 108, p. 225-234.

Reimer, P.J., Baillie, M.G., Bard, E., Bayliss, A., Beck, J. W., Bertrand, C.J.H., Blackwell, P.G., Buck, C.E., Burr, G.S., Cutler, K.B., Damon, P.E., Edwards, R.L., Fairbanks, R.G., Friedrich, M., Guilderson, T.P., Hogg, A.G., Hughen, K.A., Kromer, B., McCormac, G., Manning, S., Manning, E., Ramsey, C.B., Reimer, R.W., Remmele, S., Southon, J.R., Stuiver, M., Talamo, S., Taylor, F.W., van der Plicht, J., Weyhenmeyer, C.E., 2004, INTCAL04 Terrestrial Radiocarbon Age Calibration, 0-26 Cal kyr BP: Radiocarbon, v. 46, p. 1029-1058.

Richardson, M.J., Wimbush, M., and Mayer, L., 1981, Exceptionally strong near-bottom flows on the continental rise of Nova Scotia: Science, v. 213, p. 887-888.

Richardson, M.J. and Gardner, W.D., 1985, Analysis of suspended-particle size distribution over the Nova Scotian Continental Rise, *in* Nowell, A.R.M. and Hollister,

C.D., eds., Deep Ocean Sediment Transport – Preliminary Results of the High Energy Benthic Boundary Layer Experiment: *Marine Geology*, v. 66, p.189-203.

Robb, J.M., Hampson, J.C. and Twitchell, D.C., 1981, Geomorphology and Sediment Stability of a Segment of the U.S. Continental Slope off New Jersey: *Science*, v. 211, p.935-937.

Rona, P.A., 1969, Middle Atlantic Continental Slope of United States: Deposition and Erosion: *The American Association of Petroleum Geologists Bulletin*, v. 53, no. 7, p. 1453-1465.

Rona, P.A. and Clay, C.S., 1967, Stratigraphy and Structure along a Continuous Seismic Reflection Profile from Cape Hatteras, North Carolina, to the Bermuda Rise: *Journal of Geophysical Research*, v. 72, no. 8, p. 2107-2130.

Schlee, J.S. and Robb, J.M., 1991, Submarine Processes of the middle Atlantic continental rise based on GLORIA imagery: *Geological Society of America Bulletin*, v. 103, p. 1090-1103.

Schneider, E.D., Fox, P.J., Hollister, C.D., Needham, H.D., and Heezen, B., 1967, Further Evidence of Contour Currents in the Western North Atlantic: *Earth and Planetary Science Letters*, v. 2, p. 351-359.

Shay, T.J., Bane, J.M., Watts, D.R. and Tracey, K.L., 1995, Gulf Stream flow field and events near 68°W: *Journal of Geophysical Research*, v. 100, p. 22,565-22,589.

Sperazza, M., Moore, J.N. and Hendrix, M.S., 2004, High-Resolution Particle Size Analysis of Naturally Occuring Very Fine-Grained Sediment Through Laser Diffractometry: *Journal of Sedimentary Research*, v. 74, p. 736-743.

Stapleton, D.C., 1987. Geotechnical properties of marine sediments from the Low Level Waste Disposal Project Study areas: Northwest Atlantic. M.S. Thesis, Univ. Rhode Island, Kingston, R.I., 252 pp.

Stow, D.A.V. and Holbrook, J.A., 1984, North Atlantic contourites: an overview: *Geological Society, London Special Publications*, v. 15, p. 245-256.

Stow, D.A.V. and Shanmugam, G., 1980, Sequence of structures in fine-grained turbidites: comparison of recent deep-sea and ancient flysch sediments: *Sedimentary Geology*, v. 25, p. 23-42.

Stuiver, M., 1980, Workshop on ¹⁴C data reporting: *Radiocarbon*, v. 22, p. 964-966.

Stuiver, M. and Braziunas, T.F., 1993, Modeling atmospheric ¹⁴C influences and ¹⁴C ages of marine samples back to 10,000 BC: *Radiocarbon*, v. 35, p. 137-189.

Stuiver, M. and Polach, H.A., 1977, Discussion: Reporting of ^{14}C data: Radiocarbon, v. 19, p. 355-363.

Stuiver, M. and Reimer, P.J., 1993, Extended ^{14}C database and revised CALIB radiocarbon calibration program: Radiocarbon, v. 35, p. 215-230.

Terry, R.D. and Chiligarian, G.V., 1955, Summary of "Concerning some additional aids in studying sedimentary formations" by M.S. Shvetsov: Journal of Sedimentary Petrology, v. 25, p. 229-234.

Tucholke, B.E., Bryan, G.M. and Ewing, J.I., 1977, Gas-Hydrate Horizons Detected in Seismic-Profiler Data from the Western North Atlantic: American Association of Petroleum Geologists Bulletin, v. 61, p. 698-707.

Tucholke B. and Laine, E.P., 1982, Neogene and Quaternary development of the lower continental rise off the central U.S. east coast, *in* Watkins, J.S. and Drake, C.L., eds., Studies in Continental Margin Geology, American Association of Petroleum Geologists Memoir 34, p. 295-305.

Tucholke, B.E., Hollister, C.D., Biscaye, P.E., and Gardner, W.D., 1985, Abyssal current character determined from sediment bedforms on the Nova Scotian continental rise, *in* Nowell, A.R.M. and Hollister, C.D., eds., Deep Ocean Sediment Transport—Preliminary Results of the High Energy Benthic Boundary Layer Experiment: Marine Geology, v. 66, p.43-57.

Tucholke, B.E. and Mountain, G.S., 1986, Tertiary paleoceanography of the western North Atlantic Ocean, *in* Vogt, P.R. and Tucholke, B.E., eds., The Geology of North America, Volume M, The Western North Atlantic Region: Geological Society of America, p. 631-650.

Twichell D.C. and Roberts D.G., 1982, Morphology, distribution, and development of submarine canyons on the United States Atlantic continental slope between Hudson and Baltimore Canyons: Geology, vol. 10, p. 408-412.

Wen, B., Aydin, A. and Duzgoren-Aydin, N.S., 2002, A comparative study of particle size analysis by sieve-hydrometer and laser diffraction methods: Geotechnical Testing Journal, v. 25, p. 434-442.

Wentworth, C.K., 1922, A scale of grade and class terms of clastic sediments: Journal of Geology, v. 30, p. 377-392.

APPENDICES

APPENDIX A

SMEAR-SLIDE DATA

Core RC10-PC01

Depth(cm)	Clay	Silt	Sand	Quartz	Feldspar	Mica	Clay Minerals	Pyrite	Foraminifera	Calc. Nanoplankton	Diatoms	Radiolarian	Sponge Spicules
0	45	50	5	30	-	TR	25	-	20	15	TR	-	TR
10	40	50	10	30	TR	TR	25	-	25	15	-	-	TR
20	45	55	5	35	TR	R	25	-	25	10	-	-	TR
30	35	55	10	35	R	TR	35	-	20	TR	-	-	-
40	45	50	5	45	R	TR	40	-	10	TR	-	-	-
50	40	50	10	50	TR	TR	40	-	TR	TR	-	-	TR
60	40	55	5	45	R	R	35	-	10	TR	-	-	TR
70	40	50	10	45	TR	R	35	-	15	TR	-	-	-
80	40	50	10	45	TR	R	35	-	15	TR	-	-	-
90	40	50	10	45	R	R	35	-	15	TR	-	-	-
100	35	60	5	45	R	R	35	-	15	TR	-	-	-
298	35	45	20	25	-	R	25	-	45	10	-	-	-
798	10	55	35	55	R	10	10	-	25	0	-	-	-

Core EN101-PC01

Depth(cm)	Clay	Silt	Sand	Quartz	Feldspar	Mica	Clay Minerals	Pyrite	Foraminifera	Calc. Nanoplankton	Diatoms	Radiolarian	Sponge Spicules
2.5	70	30	-	35	TR	-	15	-	15	40	TR	-	TR
5	60	40	-	40	2	2	20	-	15	30	TR	-	TR
10	60	40	-	20	TR	-	25	-	20	30	R	-	R
15	60	40	-	40	2	-	25	-	15	30	TR	-	TR
20	55	45	-	40	TR	TR	25	5	5	10	2	-	3
25	55	45	-	30	2	-	20	-	10	35	-	-	2
30	55	45	-	25	2	-	25	-	15	35	TR	-	TR
35	55	45	-	25	TR	-	20	-	15	35	R	-	R
40	55	45	-	35	-	-	20	-	20	30	R	-	TR
50	60	40	-	20	-	-	25	-	20	35	TR	-	R
65	60	40	-	25	-	-	20	-	15	35	TR	-	TR
75	65	35	-	15	TR	-	25	-	20	35	R	-	TR
80	65	35	-	10	-	-	20	-	15	45	TR	-	R
85	65	35	-	10	-	-	25	-	10	45	TR	-	TR
90	65	35	-	10	-	-	20	10	5	45	TR	-	TR
95	55	45	-	10	-	-	20	-	5	40	TR	TR	TR
100	55	45	-	15	-	-	30	-	5	35	TR	-	TR
105	55	45	-	15	-	-	35	-	-	40	TR	-	TR
110	55	45	-	15	-	-	30	-	5	30	5	-	TR
115	55	45	-	15	-	-	25	-	15	35	5	TR	R
210	55	45	-	15	-	-	25	-	15	40	5	TR	R
220	55	45	-	15	-	-	25	-	10	35	TR	-	TR
225	55	45	-	15	-	-	25	-	15	40	R	-	R
235	40	55	5	30	-	-	20	-	10	30	R	-	R
240	40	60	-	30	-	-	20	-	10	35	R	-	R
245	30	65	5	50	-	-	15	-	10	15	R	-	R
250	55	45	-	15	-	-	25	-	10	35	R	-	R
255	45	55	-	20	-	-	15	-	20	35	R	-	R
260	60	40	-	10	-	-	20	-	10	40	R	-	R
265	55	45	-	15	5	-	20	-	10	35	R	-	R
270	45	55	-	25	-	-	20	-	15	30	R	-	R
275	55	45	-	20	-	-	20	-	15	35	R	-	R
280	55	45	-	20	-	-	20	-	15	35	R	-	R
285	55	45	-	15	-	-	25	-	15	35	R	-	R
295	55	45	-	10	-	-	20	-	15	50	R	-	R
300	60	40	-	10	-	-	20	-	10	60	R	-	R
310	60	40	-	15	-	-	25	-	10	45	R	-	R
320	60	40	-	10	-	-	25	-	15	40	TR	-	TR
340	60	40	-	15	TR	-	25	-	15	40	R	-	TR

Core EN101-PC01 (contd.)

Depth(cm)	Clay	Silt	Sand	Quartz	Feldspar	Mica	Clay Minerals	Pyrite	Foraminifera	Calc. Nannoplankton	Diatoms	Radiolarian	Sponge Spicules
345	60	40	-	15	-	-	25	-	15	40	R	-	R
350	65	35	-	15	-	-	25	-	10	40	5	TR	R
355	60	40	-	15	-	-	25	-	10	45	5	-	R
370	60	40	-	10	-	-	20	-	10	50	R	-	R
380	70	30	-	10	-	-	20	-	10	50	R	-	TR
390	70	30	-	15	-	-	25	-	10	45	R	-	TR
400	65	35	-	15	-	-	25	-	15	40	5	-	R
410	65	35	-	15	-	-	25	-	10	40	5	-	TR
420	65	35	-	15	-	-	25	R	15	40	TR	TR	TR
430	65	35	-	10	-	-	25	TR	10	40	5	-	TR
440	60	40	-	15	-	-	20	-	15	35	5	TR	R
480	70	30	-	10	-	-	20	TR	15	50	5	-	R
490	60	40	-	15	-	-	25	TR	10	35	5	-	R
500	70	30	-	10	-	-	20	TR	10	50	R	-	TR
510	70	30	-	10	-	-	25	-	15	45	R	-	TR
520	60	40	-	10	-	-	25	-	15	35	R	TR	TR
530	60	40	-	15	-	-	25	TR	15	35	5	-	TR
540	65	35	-	15	-	-	30	-	15	35	R	-	TR
550	70	30	-	15	-	-	40	TR	10	30	TR	-	TR
567	10	85	5	70	-	-	15	-	10	2	TR	-	TR
570	70	30	-	15	-	-	25	-	15	45	TR	-	TR
580	70	30	-	15	-	-	25	TR	15	45	R	TR	TR
590	65	35	-	15	-	-	25	-	15	45	R	TR	TR
600	60	40	-	15	-	-	25	R	15	40	R	TR	TR
610	65	35	-	15	-	-	25	-	15	40	5	TR	TR
620	70	30	-	15	-	-	20	-	15	50	R	TR	TR
630	70	30	-	15	-	-	25	TR	10	40	R	TR	TR
640	65	35	-	10	-	-	25	TR	15	40	R	-	TR
650	60	40	-	15	-	-	25	TR	15	35	R	-	TR
660	60	40	-	15	-	-	25	TR	10	35	R	-	TR
665	55	45	-	20	-	-	20	TR	15	35	R	-	TR
670	55	45	-	20	-	-	20	TR	15	35	R	-	TR
675	70	30	-	15	-	-	25	-	10	45	TR	-	TR
680	65	35	-	10	-	-	25	-	15	40	R	-	R
685	65	35	-	15	-	-	20	R	10	45	TR	-	TR
690	70	30	-	10	-	-	20	TR	10	45	TR	-	TR
695	65	35	-	10	-	-	25	TR	10	45	TR	-	TR
700	70	30	-	10	-	-	25	TR	10	45	TR	-	TR

Core EN101-PC01 (contd.)

Depth(cm)	Clay	Silt	Sand	Quartz	Feldspar	Mica	Clay Minerals	Pyrite	Foraminifera	Calc. Nannoplankton	Diatoms	Radiolarian	Sponge Spicules
705	65	35	-	10	-	-	25	TR	10	45	TR	-	TR
710	65	35	-	15	-	-	25	TR	10	40	TR	-	TR
715	65	35	-	10	-	-	25	TR	10	45	TR	-	TR
720	70	30	-	10	-	-	25	-	10	45	TR	-	TR
730	65	35	-	15	-	-	25	TR	10	40	TR	-	TR
740	60	40	-	15	-	-	25	TR	10	40	TR	-	TR
750	60	40	-	20	-	-	20	TR	10	45	TR	-	TR
760	65	35	-	15	-	-	25	TR	10	40	TR	-	TR
770	65	35	-	10	-	-	25	-	15	45	TR	-	TR
780	65	35	-	10	-	-	30	-	15	40	TR	-	TR
790	60	40	-	10	-	-	25	-	15	35	TR	-	TR

Core EN084-GC02

Depth(cm)	Clay	Silt	Sand	Quartz	Feldspar	Mica	Clay Minerals	Pyrite	Foraminifera	Calc. Nannoplankton	Diatoms	Radiolarian	Sponge Spicules
0	40	60	-	50	TR	-	35	-	5	-	-	-	-
5	35	60	5	50	TR	-	35	-	5	5	-	-	-
10	40	60	-	55	R	-	35	-	5	5	-	-	-
15	40	60	-	55	TR	R	40	-	-	-	-	-	TR
17	10	85	5	70	10	10	10	-	-	-	-	-	-
20	40	60	-	55	TR	TR	40	-	1	1	-	-	-
25	35	63	-	55	TR	TR	35	-	1	5	-	-	TR
30	45	55	-	50	TR	TR	40	-	1	2	-	TR	TR
35	55	45	-	40	TR	R	45	-	1	3	TR	-	TR
40	40	60	-	50	5	R	35	TR	5	1	TR	-	TR
45	60	40	-	30	-	-	60	-	5	5	-	-	-
50	25	70	5	70	R	R	25	-	1	-	-	-	-
55	40	60	-	55	5	5	30	-	-	3	-	-	-
60	45	55	-	50	TR	TR	40	-	1	5	-	-	-
65	35	60	5	60	TR	5	30	-	5	1	-	-	-
70	55	45	-	45	-	-	40	5	-	10	-	-	-
75	60	40	-	35	-	-	45	5	-	15	-	-	-
80	30	70	-	60	5	5	25	-	-	5	-	-	-
85	35	65	-	55	5	5	30	-	-	1	-	-	-
90	35	60	5	55	5	5	35	-	-	1	-	-	-
95	40	60	-	55	R	R	35	-	-	5	-	-	-
100	30	70	-	60	5	5	30	-	-	1	-	-	-
105	35	65	-	60	R	R	35	-	-	5	-	-	-
110	5	85	10	75	10	10	5	-	-	-	-	-	-
113	5	85	10	75	10	10	5	-	-	-	-	-	-
115	35	65	-	55	TR	R	35	TR	-	-	-	-	-
120	60	40	-	40	-	-	55	5	-	-	-	-	-
125	40	60	-	50	TR	R	40	TR	-	-	-	-	-
165	65	35	-	15	R	-	25	-	15	35	R	-	R
170	65	35	-	15	-	-	30	-	15	35	TR	-	TR
175	65	35	-	10	TR	TR	30	TR	15	35	TR	TR	TR
180	65	35	-	10	TR	TR	30	-	15	35	TR	-	TR
185	65	35	-	15	TR	TR	30	TR	10	30	TR	-	TR
190	65	35	-	15	TR	TR	30	TR	15	30	TR	-	TR
195	65	35	-	15	-	-	35	-	15	30	TR	-	TR
200	65	35	-	15	-	-	35	TR	20	25	TR	-	TR
205	60	40	-	10	TR	TR	30	-	15	30	TR	-	TR
210	65	35	-	15	TR	TR	30	-	15	30	TR	-	TR
215	50	50	-	20	TR	TR	35	-	20	15	TR	-	TR

Core EN084-GC02 (contd.)

Depth(cm)	Clay	Silt	Sand	Quartz	Feldspar	Mica	Clay Minerals	Pyrite	Foraminifera	Calc. Nanoplankton	Diatoms	Radiolarian	Sponge Spicules
220	65	35	-	15	TR	TR	35	TR	15	25	-	-	TR
225	65	35	-	15	TR	TR	35	TR	15	30	-	-	TR
230	70	30	-	10	-	-	40	TR	10	30	TR	-	TR
235	35	65	-	45	-	R	25	-	10	15	-	-	TR
240	40	60	-	50	TR	R	35	-	5	5	TR	-	TR
245	40	60	-	45	TR	R	40	-	5	5	TR	-	TR
250	40	60	-	55	TR	R	35	TR	5	5	TR	-	TR
255	10	85	5	75	5	10	10	-	-	-	-	-	-
260	10	85	5	80	5	10	5	-	-	-	-	-	-
265	40	60	-	55	TR	TR	40	TR	-	-	-	-	-
270	35	65	-	60	TR	TR	35	TR	-	1	-	-	-

APPENDIX B

GRAIN-SIZE DATA

Core RC10-PC01

Depth (cm)	Mean (Phi)	Std Dev	Std Err Mean	Lower 95%	Upper 95%
0	5.04	2.98	0.32	4.41	5.67
10	4.81	3.10	0.33	4.15	5.46
20	5.89	2.04	0.22	5.46	6.32
30	6.12	2.08	0.22	5.68	6.55
40	6.61	1.91	0.20	6.21	7.02
50	6.70	1.93	0.20	6.29	7.10
60	6.03	1.97	0.21	5.61	6.44
70	6.91	2.09	0.22	6.47	7.35
80	6.35	1.99	0.21	5.93	6.77
90	6.21	2.18	0.23	5.75	6.67
100	6.21	1.84	0.20	5.81	6.60

Core EN101-PC01

Depth (cm)	Mean (Phi)	Std Dev	Std Err Mean	Lower 95%	Upper 95%
2.5	7.14	2.22	0.24	6.67	7.61
5	6.36	2.78	0.29	5.77	6.95
10	7.30	1.97	0.21	6.88	7.72
15	6.88	2.40	0.26	6.37	7.39
20	6.83	2.26	0.25	6.34	7.32
25	6.46	2.03	0.22	6.03	6.89
30	6.51	1.95	0.21	6.10	6.93
35	6.29	2.05	0.22	5.85	6.72
40	6.38	2.13	0.23	5.92	6.83
50	6.72	2.24	0.24	6.25	7.20
65	6.15	1.97	0.21	5.73	6.56
75	6.38	2.10	0.22	5.93	6.82
80	7.38	1.61	0.17	7.03	7.72
85	7.24	1.82	0.19	6.86	7.63
90	7.50	1.52	0.16	7.18	7.82
95	7.18	2.07	0.22	6.74	7.62
100	7.12	2.10	0.22	6.68	7.57
105	7.12	2.10	0.22	6.68	7.57
110	7.18	1.94	0.21	6.77	7.60
115	7.21	1.88	0.21	6.80	7.62
215	6.77	2.41	0.26	6.26	7.28

Core EN101-PC01 (contd.)

Depth (cm)	Mean (Phi)	Std Dev	Std Err Mean	Lower 95%	Upper 95%
220	6.90	2.30	0.25	6.42	7.39
225	7.21	2.13	0.22	6.77	7.65
235	6.82	2.11	0.23	6.38	7.27
240	7.26	1.66	0.17	6.91	7.61
245	7.65	1.57	0.17	7.32	7.98
250	6.79	1.97	0.21	6.37	7.21
255	6.36	2.16	0.23	5.90	6.82
260	6.71	2.24	0.24	6.23	7.18
265	6.06	2.08	0.22	5.61	6.50
270	5.65	2.16	0.23	5.19	6.10
275	6.11	2.11	0.22	5.66	6.55
280	5.67	2.23	0.24	5.20	6.14
285	5.63	2.28	0.24	5.16	6.11
295	7.10	2.23	0.24	6.62	7.57
300	7.28	1.97	0.21	6.86	7.71
310	7.07	2.06	0.22	6.63	7.51
320	7.41	1.88	0.20	7.02	7.81
335	7.35	1.92	0.20	6.95	7.75
340	7.07	1.81	0.19	6.69	7.46
345	7.30	1.74	0.19	6.92	7.67
350	7.17	1.75	0.19	6.80	7.54
355	7.34	1.57	0.17	7.01	7.67
370	7.26	1.84	0.20	6.87	7.65
380	7.43	1.69	0.18	7.06	7.79
390	7.28	1.95	0.21	6.87	7.69
400	7.30	2.03	0.21	6.87	7.73
410	7.32	2.03	0.21	6.90	7.74
420	7.31	2.04	0.22	6.88	7.74
430	7.26	2.05	0.22	6.83	7.69
440	7.47	1.72	0.18	7.11	7.83
480	7.32	2.06	0.22	6.88	7.76
490	7.52	1.70	0.18	7.16	7.88
500	7.34	2.12	0.22	6.90	7.79
510	7.46	1.95	0.21	7.05	7.87
520	7.80	1.50	0.16	7.48	8.11
530	7.81	1.52	0.16	7.48	8.13
540	7.60	1.88	0.20	7.20	7.99
550	7.79	1.51	0.16	7.47	8.11
567	5.66	1.76	0.18	5.29	6.03
570	7.28	2.32	0.25	6.78	7.77
580	7.28	2.31	0.24	6.80	7.76
590	7.02	2.46	0.26	6.49	7.54
600	7.18	2.26	0.24	6.70	7.66
610	7.14	2.36	0.25	6.63	7.65
620	7.31	2.33	0.25	6.82	7.80
630	7.34	2.31	0.24	6.85	7.82

Core EN101-PC01 (contd.)

Depth (cm)	Mean (Phi)	Std Dev	Std Err Mean	Lower 95%	Upper 95%
640	7.35	2.08	0.22	6.90	7.79
650	5.95	2.08	0.22	5.51	6.39
660	6.31	2.11	0.22	5.86	6.75
665	6.10	2.32	0.25	5.60	6.59
670	7.13	1.80	0.19	6.74	7.51
675	7.28	2.18	0.24	6.81	7.75
680	7.06	2.26	0.24	6.58	7.54
685	7.57	1.91	0.20	7.17	7.97
690	7.41	2.07	0.22	6.97	7.86
695	7.80	1.95	0.21	7.39	8.21
700	7.78	1.96	0.21	7.36	8.19
705	7.62	2.23	0.24	7.15	8.09
710	7.81	1.96	0.21	7.40	8.23
715	7.52	2.26	0.24	7.05	8.00
720	7.63	1.55	0.17	7.29	7.97
725	7.63	1.54	0.16	7.31	7.96
730	7.40	1.88	0.20	7.01	7.80
735	7.57	1.53	0.16	7.24	7.89
740	7.58	1.51	0.16	7.26	7.89
745	7.57	1.52	0.16	7.25	7.88
750	7.58	1.54	0.16	7.25	7.91
760	7.63	1.52	0.16	7.30	7.95
770	7.51	1.84	0.20	7.12	7.90
780	7.54	1.72	0.18	7.17	7.91
790	7.32	2.02	0.22	6.89	7.75
800	7.48	1.81	0.20	7.09	7.87

Core EN084-GC02

Depth (cm)	Mean (Phi)	Std Dev	Std Err Mean	Lower 95%	Upper 95%
0	6.30	1.77	0.19	5.93	6.68
5	5.90	2.12	0.23	5.45	6.35
10	6.47	1.96	0.21	6.05	6.88
15	5.79	2.04	0.21	5.36	6.21
17	4.40	1.19	0.12	4.15	4.64
20	6.13	2.03	0.21	5.70	6.55
25	6.70	1.89	0.20	6.30	7.10
30	6.48	1.99	0.21	6.06	6.90
35	6.53	1.90	0.20	6.12	6.93
40	4.51	1.38	0.15	4.22	4.80
45	6.66	1.96	0.21	6.24	7.08

Core EN084-GC02 (contd.)

Depth (cm)	Mean (Phi)	Std Dev	Std Err Mean	Lower 95%	Upper 95%
50	6.62	1.53	0.16	6.30	6.94
55	6.47	1.81	0.19	6.09	6.85
60	6.73	2.00	0.22	6.30	7.16
65	6.05	1.87	0.20	5.66	6.44
70	7.32	1.84	0.19	6.94	7.71
75	7.18	1.71	0.18	6.82	7.54
80	6.13	1.90	0.20	5.74	6.53
85	7.02	1.85	0.20	6.62	7.41
90	6.74	1.88	0.20	6.35	7.14
95	6.82	1.78	0.19	6.44	7.19
100	6.74	1.88	0.20	6.35	7.14
105	6.47	1.84	0.20	6.08	6.86
110	4.65	1.50	0.16	4.34	4.97
113	3.69	0.84	0.09	3.52	3.87
120	7.28	1.42	0.15	6.98	7.58
125	6.90	1.67	0.18	6.55	7.26
165	7.07	1.87	0.20	6.68	7.47
170	7.23	1.62	0.17	6.88	7.57
175	7.24	1.62	0.17	6.90	7.59
180	7.24	1.62	0.17	6.90	7.59
185	7.27	1.62	0.17	6.92	7.61
190	7.25	1.61	0.17	6.91	7.60
195	7.25	1.61	0.17	6.91	7.60
200	7.11	1.76	0.19	6.73	7.48
205	7.07	1.77	0.19	6.69	7.45
210	6.57	2.11	0.23	6.13	7.02
215	6.33	1.98	0.21	5.91	6.74
220	6.84	2.07	0.22	6.40	7.27
225	6.80	2.08	0.22	6.35	7.24
230	6.84	1.93	0.20	6.43	7.24
235	5.13	1.88	0.20	4.74	5.52
240	6.28	1.87	0.20	5.88	6.67